# TOPK AS A NOVEL DETERMINANT OF RADIOSENSITIVITY

Giacomo Maria Pirovano

Cancer Research UK and Medical Research Council
Oxford Institute for Radiation Oncology

Clarendon Scholar
Brasenose College


**A thesis submitted for the degree of Doctor of Philosophy**
**University of Oxford, Trinity Term, 2016**


# ABSTRACT

Giacomo Maria Pirovano, Brasenose College

Submitted for the degree of DPhil, University of Oxford, Trinity Term, 2016

Radiotherapy is the use of ionising radiation to induce localised DNA damage to cancerous tissues, leading to cell death and disease control. In order to maximise tumour growth control and to limit damage of the healthy surrounding tissues and the consequent side effects for the patient, molecular determinants of tumour radioresistance are investigated as potential clinical targets.

A high-throughput siRNA colony formation assay screen in HeLa cervical carcinoma cells previously published by our laboratory identified modulators of radiosensitivity. From the list *CSF1R*, *EPHB2*, *GAK* and *TOPK*, were selected and validated. *TOPK* (T-LAK cell-originated protein kinase, also known as PDZ-binding kinase, PBK) was selected for further investigation because it is overexpressed in most malignancies but not in normal tissues, apart from testis and placenta. Knockdown of *TOPK* was shown to induce radiosensitisation in a panel of cancer cell lines with no significant effects on normal cells. A role for TOPK in the cell cycle response to ionising radiation (IR) was discovered in HCT116 colorectal cancer cells, with alterations in the $G_1$/S and $G_2$/M checkpoints. Furthermore, immunoprecipitation experiments identified a physical interaction between TOPK and CDKN1A (p21) at 8 hours after IR. Apoptosis and the number of multinucleated cells were significantly increased in *TOPK* depleted cells exposed to IR, suggesting the possibility of aberrant mitosis and mitotic catastrophe in these cells. High *TOPK* expression in early breast cancer patients was shown to be associated with poor recurrence-free survival. In addition, immunohistochemistry (IHC) analysis on samples from prostate cancer patients identified a strong correlation between high levels of TOPK and poor clinical response to radiotherapy.

In order to facilitate future *in vivo* experiments, an HCT116 shRNA stable knockdown cell line was developed and two commercially available TOPK inhibitors were tested and optimised.

Taken together, these data suggest that TOPK is a molecular determinant of radiosensitivity with a great potential for future clinical applications.

*To Marialuisa Sacchetti,*
*Stefano Pirovano.*

## ACKNOWLEDGEMENTS

First and foremost I would like to thank my supervisors, Professor Gillies McKenna for giving me the opportunity to carry out the DPhil in his laboratory and Dr Thomas Ashton for his continued support, encouragement and advice throughout the past four years. I must give a special thank you to Dr Geoff Higgins for his supervision and continuous mentoring. It has been a pleasure and an honour to work for them.

I would like to thank everyone else in the McKenna/Higgins lab, Dr Remko Prevo and Dr Gonzalo Rodriguez-Berriguete for their never-ending patience in discussing biology with me, Dr Katharine Herbert for contributing to the TOPK project, Lianne Castle, Martin-Immanuel Bittner, Daniel McGowan and Michael Skwarski, and in particular I wish the best luck to Giovanna Granata and James Coates in their DPhil careers. I would also like to thank former lab members Gagan Tiwana, Dorine Bax, Jessica Carter and Patsy Adamo.

This research would not have been completed without the collaboration of many other scientists inside and outside of the department. Between these, a special thank you to Professor Amato Giaccia and Professor Eric O'Neill, the examiners of my thesis, for their valuable feedback on my work, to Professor Ruth Muschel for the in vivo facilities, to Dr Francesca Buffa for the breast cancer patients prognostic data, to Dr Iolanda Vendrell for the mass spectrometry data, to Dr Richard Bryant, Lucia Cerundolo and Dr Clare Verrill for the immunohistochemistry data, and thank you to all those who challenged me scientifically and gave me the ideas that led to the results presented in this thesis.

Finally thank you to Cancer Research UK, the Clarendon Fund and Brasenose College for the economical contribution to my scholarship, I commit to contribute back to this virtuous cycle one day.

# TABLE OF CONTENTS

TOPK AS A NOVEL DETERMINANT OF RADIOSENSITIVITY

# ABBREVIATIONS AND ACRONYMS

| | |
|---|---|
| ˚C | Celsius degrees |
| ~ | circa |
| 53BP1 | p53-binding protein 1 |
| AKT | Protein kinase B |
| $As^{3+}$ | Arsenite |
| ATCC | American Type Culture Collection |
| ATM | Ataxia telangiectasia mutated |
| ATR | Ataxia telangiectasia and Rad3-related protein |
| BRAF | Proto-oncogene B-Raf |
| BrdU | Bromodeoxyuridine |
| BSA | Bovine serum albumin |
| Cdc2 | Cyclin-dependent kinase 1 (CDK1) |
| CDK | Cyclin-dependent kinase |
| cDNA | Complementary DNA |
| CFA | Colony formation assay |

| | |
|---|---|
| Co-IP | Co-immunoprecipitation |
| CRC | Colorectal cancer |
| CRISPR | Clustered regularly interspaced short palindromic repeats |
| CSF1R | Colony stimulating factor 1 receptor |
| cT | Clinical T-stage |
| CtIP | CtBP-interacting protein |
| DAPI | 4',6-diamidino-2-phenylindole |
| DBD | DNA-binding domain |
| DDR | DNA-damage response |
| DMEM | Dulbecco's modified Eagle's medium |
| DMSO | Dimethyl sulfoxide |
| DNA-PK | Complex formed of DNA-$PK_{cs}$ and Ku70-Ku80 |
| DNA-$PK_{cs}$ | DNA-dependent protein kinase catalytic subunit |
| DSB | Double-strand break |
| dsRNA | Double stranded RNA |
| DTT | Dithiothrietol |
| ECL | Enhanced chemiluminescence |

| | |
|---|---|
| EDTA | Ethylenediaminetetraacetic acid |
| EGFR | Epidermal growth factor receptor |
| EPHB2 | Ephrin type-B receptor 2 |
| esiRNA | Endoribonuclease-prepared short interfering RNAs |
| FACS | Fluorescence activated cell sorting |
| FBS | Foetal bovine serum |
| FDR | False discovery rate |
| FEN1 | Flap endonuclease 1 |
| FITC | Fluorescein isothiocyanate |
| FU | Follow-up |
| g | Earth's gravitational force (= 9.807 $m/s^2$) |
| $G_1$ | Gap 1 phase of the cell cycle |
| $G_2$ | Gap 2 phase of the cell cycle |
| GAK | Cyclin G-associated kinase |
| GAPDH | Glyceraldehyde 3-phosphate dehydrogenase |
| Gy | Gray (defined as the absorption of one joule of radiation energy per kilogram of matter) |
| h | Hour |

| | |
|---|---|
| H2AX | H2A histone family, member X |
| hDlg | Human homologue of Drosophila tumour suppressor Discs-Large (Dlg) |
| HI-TOPK-032 | TOPK inhibitor purchased from Sigma |
| HIST1H2AG | Histone H2A type 1 |
| HR | Homologous recombination |
| HRP | Horseradish peroxidase |
| i.v. | Intravenous |
| IAA | Iodoacetamide alkylating agent |
| IF | Immunofluorescence |
| IHC | Immunohistochemistry |
| IMRT | Intensity modulated radiotherapy |
| IP | Immunoprecipitation |
| IR | Irradiation |
| IκBα | Nuclear factor of kappa light polypeptide gene enhancer in B-cells inhibitor, alpha |
| k.o. | Knock-out |
| kb | Kilobase |
| kDa | KiloDalton |

| | |
|---|---|
| KRAS | V-Ki-ras2 Kirsten rat sarcoma viral oncogene homolog |
| Ku70 | Lupus Ku autoantigen protein p70 |
| Ku80 | Lupus Ku autoantigen protein p80 |
| LC-Ms/Ms | Liquid chromatography mass spectrometry |
| LET | Linear energy transfer |
| Lig3 | DNA ligase 3 |
| Lig4 | DNA Ligase IV |
| M-phase | Mitotic phase |
| mA | Milliampere |
| MAP2K2 | MEK2 - Dual specificity mitogen-activated protein kinase kinase 2 |
| MDC1 | Mediator of DNA damage checkpoint protein 1 |
| MDM2 | Mouse double minute 2 homologue |
| min | Minute |
| MOI | Multiplicity of infection |
| MRI | Magnetic resonance imaging |
| MRN | MRE11/RAD50/NSB1 |
| mRNA | Messenger ribonucleic acid |

| | |
|---|---|
| Ms/Ms | Mass spectrometry |
| NBS1 | Nibrin |
| NCI | National Cancer Institute |
| NF-κB | Nuclear factor kappa-light-chain-enhancer of activated B cells |
| ng | Nanograms |
| NGS | Normal goat serum |
| NHEJ | Non-homologous end joining |
| NS | Non-specific |
| NSCLC | Non-small-cell lung carcinoma |
| NT | Non-targeting |
| nt | Nucleotide |
| NTCP | Normal tissue complication probabilities |
| OTS964 | TOPK inhibitor purchased from DC Chemicals |
| p21 | CDKN1A also known as *p21waf1/cip1* |
| p38 | Mitogen-activated protein kinase |
| PARP-1 | Poly [ADP-ribose] polymerase 1 |
| PBK | PDZ-binding kinase, also known as TOPK |

| | |
|---|---|
| PBS | Phosphate buffered saline |
| PCR | Polymerase chain reaction |
| PE | Plating efficiency |
| Pen | Penicillin |
| PET | Positron emission tomography |
| PFA | Paraformaldehyde |
| PFP | Percentage of false positives |
| PI | Propidium iodide |
| PI3K | Phosphoinositide 3-kinase |
| PLK-1 | Polo-like kinase-1 |
| Polθ | POLQ, DNA polymerase theta |
| PRB | Protein running buffer |
| PRKDC | DNA-$PK_{cs}$ |
| PSA | Prostate specific antigen |
| PTEN | Phosphatase and tensin homolog |
| qPCR | Real-time polymerase chain reaction |
| Rb | Retinoblastoma protein |

| | |
|---|---|
| RFS | Recurrence-free survival |
| RIPA | radioimmunoprecipitation assay |
| RISC | RNA-Induced Silencing Complex |
| RLC | RISC-loading complex |
| RNAi | RNA interference |
| ROS | Reactive oxygen species |
| RPMI | Roswell Park Memorial Institute |
| $R_{score}$ | Radiosensitivity scores |
| RT | Room temperature |
| RT-PCR | Reverse transcriptase PCR |
| S-phase | S phase of the cell cycle |
| SD | Standard deviation |
| SDS-Page | Sodium dodecyl sulfate polyacrylamide gel electrophoresis |
| $SER_{10}$ | Survival enhancement ratio at 0.10 surviving fraction |
| SF | Surviving fraction |
| SFN | 14-3-3 protein sigma |
| shRNA | Small hairpin RNA or short hairpin RNA |

| | |
|---|---|
| siNT | Non targeting siRNA silencing |
| siRNA | Small-interfering RNA |
| siTOPK | TOPK siRNA silencing |
| SSB | Single strand break |
| TCA | Trichloroacetic acid |
| TCP | Tumour control probability |
| TdT | Terminal deoxynucleotidyl transferase |
| TFA | Trifluoroacetic acid |
| TNM | Classification of Malignant Tumours |
| TOPK | T-LAK cell-originated protein kinase |
| TOPK KD | TOPK kinase dead |
| TRIM21 | E3 ubiquitin-protein ligase TRIM21 |
| TRIM25 | E3 ubiquitin/ISG15 ligase TRIM25 |
| Tris | Tris-hydroxymethylamino methane |
| TUBA1C | Tubulin alpha-1C chain |
| TUBA8 | Tubulin alpha-8 chain |
| Tween20 | Polyethylene glycol sorbitan monolaurate |

| | |
|---|---|
| XLF | XRCC4-like factor |
| XRCC4 | X-ray repair cross-complementing protein 4 |
| XRCC6 | Ku70 - X-ray repair cross-complementing protein |
| γ-H2AX | Phosphorylated-H2AX histone |

# CHAPTER 1

# GENERAL INTRODUCTION

## 1.1 Cancer and radiotherapy

Cancer is a disease responsible for about 13% of the total deaths in humans. Every year over 7 million people die of cancer making it the second leading cause of death after heart disease [1]–[3]. Recent data produced by Cancer Research UK showed that in 2013 more than 350,000 people were diagnosed with cancer and that the related deaths were above 160,000 in 2012 in the United Kingdom [4].

Radiotherapy is used in the treatment of about 50% of all cancer patients for localised tumours and can also be used in combination with drug treatment such as chemotherapy [2], [3], [5], [6]. The decision upon the type of treatment and the use of radiotherapy, either internally or externally delivered, is taken mostly depending on the histological data of the patients and on the anatomical characteristics of the tumour site. Radiation therapy is predominantly delivered to patients with tumours located at sites such as the central nervous system, cervix, bladder, breast, lung, prostate, oesophageal, stomach and head and neck [3]. Radiotherapy treatment can also be delivered neoadjuvantly or adjuvantly with other treatments, typically surgery. In addition it can be used symptomatically to palliate symptoms in patients with incurable disease [7]–[10].

Radiotherapy relies on the DNA damage induced by radiation and aims to produce targeted damage to the tumour cells in order to induce cell death [10].

## 1.2 Ionising radiation and DNA

The interaction of radiation with any biological system consists of a series of subsequent processes that can be divided into three main phases; physical phase, chemical phase and biological phase [10]. The physical phase is the earliest set of interactions and is defined to a time range of $10^{-18}$ to $10^{-12}$ seconds. During this period of time, the charged particle interacts with the atoms that compose the tissue which can be therefore excited or ionised. An acute 1 Gy of absorbed radiation dose can produce about $10^{5}$ ionisations in a cell of 10 μm in diameter [10], producing a cascade of chemical reactions. The chemical phase consists of the molecular interactions which follow radiation. Typically, the important events of this stage are the balancing of free-radicals and scavenging factors [11], [12], which can substantially modify the amount and quality of total damage to the DNA. This phase typically spans from $10^{-12}$ to 10 seconds post irradiation [10]. The biological phase refers to all the subsequent processes including DNA-damage repair and eventually senescence or cell death few days after the damage formation [13]–[15].

It has been shown that the main factor that leads to cell lethality after ionising radiation (IR) is DNA damage [10], [13], [16] and the aim of radiotherapy is to induce DNA damage in cancer cells in order to control their development and therefore the disease.

### 1.2.1 Exogenous DNA damage

Radiotherapy consists of the use of photons with energies typically from 100 keV to several MeV to ionise the biological matter [16] and induce a cascade of events, including the breaking of chemical bonds in the DNA, generating DNA damage in a direct and indirect way (Figure 1.1)[10], [16].

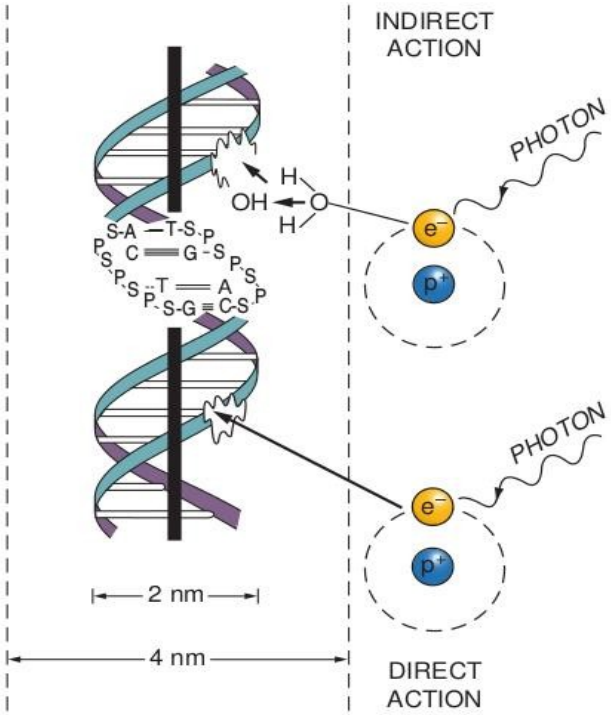


*Figure 1.1: Graphical representation of indirect (top) and direct (bottom) IR-induced DNA damage (Figure from [16]). In the cascade of interactions induced by the photon-induced ionisations, free radical molecules can be generated. These highly reactive species diffuse in the cellular nucleus and are capable of causing DNA damage. The damage can also be generated by direct interaction of the excited electron and the DNA chain.*

IR induces a vast array of DNA lesions depending on the spatial distribution of the breaks along the strands of the helical DNA structure and the complexity of the damage [10], [16], [17]. It is known [10] that 1 Gy of radiation can induce around 1000 single-strand breaks (SSBs) and around 20-40 double-strand breaks (DSBs) per cell with a total of about $10^5$ ionisations (Figure 1.2). DSBs are considered to be the main predictor of cellular outcome. The density of IR-induced damage depends also on the amount of energy released by the radiation into matter. This is described by the linear energy transfer (LET), which is the rate of energy loss along the track of an ionising particle expressed in keV/μm [10].

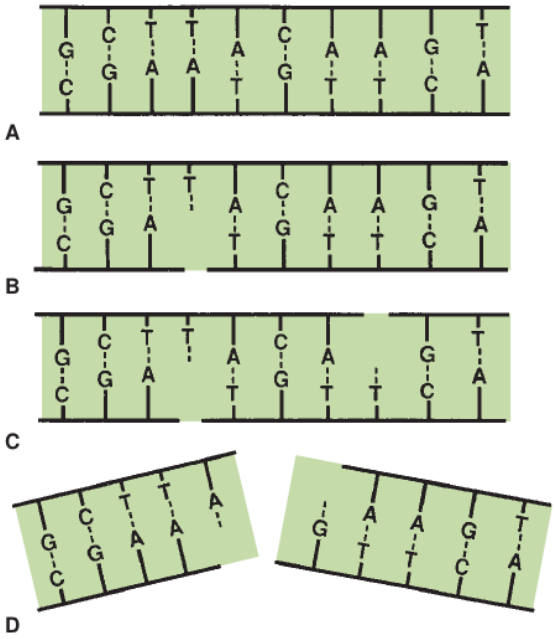


*Figure 1.2: Two-dimensional representation of the DNA double-helix structure (Figure from [16]) showing (A) Undamaged DNA, (B) A single-strand break, (C) Two single-strand breaks closely localised to form a double-strand break, and (D) A double-strand break lesion.*

### 1.2.2 Endogenous DNA damage

Because of its crucial role in carrying the genetic information, the DNA is a highly stable molecule. However, even in absence of external damaging factors, spontaneous changes in the molecular structure occur at the rate of at least 10,000 mutations per cell per day in humans [18]. Naturally occurring endogenous DNA damage can result from metabolic or hydrolytic processes and the produced reactive molecular species leading to alkylation and oxidation.

## 1.3 Cellular DNA-damage response

If left unrepaired, the damaged DNA could be replicated, and DNA mutations would be inherited by future cell generations with potential disastrous consequences for the organism. For this reason, cells have evolved a prompt and efficient DNA damage response (DDR), which repairs the DNA in order to limit the detrimental effects on the cell. The DDR is a complex coordinated process involving many different steps with multiple different proteins and pathways, and is an area of intense ongoing academic investigation. As an initial event, the DNA damage is identified by sensing proteins which trigger a signalling cascade and help chromatin to unwind in order to grant access to the damaged DNA site for repair to occur. Modifications in the cell behaviour, such as cell cycle arrest through checkpoint activation, allow the cell to prioritise the repair over other cellular activities such as DNA replication and cellular division [10], [19]–[22].

### 1.3.1 Early cellular response to DNA damage

The earliest response to the DNA damage is mediated by a group of proteins considered to be the sensors of the damage [10]. In the literature some conflicting evidence can be found about the exact sequence of events that trigger the DDR. This could be due to cell-line specific differences and is still under investigation. The sensor proteins actively survey the DNA and are activated in seconds or minutes after the induced damage. This process triggers the DDR and the following pathways for programmed cell death [15], DNA repair [23], and temporary cell cycle arrest [22], [24]. The following description is not an exhaustive description of these complex processes but only aims at giving a general idea and introducing the main players of this complex cellular mechanism.

One of the earliest events for the detection and localisation of DSBs, happening within 5-30 minutes after the damaging event, is the

phosphorylation of the histone H2AX at serine 139 to generate γ-H2AX by the ataxia telangiectasia mutated (ATM) protein. This co-localises with the DNA damage site, binding to the double-stranded DNA either side of the DSB, and can be detected with immunofluorescence techniques in the form of foci [25], [26]. The steps required for this process are still under investigation and contrasting evidence is provided in literature. The damage site is recognised by the MRN complex, comprised of the MRE11, RAD50 and NBS1 proteins. Consequently the γ-H2AX histone binds to a larger region of 2 Mbp to 30 Mbp either side of the DSB in a complex with MDC1 [10]. Other proteins are responsible for early damage recognition and phosphorylation of H2AX. These are the DNA-PK complex, formed of DNA-$PK_{cs}$ and Ku70-Ku80, and ATR, which are recruited at the damage site at an early stage.

In eukaryotic cells, after the damage has been recognised and localised, DNA DSBs can be repaired by two mayor pathways: non-homologous end joining (NHEJ) and homologous recombination repair (HRR or HR) [10], [16], [27]. In mammalian cells, the choice of repair is determined by the phase of the cell cycle, by the abundance of repetitive DNA, and by other factors which are still unknown [28].

### 1.3.2 Non-homologous end joining repair

Non-homologous end joining (NHEJ) is responsible for repairing about 80% [29] of DNA DSBs and is activated very quickly, only a few minutes after the DNA has been damaged. It is a less accurate process compared to its competing pathway, homologous recombination, and it does not require a homologous stretch of DNA as a template. NHEJ consists in the joining of two DSB ends, which may involve the loss of genetic information, with the potential risk of fatal cellular repercussions. The efficacy of NHEJ in the cell survival depends on the fact that only a small percent of the genome contains coding regions [18] and the repair of these regions does not have to

involve faithful copying using the sister chromatid as a template to permit cell survival.

After sensing the DSB damage, the main steps of NHEJ involve nucleases to remove the damaged DNA, polymerases to synthesise the new sequence and ligases to bind the DNA ends and restore a continuous molecule as described in Figure 1.3.

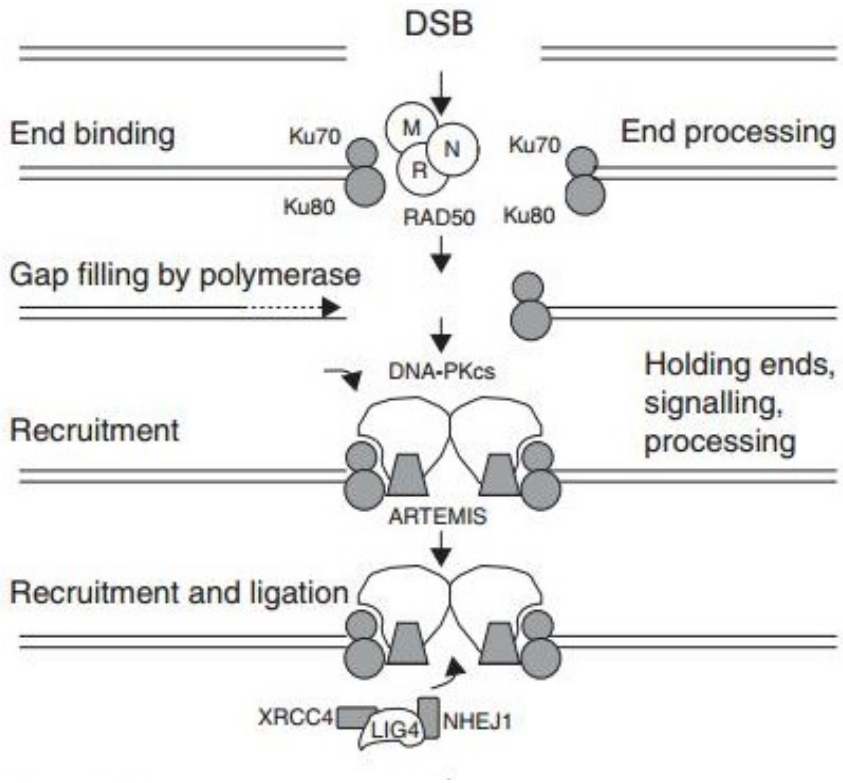


*Figure 1.3: Schematic representation of double-strand break repair via non-homologous end joining (Figure from [10]). The heterodimers Ku70 and Ku80 bind to the DNA ends together with the MRN complex and start the recruitment of PRKDC, Artemis and, subsequently, the ligation proteins XRCC4, XLF and DNA Ligase IV. The NHEJ repair pathway can lead to small deletions or insertions in the DNA sequence in order to preserve genetic stability.*

Within seconds after DSB formation, the heterodimers Ku70 and Ku80 bind to the DNA ends. This high affinity interaction serves for protecting the DNA ends from exonuclease degradation and to recruit PRKDC to the damaged site [30]. PRKDC, the DNA-dependent protein

kinase catalytic subunit (also known as DNA-$PK_{cs}$), forms a physical bridge between the two broken ends and, at the same time, phosphorylates a large number of substrates. X-ray repair cross-complementing protein 4 (XRCC4), XRCC4-like factor (XLF) and DNA Ligase IV assemble at the site as well and start a complex DNA-damage response cascade [10], [30]–[32]. When the damage is complex and it involves a large area of the DNA chain, other important elements of the repair process are needed in order to overcome the complexity in rejoining the loose DNA ends. These include Artemis, which is recruited to bind to the DNA in order to process the loose ends to make them suitable for ligation [33]. The translation synthesis polymerases Polλ, Polμ and TdT (terminal deoxynucleotidyl transferase) perform gap filling, introducing complementary bases in the single-stranded regions at either side of the break in order to make these regions double-stranded. For this reason breaks repaired via NHEJ often show small insertions [10]. The final step is the ligation of the adjoining ends carried out by ligase IV together with XRCC4 and XLF [34], [35] (Figure 1.3).

Under particular circumstances, such as the absence of Ku, Lig4 or DNA-$PK_{cs}$, NHEJ is substituted by alternative end-joining (Alt-EJ) [36], which has been described as a DSB repair pathway. Alt-EJ is commonly associated with high levels of chromosomal rearrangements and is considered to be highly mutagenic. This process is mediated via FEN1, CtIP, MRN complex, PARP-1 and DNA ligase 3 (Lig3) and it has been recently linked to the low fidelity DNA polymerase Polθ (POLQ) [37] but the mechanism determining the choice of classic NHEJ or Alt-EJ is still unclear and is under investigation [38]–[41].

### 1.3.3 Homologous recombination repair

Homologous recombination repair (HR) is considered to be an error-free pathway that uses the undamaged sister chromatid as a template to repair a double strand break. Because the sister chromatid is required as a template, it is only possible for a cell to undergo HR once the DNA has been replicated, which occurs in the S-phase of the cell cycle. HR is a process that can take up to 6 hours or more to be completed (Figure 1.4) [10].

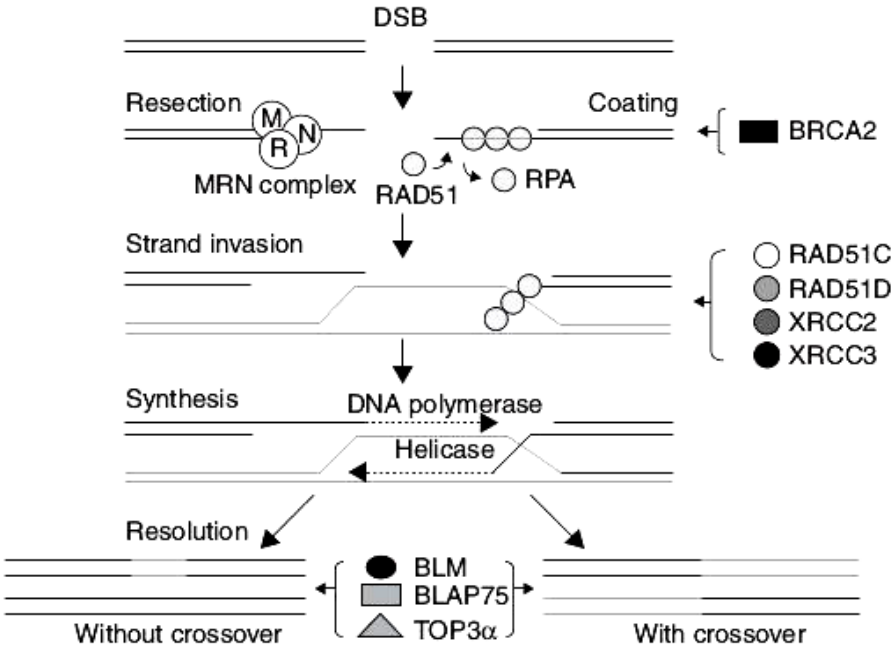


*Figure 1.4: Schematic representation of double-strand break repair by homologous recombination (Figure from [10]). The MRN complex recruits Rad51 protein while RPA protein coats the DNA strand. After strand invasion of the sister chromatid, helicases unwind the DNA and polymerases use the sister chromatid as a template to faithfully repair the DNA damage.*

Figure 1.4 shows a schematic representation of double-strand break repair by homologous recombination. The first step in the process is carried out by an exonuclease making a 3' overhang to create a single-stranded DNA region (ssDNA) around the DSB. This process is mainly executed by MRE11, a component of the MRN complex. The

ssDNA is then immediately coated with replication protein A (RPA). RPA is then replaced by RAD51, which promotes the subsequent identification of the DNA homologue and the strand invasion helped by several paralogue proteins, such as RAD51C and RAD51D. The Breast Cancer susceptibility gene 2 (BRCA2) promotes the assembly and formation of the RAD51 nucleoprotein onto the ssDNA by blocking ATP hydrolysis. The hosting undamaged chromatid gets unwound by helicases, allowing DNA polymerases to carry out the error-free DNA synthesis using the other strand as a template. Different enzymes called resolvases then cut the DNA at the crossover sites. Once repair has been completed by DNA polymerases, two double Holliday junctions are formed. These structures are resolved by resolvases such as GEN1, the BLM/TOP3a/BLAP75 complex and the MUS81/EME1 complex, which nick and then rejoin the DNA to separate the sister chromatids [10], [21], [42].

### 1.3.4 Cell cycle modifications

The cell cycle is a complex orchestrated sequence of macromolecular events that allows the cell to duplicate into two daughter cells identical to the parental. All non-germ eukaryotic cells achieve this through mitosis. During mitosis the cell has to duplicate all its cellular components and in particular its DNA and then divide correctly into two identical cells. The cell cycle of somatic cells can be divided into four phases [43], [44]:

- $G_1$ – Gap phase 1, the longest phase during which the cell is preparing for replication
- S – DNA synthesis phase, during which the DNA is replicated and a complete copy of each chromosomes is made
- $G_2$ – Gap phase 2, during which the cell checks if the DNA was properly replicated

- M – Mitosis, during which the cell distributes chromosomes and divides into two identical daughter cells.

After mitosis cells can also stop proliferating and enter a quiescent state called $G_0$ (Figure 1.5).

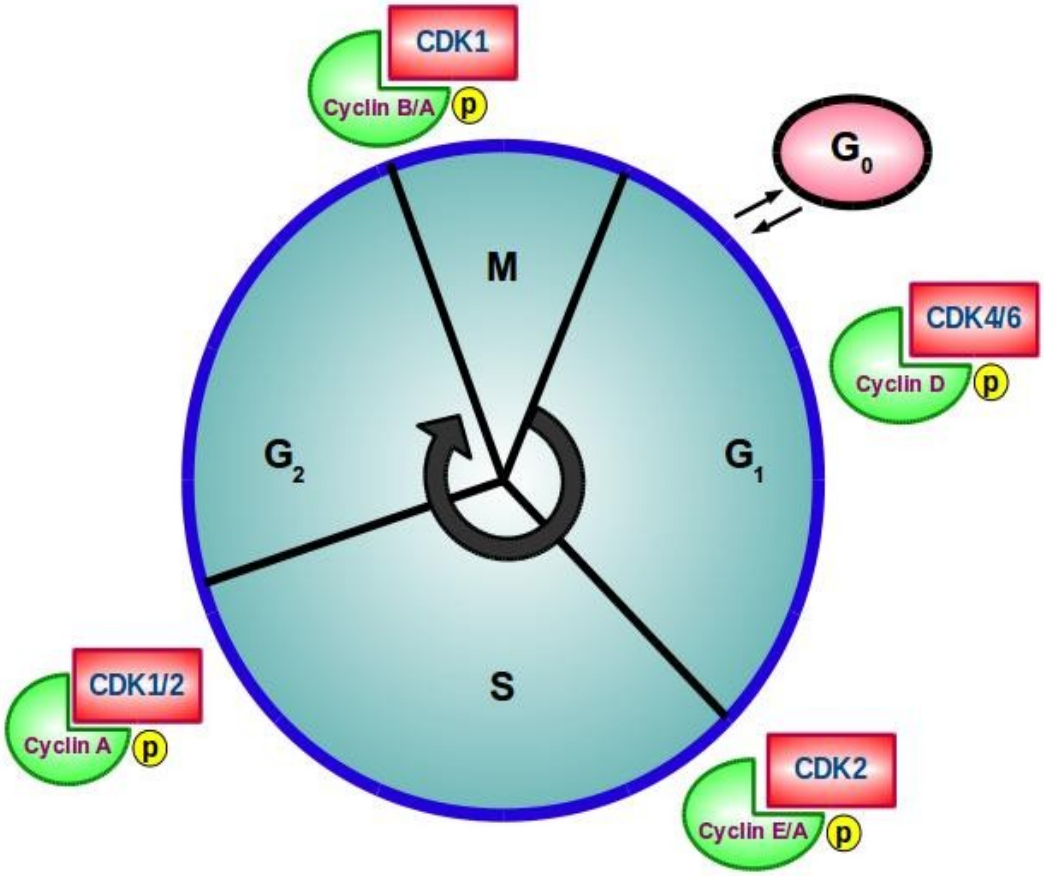


*Figure 1.5: Schematic representation of the cell cycle outlining the four different stages that lead to cell division: $G_1$, S, $G_2$, M. The progression from each stage to the next one is tightly regulated by the CDK/Cyclin complexes which control protein phosphorylation. Cells can also exit the cell cycle after mitosis and enter a transient or permanent state of quiescence called $G_0$.*

Cellular division must be precisely controlled and timed to complete the developmental process of a tissue or organism and in order to properly replicate the genome and guarantee functional offspring. For this reason, progression through different cell cycle stages is regulated by heterodimeric protein kinases formed by a regulatory

subunit called cyclin and a catalytic subunit called cyclin-dependent kinase or CDK. Polyubiquitinylation is the process needed for marking proteins for degradation by proteasomes to ensure irreversible cell-cycle progression. CDK/Cyclin complexes regulate the activity of a set of proteins which promote DNA replication and mitotic division through inhibitory and activational kinase activity. Each CDK can interact with different cyclins and have different substrates depending on the formed heterodimer, and cells employ a set of mechanisms for regulating the activity of CDK/Cyclin complexes.

CDK/Cyclins are divided into three classes depending on the cell cycle stage they are involved in: $G_1$ CDK/Cyclins, S-phase CDK/Cyclins and mitotic CDK/Cyclins [44].

$G_1$ CDK4/6/Cyclin D regulate via phosphorylation of the transcription factors of those genes required for the proper chromosome replication. S-phase CDK2/Cyclins E/A are synthesised in late $G_1$ but remain bound to their inhibitors and therefore inactive until $G_1$ CDK/Cyclin complexes reach their maximal activity and phosphorylate them. This process is favoured by the SCF complex (F-box containing complex, an ubiquitin-protein ligase) which polyubiquitinylates them resulting in a sudden increase of S-phase activity during which pre-replication processes are started. Mitotic CDK1/Cyclin B/A complexes are synthesised during late S and $G_2$ and get activated to start mitosis. Their dephosphorylation leads to the decondensation of chromosomes, reassembly of the nuclear envelope and nuclear pore complexes around the segregated chromosomes to form the two daughter nuclei, and cytokinesis to complete cell division [44].

As cells are constantly exposed to damage, surveillance mechanisms known as checkpoints (also known as restriction points or R points) evolved to ensure that the cell is competent to undergo major cell-cycle transitions only after the previous step has been completed. Checkpoints are controlled by the CDK/Cyclin complexes at different

stages of the cell cycle, as shown in Figure 1.5 above. When a CDK catalytic subunit forms a complex with the correspondent cyclin regulatory subunit, the CDK protein kinase is activated to trigger specific cell cycle events by phosphorylating proteins. The expression of cyclins varies depending on the cellular stage of the cell, whereas CDKs are regulated by controlled transcription, inhibition, and proteolysis which separates the complex, rendering it inactive. The variations in the expression profile of cyclins is represented in Figure 1.6.

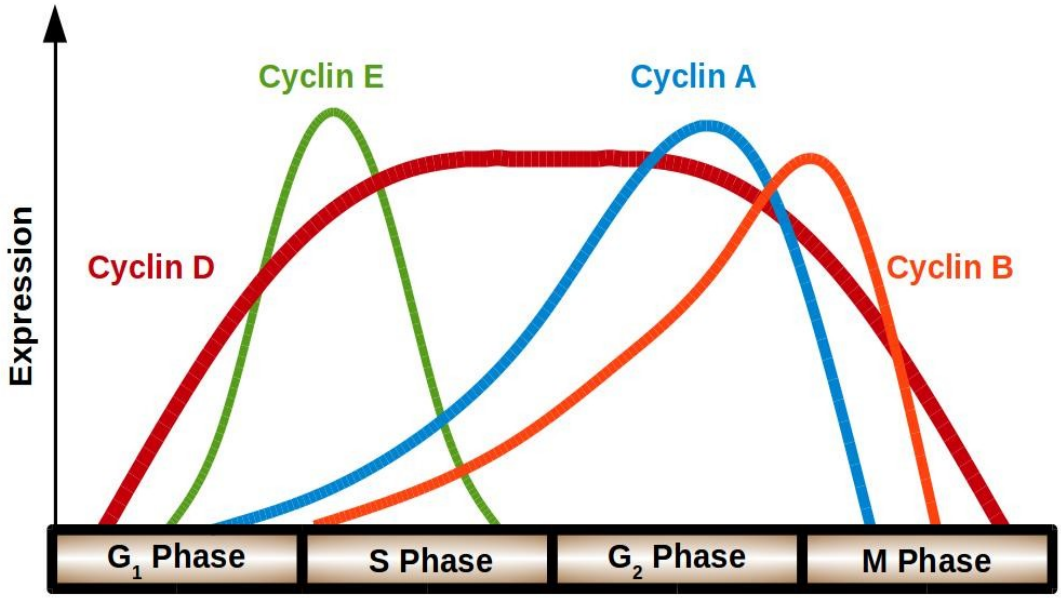


*Figure 1.6: Cyclins are expressed depending on the cell-cycle stage and regulate progression through it.*

Different categories of checkpoints exist including the $G_1$ checkpoint that ensures the cell is large enough to start division, intra S-phase and $G_2$/M checkpoints which ensure that DNA replication is completed, spindle-assembly checkpoints which check all chromosomes kinetochores are attached to spindle microtubules, spindle-position checkpoints to ensure chromosomes are segregated to daughter cells correctly, and DNA-damage checkpoints which check that damaged

DNA has been repaired and are activated in response to genotoxic stress such as IR-induced DNA damage.

After DNA damage, the cell cycle DNA damage checkpoints are activated, and as a consequence cell cycle progression is halted [10], [18], [21], [45]–[48]. In many cancers checkpoints are overcome, leading to uncontrolled proliferation and accumulation of DNA mutations [46], [49].

The DDR to ionising radiation is a complex cascade of events that allow the cell to avoid replicating damaged DNA. Loss of replication control is a fundamental hallmark of cancer which confers its malignant characteristics [46], [49]. As previously described in the “Early cellular response to DNA damage“ section, this process is initiated by the phosphorylation of histone H2AX and of 53BP1 by ATM and ATR which trigger the damage signalling process. This process involves many other proteins such as tumour suppressors and proto-oncogenes (Figure 1.7). To orchestrate the global cellular response to DSBs efficiently, ATM and ATR regulate the checkpoint mediators and the transducer kinases, CHK1 and CHK2.

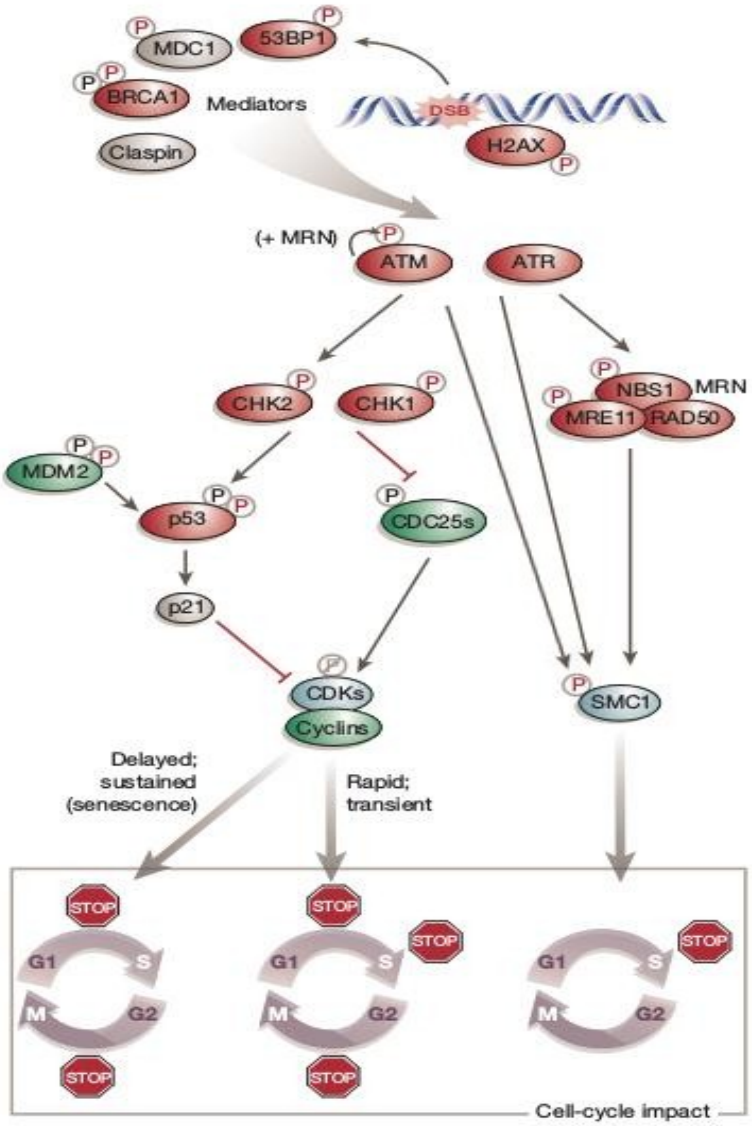


*Figure 1.7: Schematic representation of the activation of checkpoints as a response to double-strand breaks. Tumour suppressors are shown in red and proto-oncogenes are shown in green.*

*Figure from [45].*

ATR has a role in initiating the cellular response to replication-fork arrest induced by either DNA damage or other stresses, whereas ATM initiates the response to DNA damage in terms of checkpoint activation.

Known checkpoint mediators for the ATM signalling cascade include MDC1 (mediator of DNA damage checkpoint 1; NFBD1), 53BP1 and BRCA1, and for the ATR-controlled checkpoint signalling, claspin. Claspin is a mediator protein that selectively interacts with chromatin structures created by active replication forks, and is thought to be required for activation of CHK1.

CHK1 can induce intra-S phase checkpoint activation with consequent arrest through inhibitory phosphorylation of CDC25s and SMC1. Once the DNA damage has been repaired, CDC25s are activated, leading to the removal of inhibitory phosphate residues from target CDKs, with consequent CDK/Cyclin complex formation and cell cycle progression.

ATM-mediated phosphorylation of CHK2 promotes phosphorylation of p53, encoded by the *TP53* gene, which is a pro-apoptotic protein often referred to as “the guardian of the genome” [50], and a negative regulator of p53, MDM2, disrupting the balance between the two. After IR-induced DNA damage, unbalanced high levels of p53 trigger the transcription of p21 (*CDKN1A* also known as *p21waf1/cip1*), an inhibitor of CDK1 and CDK2 [18], [21], [45], [51]. High levels of p21 inhibit the phosphorylation of CDKs through its N-terminal homologous sequence, consequently inhibiting the formation of the CDK/Cyclin complex and therefore inactivating CDK activity and cell cycle progression [45], [52]–[55]. This set of events leads to checkpoint activation and cell cycle arrest at the $G_1$/S and $G_2$/M checkpoints [44], [45].

$G_1$ and S phase cell-cycle arrests prevent damaged DNA from being replicated, which could induce mutations in the genome and chromosomal rearrangements. $G_2$/M checkpoint activation and cell-cycle arrest allows repair of the damaged DNA before mitosis. This repair can be mediated by homologous recombination, using the available sister chromatid as a template for repair [44].

The induced imbalance between levels of p53 and MDM2 leads to increased apoptotic cell death, and for this reason p53 is classified as a strong tumour suppressor. However, p53 is found to be mutated in more than 50% of human cancers [56] and is known to be involved in many other pathways and damage response cascades [10], [18], [21].

Another key player for the transition from $G_1$ to S phase is the E2F transcription factor, which is required to regulate many of the genes necessary to start DNA replication, and which is kept inactive in $G_1$ phase by binding to the retinoblastoma protein (Rb). In normal conditions, the $G_1$ CDK/Cyclin complexes phosphorylate Rb with a consequent separation from E2F, permitting progression to S phase. IR induced activation of p53 promotes expression of p21, which is then responsible for inhibiting the CDK/Cyclin complex with a consequent inhibition of cell-cycle progression [10].

S-phase checkpoints are regulated by Chk1 and Chk2, which are direct targets of ATR and ATM respectively. Ionising radiation induces ATR and ATM mediated activation of Chk1 and Chk2, which induces an increase in phosphorylated CDK2 and a consequent slower progression through S phase [10].

IR induces a temporary arrest at the $G_2$/M checkpoint in cancer cells [24], [57], which is required to allow DNA damage to be repaired before entry into mitosis [51]. The $G_2$/M checkpoint is regulated by the CDK1/Cyclin B complex which must be dephosphorylated to become active and could be ATM/ATR-dependent or -independent [10]. A post-translational role for p53 and p21 in regulating and sustaining the $G_2$/M arrest has been thoroughly investigated and described [24], [52]–[54], [57].

## 1.4 Radiotherapy in the clinic

As previously stated, radiotherapy is the use of radiation to kill tumour cells and subsequently control the tumour growth. Therefore, targeted dose escalation is essential and has to take into account the balance between tumour-specific damage and the damage of the surrounding healthy tissues. A high-dose treatment might increase the DNA damage in the tumour cells and tumour cell death, but can also induce mutations and cell death in the surrounding healthy tissues, causing unacceptable side effects. Therefore, the delivery of the treatment is limited by the dose tolerance of the normal tissues [58].

Different approaches can be adopted in order to minimise the radiation dose delivered to the normal tissues. Modern technologies allow the three dimensional tumour mass to be defined to locally target the radiation dose. These technologies include computed tomography (CT), magnetic resonance imaging (MRI) and positron emission tomography (PET). CT is based on the absorbance curve variations of monochromatic X-rays to discriminate between different tissues. Modern machines scan the patient from different angles with a rotating X-ray emitter, conferring a three dimensional reconstruction of the scanned body and a better dose distribution with a final resolution of about 0.5 mm. For MRI, the patient is submerged in a combination of a static or gradient magnetic field and a radio-frequency electromagnetic field. The consequent proton spin alignment, excitation and relaxation produce a signal that can be detected and reconstructed computationally. MRI spatial resolution is lower compared to CT (1.5 to 2.00 mm) but MRI does not have any risk in terms of dose to the patient, and therefore live imaging is possible with a time resolution of about 50 ms. PET scans are based on the use of a positron emitting radionuclide as a tracer. The

radionuclide with a short half life, typically fluorine-18 with a half life of 109.8 minutes, is injected in the patient and binds to highly-metabolic cells, such as the cancerous tissues. The emission of a positron and the subsequent positron-electron annihilation produces two back-to-back 511 keV photons which can be detected to localise the tumour. The principal downside of this particular technique is the difficulty of producing and handling a radionuclide with a short half life. These different imaging techniques help to spatially define the tumour and to deliver radiotherapy locally. Another approach to improve radiotherapy localisation to the target tissue is the use of higher mass particles such as protons and carbon ions. Their distribution of energy loss when interacting with matter peaks at the end of the particle path. This is known as Bragg's peak, and can be shaped in order to colocalise with the tumour. However, a downside of this approach is that it needs a synchrotron machine to produce and accelerate the particles at the desired energy, and these machines are very expensive to build and to maintain.

As a consequence, a different approach is needed in order to widen the therapeutic window to achieve tumour control with lower doses to the patient and a consequent reduction in early and late toxicity.

### 1.4.1 The therapeutic window

The balance between tumour control and normal tissue complications can be depicted as hypothetical curves for tumour control probability (TCP) and normal tissue complication probability (NTCP), as illustrated in Figure 1.8. As TCP increases with cumulative dose, the NTCP also increases. The region between these curves is called the “therapeutic window” [10] in which a curative dose can be delivered effectively. Avoiding normal tissue complications by achieving better dose localisation to the tumour widens this therapeutic window by shifting the NTCP curve to the right, providing the opportunity to escalate the radiation dose and therefore increase tumour-specific damage,

leading to disease control. At the same time, to achieve greater widening of the therapeutic window, factors that shift the TCP curve to the left must be determined and assessed.

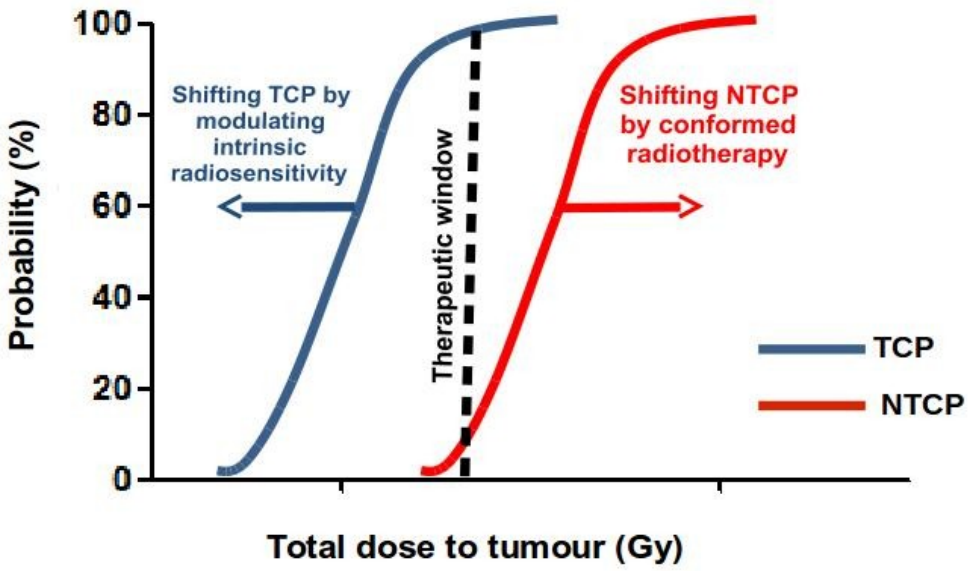


*Figure 1.8: Graphical representation of the typical dose response. Tumour control probability (TCP),in blue, and normal tissue control probability (NTCP), in red, outline the therapeutic window of intervention. The shifting of these two curves apart is an essential strategy to improve radiotherapy and clinical outcome.*

One major determinant of the TCP curve is intrinsic radiosensitivity [46], [49], [59]. An attractive approach is to shift the probability of achieving tumour control towards the left, by modulating the intrinsic radiosensitivity of the tumour cells without affecting the normal tissues. Sensitising the tumour to radiation in this way would achieve the same level of TCP with lower total dose and therefore benefit the patient. For this reason it is potentially viable to tune intrinsic rasiosensitivity or radioresistance in order to obtain a differential response to the same radiation dose based on intrinsic gene expression differences between tumour cells and healthy tissues [60].

## 1.5 Intrinsic radiosensitivity

Genetic variations in tumour cells give rise to unique phenotypes that confer a differential susceptibility to ionising radiation treatment compared to the healthy cells [46], [49]. This variation of intrinsic radiosensitivity impacts the radiation response at different clinical endpoints, including survival, local control and disease free survival [61].

One of the gold standard approaches to test intrinsic radiosensitivity *in vitro* is the colony formation assay (CFA) with the use of small-interfering RNAs (siRNA) for gene silencing [62]–[66]. This technique tests the ability of single cells to proliferate into a colony after radiation, without the target gene being expressed.

### 1.5.1 Gene silencing and molecular targeting

siRNA gene silencing consists of transfecting cells with short double-stranded RNA (dsRNA), typically 20-25 base pairs in length, engineered to target a specific gene. The transfected siRNA induces a RNA interference phenomenon (RNAi) which targets a specific mRNA and degrades it before it can be translated into protein [43]. The double-stranded RNA is recognised and cleaved in the cellular cytoplasm by a RNase III family endonuclease called Dicer. The product of such a cleavage is a two-nucleotide long 3' overhang which will then form a complex with a ribonucleoprotein called RNA-induced silencing complex (RISC) [43], [66], [67]. This complex mediates the unwinding of the siRNA duplex inducing a high affinity with a target mRNA in a sequence-specific manner. The binding to the mRNA induces a cut in the middle of the sequence mediated by Slicer, an Argonaute protein with a RNase H-like domain called PIWI, which is part of the RISC complex. The cleaved mRNA is then recognised as aberrant and degraded by nucleases present in the cytoplasm and

therefore does not get translated into a protein product as described in Figure 1.9 [66].

The major weakness of using siRNA relates to off-target effects. The transfected siRNA can present multiple mRNA affinities and therefore silence different unwanted targets [66]. To remedy this problem, an appropriate deconvolution experiment can be performed to test the specificity of the the gene knockdown.

Another disadvantage in the siRNA technique is the transient nature of the knockdown. To obviate this issue short-hairpin RNA shRNA can be used instead. As shown in Figure 1.9 the shRNA gene-silencing technique consists of transfecting cells with a plasmid able to express the shRNA sequence, a precursor of the siRNA. The shRNA gets then processed by the dicer into siRNA in the cellular cytoplasm resulting in the target-gene silencing [66].

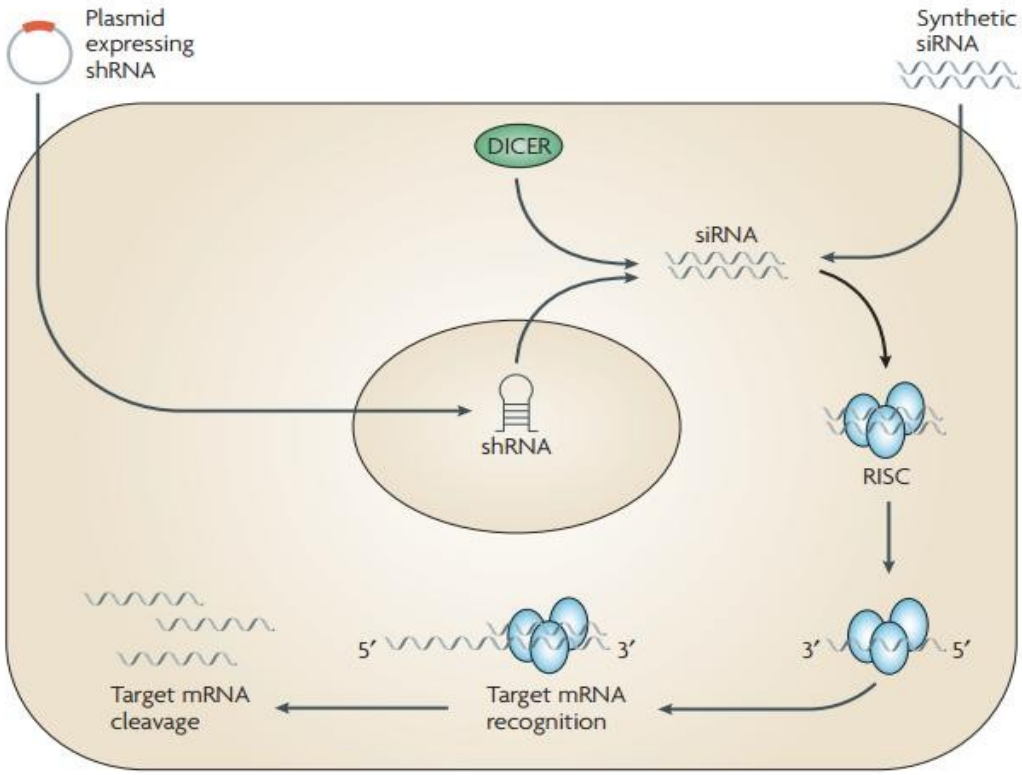


*Figure 1.9: Schematic representation of shRNA and siRNA mechanisms of action (Figure from [66]). A plasmid expressing shRNA can be stably transfected in a cell. This will constantly generate dsRNA which is then uncoupled and generates a ssRNA siRNA able to target a specific mRNA sequence and, with the contribution of a Dicer and the RISC complex, disrupt its translation. These two techniques are widely used in stable and transient gene silencing.*

Another approach to increase intrinsic tumour radiosensitivity is the inhibition of specific targets at the post-translation stage [68]. This can be accomplished by the chemical development of specific drugs able to bind to and alter the role of specific proteins. A good example of this technique, with wide clinical potentiality, is the use of molecular drugs targeting epidermal growth factor receptor (EGFR), such as monoclonal antibodies like Cetuximab, or drugs that inhibit EGFR phosphorylation [10]. The overexpression of EGFR has been shown to be correlated with poor clinical outcomes in patients

because of its induced radioresistance [10], [69] and the use of such drugs results in reduced cell proliferation *in vitro* [10] and *in vivo* [70].

### 1.5.2 siRNA screening to identify radiosensitisers

The technique of siRNA silencing of a single gene or a pool of genes has opened the way to high-throughput screening (HTS) to identify radiosensitivity modulators. These screens can have different endpoints such as cell death via apoptosis, cell proliferation, micronuclei formation, DNA-damage foci quantification, cell growth and survival, and colony formation.

The colony formation assay (CFA) is the gold standard for determining radiation sensitivity because it allows the assessment of the loss of proliferative potential (clonal inactivation) caused by radiation treatment. This assay measures the ability of a singular cell to replicate into a colony up to 2 weeks after the treatment. Previous work in our lab involved the development of a high-throughput version of the CFA in a 96-well plate format, which enabled the screening of a library of siRNAs [64]. Using this technique, a set of 709 kinases was previously screened to identify which genes modified the cellular response to radiation in terms of colony formation. The screening was performed in two repeats on HeLa cells using 7 Gy IR, and produced a ranked list of the tested genes depending on their effect on radiosensitisation.

From this list of kinases, one of the best targets for further study was the T-LAK cell-originated protein kinase, TOPK (also known as PDZ-binding kinase PBK), whose role will be investigated in this thesis. The selection criteria of this gene as a valid candidate for investigation include its novelty in the context of radiation, its differential expression between normal and cancer tissues, and the availability of reagents to allow its study. This choice will be discussed in more depth in the following chapters of this thesis.

### 1.5.3 T-LAK cell-originated protein kinase

TOPK is a Ser/Thr protein kinase of 322 amino-acids (Figure 1.10) first identified in 1999 from a lymphokine-activated killer T (T-LAK) cell subtraction cDNA-fragment library [71]. The same protein was identified the following year in a hDlg two-hybrid screen [72]. TOPK has been shown to be a member of the MAPKK family, the mitogen-activated protein kinase cascade responsible for many cellular functions [71]. TOPK phosphorylates p38 and is phosphorylated during mitosis by cdc2/Cyclin B [71], [72] and during spermatogenesis [73]. Its depletion has been shown to lead to multinucleation in HeLa cells [74].


*Figure 1.10: Schematic representation of the PBK/TOPK protein structure showing the N- and C-terminus, the kinase domain and the PDZ-interaction domain.*

One of the reasons why *TOPK* is an attractive candidate as a radiosensitising gene is its differential expression between normal and cancerous tissues. It has been shown that *TOPK* is expressed only in testis and placenta [71]–[74] and is upregulated in most cancers [75], [76]. Furthermore, high levels of TOPK have been linked to poor clinical outcomes for many different types of cancer. *TOPK* expression has been shown to correlate with adverse outcomes in terms of overall survival and recurrence free survival in breast cancer patients

[77]. The role of TOPK as a prognostic marker and its adverse effects on tumour control have also been shown in non-small-cell lung cancer (NSCLC), where it has been positively correlated with p53 mutant expression levels and where of the highest *TOPK* expression was noted in lymph nodes and metastases [78]–[80]. Levels of TOPK were also shown to commensurate with invasiveness and cancer stage in prostate cancer, with higher levels of expression in circulating tumour cells (CTCs) and negative effects on patient outcomes. A correlation with invasiveness was also confirmed using *in vitro* assays [81], [82]. In colorectal cancer, levels of TOPK were correlated with levels of interlukin-8 (IL-8 or CXCL8) [83] and *KRAS* and *BRAF* mutations [84], and a prognostic role of TOPK for predicting poor clinical outcomes was suggested.

These publications outline a clear role for TOPK in influencing clinical outcomes, making it an interesting clinical target for further study.

TOPK has been studied previously in absence of DNA damage. Published works have been showing that overexpressed TOPK immunoprecipitate with α-tubulin and with both Cyclin B1 and CDK1 in COS-7 cells [74]. In HEK293 cells overexpressing TOPK and in HCT116 untransfected cells, TOPK has been shown to participate in a positive phosphorylation loop with ERK2 [85] and a physical interaction between TOPK and PTEN was identified in HeLa cells through immunoprecipitation experiments [86]. It has been also shown that TOPK phosphorylates p38 in TOPK-overexpressed COS-7 cell lysates and in a kinase assay *in vitro* [71]. In lung cancer cell lines TOPK has been reported to participate to the PI3K/AKT pathway and influence cell migration through a negative correlation with the levels of PTEN and an increased level of phospho-AKT [80]. In breast cancer TOPK has been published for its ability in phosphorylate histone H3 *in vitro* and *in vivo* [87].

None of the published works was performed after IR-induced DNA damage and TOPK has only been studied in response to doxorubicin treatment [88], [89], arsenite ($As^{3+}$) treatment [90] and ultraviolet radiation (UV-B) [91]. After doxorubicin treatment, overexpression of TOPK in HT1080 cells has been shown to physically interact with p53 and attenuate the $G_2$/M checkpoint [89] and TOPK knockdown in HCT116 cells increased p53-dependent overexpression of p21, elongated the doubling time through accumulation in $G_2$/M and increased the levels of apoptosis [88]. After UV-induced DNA damage TOPK depletion has been shown to reduce the number of γ-H2AX foci and decrease cell survival in MCF-7 cells [91]. After arsenite treatment TOPK has been published to bind to H2AX, colocalise with γ-H2AX foci and inhibit apoptosis in RPMI7951 cells [90].

At the time of writing this was the first study to investigate the role of TOPK in the radiation response, and the radiosensitisation observed in the kinase screen in HeLa cells after siRNA-mediated *TOPK* knockdown was the first result suggesting that *TOPK* could be a potential radiosensitising target gene.

## 1.6 Aim of this thesis

Our laboratory previously performed and published a HTS using a kinase library of 709 siRNAs to identify novel genes that alter intrinsic radiosensitivity.

The aim of this doctorate thesis is to study some of the identified novel genes. In particular this thesis focuses on the identification and validation of a novel role for the T-LAK cell-originated protein kinase TOPK, as a potent modulator of radiosensitisation. The thesis aims to address the following questions:

- Is TOPK a modulator of radiosensitivity in a range of cancer cell lines?
- Is TOPK a modulator of radiosensitivity in normal tissue cells?
- Does knock-out of TOPK cause radiosensitisation?
- Is TOPK overexpressed in cancer?
- Does depletion of TOPK affect the DNA damage response?
- How does TOPK depletion alter the cell cycle of asynchronous cells in response to radiation?
- Can depletion of TOPK alter the $G_1$/S or $G_2$/M checkpoints in response to radiation in synchronised cells?
- Is nuclear morphology affected by radiation following TOPK depletion?
- How is cell death altered by radiation following TOPK depletion?
- Which proteins physically interact with exogenously expressed TOPK?

- Can putative TOPK interaction partners interact with endogenous TOPK, and are the interactions radiation-dependent?
- Does TOPK expression affect prognosis?
- Does stable knockdown of TOPK cause radiosensitisation?
- Does inhibition of TOPK cause radiosensitisation?
- Can TOPK depletion sensitise to widely used chemotherapeutics?

The presented results show TOPK to be a tumour specific modulator of radiosensitivity, and provide a possible mechanistic description of its role in the cellular response to ionising radiation in terms of cell-cycle progression modifications, increased apoptosis, altered cell morphology and impaired cellular growth. Furthermore, prognostic data and immunohistochemical data show the effect of *TOPK* expression on clinical outcome.

We therefore propose that TOPK inhibition may be of significant clinical benefit by increasing tumour radiosensitivity without exacerbating radiation induced side-effects, and that TOPK could be targeted in order to widen the therapeutic window and improve cancer treatment.

# CHAPTER 2

# MATERIALS AND METHODS

## 2.1 Cell culture

### 2.1.1 Cell line maintenance

HCT116 (colorectal), HeLa (cervical), MRC5 (lung fibroblast), HFL-1 (lung fibroblast), DU145 (prostate), PC3 (prostate), H1299 (lung), T24 (bladder) cell lines were purchased from American Type Culture Collection (ATCC). SQ2OB (head and neck) cells were provided by Dr. Ralph Weichselbaum (University of Chicago, Chicago, IL). HeLa, SQ20B, DU145, PC3, HCT116 and H1299 cells were maintained in Dulbecco's modified Eagle's medium (DMEM, Sigma) supplemented with 10% foetal bovine serum (FBS). The T24 cell line was maintained in Roswell Park Memorial Institute (RPMI-1640, Sigma) media supplemented with 10% FBS. MRC5 cells were maintained in minimum essential medium (MEM, Sigma) supplemented with 10% FBS. HFL-1 cells were maintained in DMEM/F-12 Ham’s media supplemented with 10% FBS. The HAP1 cell lines were purchased from Horizon Discovery and maintained in Iscove's Modified Dulbecco's Medium (IMDM). All cell lines were authenticated by LGC standards (ATCC) by short tandem repeat (STR) profiling. The SQ20B cell line was authenticated by the laboratory of Professor Ruth Muschel using STR profiling. All cell lines were tested for mycoplasma using MycoAlert (Lonza).

### 2.1.2 Cell line storage and resuscitation

Cells were kept in cryovials stored in vapour phase liquid nitrogen. Cells were thawed in a water bath at 37°C. Cells were immediately diluted in 10 ml of media in a 50 ml falcon tube and centrifuged at 240 x g for 5 minutes. The media was removed, and the cells were re-suspended in 5 ml of media and seeded in a T25 flask.

### 2.1.3 Passaging cell lines

The media was removed from the flasks. Cells were washed in 5-10 ml of 1 x phosphate buffered saline (1xPBS) and 1-2 ml of trypsin-ethylenediaminetetraacetic acid (EDTA) was added to the flask. Cells

were then returned to the 37°C incubator for 5-10 minutes. Medium was added after cells had lifted, and the cell suspension was diluted appropriately in medium. Typically the cells were passaged at 1:10, 1:12 or 1:20 and returned to the incubator. Cell lines were passaged for a maximum of 3 weeks, and were passaged when cells reached ~ 60-80% confluency. Cells were cultured in incubators at 37°C supplied with 5% $CO_2$.

### 2.1.4 Cell counting

The cells were trypsinised as described above. A 50 µl cell suspension was diluted 1:10 in DMEM in a microcentrifuge tube and counted using the Scepter 2.0 (Millipore) hand held automated cell counter.

### 2.1.5 Cell synchronisation

Cell synchronisation in $G_1$/S phase was achieved using a double-thymidine block in a 6-well plate format. On day 0, when cells reached 25-30% confluency, thymidine was added to each well at a concentration of 2 mM, and the plates were returned to the incubator for 18 hours. The next day the medium was removed and the cells were washed with 1 ml of 1xPBS. After the wash, fresh medium was added to release the cells from the first block. 9 hours after release, thymidine was added for a second block at a concentration of 2 mM. On day 2, 17 hours after the second thymidine treatment, the cells were released by washing twice with 1xPBS and adding fresh medium. Cell synchronisation in $G_2$/M phase was achieved using a nocodazole block in a 6-well plate format. 50 ng/ml of nocodazole was added to adherent cells at about 50-60% confluency. After 14 hours, the cells were released by washing off the nocodazole, washing twice with 1 ml of 1xPBS, and adding fresh media. Cell cycle stage was confirmed by propidium iodide FACS analysis.

## 2.2 SDS-Page and Immunoblotting

### 2.2.1 Buffers and reagents

| Buffer Name | Buffer composition |
|---|---|
| 20 x running buffer purchased from Expedeon | 0.8 M Tricine, 1.2 M Tris, 2% SDS, 50 mM sodium bisulfite. Diluted in $dH_2O$ to 1 x working condition |
| Western transfer buffer | 25 mM Tris, 190 mM glycine, 20% methanol made up to 1 L in $dH_2O$ |
| Stripping buffer purchased from Millipore | ReBlot Plus Mild Antibody Stripping Solution, 1:10 dilution with $dH_2O$ |
| LDS Sample Loading Buffer (4X) purchased from Expedeon supplemented with 20 mM of Dithiothreitol (DTT) reducing agent | 40% glycerol, 4% lithium dodecyl sulfate (LDS), 4% Ficoll*- 400, 0.8 M triethanolamine-Cl pH 7.6, 0.025% phenol red, 0.025% coomassie G250, 2mM EDTA disodium |
| Lysis buffer: RIPA Lysis buffer purchased from Thermoscientific supplemented with protease inhibitor (Roche) and phosphatase inhibitor cocktail 2 (Sigma) | 1 ml of RIPA lysis buffer: 25 mM Tris-HCl (pH7.6), 150 mM NaCl, 1% NP-40, 1% sodium deoxycholate, 0.1% SDS<br>143 µl of 7x protease inhibitor, 10 µl of phosphatase inhibitor cocktail |
| TBS-T | 100 ml 10xTBS, 1 ml Tween diluted to 1 L with $dH_2O$ |
| Blocking Reagent | TBST-Milk (5% w/v Marvel powder milk in TBST) or TBST-BSA (5% w/v Bovine Serum Albumin, Sigma) |
| Immobilon Western Chemiluminescent | HRP Substrate from Millipore, used according to the manufacturer's instructions |
| BCA protein assay kit purchased from Thermoscientific | Reagent A- sodium carbonate, sodium bicarbonate, bicinchoninic acid and sodium tartrate in 0.1 M sodium hydroxide<br>Reagent B- 4% cupric sulfate |
| Amersham Protran Premium 0.2 nitrocellulose membrane (GE Healthcare) | |
| RunBlue® pre-cast gels (Expedeon) | |

*Table 2.1: Formulation and preparation of buffers used for immunoblotting*

### 2.2.2 Protein lysate preparation

Cells grown in 6-well plates were lysed in 120 µl/well RIPA lysis buffer with inhibitors, as described in Table 2.1, using a cell scraper. Cell lysates were transferred to 1.5 ml microcentrifuge tubes, incubated on ice for 5 minutes and then sonicated for 10 seconds. Lysates were centrifuged at 25000 x g in a 4°C centrifuge for 10 minutes. Supernatants were transferred to fresh microcentrifuge tubes and stored at -80°C until further use.

### 2.2.3 Protein concentration quantification

Protein extracts were quantified using a bicinchoninic acid assay (BCA) kit (Thermoscientific) according to the manufacturer's instructions. Briefly, 2 µl of protein lysates were pipetted in triplicate into a 96-well plate. A standard curve was produced using bovine serum albumin (BSA), with concentrations ranging between 0 µg/ml and 2000 µg/ml. 200 µl of the reagent mixture was added to each well containing sample or standard, and incubated at 37°C for 30 minutes. The absorbance was read at a wavelength of 562 nM using a POLARstar Omega plate reader (BMG Labtech). Protein concentrations for samples were calculated using the standard curve.

### 2.2.4 SDS-PAGE

RunBlue pre-cast 4-12% gradient SDS-PAGE gels, RunBlue running buffer and loading buffer were purchased from Expedeon. 25% loading buffer was added to protein extracts and denatured for 10 minutes at 72°C in a heat block prior to loading, and 15-30 µg of protein sample was loaded per lane on an SDS-PAGE gel. Dual color precision plus protein standards purchased from Bio-Rad were run alongside all samples. Gels were run for 1 hour at 150 V.

### 2.2.5 Immunoblotting

The XCell II™ Blot Module (Invitrogen) was used to set up the transfer. Hybond nitrocellulose transfer membrane (GE-healthcare) and the SDS gel were sandwiched between two sheets of Whatman paper and

compressed with sponges. The proteins were transferred onto the nitrocellulose membrane in tris glycine transfer buffer at 30 V for 1 hour. Next, the membranes were blocked in 5% blocking agent for 1 hour at room temperature. Primary antibodies were diluted to the manufacturer's recommendations in 5% BSA/TBS-T or 5% Milk/TBS-T. A list of all antibodies and their working concentrations can be found in Table 2.2.

| Target | Additional information | Western blot dilution | Protein Size (kDa) | Host | Cat # |
|---|---|---|---|---|---|
| **TOPK** | Used for WB and IP | 1:1000 (BSA) | 36 | Mouse | Sigma SAB5300406 clone 2C8 |
| **Phospho-TOPK** | Used for WB and IHC | 1:1000 (BSA) | 40 | Rabbit | Cell Signaling Technology #4941 |
| **Antiflag M2** | FLAG; peptide sequence DYKDDDDK | 1:500 (milk) | | Mouse | Sigma F3165 |
| **Cyclin E1** | (HE12) | 1:1000 (BSA) | 48 | Mouse | Cell Signaling Technology #4129 |
| **Cyclin B1** | | 1:1000 (BSA) | 55 | Rabbit | Cell Signaling Technology #4138 |
| **Phospho-cdc2** | (Tyr15) | 1:1000 (BSA) | 34 | Rabbit | Cell Signaling Technology #4539 |
| **Cdc2** | CDK1 | 1:1000 (BSA) | 34 | Mouse | Cell Signaling Technology #9116 |
| **Phospho-histone H3** | | 1:1000 (BSA) | 17 | Rabbit | Cell Signaling |

| | | | | | |
|---|---|---|---|---|---|
| | | | | | Technology #3377 |
| **TOPK** | Used for IHC | 1:50 | 36 | Rabbit | Cell Signaling Technology #4942 |
| **p21** | CDKN1A | 1:1000 (BSA) | 21 | Rabbit | Cell Signalling Technology #2947 |
| **DNA-PK$_{cs}$** | catalytic subunit of DNA-PK involved in NHEJ signalling | 1:500 (milk) | 450-465 | Mouse | BD Pharmingen Cat No.556456 |
| **Vinculin** | membrane-cytoskeletal protein (loading control) | 1:40000 (milk) | 124 | Mouse | Abcam ab18058 |
| **β-Actin** | nonmuscle cytoskeletal actin (loading control) | 1:20000 (milk) | 45 | Mouse | Sigma A1978 |
| **Anti-rabbit secondary antibody** | ImmunoPure Goat Anti-Rabbit IgG (H L), peroxidase conjugated | 1:20000 | | Rabbit | Thermoscientific 31460 |

| | | | | | |
|---|---|---|---|---|---|
| **Anti-mouse secondary antibody** | ImmunoPure Rabbit Anti-mouse IgG (H L) | 1:20000 | | Mouse | Thermoscientific 31335 |

*Table 2.2: Details of antibodies and their working concentrations*

Primary antibody incubations were performed overnight at 4°C. Three washes of 1 hour were conducted with TBS-T between primary and secondary antibody incubation. Secondary HRP-conjugated anti-mouse and anti-rabbit antibodies (Thermofisher) were diluted to a concentration of 1:20000 in 5% Milk/TBS-T. Membranes were washed 3 times in TBS-T and incubated with Immobilon Western Chemiluminescent HRP Substrate (Millipore) for five minutes. Membranes were visualised using photographic film (FujiFilm SuperRX) and an X-ray developer (CP 1000, AGFA).

### 2.2.6 Stripping and re-probing

Blots were stripped in 10 ml stripping buffer (Millipore) for 15 minutes at room temperature. The membrane was washed in TBS-T for 5 minutes. The blots were then blocked in blocking buffer and incubated with the desired antibodies as described above in Table 2.2.

## 2.3 Forward shRNA transfection

GIPZ™ Lentiviral shRNA particles were purchased from Dharmacon™ GE Healthcare. The gene target mature antisense sequence is specified in Table 2.3 below:

| Construct symbol | Mature Antisense | Volume/Vial | Quantity |
|---|---|---|---|
| **shTOPK_1** | AATGTTACAGTTTACAGCG | 25 µl | 2 |
| **shTOPK_2** | AGAGTCTAATAACTACTGA | 25 µl | 2 |
| **shTOPK_3** | TAATGTTACAGTTTACAGC | 25 µl | 2 |

*Table 2.3: GIPZ Lentiviral TOPK constructs*

HCT116 cells were plated in a 96-well plate at a concentration of 8000 cells/well. The next day the purchased viruses were diluted in DMEM without FBS (D0) as described in Table 2.4 and added directly to the cells after medium was washed off. Each well was topped up with D0 medium to reach a total volume of 50 µl/well. After 4-6 hours incubation, 150 µl of DMEM with 10% FBS (D10) were added to each well.

| shRNA | Multiplicity of Infection (MOI) | | | | |
|---|---|---|---|---|---|
| shNS | 0 | 1 | 5 | 10 | 20 |
| shTOPK_1 | 0 | 1 | 5 | 10 | 20 |
| shTOPK_2 | 0 | 1 | 5 | 10 | 20 |
| shTOPK_3 | 0 | 1 | 5 | 10 | 20 |

*Table 2.4: Experimental setup for Lentiviral transduction*

48 hours after transduction plates were monitored under a fluorescence microscope to qualitatively evaluate the transfection

efficiency based on the number of GFP (green fluorescent protein) positive cells. Cells were then lifted with trypsin and transferred to a new 24-well plate with fresh D10 medium. The following day 2 µg/ml puromycin were added to select the cells expressing the viral-induced vector. Selection was carried for the following 6-9 days. Cells were transferred in a 6-well plate when 80-90% confluent and then lysed for western blot knockdown evaluation (see chapter 2.2 “SDS-Page and Immunoblotting“). A non-specific shRNA control was used (shNS).

## 2.4 Reverse siRNA transfection

Unless otherwise stated, transfections were performed in 6-well plates 72 hours before lifting and replating the samples. siRNAs (Ambion) were diluted in Opti-MEM (Invitrogen) and the INTEFERin-HTS transfection reagent (Polyplus) was diluted in RNase free water. The final siRNA concentration was 20 or 40 nM depending on cell line. Reagent complexes were formed in 1.5 ml microcentrifuge tubes using the conditions stated in Table 2.5. The diluted siRNA was added to the diluted INTERFERin-HTS and incubated for 30 minutes at room temperature before addition to a suspension of 180,000 cells per well in a 6-well plate.

| Cell line | siRNA final concentration (nM) | INTERFERin-HTS concentration (µl/well) |
|---|---|---|
| **HeLa** | 20 | 1.0 |
| **HCT116** | 20 | 1.0 |
| **H1299** | 20 | 1.0 |
| **SQ20B** | 20 | 1.2 |
| **HFL-1** | 20 | 2.0 |
| **MRC5** | 40 | 1.8 |
| **PC3** | 20 | 1.0 |
| **T24** | 20 | 1.4 |
| **DU145** | 20 | 1.0 |

*Table 2.5: Transfection conditions for different cell types in 6-well plates*

## 2.5 Colony formation assay

siRNA transfected cells were plated in 6-well plates in triplicate wells in 2 ml of medium, allowed to settle for 4 to 6 hours and then given the appropriate dose of IR using an IBL637 caesium-137 irradiator. The cells were cultured for two weeks, stained with crystal violet and counted using a GelCount colony counter (Oxford Optronix). Plated cell numbers are shown in Table 2.6 below.

| Cell line | Number of plated cells/well | | | |
|---|---|---|---|---|
| | **0 Gy** | **2 Gy** | **4 Gy** | **6 Gy** |
| **HeLa** | 200 | 400 | 800 | 2000 |
| **HCT116** | 200 | 400 | 800 | 1600 |
| **H1299** | 200 | 400 | 800 | 3200 |
| **SQ20B** | 400 | 800 | 1600 | 3200 |
| **HFL-I** | 1000 | 2000 | 4000 | 8000 |
| **MRC5** | 800 | 1600 | 4000 | 8000 |
| **PC3** | 400 | 800 | 1600 | 3200 |
| **T24** | 200 | 400 | 800 | 1600 |
| **DU145** | 200 | 400 | 800 | 1600 |
| **HAP1** | 200 | 400 | 800 | 3200 |

*Table 2.6: Plated cell numbers for the colony formation assay*

## 2.6 Irradiation

All irradiations were performed at the indicated dose using the caesium-137 irradiator, Gamma Service: GSR D1; dose rate 1.938 Gy/min.

## 2.7 Statistical analysis for the CFA

Survival data was curve fitted using GraphPad Prism by non-linear regression of the linear quadratic equation (1):

$$S = \exp -(\alpha D + \beta D^2) \quad (1)$$

Where S denotes surviving fraction, D (Gy) is radiation dose and α ($Gy^{-1}$) and β ($Gy^{-2}$) are the two variables to fit. The sensitisation enhancement ratio was calculated at 10% surviving fraction ($SER_{10}$) using α ($Gy^{-1}$) and β ($Gy^{-2}$) estimated coefficients as described in equation (2):

$$SER = D_{untreated} / D_{treated} \quad (2)$$

The $D_{untreated}$ and $D_{treated}$ values were calculated using α ($Gy^{-1}$) and β ($Gy^{-2}$) coefficients that yielded 10% survival by solving the quadratic equation (3) below:

$$\beta D^2 + \alpha D - 2.3026 = 0 \quad (3)$$

A factorial 2-way ANOVA was performed with survival as the dependent variable, and with dose levels (2, 4 and 6 Gy) and treatment (control/DMSO, siRNA/TOPKi) as the two factors. p-values produced were for interaction between treatment and dose.

## 2.8 qPCR

Cell plated in a 6-well format were washed with 1 ml of 1xPBS, and then the GenElute kit (Sigma) was used to extract RNA from the cells according to the manufacturer's instructions. RNA was eluted from the wash column in 40 µl of elution buffer. RNA concentrations were determined using a Nanodrop 1000 spectrophotometer (Thermo Scientific). cDNA was prepared from 500 ng total RNA using an Affinity script cDNA synthesis kit (Agilent) according to the manufacturer's instructions. qPCR reactions were set up using qPCR Brilliant SYBR green (Agilent) according to the manufacturer's instructions and were run on a MX3005P qPCR machine (Agilent Technologies). The reactions were prepared using a final primer concentration of 2 µM and 2 µl of cDNA template. Amplification of GAPDH was used as a loading control. All primers were ordered from Eurofins MWG Operon.

Primer forward (F) and reverse (R) sequences 5' to 3' are described below in Table 2.7:

| Target | Primer sequence |
|---|---|
| **GAPDH-F** | CCGCATCTTCTTTTGCGTCGC |
| **GAPDH-R** | AAATGAGCCCCAGCCTTCTCCATG |
| **TOPK-F** | GACTCTGGACTGAGAGTGGC |
| **TOPK-R:** | TAAACGGAGAGGCCGGGATA |

*Table 2.7: qPCR primers sequences*

## 2.9 TOPK plasmids

Vectors coding for TOPK wild-type (pCMV6-TOPK-Myc-DDK) and the TOPK K64M kinase mutant (pCMV6-TOPK-K64M-Myc-DDK) cDNA clones were purchased from Origene. Both the TOPK wild-type and TOPK K64M cDNA clones are 969 bp in length, and differ in sequence at only two bases to confer the K64M mutation. K64 is encoded by AAA in the TOPK wild-type, whereas M64 is encoded by ATG in the TOPK K64M kinase dead mutant. The empty vector control was pCMV6-Myc-DDK.

pCMV6-TOPK-K64M-Myc-DDK DNA sequence:

ATGGAAGGGATCAGTAATTTCAAGACACCAAGCAAATTATCAGAAAAAAAGA
AATCTGTATTATGTTCAACTCCAACTATAAATATCCCGGCCTCTCCGTTTATGC
AGAAGCTTGGCTTTGGTACTGGGGTAAATGTGTACCTAATGAAAAGATCTCC
AAGAGGTTTGTCTCATTCTCCTTGGGCTGTAATGAAGATTAATCCTATATGTAA
TGATCATTATCGAAGTGTGTATCAAAAGAGACTAATGGATGAAGCTAAGATTT
TGAAAAGCCTTCATCATCCAAACATTGTTGGTTATCGTGCTTTTACTGAAGCC
AGTGATGGCAGTCTGTGTCTTGCTATGGAATATGGAGGTGAAAAGTCTCTAA
ATGACTTAATAGAAGAACGATATAAAGCCAGCCAAGATCCTTTTCCAGCAGC
CATAATTTTAAAAGTTGCTTTGAATATGGCAAGAGGGTTAAAGTATCTGCACC
AAGAAAAGAAACTGCTTCATGGAGACATAAAGTCTTCAAATGTTGTAATTAA
AGGCGATTTTGAAACAATTAAAATCTGTGATGTAGGAGTCTCTCTACCACTGG
ATGAAAATATGACTGTGACTGACCCTGAGGCTTGTTACATTGGCACAGAGCC
ATGGAAACCCAAAGAAGCTGTGGAGGAGAATGGTGTTATTACTGACAAGGC
AGACATATTTGCCTTTGGCCTTACTTTGTGGGAAATGATGACTTTATCGATTC
CACACATTAATCTTTCAAATGATGATGATGATGAAGATAAAACTTTTGATGAA
AGTGATTTTGATGATGAAGCATACTATGCAGCCTTGGGAACTAGGCCACCTA
TTAATATGGAAGAACTGGATGAATCATACCAGAAAGTAATTGAACTCTTCTCT
GTATGCACTAATGAAGACCCTAAAGATCGTCCTTCTGCTGCACACATTGTTGA
AGCTCTGGAAACAGATGTCTAG

Plasmid amplification was performed by transforming One Shot® TOP10 Chemically Competent E.coli (Thermo Fisher Scientific) following the manufacturer's instructions. Colonies were plated on LB agar plates containing 50 mg/ml ampicillin, grown overnight and then transferred to 10 ml LB medium containing 50 mg/ml ampicillin. The next day, bacteria culture was expanded into 200 ml LB broth media. For DNA extraction from the transformed bacteria, 50 ml of culture was centrifuged at 6000 x g for 15 minutes, 4˚C. DNA purification was then performed using the QUIAGEN Plasmid *Plus* Kit (Quiagen) according to manufacturer's instructions, using a vacuum pump to eliminate the flow through. The concentration of the DNA was quantified using a Nanodrop 1000 spectrophotometer (Thermo Scientific).

## 2.10 TOPK inhibitor

The OTS964 TOPK inhibitor (Figure 2.1, Table 2.8) was purchased from DC Chemicals, Room 610,Building 15, Jinxiang Rd 201,Pudong District, Shanghai, China. 200150. Catalogue number: DC7723. Purity > 99%.

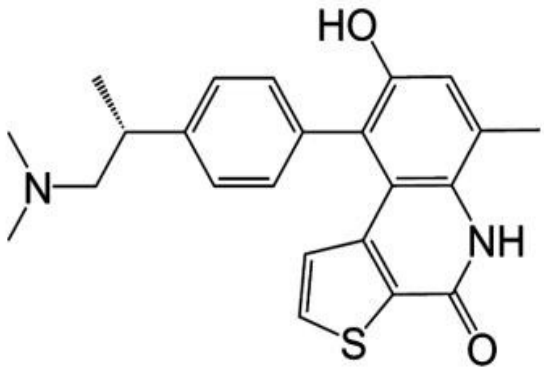


*Figure 2.1: Molecular representation of the OTS964 TOPK inhibitor [111].*

| Name | Molecular Weight | Formula | Solubility | Storage |
|---|---|---|---|---|
| **OTS964** | 378.49 | $C_{22}H_{22}N_2O_2S$ | DMSO | -20˚C Powder |

*Table 2.8: Details of the OTS964 TOPK inhibitor*

OTS964 was dissolved in DMSO, and aliquots were stored at -80˚C.

## 2.11 Immunoprecipitation protocol

### 2.11.1 Transfection

HCT116 cells were expanded into 4 x T175 flasks per condition (Empty Vector, TOPK, TOPK kinase dead) or one T75 flask per condition, depending on the experimental endpoint (see Table 2.9 below). The next day, when cells reached

| Flask type | Lipofectamine 2000 final concentration | Plasmid DNA final concentration | Total media in each flask |
|---|---|---|---|
| **T75** | 0.25% | 0.5 µg/ml | 10 ml |
| **T175** | 0.5% | 1 µg/ml | 20 ml |

*Table 2.9: Transfection conditions for the immunoprecipitation experiments*

### 2.11.2 Irradiation

The next day cells were irradiated with a dose of 4 Gy gamma rays and lysates were collected 8 hours after irradiation.

### 2.11.3 Immunoprecipitation

All of the following steps were performed on ice. Each flask was washed twice with ice cold 1xPBS. The PBS was carefully removed and 250 µl of RIPA lysis buffer (Thermo Scientific, 25 mM Tris-HCl pH 7.6, 150 mM NaCl, 1% NP-40, 1% sodium deoxycholate, 0.1% SDS) with 1 x protease inhibitor cocktail (Roche) and 1 x phosphatase inhibitor cocktail 2 (Sigma) was added. The cells were then scraped and transferred into 1.5 ml microcentrifuge tubes. Benzonase was added at a concentration of 1 µl/ml of lysate. The samples were then incubated for 30 minutes on a rotating wheel at 4°C. The samples were then passed through a 26 gauge needle 3-5 times and centrifuged at 25000 x g for 10 minutes. The supernatant was transferred in a fresh 1.5 ml tube containing 20 µl of A/G bead slurry for preclearing and incubated on a rotating wheel for 1 hour at 4°C.

The beads were previously washed three times with RIPA buffer. The samples were then centrifuged at 60 x g. For the input samples, 25 µl of supernatant was collected. The remainder of the supernatant was incubated overnight with 40 µl anti-Flag M2 agarose beads (Sigma) per condition at 4˚C with rotation. When the IP was performed to investigate interactions between endogenously expressed proteins, samples were incubated with the target antibody overnight with rotation and the next day incubated with A/G beads for 4 hours with rotation. The beads were then centrifuged at 60 x g at 4˚C for 2 minutes. Lysis buffer without protease inhibitors was used to wash the beads three times before the supernatant was completely removed and the bound proteins were eluted. For samples intended for LC-Ms/Ms analysis the washes were performed in a detergent-free washing buffer instead of RIPA (50 mM Tris-HCl, pH 7.4 with 150 mM NaCl).

### 2.11.4 Elution

For high throughput LC-Ms/Ms analysis, proteins were eluted by washing beads five times with 100 µl of a solution of 25 mM Na-Hepes pH 7.5, 100 mM NaCl, 1 mM PMSF, 0.2 µg/µl 3X Flag Peptide. For SDS-PAGE, samples were eluted using 30 µl of 2 x loading buffer (Expedeon, 40% glycerol, 4% lithium dodecyl sulfate, 4% Ficoll*-400, 0.8 M triethanolamine-Cl pH 7.6, 0.025% phenol red, 0.025% coomassie G250, 2 mM EDTA disodium) with 20 mM DTT. The gel was either stained with InstantBlue coomassie stain (Expedeon) and band extracted for mass spectrometry, or it was transferred to a membrane for western blotting. For transfection efficiency analysis the gel was stained with SYPRO Ruby Gel Staining kit (Thermo Fisher Scientific, #S12000) and visualised under ultraviolet light.

### 2.11.5 Sample preparation for mass spectrometry

For high throughput LC-Ms/Ms analysis, DTT (Sigma) was added to the samples to a final concentration of 5 mM. Samples were vortexed and

incubated at room temperature for 60 minutes. IAA iodoacetamide alkylating agent (Sigma) was added to the samples to a final concentration of 20 mM. The samples were vortexed and incubated at room temperature for 60 minutes. TCA (24% Trichloroacetic acid diluted in $dH_2O$) was then added to the samples to a final concentration of 6%, and the samples were vortexed, incubated for 2 hours at 4°C, and then centrifuged at 12000 x g for 30 minutes at 4°C. The supernatant was carefully removed and 1 ml of ice cold acetone was added to the pellet. The samples were then centrifuged at 12,000 x g for 5 minutes, the supernatant was carefully removed, and the pellets were allowed to air dry. The pellet was then reconstituted with urea buffer (8 M urea in 20 mM HEPES, pH 8), trypsin beads (Pierce-Perbio, 20230) were added and the samples were incubated at 37°C for 16 hours with shaking for protein digestion. After digestion, TFA was added, and then the samples were centrifuged at 2000 x g and passed through a C18+carbonSpintip (Glygen) tube as indicated by the manufacturer, and after four washes (first two washes were performed with 200 µl of 70% ACN, 30% $H_2O$, 0.1% formic acid, the last two washes were performed in 200 µl of 99% ACN, 1% $H_2O$, 0.1% formic acid) were eluted into a fresh Eppendorf tube. Samples were stored at -20°C until LC-MS/MS was performed.

## 2.12 Flow cytometry

### 2.12.1 Cell cycle analysis by propidium iodide staining

Cells were lifted using Trypsin-EDTA, re-suspended in medium, transferred into FACS tubes and pelleted by centrifugation at 200 x g for 5 minutes. The medium was removed and cells were fixed in ice-cold 70% ethanol. Samples were then centrifuged at 400 x g for 5 minutes and the ethanol was removed. The cells were washed once in 1xPBS to remove the ethanol, and then 300 µl propidium iodide (PI) staining solution (50 µg/ml PI, 200 µg/ml RNase) was added. Cells were vortexed briefly and incubated at room temperature in the dark for 10 minutes. Stained cells were analysed using a FACSort flow cytometer (Becton Dickinson). The cytometer settings were set at a flow rate of 150-300 events per second and the working voltage varied between 200 V and 400 V. Histogram plots were produced using open source Flowing Software 2.5.1.

### 2.12.2 Annexin-V/Propidium iodide staining

Cells were stained with Annexin-V and propidium iodide using the Annexin-V-FLUOS staining kit (Roche). Cells were washed with 1xPBS, lifted in trypsin-EDTA, re-suspended in medium, transferred to FACS tubes and spun down at 200 x g for 5 minutes. The pellet was washed with 1 ml 1xPBS and resuspended in 100 µl of Annexin-V staining solution (2 µl Annexin-V and 2 µl propidium iodide diluted in 100 µl Roche provided incubation buffer per sample). FACS tubes were gently vortexed and immediately analysed with the FACSort flow cytometer.

### 2.12.3 BrdU/Propidium iodide staining

20 µM BrdU (Sigma) was added to adherent cells in a 6-well plate 30 minutes before being lifted. After samples had been fixed in 70% ethanol and subsequently washed with 1xPBS, 2 M HCl containing 0.1 mg/ml pepsin was added and samples were incubated at room temperature for 20 minutes. Samples were then washed three times

with 2% FBS (Foetal Bovine Serum)/1xPBS and then resuspended in 100 µl of 2% FBS/1xPBS with 1 µl Mouse anti-BrdU monoclonal antibody (1:100, BD Bioscience). After 90 minutes incubation at room temperature, mixing every 30 minutes, 1xPBS was added, samples were centrifuged at 350 x g and the pellet was resuspended in 100 µl 2% FBS/1xPBS with 0.5 µl Goat anti-Mouse AF488 antibody (1:200 dilution) and incubated for 60 minutes at room temperature in the dark, mixing every 30 minutes. Finally samples were washed in 1 ml 1xPBS and resuspended in 0.5 ml 1xPBS containing 50 µg/ml propidium iodide, diluted as necessary to give a flow rate on the FACSort cytometer (Becton Dickinson) between 150 and 300.

## 2.13 Immunofluorescence

### 2.13.1 Immunofluorescence analysis

siRNA-transfected cells were plated in 96-well plates. At various time-points following IR treatment, cells were washed with 200 µl 1xPBS and fixed with 100 µl 3% paraformaldehyde in 1xPBS for 10 minutes. After washing with 200 µl 1xPBS, cells were blocked and permeabilised in 100 µl 1xPBS with 0.1% Triton, 1% BSA and 1% Goat serum at room temperature for at least 1 hour. The blocking buffer was removed and cells were probed with anti-γ-H2AX Ser139 (Upstate/Millipore, #05-636) and anti-53BP1 (Cell Signaling Technology, #4937S) antibodies at a concentration of 1:1500 and 1:800, respectively diluted in 1% BSA, 1% Goat serum in 1xPBS overnight at 4˚C. Plates were washed thrice with 200 µl 1xPBS with the second wash lasting 10 minutes. The cells were then incubated with Alexa Flour 488 goat anti-mouse (Invitrogen #A11001, 1:2000) or Alexa Fluor 568 Goat Anti-Rabbit (Invitrogen # A11011, 1:2000) conjugated secondary antibodies and 0.5 µg/ml 6-diamidino-2-phenylindole (DAPI) for at least 1 hour in the dark. Once more, plates were washed thrice with 200 µl 1xPBS. Foci were detected using the IN Cell Analyzer 1000 automated epifluorescence microscope (GE Healthcare). Foci were quantified using the IN Cell Analyzer Workstation software (v3.5). A minimum of 500 cells per well were counted per condition.

### 2.13.2 Hoechst apoptosis analysis

Cells were plated in 96-well plates (six wells/condition). On the appropriate day after irradiation 20 µg/ml Hoechst was added to each well, and the plates were incubated for 30-40 minutes. The plates were then analysed using the IN Cell Analyzer 1000 automated epifluorescence microscope (GE Healthcare). The total cell number and the number of cells with bright nuclei were quantified using the IN

Cell Analyzer Workstation software (v3.5). The threshold for bright nuclei was set to include apoptotic nuclei, but not mitotic nuclei in which the DNA is condensed.

### 2.13.3 Cell morphology analysis

Cells were allowed to adhere to glass coverslips on the bottom of each well in a 24-well plate. Cells were fixed with 70% ice-cold methanol for 10 minutes and then incubated with 250 µl of 1xPBS containing 1 µg/ml DAPI and 1 µg/ml FITC. The coverslips were then washed, removed from wells and mounted on a microscope slide using VECTASHIELD antifade mounting media. Samples were analysed with a confocal microscope (Zeiss710, Zeiss) and cell morphology were scored using a cell counter plug in (ImageJ open source software).

## 2.14 COMET assay

Reagents were prepared as described in Table 2.10.

| Reagent name | Reagent composition |
|---|---|
| Agarose for slides coating | Normal melting point agarose (1%) in distilled water. 800 µl molten normal melting point agarose was added on each slide after being heated carefully in microwave. A coverslip was added on top and was left to set for 5 minutes. The coverslip was then removed and slides were left to air dry overnight. |
| Low melting point agarose | 1% Low Melt Agarose (BioRad #1613111) in 1xPBS was kept at 37˚C in the water bath for the duration of the experiment. |
| Lysis Buffer | 2.5 M NaCl, 100 mM EDTA disodium salt, Tris base 10 mM in distilled water, pH 10.5 (adjusted with NaOH). Stored at 4˚C. Prior to use, the solution was completed by adding a mixture of 1 ml DMSO and 1 ml Triton X-100 to 98 ml cold lysis buffer. |
| Electrophoresis Buffer | 300 mM NaOH, 1 mM EDTA and 1% DMSO in distilled water, pH > 13. Stored at 4°C. |
| Neutralisation Buffer | Tris-HCl 500 mM, pH 8.0 |
| Distilled water pH 8.0 | MilliQ water – KOH was added drop-wise to adjust the pH to 8. |
| Staining buffer | SYBR Gold (SYBR® Gold Nucleic Acid Gel Stain, # S-11494) diluted 1:10000 in distilled water, pH 8.0 |

*Table 2.10: Reagents used for COMET analysis*

After radiation treatment, cells were lifted at the appropriate time point and transferred into a 1.5 ml tube. 1 ml of Low Melt Agarose was then added, samples were mixed gently by pipetting up and down and immediately transferred to a slide on ice. A coverslip was added on top to level the agarose. When the sample was solidified on the slide, after about 5 minutes, slides were transferred to a coplin jar containing fresh cold alkaline lysis solution and incubated in the dark at 4˚C for one hour. The slides were then placed side by side in a dark horizontal electrophoresis tank filled with fresh cold electrophoresis buffer. The samples were left for 30 minutes for alkaline unwinding in the dark inside the tank. The samples were subjected to electrophoresis at 25 V for 25 minutes, at a current of 300 mA. After electrophoresis, slides were removed carefully from tank and rinsed with 1 ml of neutralisation buffer for 5 minutes twice, and then allowed to air dry overnight. The next day, the slides were hydrated in distilled water at pH 8.0 for 30 minutes, and then 1 ml of staining buffer was added for 30 minutes. The samples were then washed with water and left to dry overnight. The samples were scored under a fluorescence microscope (Nikon 90i, Nikon) at 459 nm excitation wave length, using Komet 5.5 Software (Andor Technology).

## 2.15 Prognostic analysis

Prognostic analysis was carried out by Dr. Francesca Buffa as previously described [92], [93]. Briefly, the prognostic meta-analysis was carried out using the rmeta R package (http://cran.r-project.org/). A fixed-effect model was used. The log hazard ratios and standard errors were obtained for each study from Cox proportional hazards regression, study results were combined using the generic inverse-variance method. The variance was estimated as the square of the standard errors. This follows a Chi-Squared distribution with approximately k-1 degrees of freedom (k=number of studies). The patient numbers and treatment information for the data sets were as follows:

- GSE6532: Early stage breast cancer patients given adjuvant tamoxifen [94]. GSE6532Oxf, GSE6532KI, GSE6532GUY datasets contain 98,136 and 87 patients, respectively.
- GSE2034: 286 patients with early breast cancer not receiving either adjuvant or neoadjuvant therapy. 219 patients received breast conserving surgery and 67 were given radical mastectomy. 248 patients received radiotherapy [95].
- GSE9195: 77 early stage breast cancer patients which were treated with adjuvant tamoxifen monotherapy [94].
- GSE1456: 159 patients early breast cancer patients. 104 receiving adjuvant tamoxifen or chemotherapy [96].

## 2.16 Immunohistochemistry analysis

Prostate cancer samples for IHC and associated anonymous follow up data (ORB ethics 09/H0606/5+5) were a kind courtesy of Dr Richard J Bryant (Nuffield Department of Surgical Sciences, University of Oxford).

The biopsy samples had been fixed in formalin and embedded in paraffin before they were archived in 4 µm sections mounted on a microscope slide. The cohort included n=128 patients who received radical localised radiotherapy with curative intent. Prostate biopsies were collected at the time of diagnosis.

### 2.16.1 Staining

Samples staining was a kind courtesy of Lucia Cerundolo (Nuffield Department of Surgical Sciences, University of Oxford).

On day 1 slides were submerged in Histo-Clear II solution (National Diagnostic – HS-202) twice for 5 minutes with gentle shaking. Slides were then submerged in sequence for 5 minutes in ethanol at different dilutions in $H_2O$ (100% two times, 90%, 70%). To prevent background staining slides were then washed for 10 minutes in 10% hydrogen peroxide in methanol. Slides were then submerged in 90% and consequently in 70% ethanol and three times in fresh $H_2O$ (5 minutes incubation for each step). Slides were then submerged 10 minutes in Na citrate for de-masking at a temperature of just below 100˚C (to prevent boiling). Slides were then incubated at RT for 10 minutes and then incubated for 30 minutes at RT in 5% normal goat serum (NGS) in PBS in order to quench non-specific immunoproteins. 110 µl of primary antibody were then added to each sample. The antibody used for detecting TOPK was purchased from Cell Signaling Technology (#4942S) and used at a diluted concentration of 1:50 in 5% NGS/PBS. Samples were incubated overnight in a humidity chamber at 4˚C.

On day 2 slides were washed twice by submersion in PBS with gentle rocking for five minutes. Secondary antibody was then added at a 1:250 dilution in 5% GS/PBS and incubated at RT for 45 minutes in a humidity chamber. The antibody used was purchased by Vector Laboratories (BA-1000, 1.5 mg/ml biotinylated Anti-Rb IgG affinity purified). After incubation the slides were washed in PBS for 5 minutes at RT. ABC reagent was then added (RTU Vectastain - Vector Laboratories PK-7100) for exactly 15 minutes in the humidity chamber at RT. After exactly 15 minutes each slide was washed with PBS for three times. DAB substrate kit for peroxidose SK-4100 – Vector Laboratories was then added for exactly 5 minutes and slides were then washed with PBS first and then with $H_2O$. Harris Hematoxilin (SIGMA HHS32-1L) was added for 15 seconds and then washed off with water. Slides were then dehydrated by incubating for about 1 minute in subsequently 70%, 90%, 100% ethanol. Finally samples were covered carefully with a coverslip with mounting medium Omnimount (National Diagnostic – HS-110).

### 2.16.2 Scoring

Scoring was kindly performed by Dr Clare Verrill, pathologist (Nuffield Department of Surgical Sciences & Department of Cellular Pathology, University of Oxford).

A four-point staining intensity scoring system was devised for determining the relative expression of TOPK in cancer specimens. The maximum staining intensity score ranged from 0 (no expression) to 3 (maximal expression). Samples were scored for nuclear TOPK expression and for cytoplasmic TOPK expression. A relative percentage of cancer cells with the assigned protein intensity was also given. The intensity and percentage scores were multiplied to give a *TOPK* expression score (0-300) for nuclear or cytoplasmic expression. Total *TOPK* expression was obtained by addition of the nuclear and cytoplasmic score (0-600).

### 2.16.3 Statistical methods and patient survival analysis

Patients survival curves were obtained by Kaplan-Meier analysis using a log rank test and SPSS statistic 22 software (IBM, Portsmouth, UK). All statistical tests were performed as two-tailed tests. Differences were considered significant at a p-value of less than 0.05 ($p<0.05$).

# CHAPTER 3

# IDENTIFICATION OF TOPK AS A MOLECULAR DETERMINANT OF RADIOSENSITIVITY

## 3.1 Introduction

Finding and targeting novel genes that regulate radiation response in tumours would widen the therapeutic window between tumour control probability and normal tissue complication probability, allowing better disease control and improved patient survival. It is therefore crucial to identify *in vitro* those modulators of radiosensitivity which could be translated into the clinic and the colony formation assay (CFA) has become the gold standard for assessing radiation treatment *in vitro* [62].

Our laboratory has recently developed a 96-well plate colony formation assay, enabling the screening of novel radiosensitising targets with a high-throughput approach with the use of siRNA gene silencing [64]. In order to identify novel radiosensitising genes, Dr. Gagan Tiwana and Dr. Remko Prevo in our laboratory used this assay to perform an siRNA screen in HeLa cells treated with 0 Gy and 7 Gy IR, after pooled siRNA gene knockdown targeting kinases. HeLa cells were chosen because they form distinct and tight colonies, have a good transfection efficiency, and are a widely used cancer model. A colony was considered to be a group of about 50 cells or more, and the number of cells plated was optimised to make it possible to calculate the surviving fraction (SF). Figure 3.1A shows an example of an irradiated and an unirradiated 96-well plate showing a difference in colony formation post 7 Gy IR and siRNA treatment. In this example the magnified well shows radiosensitisation due to thiamine pyrophosphokinase-1 (TPK1) siRNA knockdown [64]. A non-targeting siRNA (siNT) was used as a negative control (average plating efficiency: 28%, average surviving fraction at 7 Gy: 0.084) and DNA-$PK_{cs}$ was used as a positive control (average surviving fraction at 7 Gy: 0.0038). A radiosensitisation score ($R_{score}$) was calculated in order to

rank the genes as described in equation (4) below, with low values representing greater radiosensitisation [64].

$$R_{score} = (normalised\ SF - 1) / (mean\ absolute\ deviation\ of\ normalised\ siNT\ SF) \quad (4)$$

The process included two phases, a primary screen to identify genes whose depletion increased radiosensitivity from a pool of 709 siRNAs (siRNA library: Dharmacon ON-TARGET *plus*), and a secondary screen (siRNA library: Dharmacon siGENOME) of the top 76 genes that showed radiosensitising properties in the primary screen. Both screens were performed in two replicates, and a heat map showing the top candidate genes, ordered by rank-product between the two repeats, of the secondary screen is shown in Figure 3.1B. The screen identified known modulators of radiosensitivity, including DNA-$PK_{cs}$ (PRKDC) and ATM (Figure 3.1B) as genes with low $R_{score}$ rankings, confirming the ability of the screening technique to identify radiosensitising genes Figure 3.1C.

The screen identified a large list of candidate genes that needed further validation and investigation.

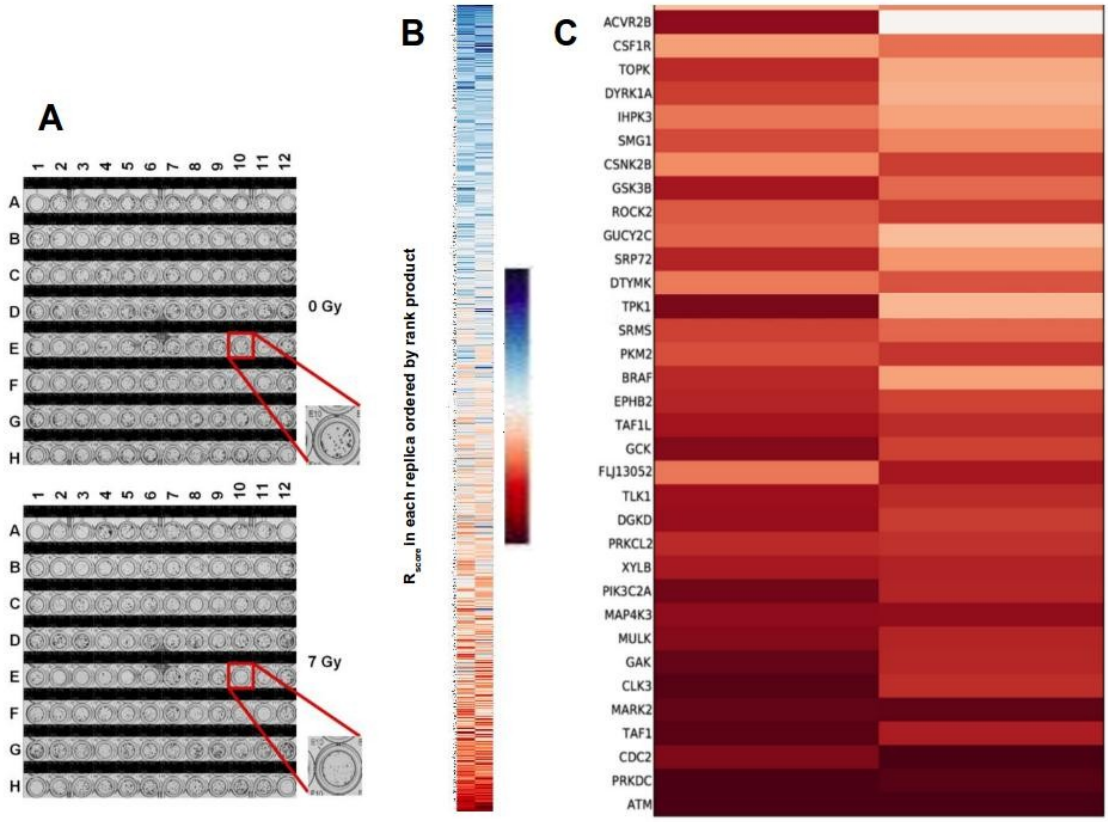


*Figure 3.1: A high-throughput colony formation screen performed by Gagan Tiwana and Remko Prevo in our laboratory identified a list of candidate genes that modulate radiosensitivity in HeLa cells (adapted and permission gained from [64]). (A) An example of two 96-well plates either unirradiated (top) or irradiated (bottom). Each well represents a gene knockdown. The two magnified wells show the difference in colony formation after 7 Gy IR for the same siRNA treatment (in this example siRNA targeting TPK1). (B) Heat map of the kinase primary screen showing the two repeats (left and right) ordered by $R_{score}$ ranking of the investigated 709 kinase genes. Radioprotection is labelled in blue and radiosensitisation in red. (C) A magnification of the greatest modulators of radiosensitivity after siRNA knockdown identified in the secondary screen (showing the top 34 genes out of 76). It is interesting to note that some of the genes identified by the screen are, as expected, known determinants of radiosensitivity such as DNA-$PK_{cs}$, ATM, CDC2.*

Targets were ranked based on their $R_{score}$ and the rank product was generated between replicate runs for both the primary and the secondary screen as described previously [64]. Figure 3.2A and Figure

3.2B show two separate repeats of the secondary screen, in which only the top 76 radiosensitising siRNAs from the primary screen were tested. In both repeats of the secondary screen, knockdown of *GAK*, *EPHB2*, *CSF1R* and *TOPK* caused reproducible radiosensitisation in HeLa cells.

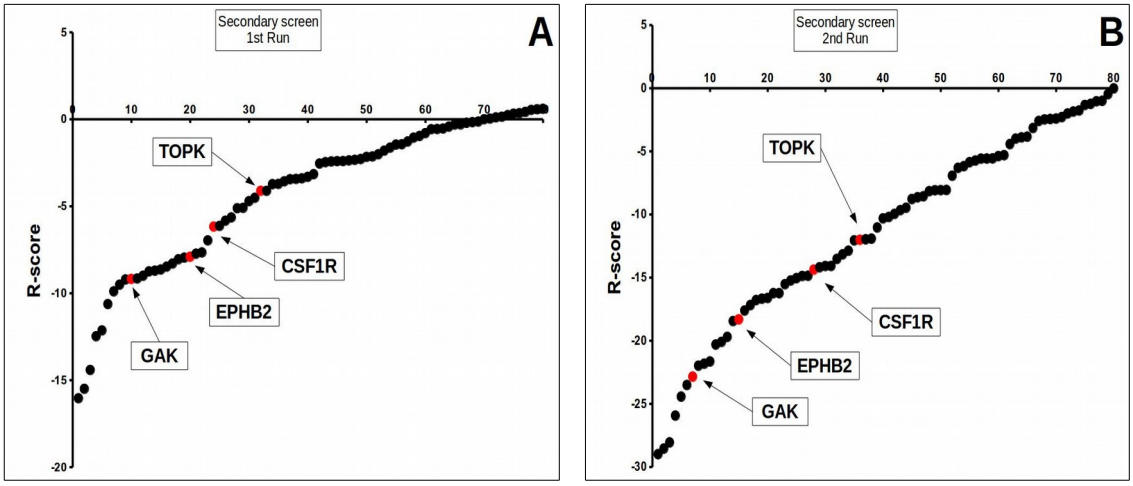


*Figure 3.2: Secondary screen dot-plot of the $R_{score}$ for each kinase gene in HeLa cells. (A) The first repeat. (B) The second repeat. The selected genes CSF1R, EPHB2, GAK and TOPK are shown in red and are labelled. The $R_{score}$ indicates the degree of radiosensitisation (for negative values) or radioprotection (for positive values). siRNAs that reduced the plating efficiency under a level of 5% were excluded from the analysis. Adapted and permission gained from [64].*

## 3.2 Results

### 3.2.1 Gene selection and validation

The criteria used to determine which genes to investigate further were as follows:

- Novelty in the context of radiation. A literature research was performed to assess whether the gene was already known as radiosensitiser.
- Differential expression. The Oncomine 3.0 [75], [76] database was used to evaluate the tumour and normal tissue expression profile of the candidate gene. An ideal modulator of radiosensitivity is differentially expressed in tumour and normal tissues. Targeting of differentially expressed genes may allow widening of the therapeutic window in the clinic.
- Availability of reagents for further studies. In order to determine the mechanism of action of radiosensitisation, reagents such as antibodies are essential. Reagent availability was therefore determined by literature searching and checking various scientific suppliers.

This preliminary approach identified a list of potentially interesting candidates, four of which will be presented in this chapter. Before considering these genes as potential modulators of radiosensitivity, their validation and a mechanistic characterisation was needed.

The selected candidate genes for further investigation are described in Table 3.1 and are represented in red in the dot-plot of the $R_{score}$ of the two repeats of the secondary screen in Figure 3.2.

| Candidate | Full name | Known function | Screening final ranking [64] |
|---|---|---|---|
| ***CSF1R*** | Colony stimulating factor 1 receptor | Controls the production, differentiation and functions of macrophages. It is also upregulated in different leukaemias and may be involved in mammary carcinogenesis [97], [98] | **24$^{th}$** |
| ***EPHB2*** | Ephrin type-B receptor 2 | Regulates glioma cell adhesion, growth and invasion [99], [100] | **20$^{th}$** |
| ***GAK*** | Cyclin G-associated kinase | Androgen receptor related gene involved in prostate cancer development [101] | **10$^{th}$** |
| ***TOPK*** | T-LAK cell-originated protein kinase (also known as PBK, PDZ-binding kinase) | MAPKK-like kinase, can be a substrate for CDK1/Cyclin B. Phosphorylated in mitosis. Role in proliferation. Suppression induces multinucleation [71], [72], [74] | **32$^{nd}$** |

*Table 3.1: Kinome targets chosen for further investigation. The known function column gives a short description of the most relevant published literature. The screening final ranking column represents the final ranking for each siRNA on the*

*list of radiosensitisers with 1 being the most radiosensitising siRNA. The final ranking was calculated based on the $R_{score}$ of the different repeats of the screen.*

The first step taken to validate the selected four candidate genes, *CSF1R*, *EPHB2*, *GAK* and *TOPK* was to test whether radiosensitisation was also observable in cell lines other than HeLa following siRNA-mediated depletion of the gene activity. A set of 6-well plate CFAs were conducted in a panel of different cancer cell lines and the data is presented in Figure 3.3 for HeLa (cervix adenocarcinoma) cells, in Figure 3.4 for SQ20B (laryngeal carcinoma) cells, and in Figure 3.5 for T24 (bladder carcinoma) cells.

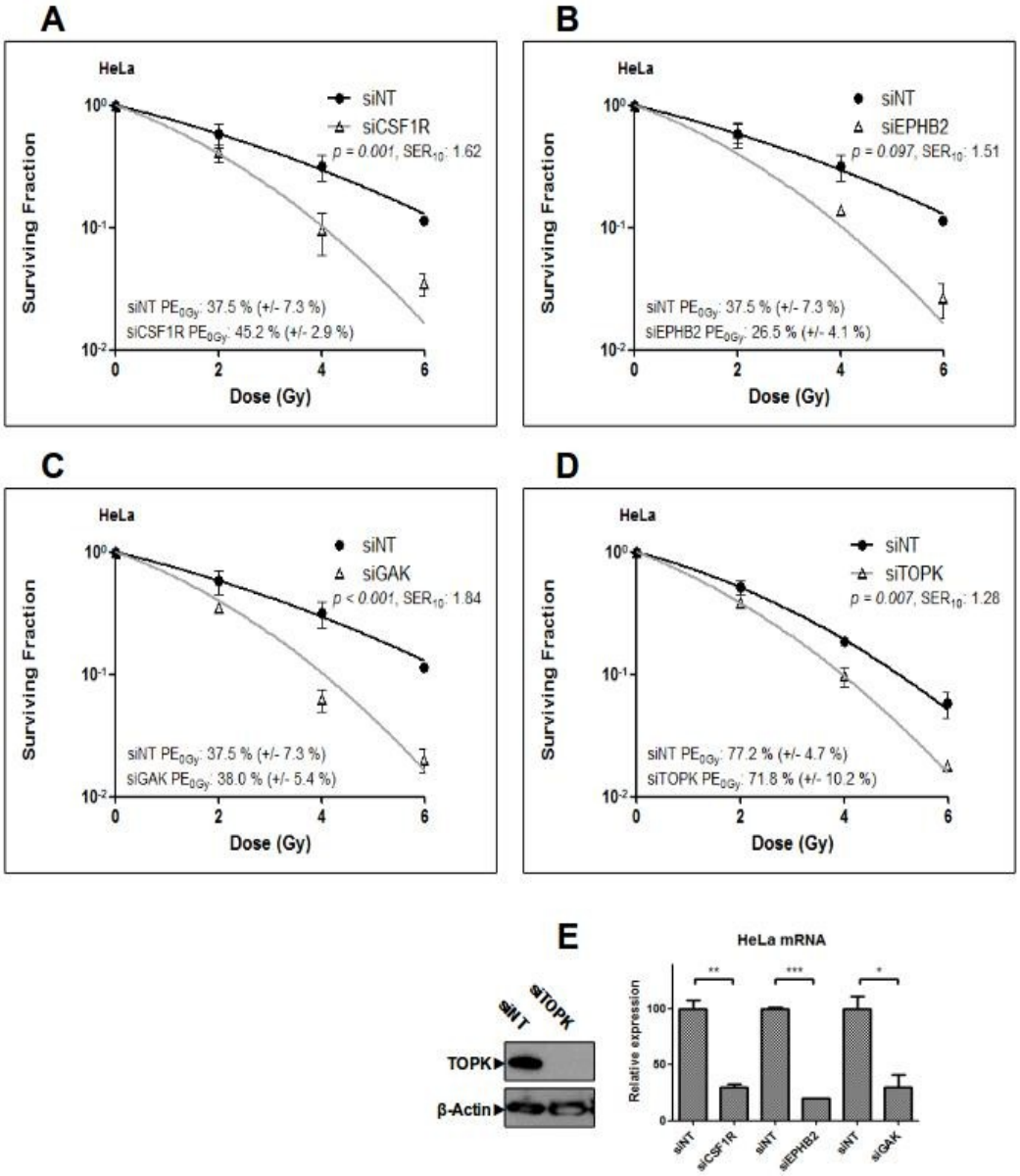


*Figure 3.3: CFAs in HeLa cells to validate the four selected genes. HeLa cells were transfected with the indicated siRNA. After 48 hours the cells were lifted, counted, replated in fresh medium and irradiated at either 2 Gy, 4 Gy or 6 Gy. Colonies were stained and counted after 2 weeks. siRNA knockdown of CSF1R (A), EPHB2 (B), GAK (C) and TOPK (D) caused radiosensitisation in HeLa cells. (E) CSF1R, EPHB2 and GAK knockdown was confirmed with qPCR, and TOPK knockdown was confirmed by immunoblotting.*

*All data are representative of three independent experiments and presented as mean +/- SD from triplicate wells. Cells were transfected with the indicated siRNA at 20 nM final concentration. Colonies were stained and counted about 2 weeks*

*after IR depending on growth rate. p-values were generated by factorial 2-way ANOVA. PE = Plating Efficiency. $SER_{10}$ = Sensitisation Enhancement Ratio at 0.1 surviving fraction calculated from non-linear regression of linear quadratic model. Student's t-test was calculated for the statistical significance of qPCR knockdown levels. *p<0.05, **p<0.01, ***p<0.001.*

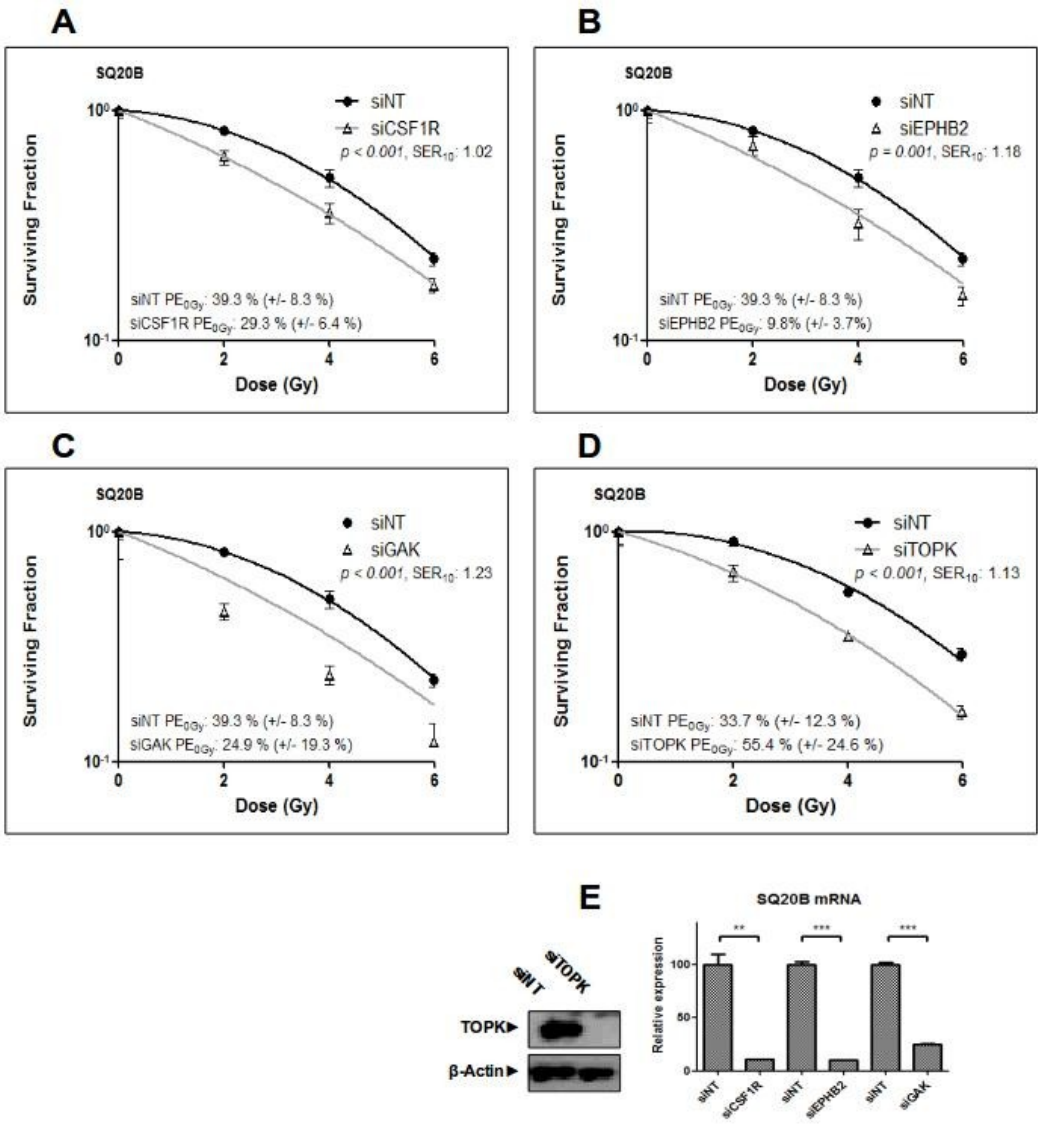


*Figure 3.4: CFA with SQ20B cells to validate the four selected genes. (A) CSF1R siRNA knockdown caused radiosensitisation in SQ20B cells. (B) Survival curves for EPHB2 showed a significant radiosensitisation on SQ20B cells. (C) siGAK showed the greatest radiosensitisation in SQ20Bs. (D) TOPK knockdown showed a significant radiosensitising effect in SQ20B. (E) CSF1R, EPHB2 and GAK knockdown*

*was confirmed with qPCR, TOPK knockdown was confirmed by immunoblotting.*

*All data are representative of three independent experiments and presented as mean +/- SD from triplicate wells. Cells were transfected with the indicated siRNA at 20 nM final concentration. Colonies were stained and counted about 2 weeks after IR depending on growth rate. p-values were generated by factorial 2-way ANOVA. PE = Plating Efficiency. $SER_{10}$ = Sensitisation Enhancement Ratio at 0.1 surviving fraction calculated from non-linear regression of linear quadratic model. Student's t-test was calculated for the statistical significance of qPCR knockdown levels. **p<0.01, ***p<0.001.*

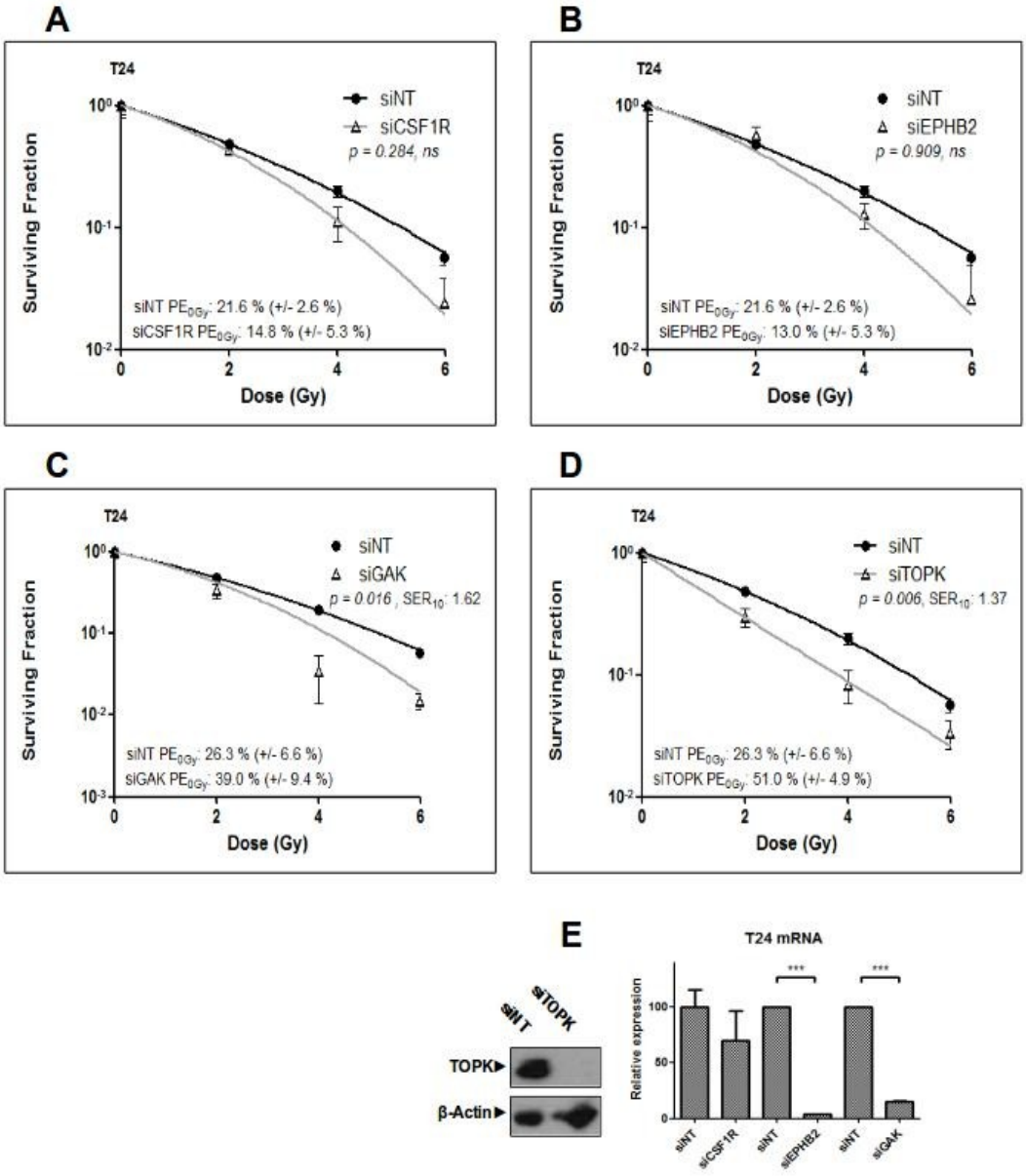


*Figure 3.5: CFA in T24 cells to validate the four selected hits. (A) CSF1R siRNA knockdown did not show a significant radiosensitisation in T24 cells. (B) Survival curves for EPHB2 showed poor radiosensitisation in T24 cells. (C) GAK siRNA knockdown shows the most evident radiosensitisation. (D) TOPK showed a good radiosensitisation in T24 when knocked-down. (E) CSF1R, EPHB2 and GAK knockdown were confirmed with qPCR, TOPK knockdown was confirmed by immunoblotting.*

*All data are representative of three independent experiments and presented as mean +/- SD from triplicate wells. Cells were transfected with the indicated siRNA at 20 nM final concentration. Colonies were stained and counted about 2 weeks*

*after IR depending on growth rate. p-values were generated by factorial 2-way ANOVA. PE = Plating Efficiency. $SER_{10}$ = Sensitisation Enhancement Ratio at 0.1 surviving fraction calculated from non-linear regression of linear quadratic model. Student's t-test was calculated for the statistical significance of qPCR knockdown levels. ***p<0.001.*

In order to investigate the effect of depletion of the *CSF1R, EPHB2, GAK and TOPK* genes on intrinsic radiosensitivity, HeLa, SQ20B and T24 cells were transfected with the indicated siRNAs. After 48 hours cells were lifted, counted, replated in fresh medium and irradiated at either 2 Gy, 4 Gy or 6 Gy. Colonies were stained and counted about 2 weeks post IR depending on growth rate. Finally, the surviving fraction was determined for each dose and the Sensitisation Enhancement Ratio ($SER_{10}$) was calculated at 0.1 surviving fraction from non-linear regression of the linear quadratic model. Statistically significant radiosensitisation was observed following knockdown of *CSF1R, EPHB2, GAK and TOPK* in HeLa cells, with $SER_{10}$ values of 1.62, 1.51, 1.84 and 1.28, respectively (Figure 3.3). A statistically significant radiosensitisation was also observed following knockdown of *CSF1R, EPHB2, GAK and TOPK* in SQ20B cells, with $SER_{10}$ values of 1.02, 1.18, 1.23 and 1.13, respectively (Figure 3.4) and following knockdown of the *GAK and TOPK* genes only in T24 cells, with $SER_{10}$ values of 1.62 and 1.37, respectively (Figure 3.5). Knockdown of *CSF1R* gene expression could not be achieved in T24 cells, which may explain why significant radiosensitisation was not observed, but it is unclear why significant radiosensitisation was not observed following *EPHB2* knockdown in T24 cells.

As *CSF1R* and *EPHB2* knockdown did not radiosensitise T24 cells, it was decided not to investigate these two genes further. From CFA results the greatest radiosensitising effects were observed after *GAK* and *TOPK* knockdown.

As previously stated, the ideal gene for modulating radiosensitivity as a potential clinical target would show a differential effect between normal and cancerous tissue. If a gene is not expressed in normal tissue, its siRNA-mediated knockdown should not be effective and should not modify the cellular behaviour in terms of radiosensitisation. In order to test whether the radiosensitising effect of the knockdown of *GAK* or *TOPK* was tumour specific, a set of CFAs was performed in HFL-1 and MRC5 cells (normal lung fibroblasts). These two normal cells were chosen based on their ability to form countable colonies in CFAs.

*GAK* knockdown showed radiosensitisation with an $SER_{10}$ of 1.19 in HFL-1 cells and a greater radiosensitisation with a $SER_{10}$ of 1.32 in MRC5 cells, whereas *TOPK* knockdown did not induce any detectable effects (Figure 3.6). Levels of *TOPK* expression were not detectable in both cell lines, and therefore it was not possible to determine the efficiency of the siRNA-mediated knockdown.

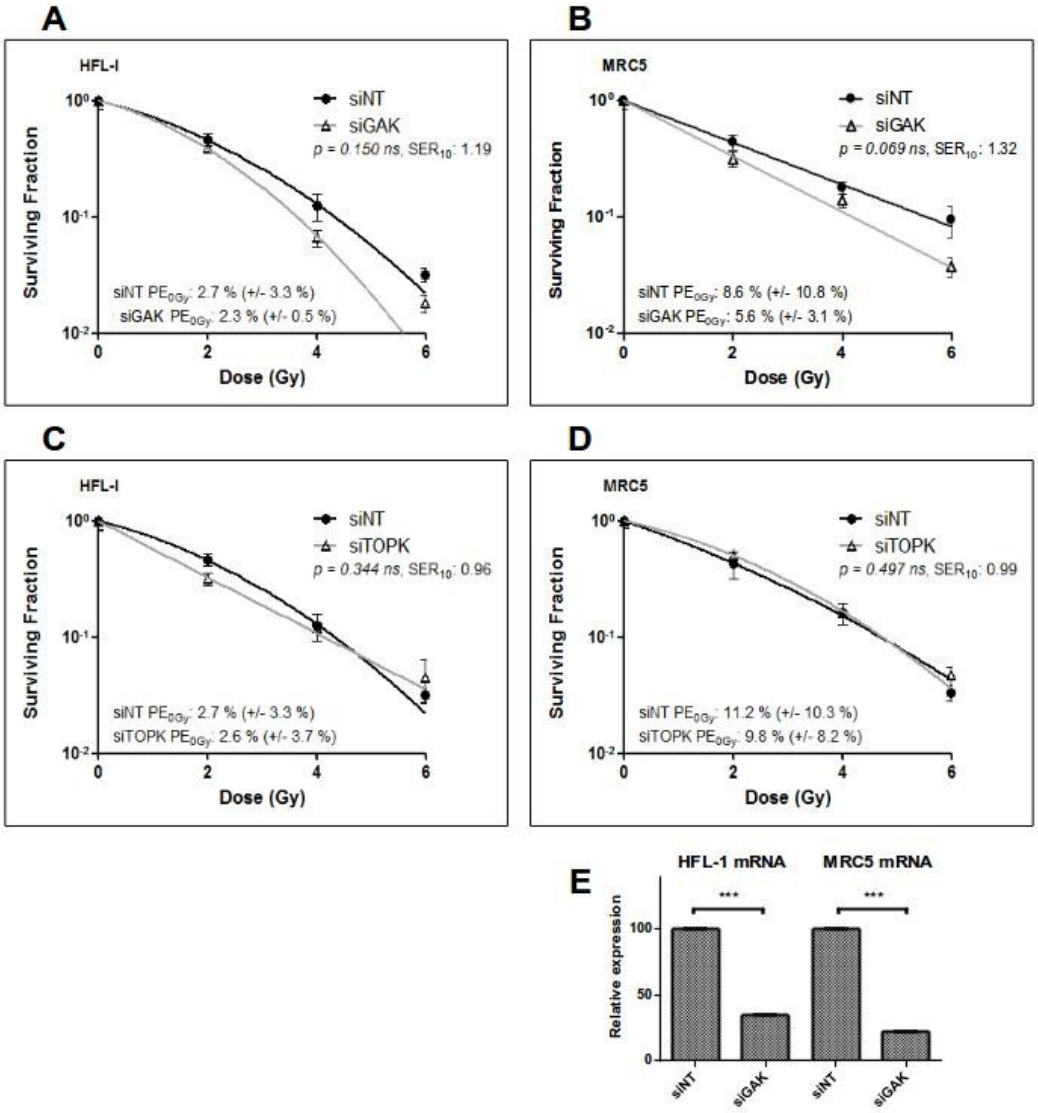


*Figure 3.6: CFAs in HFL-1 and MRC5 normal cells to test radiosensitisation due to GAK or TOPK depletion. (A) GAK siRNA knockdown showed radiosensitisation in HFL-1 cells with a $SER_{10}$: 1.19. (B) GAK siRNA knockdown showed radiosensitisation in MRC5 cells with a $SER_{10}$: 1.32. (C) TOPK depletion did not show any significant radiosensitisation in HFL-1 cells. (D) TOPK depletion did not show any significant radiosensitisation in MRC5 cells. (E) GAK knockdown was confirmed with qPCR in both cell lines, but TOPK levels were undetectable in both cell lines by immunoblotting.*

*All data are representative of three independent experiments and presented as mean +/- SD from triplicate wells. Cells were transfected with the indicated siRNA at 20 nM final concentration. Colonies were stained and counted about 2 weeks after IR depending on growth rate. p-values were generated by factorial 2-way*

*ANOVA. PE = Plating Efficiency. $SER_{10}$ = Sensitisation Enhancement Ratio at 0.1 surviving fraction calculated from non-linear regression of linear quadratic model.*

Although *GAK* knockdown caused a radiosensitisation effect that was non-significant, *TOPK* siRNA depletion did not show any significant radiosensitising effects on HFL-1 and MRC5 cells, with $SER_{10}$ values of 0.96 and 0.99, respectively. These survival curves showed that siRNA-mediated knockdown of *TOPK* does not induce radiosensitisation in the two normal tissue cell lines tested.

As previously stated, one of the criteria for target selection was the differential expression between normal and cancerous tissues. For this reason the Oncomine 3.0 [75], [76] database entry for each gene was checked and is shown in Figure 3.7.

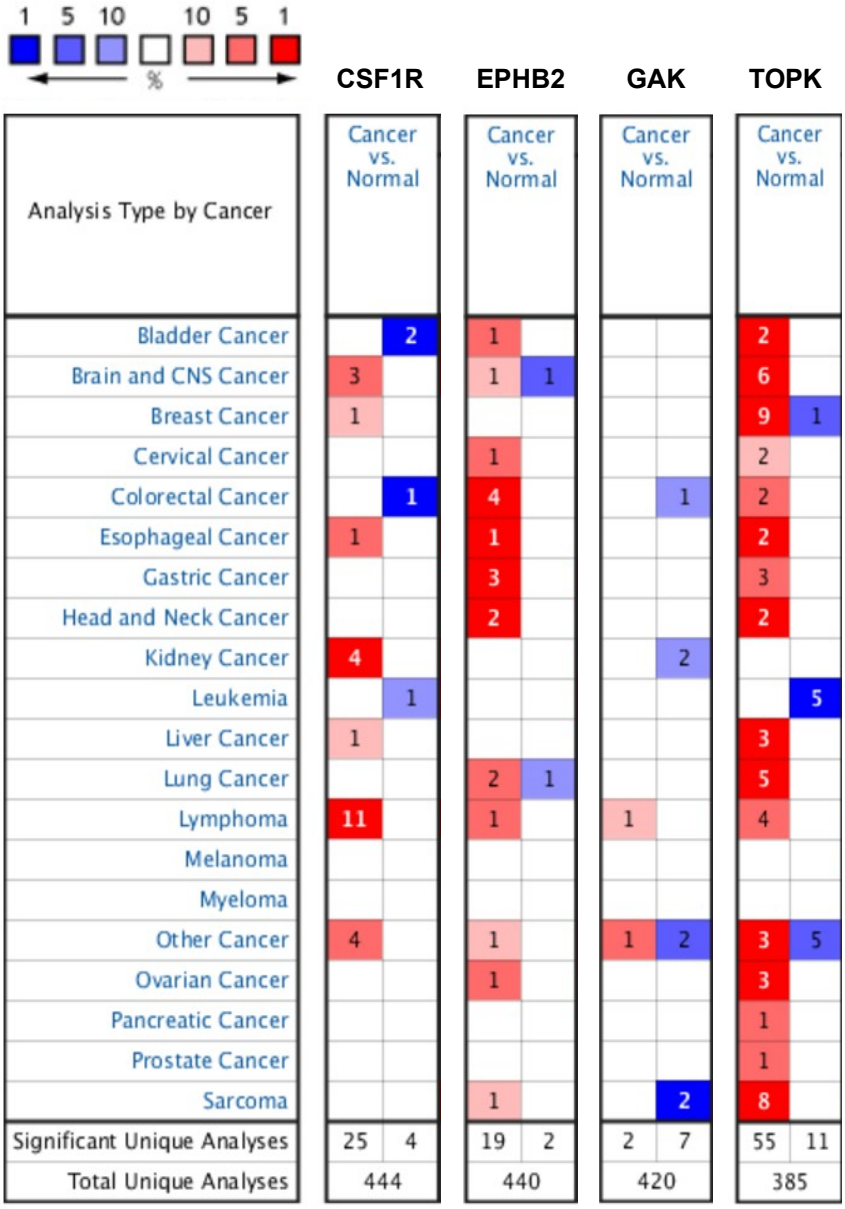


*Figure 3.7: Oncomine 3.0 Database disease summary for CSF1R, EPHB2, GAK and TOPK.*

*Data were retrieved from the Oncomine cancer microarray database through the Oncomine web platform described in [75], [76]. Data represent the up-to-date collection of all the published works containing microarray data about the enquired gene. The total number of studies considered is indicated in the "Total Unique Analyses" field, where the "Significant Unique Analyses" field indicates the significant analysis based on the selected threshold. Colours are Z-score normalised and represent least expressed (blue) to most expressed (red). The*

*number in each square indicates the amount of significant studies in which the gene had differential expression in cancer compared to normal tissue.*

*Threshold was established using the suggested values from [75] (p-value) $1x10^{-4}$. Fold change 2. Gene rank top 10%. Red indicates relative overexpression and blue indicates relative underexpression. The number in each square represents the number of studies analysed to produce the data.*

Figure 3.7 presents the Oncomine 3.0 database entry for each gene. Data are presented in red or blue depending on the gene mRNA levels, being overexpressed or underexpressed respectively in each cancer type. The number in the coloured square indicates the amount of significant studies in which the gene had differential expression in cancer compared to normal tissue. *CSF1R* is overexpressed in seven of the total number of considered cancers and is underexpressed in three of them including bladder cancer. This might explain why CFAs did not show radiosensitisation nor gene knockdown in the T24 bladder cancer cell line. *EPHB2* is overexpressed in the majority of the considered cancers and is underexpressed in two. Oncomine reports *GAK* to be overexpressed in only two cancers and underexpressed in four. Data for *TOPK* expression show a very marked overexpression in the majority of the reported cancer types and underexpression in three of them. The clear differential *TOPK* expression between cancer and normal tissues suggested that *TOPK* would be a good candidate for further study.

Furthermore, in order to confirm that *TOPK* has differential expression between normal and cancer tissues at a protein level, immunoblotting was performed to investigate TOPK levels in cell lysates from a set of different cancer cell lines and two normal tissue cell lines. The membrane was probed using an anti-TOPK antibody to detect the protein at the expected size of ~ 40 kDa. The tested cell lines are

listed in Table 3.2 and the resulting immunoblot is presented in Figure 3.8.

| | |
|---|---|
| **DLD1** | Colorectal adenocarcinoma |
| **A549** | Lung carcinoma |
| **H460** | Lung carcinoma |
| **HeLa** | Cervix adenocarcinoma |
| **SQ20B** | Laryngeal carcinoma |
| **T24** | Bladder carcinoma |
| **HCT116** | Colon carcinoma |
| **H1299** | Non-small cell lung carcinoma |
| **MRC5** | Normal lung tissue |
| **HFL-1** | Foetal normal lung fibroblast |

*Table 3.2: List of the cell lines tested for TOPK protein level. Two normal tissue cell lines were included (MRC5 and HFL-1). All cell lines were authenticated by STR profiling.*

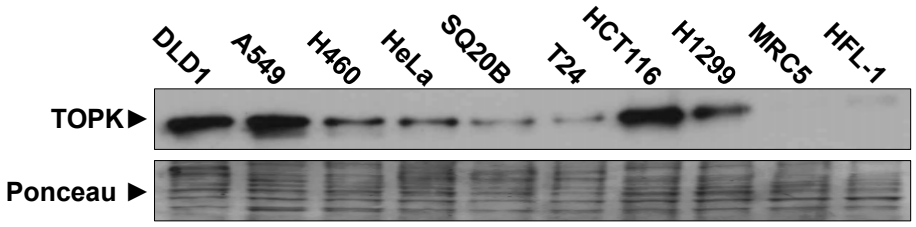


*Figure 3.8: Immunoblotting of different cancer and normal tissue cell lysates revealed detectable levels of TOPK protein only in the cancer cell lines. The Ponceau staining of the membrane is shown as a protein loading control.*

Levels of TOPK varied between the tested cell lines but showed a striking difference between cancer cell lines (DLD1, A549, H460, HeLa, SQ20B, T24, HCT116 and H1299) and normal cells (MRC5 and

HFL-1). Highest TOPK protein levels were detected in the DLD1, A549, HCT116 and H1299 cell lines.

These observations suggested that *TOPK* was the leading candidate for further investigation. Therefore this thesis will focus on the study of *TOPK*.

### 3.2.2 Identification of *TOPK* as modulator of radiosensitivity

The T-LAK cell-originated kinase TOPK, also known as PDZ-binding kinase (PBK), is a 322 amino-acid Ser/Thr kinase first identified in 1999 [71].

One of the reasons that makes *TOPK* an attractive candidate as a modulator of radiosensitisation is its differential expression between normal and cancerous tissues (Figure 3.7 and Figure 3.8) and the consequent radiosensitisation of cancer cells with no effects on normal tissues after siRNA knockdown (Figure 3.3, Figure 3.4, Figure 3.5, Figure 3.6 and Figure 3.6).

In order to investigate the effect of *TOPK* knockdown in other cell lines, CFAs after TOPK depletion were performed on a panel of cancer cell lines including HCT116 (colorectal cancer), H1299 (non-small cell lung carcinoma), DU145 (prostate cancer), and PC3 (prostate adenocarcinoma). The results are presented in Figure 3.9. Depletion of TOPK showed significant radiosensitisation in HCT116 (Figure 3.9A), H1299 (Figure 3.9B), DU145 (Figure 3.9C), and PC3 (Figure 3.9D) cell lines. In particular the HCT116 and DU145 cell lines showed the strongest effect with an $SER_{10}$ of 1.45 and 1.55, respectively. The $SER_{10}$ for H1299 cells was 1.28, and for PC3 cells was 1.35. The level of *TOPK* knockdown, shown by immunoblotting, was good in HCT116, H1299 and DU145. Although incomplete knockdown was observed in PC3 cells, this was still sufficient to induce radiosensitisation. Either β-Actin or Vinculin were used as a loading control. These data suggest

that targeting TOPK could improve sensitivity to radiation in a range of tumour types, making this an attractive possible clinical approach.

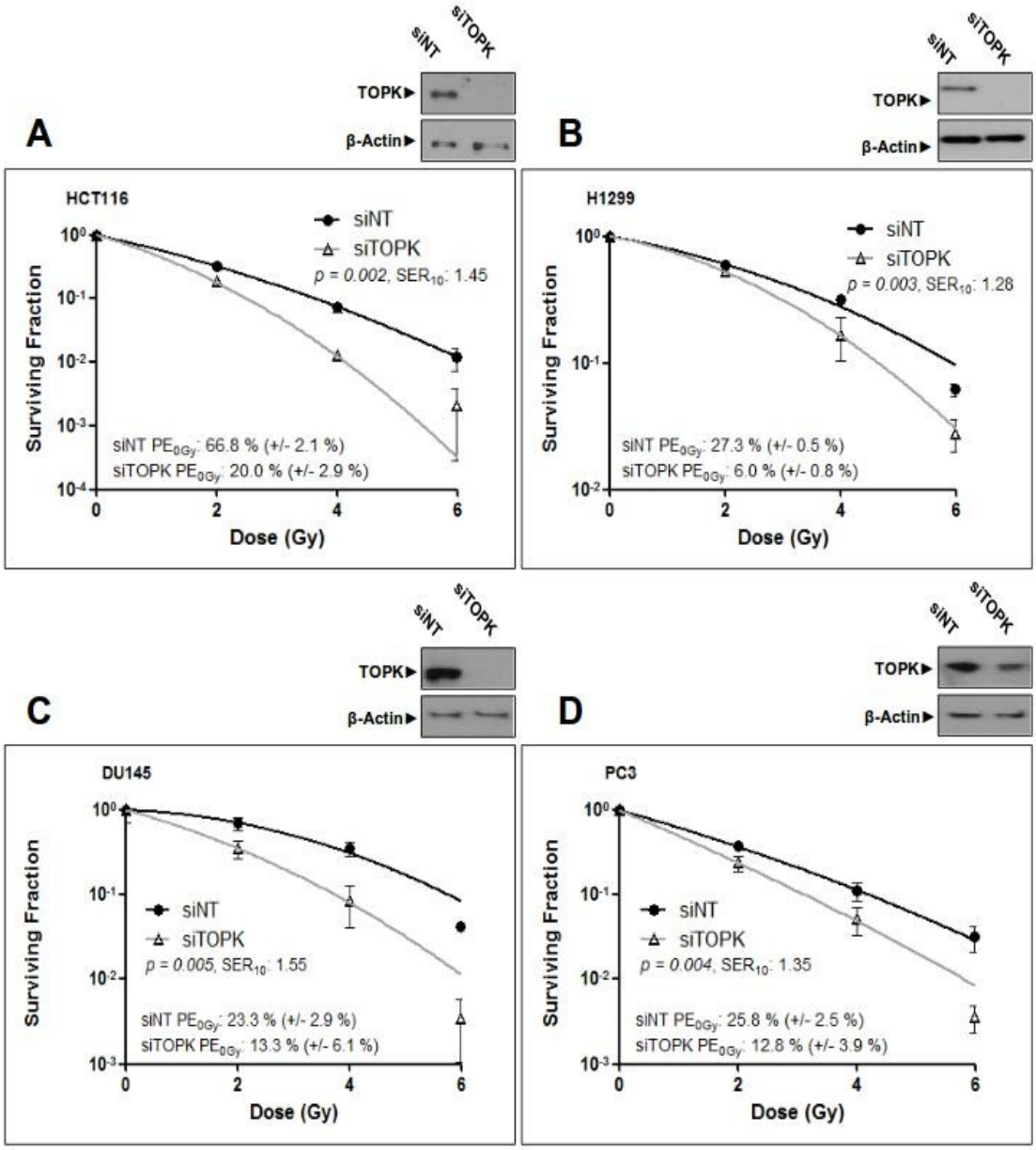


*Figure 3.9: TOPK knockdown causes radiosensitisation in multiple cancer cell lines. (A) Colony formation assay (CFA) in HCT116 cells. (B) CFA in H1299 cells (C) CFA in DU145 cells (D) CFA in PC3 cells. For all the four cell lines TOPK knockdown was confirmed by immunoblotting (inset).*

*All data are representative of three independent experiments and presented as mean +/- SD from triplicate wells. Cells were transfected with the indicated siRNA*

*at 20 nM final concentration. Colonies were stained and counted about 2 weeks after IR depending on growth rate. p-values were generated by factorial 2-way ANOVA. PE = Plating Efficiency. $SER_{10}$ = Sensitisation Enhancement Ratio at 0.1 surviving fraction calculated from non-linear regression of linear quadratic model.*

### 3.2.3 Validation of TOPK as modulator of radiosensitivity

In order to exclude possible off-target effects, a deconvolution CFA was performed using the HCT116 cell line. The cells were transfected either with siTOPK_1 or siTOPK_2 siRNAs at 20 nM final concentration. These two different siRNA constructs target different regions within the *TOPK* gene. After 72 hours the cells were then lifted, replated and irradiated. Colonies were counted after 2 weeks. The produced survival curves are shown in Figure 3.10A:

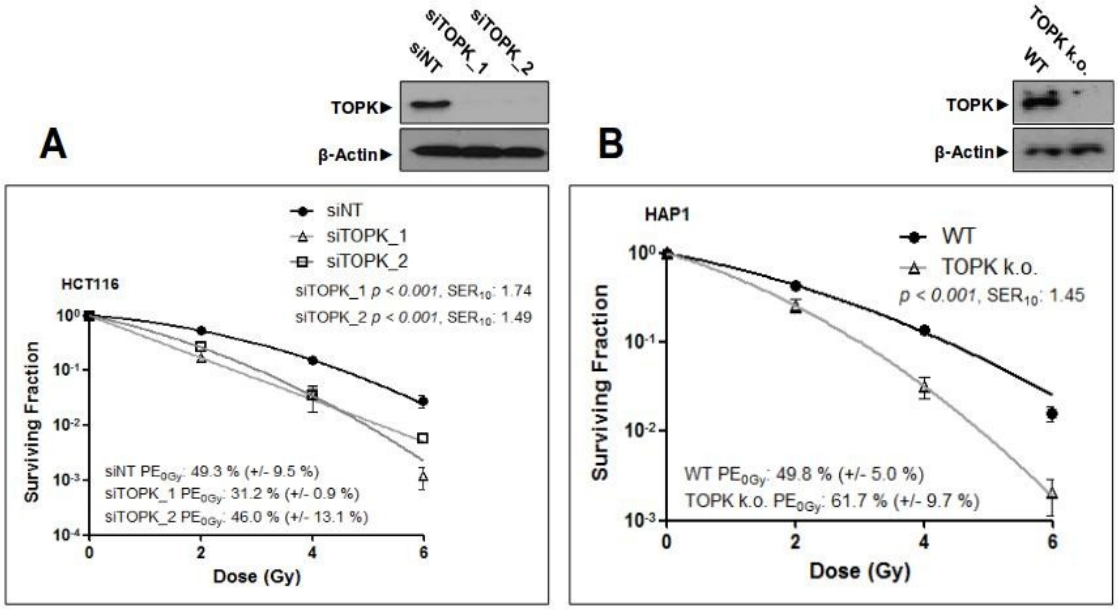


*Figure 3.10: (A) Colony formation assay (CFA) in HCT116 cells irradiated 72 hours post Ambion siRNA transfection at 20 nM final siRNA concentration with either non-targeting (siNT), siTOPK_1 or siTOPK_2. (B) HAP1 wild type (WT) cells expressing TOPK showed a statistically significant radioresistance when compared to the HAP1 TOPK knock-out (k.o.) cell line. TOPK knockdown or knock-out was confirmed by immunoblotting (inset).*

*All data are representative of three independent experiments and presented as mean +/- SD from triplicate wells. HCT116 c*ells were transfected with the indicated siRNA at 20 nM final concentration. Colonies were stained and counted about 2 weeks after IR depending on growth rate. *p-values were generated by factorial 2-way ANOVA. PE = Plating Efficiency. $SER_{10}$ = Sensitisation Enhancement Ratio at 0.1 surviving fraction calculated from non-linear regression of linear quadratic model.*

The survival curves in Figure 3.10A showed a significant radiosensitisation for both the siRNAs si*TOPK*_1 and si*TOPK*_2, with a $SER_{10}$ of, respectively, 1.74 and 1.49, suggesting a gene-specific effect on colony formation due to siRNA silencing of *TOPK*.

Furthermore, a HAP1 *TOPK* knock-out (TOPK k.o.) cell line was purchased from Horizon Discovery. This cell line is an adherent haploid cell line derived from the KBM-7 leukaemia cell line in which the gene of interest, *TOPK*, was knocked-out by the Clustered

regularly-interspaced short palindromic repeats (CRISPR/Cas9) technique. By comparing the TOPK k.o. line to the parental cell line, HAP1 wild type (WT), it was possible to test the effects of lack of TOPK on radiosensitivity in a colony-formation assay. The results are shown in Figure 3.10B and reveal a pronounced radiosensitising effect associated with *TOPK* knock-out, with a $SER_{10}$ of 1.45 and a p-value of less than 0.001. The protein expression level for TOPK and the β-Actin loading control were tested with immunoblotting on cell lysates. Taken together, these results suggest that the radiosensitisation observed following *TOPK* depletion is not due to an unknown off-target effect.

## 3.3 Discussion

The need to identify novel modulators of radiosensitivity led our laboratory to develop a high-throughput kinase screen in 96-well plate format. This technique, based on the ability of cells to form colonies after a specific gene knockdown and ionising radiation, was used to screen a total of 709 kinases, producing a ranking based on the radiosensitisation of HeLa cells after siRNA knockdown [64]. One of the limitations of this assay is the use of only one cell line. The HeLa cell line was chosen because it is a very well described cancer model, and because of its ability to form countable colonies in a 96-well plate. However, a response observed using the HeLa cell line is not necessarily representative of responses observable using other cell lines. Another limitation of the screen is the possibility of off-target effects with the potential of consequent false-positive or false-negative results. These limitations make further investigation and validation of candidate radiosensitising genes a necessity.

From the list of kinases with the highest rank product, shown in Figure 3.1, four genes were selected for further investigation and validation based on their novelty in the context of radiation, their differential expression in normal tissues compared to cancerous tissues, and the availability of reagents. These genes were *CSF1R*, *EPHB2*, *GAK* and *TOPK* (Figure 3.2).

*CSF1R*, Colony Stimulating Factor 1 receptor, has been described as a key regulator of monocyte differentiation and of the generation of tissue-resident macrophages. It has also been shown to be upregulated in different leukaemias and may be involved in mammary carcinogenesis [97], [98], [102]. In the presented study it was shown to radiosensitise HeLa and SQ20B cells but not T24 cells. Furthermore the available expression data showed overexpression of *CSF1R* in a limited number of cancers (Figure 3.7).

*EPHB2*, Ephrin type-B receptor 2, has been shown to regulate glioma cell adhesion, growth and invasion. It is a prognostic factor and a drug target for the treatment of colorectal cancer and is often mutated in prostate cancer [99], [100], [103]–[105]. Here it was presented as a modulator of radiosensitivity in HeLa and SQ20B cells, but not in the T24 cell line. Expression data in Figure 3.7 from the Oncomine 3.0 database showed overexpression of *EPHB2* in a number of cancers and underexpression in only two types.

*GAK*, Cyclin G-asociated kinase, is an androgen receptor related gene that is involved in prostate cancer development. It regulates epidermal growth factor receptor signalling and promotes microtubule outgrowth during spindle assembly [101], [106], [107]. In this study it was shown to induce significant radiosensitisation after siRNA knockdown in all cancer cell lines tested. However, radiosensitisation was observed following GAK depletion in HFL-1 and MRC5 normal cells, and expression levels did not suggest overexpression of *GAK* in the majority of cancers.

*TOPK* was identified as a strong modulator of radiosensitivity in a panel of cancer cell lines with no effects on normal tissues. Furthermore, Oncomine 3.0 data revealed *TOPK* overexpression in the majority of cancer types. Therefore *TOPK* was the most promising candidate, and was chosen for further studies.

TOPK, also known as PDZ-binding kinase (PBK), is a 322 amino-acid Ser/Thr kinase first identified in 1999 [71]. Its differential expression between normal and cancerous tissues and its known correlation with bad outcome when upregulated in tumours suggested it could be an attractive candidate as a modulator of radiosensitivity. It has been shown that *TOPK* expression in normal tissues is restricted to testis and placenta [71]–[74] and that it is upregulated in most cancers.

High levels of TOPK have been linked to poor clinical efficacy in many different studies. In breast cancer patients *TOPK* expression has been shown to correlate with adverse outcomes in terms of overall survival and recurrence free survival [77]. Its adverse effects on tumour control have also been shown in non-small-cell lung cancer (NSCLC), where *TOPK* has been positively correlated with p53 mutant expression levels with highest *TOPK* expression in lymph nodes and metastases [78]–[80]. In prostate cancer patients levels of TOPK were also shown to commensurate with invasiveness and cancer stage, with higher levels of expression in circulating tumour cells (CTCs) and a negative effect on clinical outcome. In colorectal cancer, levels of TOPK were correlated with levels of interlukin-8 (IL-8 or CXCL8) [83] and *KRAS* and *BRAF* mutations [84], and a prognostic role of TOPK for predicting poor clinical outcomes was suggested.

The Oncomine 3.0 Database entry for this gene [75], [76] confirmed that *TOPK* is overexpressed in most cancerous tissues as shown in Figure 3.7.

Previous studies have tried to identify the mechanisms of action of TOPK in different cellular contexts. It has been shown that TOPK phosphorylates p38 [71] and that it is able to downregulate PTEN expression with consequent phosphorylation of AKT and an increased cell migration and invasion effect [80]. TOPK was shown to serve as an oncogenic kinase that exerts positive feedback loop on ERK2 which promotes colorectal cancer formation *in vitro* and *in vivo* [85]. Hu et al. (2010) showed a direct interaction between TOPK and the tumour-suppressor p53, with consequent regulation of p21 expression and effects on cellular growth [88]. A major role for TOPK during mitosis has also been described. It was described in HeLa as a regulator of the mitotic C2H2 zinc finger proteins [108] and to participate together with PTEN in CHFR mediated mitotic checkpoint activation [86]. TOPK phosphorylates histone H3 (Ser10), which is needed for the initiation

of metaphase, and *TOPK* down-regulation with RNAi results in cytokinetic failure and cell cycle arrest [109], [110]. Furthermore, a positive regulatory role in proper chromosomal separation has been described for TOPK [74], [109].

In the context of DNA damage, TOPK has only been studied in response to doxorubicin or arsenite treatment [88], [89] and ultraviolet radiation (UV-B) [90], [91] showing an inhibition of the damage-induced checkpoint activation and, when depleted, a decreased phosphorylation of the H2AX histone [91].

To the best of my knowledge, the radiosensitisation observed in this study after siRNA knockdown of *TOPK*, presented in Figure 3.3-3.5, is the first study of *TOPK* in the context of ionising-radiation induced DNA damage.

The radiosensitising effect of TOPK depletion was tested in a colony formation assay (CFA) format in a panel of different cancer cell lines. Furthermore, these CFAs were performed in a 6-well plate format rather than the 96-well plate format used for screening, which allows a better discrimination of colonies for more precise counting. Whereas the screen tested only 0 Gy and 7 Gy, these 6 well CFAs tested four different radiation doses (0, 2, 4 and 6 Gy) to investigate the dose-dependency of the effect.

The differential expression between normal and cancerous tissues (Figure 3.7) was confirmed on a protein level with immunoblotting of whole cell lysates from a panel of cancer cell lines and two normal cell lines which did not show a detectable band (Figure 3.8). CFAs using two normal cell lines not expressing *TOPK* showed no radiosensitisation following TOPK depletion, suggesting a potential tumour-specific role for TOPK in the response to ionising radiation (Figure 3.6C and D).

*TOPK* was shown to be expressed in a panel of cancer cell lines, and its depletion was shown to radiosensitise HeLa, T24, SQ20B, HCT116, H1299, DU145 and PC3 cells. However, for the following experiments and mechanistic investigations HCT116 cells were chosen as the most suitable model. This is because HCT116 cells have a high level of *TOPK* expression, as shown in Figure 3.8, and convincing radiosensitisation was observed after siRNA mediated knockdown of *TOPK*, with an $SER_{10}$ of 1.45. Furthermore high levels of TOPK have been previously shown to be correlated with a lower survival and disease-free survival in colorectal cancer patients [83] and to be an unfavourable prognostic indicator in patients with sporadic *KRAS* or *BRAF* mutations [84]. HCT116 have been shown to form xenograft tumours in mice, so this cell line could be a good model for future *in vivo* experiments [85]. Mechanistic studies have shown an interaction between TOPK and the DNA-binding domain of p53 and an increase in levels of apoptosis after doxorubicin treatment in HCT116 [88]. The OTS964 TOPK inhibitor has been tested on HCT116 with an $IC_{50}$ of 33 nM [111]. Furthermore, HCT116 form very defined and countable colonies in a CFA, are p53 wild type, and are relatively easy to transfect. Therefore the studies presented in the subsequent sections of this thesis will focus on HCT116.

Gene silencing is a potent tool for discover new targets but can be frequently influenced by the discovery of false-positives. These arise from unspecific targeting of the siRNAs which might induce silencing of random genes which will affect the final endpoint [112]. It becomes crucial then to validate siRNA silencing by excluding the possibility of the observed effect to be off-target.

A deconvolution experiment was performed in HCT116 cells in order to exclude the possibility of an off-target effect of the siRNA. Two new siRNA sequences, si*TOPK*_1 and si*TOPK*_2, caused a significant radiosensitisation in a CFA format (Figure 3.10A). The

radiosensitisation effect was further confirmed using the HAP1 *TOPK* knock-out cell line (Figure 3.10B).

A further experiment to exclude off-target effects was performed by overexpressing an siRNA-resistant *TOPK* vector in HCT116 cells (data not shown). The goal was to rescue the radiosensitisation observed after siRNA-mediated knockdown of *TOPK*. Unfortunately the experiment did not work. There could be multiple explanations for this, including an inappropriate level of TOPK protein overexpression, or inappropriate timing of *TOPK* expression. Addressing these issues was beyond the scope of this work.

Taken together these results identify TOPK as a molecular regulator of radiosensitivity with broad potential for further mechanistic studies and possible future clinical applications.

# CHAPTER 4

# THE RESPONSE TO IONISING RADIATION IN TOPK-DEPLETED CELLS

## 4.1 Introduction

*TOPK* was selected from a list of candidate genes identified by a high-throughput CFA screen of 709 kinases as a potential regulator of the radiation response in cancer cells. In this study, an increased radiosensitisation after siRNA *TOPK* knockdown was observed in a panel of cancer cell lines, with no effect on normal tissues. Furthermore, *TOPK* is overexpressed in cancer, conferring poor prognosis, and is not expressed in most normal tissues. These findings made TOPK an ideal clinical target candidate, but did not reveal a mechanism of action for the radiosensitisation.

In order to explore the role of TOPK in altering tumour radiosensitivity, its effects on the cellular response to ionising radiation were investigated. Several approaches were undertaken to investigate different endpoints in irradiated HCT116 cells following TOPK depletion.

Various previous studies have implicated TOPK in cell proliferation and cell migration. In absence of DNA damage, overexpressed *TOPK* has been shown to immunoprecipitate with α-tubulin and with both cyclin B1 and CDK1 in COS-7 cells [74]. It has been also shown that TOPK phosphorylates p38 in *TOPK*-overexpressed COS-7 cells and in a kinase assay *in vitro* [71]. TOPK was shown to participate to the PI3K/AKT pathway and influence cell migration [80]. This study revealed a negative correlation of the levels of TOPK protein with the levels of PTEN and a consequent positive correlation with the levels of phospho-AKT in lung cancer cell lines. Furthermore in breast cancer TOPK has been shown to phosphorylate histone H3 *in vitro* and *in vivo* [87]. A two-hybrid screen identified an interaction of TOPK with the PDZ2 domain of hDlg tumour suppressor [72] and IκBα leading to NF-κB activation [113]. In HEK293 cells overexpressing *TOPK* and in

HCT116 untransfected cells, TOPK has been shown to participate in a positive phosphorylation loop with ERK2 [85].

Prior to the present work, the role of TOPK in the cellular response to IR-induced DNA damage has not been published in the literature. In the context of DNA damage, TOPK has only been studied in response to doxorubicin treatment [88], [89], arsenite ($As^{3+}$) treatment [90] and ultraviolet radiation (UV-B) [91]. Overexpression of *TOPK* in fibrosarcoma cells (HT1080) has been shown to physically destabilise tumour-suppressor p53 and attenuate the $G_2$/M checkpoint after doxorubicin treatment [89]. Furthermore it has been shown that *TOPK* knockdown in HCT116 cells increases p53-dependent overexpression of p21 and elongates the doubling time through accumulation in $G_2$/M together with an increase in the levels of apoptosis after doxorubicin treatment [88]. In the context of UV radiation, *TOPK* depletion has been shown to reduce the number of γ-H2AX foci and decrease cell survival in human breast adenocarcinoma cells (MCF-7) [91]. TOPK has also been shown with LC-Ms/Ms (liquid chromatography mass spectrometry) to bind to H2AX, colocalise with γ-H2AX after UV damage and inhibit arsenite-induced apoptosis in melanoma cells (RPMI7951) [90].

In contrast with doxorubicin, UV light and arsenite, radiation-induced DNA damage consists mostly of direct and indirect double-strand breaks [10]. When the DNA is damaged a prompt and efficient DNA damage response (DDR) occurs in order to repair the break and limit the detrimental effects on the cell. The DDR is a complex coordinated process involving many different steps with multiple different proteins and pathways which depend also on the type of damage, and is an area of intense ongoing academic investigation. One of the earliest events in this process is the identification of the DNA damage site, which allows the recruitment of the proteins that are needed for DNA repair. This step can be monitored with immunofluorescence (IF)

techniques which allow the formation of DNA damage foci at repair sites to be observed. The phosphorylation of histone H2AX and the localisation of 53BP1 at the damaged site are broadly used to evaluate the levels of DNA damage after double-strand breaks (DSBs) in terms of early damage signalling at few minutes after IR and in terms of persistent DNA damage at later time points following IR [10].

The COMET assay may also be used to study IR-induced DNA breaks, signalling and repair. The COMET assay (also known as Single Cell Gel Electrophoresis assay) uses an electric field to induce migration of the denatured DNA in an agarose gel. With this technique it is possible to quantify the DNA damage by measuring the length of the tail produced by the unwound DNA migration (tail momentum).

Another important event in the DDR is activation of cell cycle checkpoints. The activation of the $G_1$/S, intra-S and $G_2$/M checkpoints temporarily halts progression through the cell cycle in order to allow the faithful repair of the damage before the cell divides. This is a crucial mechanism for the maintenance of genetic stability and could lead to senescence ($G_0$) or cell death when the damage is not repaired [10], [43]. Flow cytometry can be a useful method to divide a cell population depending on the phase f the cell cycle for each cell. In particular propidium iodide (PI) could be used to determine the DNA content of each nucleus and therefore whether a cell is in $G_1$ or $G_2$/M phase, and bromodeoxyuridine (BrdU) can be used to distinguish early and late S phase based on its levels of incorporation in newly synthesised DNA.

The two major types of cell death after irradiation are apoptosis and mitotic catastrophe. Mitotic catastrophe is sometimes considered as an aberrant mitosis followed by apoptosis, and is one of the major events post radiotherapy, especially in solid tumours [114].

Apoptosis occurs when the cellular genetic stability is irreversibly lost and it is then easier to limit the damage to the organism by killing the cell via a programmed cell death pathway. The most evident hallmarks of apoptosis include cell shrinkage, membrane permeabilisation and disruption, and chromosome condensation [21]. A key player of this process is p53 [46], [115]. Under normal conditions p53 is constantly degraded by its binding partner MDM2, forming a balanced equilibrium. After IR injury, ATM phosphorylates p53 and MDM2, disrupting the balance. As a consequence the excess in activated p53 can lead to apoptosis through the activation of pro-apoptotic genes such as BAX and PUMA [10], [21], [46]. Annexin V can be used to detect cells that have expressed phosphatidylserine (PS) on the cell surface, an event which occurs in the early stages of apoptosis.

Mitotic catastrophe is the improper completion of cell division and is morphologically associated with the accumulation of multinucleated cells with the presence of chromosome aberrations and micronuclei, and has been linked to abnormal CDK1/Cyclin B activation [10]. $G_2$ and mitosis checkpoints are involved in preventing mitotic catastrophe by ensuring the correct completion of DNA replication before progression through mitosis, and the bypass of these checkpoints permits premature mitosis with unrepaired or not fully replicated DNA leading to this form of cell death [10], [21], [114]. Mitotic catastrophe is a delayed form of cell death and can occur a few days after treatment [114]. For these reasons, and because a role for TOPK in mitosis has been thoroughly described in the absence of ionising radiation [74], [86], [108]–[111], mitotic catastrophe was studied.

In order to better understand the mechanism behind TOPK modulation of radiosensitivity, a series of different immunoprecipitations were performed using different approaches to identify which proteins might

interact with TOPK at 8 hours after 4 Gy IR in HCT116 cells. Immunoprecipitation is a technique used to separate (pull down) a target molecule and its interacting partners from the whole cellular lysate with the use of a specific antibody. The molecules that are pulled-down are then eluted and analysed in order to identify interactions. Immunoprecipitation can be performed after overexpression and flag pull down or at the endogenous level using a specific antibody.

## 4.2 Results

### 4.2.1 TOPK depletion alters the early response to radiation-induced DNA damage

The earliest cellular response to DNA double-strand breaks (DSBs) involves the phosphorylation of the histone H2AX, forming γ-H2AX foci which localise at the damage site. Simultaneously 53BP1 also localises at the same DNA region. These two early events trigger the DNA-damage response and help to recruit DNA repair proteins to the DSB [10], [21], [25].

In order to test whether TOPK-dependent radiosensitisation was due to impaired DNA repair machinery, the kinetics of γ-H2AX and 53BP1 foci formation and resolution after 4 Gy IR were investigated in HCT116 cells. This experiment was a time course from 30 minutes, when the γ-H2AX and 53BP1 foci formation are expected to reach a peak [25], [116], to 24 hours after IR. Foci can be quantified in cellular nuclei by immunofluorescence techniques. A primary antibody binding to either γ-H2AX or 53BP1 was used with a fluorescent labelled secondary antibody with excitation at 488 nm (green) and 568 nm (red), respectively. The nuclei were stained with the fluorescent nuclear dye, DAPI (blue), and the average number of foci per cell was counted automatically using the InCell Analyzer. The results, shown in Figure 4.1A, revealed a small but significant difference in the number of foci between cells transfected with NT siRNA and cells transfected with *TOPK* siRNA at 30-minutes with a p-value of less than 0.1, although this difference was not observed at the later time points. Similar kinetics were observed also when scoring cells for 53BP1 foci as shown in Figure 4.1B. However, these differences are not observed at 4, 8 and 24 hours post IR, suggesting that TOPK might not have a prominent role in the signalling of DSBs induced by IR.

To determine whether the observed kinetics of DDR foci resolution correlated with the persistence of DNA breaks, the levels of DNA damage were tested using an alkaline COMET assay and the cellular growth rate was monitored *in vitro* by resuspending trypsinised cells and counting them.

A primary antibody binding to either γ-H2AX or 53BP1 was labelled with fluorescent secondary antibody with excitation at 488 nm (green) and 568 nm (red) respectively. The nuclei were stained with fluorescent DAPI (blue) staining and the average number of foci per cell was counted automatically using the InCell Analyzer. The COMET assay consisted of encapsulating a low-density cell suspension in low-melting agarose on a microscope slide. Samples were then lysed with an alkaline lysis buffer in order to permeabilise the cell membranes and disrupt the DNA double helix, and were subjected to electrophoresis at 25 V for 25 minutes, at a current of 300 mA. The electric field allows the damaged DNA strand to migrate out of the nucleus into the agarose gel. This process forms a *tail* drawn from the nucleus which is detectable with DNA staining and is correlated in length and intensity to the amount of initial DNA damage. Samples were stained with SYBR Gold nucleic acid gel stain which has an excitation maximum at 300 nm (yellow). The tail momentum was quantified using Komet 5.5 Software (Andor Technology).

The obtained results are shown in Figure 4.1 below.

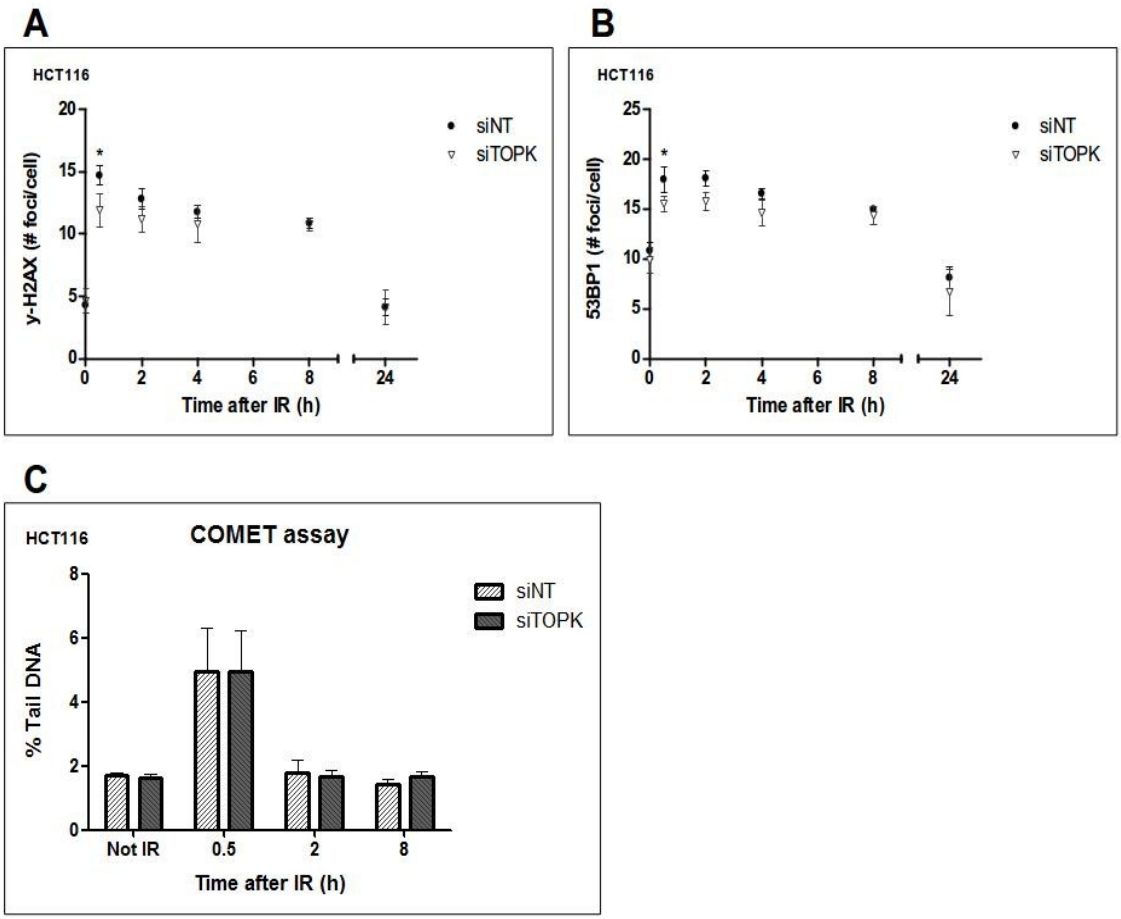


*Figure 4.1: The role of TOPK in the early DNA-damage response. (A) The number of γ-H2AX foci per cell at 0 hours, 0.5 hours, 2 hours, 4 hours, 8 hours and 24 hours following 4 Gy IR, 72 hours after transfection with NT or TOPK siRNAs. (B) The number of 53BP1 foci per cell at 0 hours, 0.5 hours, 2 hours, 4 hours, 8 hours and 24 hours after 4 Gy IR. (C) Alkaline COMET assay to quantify the amount of DNA damage at 0 hours, 0.5 hours, 2 hours and 8 hours following 4 Gy IR, 72 hours after transfection with NT or TOPK siRNAs.*

*Unpaired two-sided student's t-test* *$p<0.05$.

The COMET assay (Figure 4.1C) showed no significant differences between the cells transfected with *TOPK* or NT siRNAs in terms of DNA damage after 4 Gy IR at 30 minutes, 2 hours and 4 hours post irradiation.

These results suggested that the increased radiosensitivity observed in the CFAs after irradiation following *TOPK* knockdown in HCT116

cells was probably not due to impaired DNA-damage response machinery. The COMET assay did not show any difference in terms of DNA damage for siNT and si*TOPK* at any time point. As a role has already been described for TOPK in cell cycle progression, it was therefore speculated that the small difference at 30-minutes for γ-H2AX and 53BP1 foci presented in Figure 4.1A and B might be due to alterations in the cell cycle progression in the TOPK-depleted cells.

### 4.2.2 IR-induced alteration of the cell cycle profile after TOPK depletion

One of the consequences of IR-induced DNA damage is the alteration of the cell cycle to allow completion of DNA damage repair in order to avoid the potential catastrophic consequences of undergoing mitosis with persistent DNA damage. Ionising radiation induces a series of events that allow the cell to repair the DNA damage. One of these events is the activation of the $G_1$/S and $G_2$/M cell cycle checkpoints [21], [46], [57]. Checkpoint activation is a complex cellular process which inhibits cell cycle progression until the DNA damage has been appropriately repaired. If this inhibition of cell cycle progression is not overcome, the cell may undergo quiescence or programmed cell death [10], [21], [46], [51].

To investigate the role of TOPK in this process, the cell cycle profile was examined at different time points in TOPK-depleted HCT116 cells after 4 Gy irradiation.

In order to study cell cycle modifications, flow cytometry analysis was performed using Bromodeoxyuridine (BrdU) in combination with propidium iodide (PI). BrdU was added at 20 μM concentration to living cells 30 minutes before being lifted and fixed. BrdU is a thymidine analogue and gets incorporated into the newly synthesized DNA of replicating cells during S phase of the cell cycle. PI is an intercalating agent and a fluorescent molecule which binds to the DNA and makes it possible to distinguish the cell cycle stage based on

the DNA content differences in each phase. These two molecules were used in combination in flow cytometry experiments to divide the cell population into four different groups depending on the cell cycle stage ($G_1$, early S, late S, $G_2$/M) as shown in Figure 4.2 and Figure 4.3. $G_1$ cells have low PI signal and low BrdU signal, early S phase cells have low PI signal and high BrdU signal, late S phase cells have high PI signal and high BrdU signal and $G_2$/M cells have high PI signal and low BrdU signal.

The depletion of TOPK via siRNA in unirradiated cells, shown in Figure 4.2A, did not alter the asynchronous population compared to the control cells (siNT), as visible in the propidium iodide (PI) plot in the left box and Table 4.1. A time course experiment with BrdU and PI was performed in order to distinguish the four phases of the cell cycle: $G_1$ (bottom-left quadrant), early S-phase (top-left quadrant), late S-phase (top-right quadrant), and $G_2$/M (bottom right quadrant).

From these results (shown in Figure 4.2 and quantified in Table 4.1) a detectable difference in the cell cycle progression after 4 Gy IR was shown for cells in which *TOPK* was knocked-down. Despite the observed difference was not huge if compared to previously-published variations in the cell cycle profile after IR [117], it was consistent throughout different repeats. The control population showed a faster decrease in the $G_1$ peak at 2 hours after IR (A decrease of 8.25% in the $G_1$ population after 2 hours for the siNT compared to a 1.40% decrease in the $G_1$ population after 2 hours for the si*TOPK*). There was a corresponding increase in the $G_2$/M population which is mostly noticeable at 6 to 12 hours post IR (47.15% $G_2$/M population for the siNT compared to the 33.40% $G_2$/M population for the si*TOPK* at 8 hours post IR). Cells depleted of TOPK showed a weaker accumulation in $G_2$/M, with a greater population of cells appearing to be in $G_1$ at 8 hours post IR (38.16%, compared to 20.31% for the siNT), suggesting

a possible deficiency in the cellular response to the DNA damage in terms of checkpoint activation.

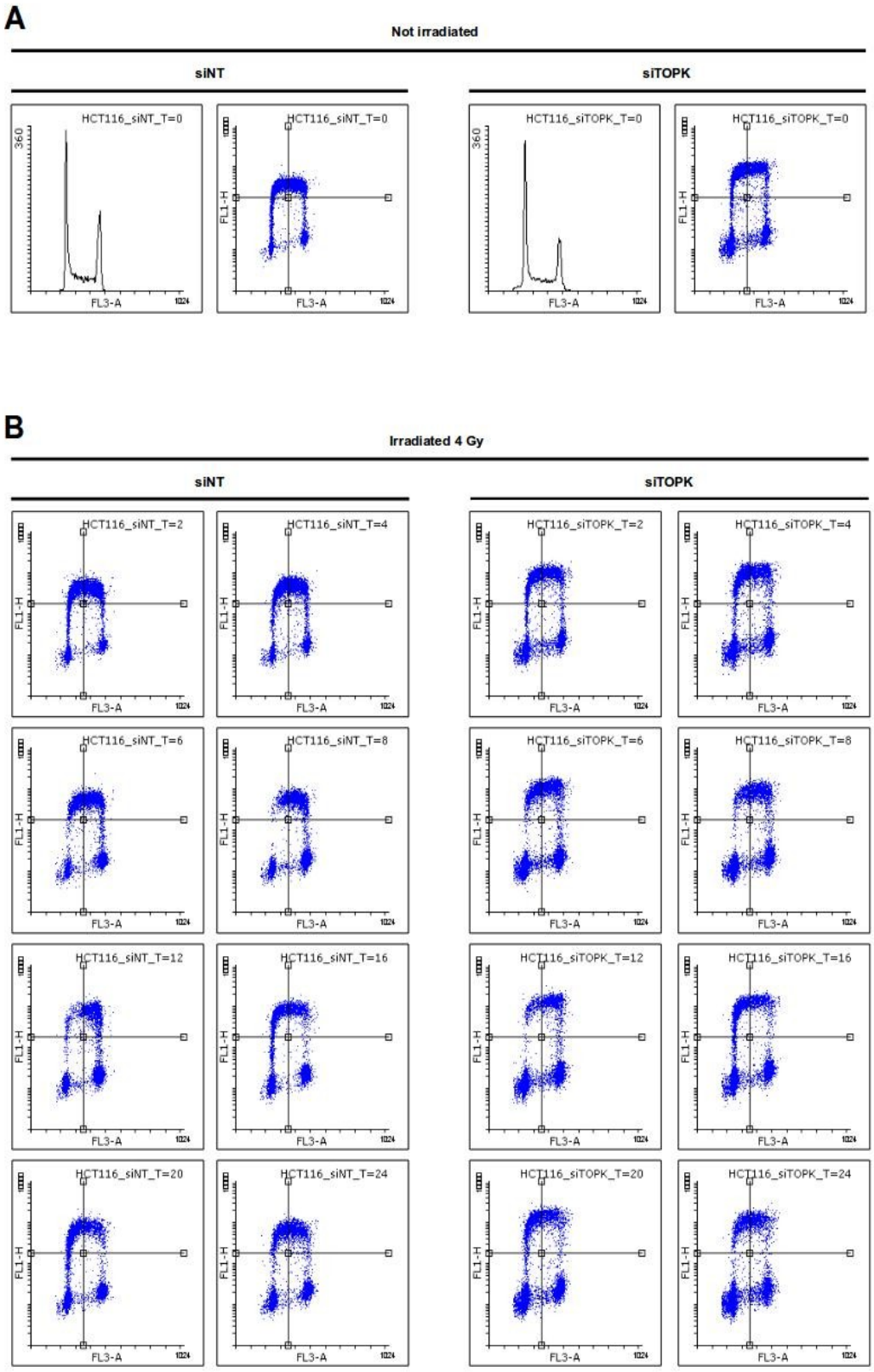


*Figure 4.2: Cell cycle progression of HCT116 cells post TOPK siRNA depletion. (A)*

*Unirradiated cells transfected with either NT or TOPK siRNAs showing a propidium iodide (PI) histogram profile in the left box and a Bromodeoxyuridine (BrdU) vs PI dot plot in the box on the right. (B) The time course of the cell progression after 4 Gy IR was monitored using PI vs BrdU staining. Cells were irradiated with 4 Gy IR at 72 hours post siRNA transfection and then fixed at different time points. BrdU was added 30 minutes before lifting each sample to allow incorporation into the DNA. After fixation, PI was added to intercalate with the DNA. Samples were analysed using flow cytometry.*

*The quantitative description of these flow cytometry dot plots was performed with Flowing Software and can be found below in Table 4.1.*

| **HCT116 population cell cycle progression (%)** | | | | | | | | | | |
|---|---|---|---|---|---|---|---|---|---|---|
| | | **Time post 4 Gy IR (h)** | | | | | | | | |
| | | **0** | **2** | **4** | **6** | **8** | **12** | **16** | **20** | **24** |
| **siNT** | **$G_1$** | 33.60 | 25.35 | 18.40 | 14.59 | 20.31 | 24.36 | 36.22 | 35.93 | 33.59 |
| | **Early S** | 24.66 | 26.23 | 26.14 | 19.32 | 7.05 | 4.38 | 15.36 | 25.53 | 16.55 |
| | **Late S** | 18.02 | 22.91 | 23.16 | 27.64 | 25.49 | 18.77 | 11.32 | 11.12 | 20.00 |
| | **$G_2$/M** | 23.59 | 25.41 | 32.21 | 38.42 | 47.15 | 52.49 | 37.10 | 27.41 | 29.84 |
| **si*TOPK*** | **$G_1$** | 38.61 | 37.21 | 37.21 | 33.45 | 38.16 | 38.36 | 51.73 | 48.41 | 47.56 |
| | **Early S** | 21.67 | 22.08 | 22.08 | 17.46 | 7.96 | 5.26 | 15.65 | 18.15 | 12.22 |
| | **Late S** | 17.67 | 17.75 | 16.63 | 19.75 | 20.48 | 16.63 | 10.20 | 11.92 | 14.11 |
| | **$G_2$/M** | 22.05 | 22.94 | 24.05 | 29.34 | 33.40 | 39.76 | 22.40 | 21.49 | 26.09 |

*Table 4.1: Quantification of the flow cytometry dot plots for asynchronous HCT116 cells presented in Figure 4.2A and B above. Proportions were calculated with Flowing Software. $G_1$: bottom-left quadrant. Early S: top-left quadrant. Late S: top-right quadrant. $G_2$/M bottom-right quadrant.*

Figure 4.2 showed that TOPK depletion via siRNA caused a small but detectable reduction in the accumulation of cells at $G_2$/M post irradiation. One possible interpretation of this experiment is that cells in which TOPK is depleted arrest in $G_1$ in response to IR. Another interpretation is that the cells do not arrest at the $G_2$/M checkpoint in response to IR. In order to distinguish between these possibilities, a time course experiment was conducted in HCT116 cells after release from a double-thymidine block to synchronise the cells at the $G_1$/S

boundary. High concentrations of thymidine interrupt DNA replication, therefore halting cells before they enter S phase [118]. The double-thymidine block was achieved by incubation with 2 mM thymidine for 18 hours, then release for 9 hours in fresh medium followed by another 17 hours thymidine at 2 mM. This technique synchronises cells at the $G_1$/S phase boundary.

The experiment examined cell cycle progression using both PI and BrdU staining of the same sample.

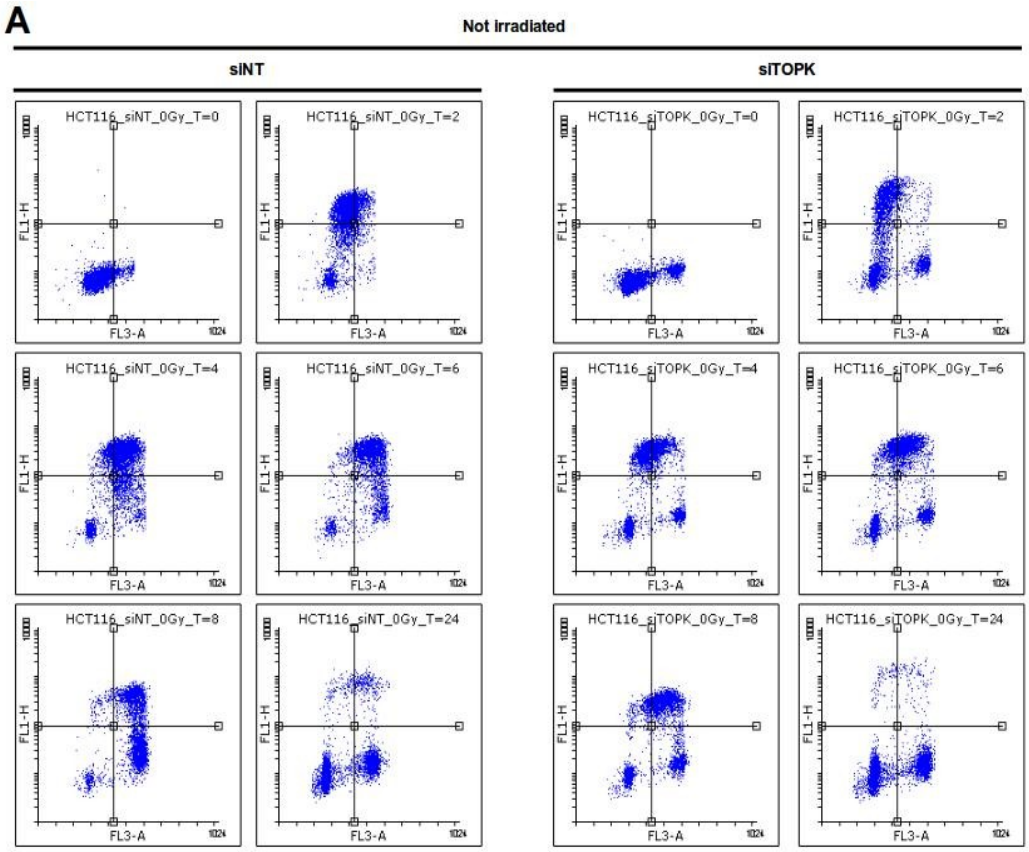

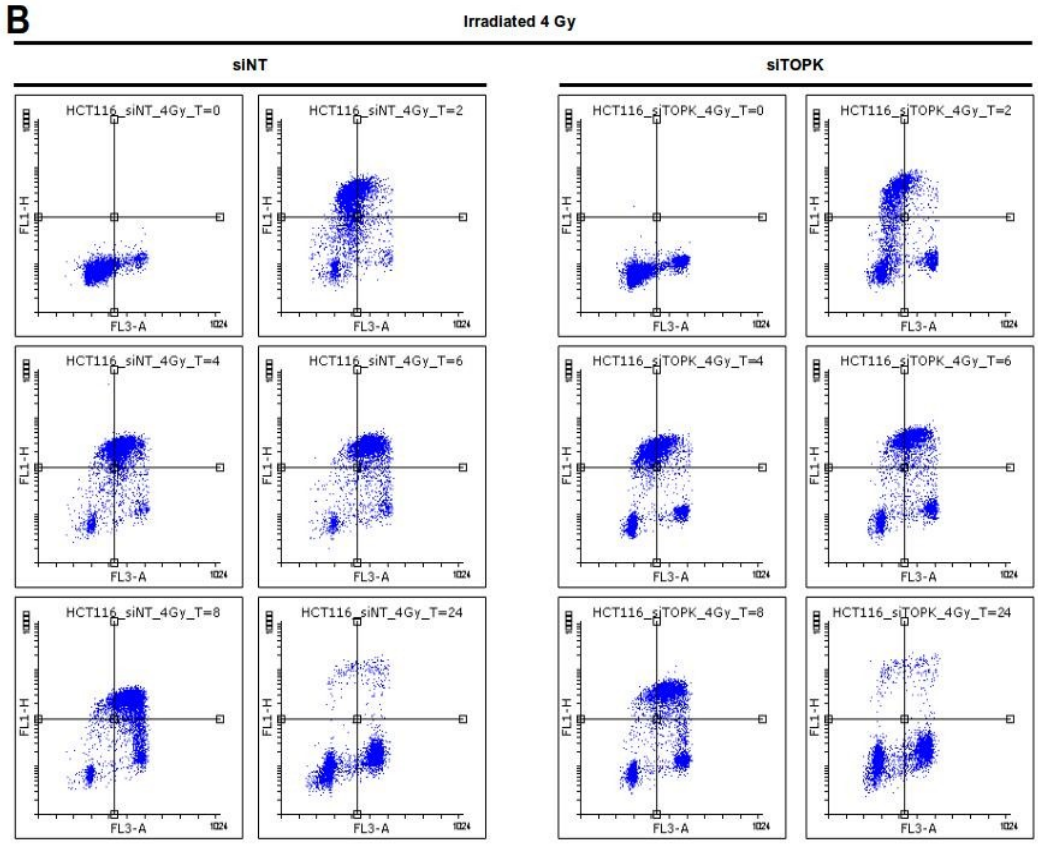


*Figure 4.3 Progression of double thymidine block synchronised HCT116 cells through the cell cycle. BrdU was added to the medium 30 minutes before collecting and fixing the samples to allow its incorporation. (A) PI vs BrdU plot comparing siNT and siTOPK cells. Cells were transfected with siRNA and synchronised in $G_1$ with a double-thymidine block. Samples were then released into fresh medium and collected at each time point. (B) $G_1$ synchronised HCT116 cells were synchronised in $G_1$ with a double-thymidine block and then irradiated with 4 Gy IR at T = 0, 72 hours post siRNA transfection. Cells were then released and collected at the various time points for flow cytometry analysis.*

*The quantitative description of these flow cytometry dot plots can be found below in Table 4.2 for unirradiated samples and in Table 4.3 for irradiated samples.*

| Synchronised HCT116 population cell cycle progression (%) Not irradiated | | | | | | | |
|---|---|---|---|---|---|---|---|
| | | Time post release (h) | | | | | |
| | | 0 | 2 | 4 | 6 | 8 | 24 |
| siNT | $G_1$ | 95.59 | 23.67 | 14.89 | 9.56 | 8.99 | 56.33 |
| | Early S | 0.02 | 60.24 | 17.22 | 4.88 | 3.54 | 3.09 |
| | Late S | 0.00 | 13.52 | 55.50 | 69.45 | 39.87 | 5.98 |
| | $G_2$/M | 4.39 | 2.57 | 12.38 | 16.11 | 47.60 | 34.60 |
| si*TOPK* | $G_1$ | 94.28 | 48.70 | 30.83 | 25.23 | 22.55 | 58.27 |
| | Early S | 0.00 | 42.51 | 37.56 | 18.42 | 9.62 | 2.24 |
| | Late S | 0.00 | 6.66 | 29.49 | 42.44 | 47.85 | 2.61 |
| | $G_2$/M | 5.72 | 2.13 | 2.11 | 13.91 | 19.98 | 36.88 |

*Table 4.2: Quantification of the flow cytometry dot plots for unirradiated synchronous HCT116 cells presented in Figure 4.3A above. Proportions calculated with Flowing Software. $G_1$: bottom-left quadrant. Early S: top-left quadrant. Late S: top-right quadrant. $G_2$/M bottom-right quadrant.*

| Synchronised HCT116 population cell cycle progression (%) 4 Gy irradiated | | | | | | | |
|---|---|---|---|---|---|---|---|
| | | Time post release (h) | | | | | |
| | | 0 | 2 | 4 | 6 | 8 | 24 |
| siNT | $G_1$ | 92.96 | 23.71 | 14.98 | 11.53 | 10.01 | 49.95 |
| | Early S | 0.00 | 48.34 | 17.52 | 8.75 | 5.70 | 2.07 |
| | Late S | 0.00 | 22.67 | 58.55 | 64.80 | 65.87 | 3.25 |
| | $G_2$/M | 7.04 | 5.27 | 8.95 | 14.92 | 18.42 | 44.72 |
| si*TOPK* | $G_1$ | 85.32 | 44.02 | 28.61 | 25.31 | 26.51 | 51.55 |
| | Early S | 0.02 | 30.73 | 31.66 | 16.45 | 8.62 | 2.69 |
| | Late S | 0.00 | 9.55 | 26.05 | 40.03 | 44.63 | 3.08 |
| | $G_2$/M | 14.66 | 15.69 | 13.68 | 18.20 | 20.24 | 42.68 |

*Table 4.3: Quantification of the flow cytometry dot plots for irradiated synchronous HCT116 cells presented in Figure 4.3B above. Proportions calculated with Flowing Software. $G_1$: bottom-left quadrant. Early S: top-left quadrant. Late S: top-right quadrant. $G_2$/M bottom-right quadrant.*

Figure 4.3A is a BrdU vs PI dot plot distribution analysed by flow cytometry. Unirradiated HCT116 cells were synchronised at the $G_1$/S boundary using a double-thymidine block, and then released into fresh medium at time T = 0, 72 hours after siRNA transfection.

Cells depleted of TOPK showed a delayed exit from $G_1$ into S-phase after release when compared to the control (a 71.92% decrease in the $G_1$ population was observed after 2 hours for the control cells compared to a 45.58% decrease in the $G_1$ population after 2 hours for the cells depleted of TOPK as presented in Table 4.2 for the unirradiated samples). Despite the difference was small if compared to previously-published work [117], it was consistently detectable throughout repeats. This delayed $G_1$ exit was also observed in the irradiated TOPK-depleted cells when compared to the irradiated control as shown in Figure 4.3B and quantified in Table 4.3 (a 69.25% decrease in the $G_1$ population after 2 hours for the control compared to a 41.30% decrease in the $G_1$ population after 2 hours for the cells depleted of TOPK, as presented in Table 4.3 for the irradiated samples). At 24 hours post release, the samples had an asynchronous profile, suggesting that the majority of cells continued to cycle.

As TOPK depletion was shown to delay the progression into S phase following IR, an experiment was conducted to investigate the changes in the expression of cell cycle markers after release from a double thymidine block. HCT116 cells were transfected with NT or *TOPK* siRNAs, arrested at the $G_1$/S boundary by double-thymidine block, irradiated with 4 Gy 72 hours after the transfection, and then released into fresh medium. The antibodies used were against TOPK and phospho-TOPK to study potential changes in expression and phosphorylation of TOPK, histone H3 and phospho-histone H3 in order to study mitotic progression, cyclin E1 which regulates the $G_1$/S transition, cyclin B1 and CDK1 which regulate the $G_2$/M transition, and

p21, a known CDKs inhibitor. Vinculin was used as a loading control. The immunoblot is shown in Figure 4.4.

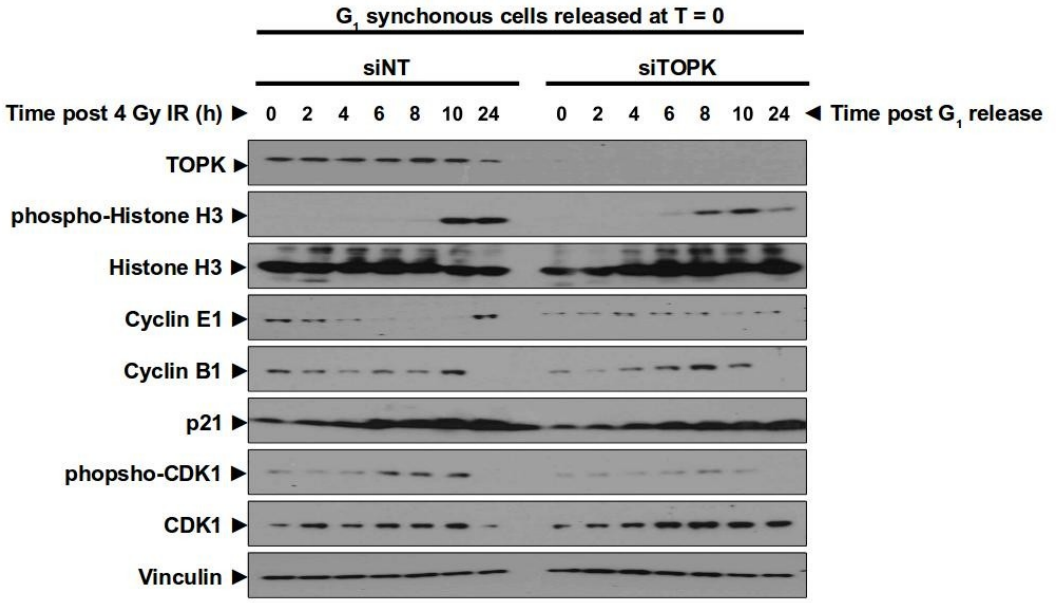


*Figure 4.4: Immunoblotting of the whole cell lysate of synchronised cells. Samples were transfected with siRNA and synchronised with a double-thymidine treatment. Cells were irradiated at time T = 0 and released immediately after into fresh medium. At each time point, cells were lysed in RIPA buffer containing phosphatase and protease inhibitors. Lysates were run on an SDS-Page gel and transferred to a membrane for immunoblotting. TOPK knockdown was confirmed using an anti-TOPK antibody. Phospho-histone H3 was used to monitor mitosis. Cyclin E1, cyclin B1, CDK1, pCDK1 and p21 levels were also investigated. Vinculin was used as loading control. Representative of n = 3 independent repeats.*

The immunoblotting presented in Figure 4.4 showed differences between the control and TOPK depleted cells. TOPK immunoblotting confirmed *TOPK* expression in the control samples and *TOPK* knockdown in the TOPK depleted samples. An anti phospho-TOPK antibody was used to investigate the phosphorylation of TOPK during mitosis in agreement with previous literature [71], [72], [87], [108], [109], which was demonstrated by an increase in band intensity at 8 hours after release (data not shown). Levels of total TOPK did not change significantly over time. This observation was in contrast with

published data showing an increase in *TOPK* expression levels at 7-9 hours post $G_1$ synchronisation and release in HeLa cells [74] and an increase at 9 hours post early S synchronisation in T47D (breast cancer) [87]. This discrepancy might be due to cell line specificity or to an IR-dependent effect. The phosphorylation of TOPK correlated with the entry into mitosis at 8 hours, as assessed by BrdU staining in Figure 4.3. Comparison with the cell cycle progression in Figure 4.3 also agrees with cyclin E1 being expressed at its highest level at the $G_1$/S transition in the control samples, with the strongest band in the earliest time points (T = 0 and T = 2) and at the latest time point (T = 24) as expected, whereas the TOPK depleted samples had a consistently low level of cyclin E1 expression at all time points. Cyclin B1 expression peaked at 10 hours after radiation for the control cells, reflecting a coordinated progression through the cell cycle until mitosis is reached at around 10 hours after release. The TOPK depleted cells had a weaker band at the earliest time points (T = 0 and T = 2), with a peak in expression at 8 hours. Levels of CDK1, the kinase controlling entry into mitosis, peaked at 6 to 10 hours in both the control and TOPK depleted cells. In stark contrast, phosphorylation of CDK1 was only observed in the control cells. A previous publication showed a small decrease in CDK1 and cyclin B1 expression after TOPK depletion in unirradiated HeLa cells [74]. The membrane was also immunoblotted for histone H3 and phospho-histone H3. The phosphorylated form of this histone is known to be a marker for mitosis [21], [119] which has also been shown to be phosphorylated directly by TOPK [87]. For the control cells, the histone was phosphorylated at 10 and 24 hours post release, whereas in the cells depleted of TOPK it was found to be phosphorylated at 8 and 24 hours with a peak band intensity at 10 hours post release. The level of expression of p21 did not show a dependency on the levels of TOPK which is in contrast with the increase of p21 levels after *TOPK* knockdown in HCT116 which have been previously published [88].

The lower levels of cyclin E1 in the TOPK depleted samples are consistent with a more protracted exit from $G_1$ into S phase, in agreement with the BrdU staining shown in Figure 4.3.

Interestingly, these results also suggest that in TOPK depleted samples, the $G_2$/M DNA damage checkpoint is impaired, as CDK1 is not phosphorylated, an event required to arrest the cells at the checkpoint. This promotes premature entry into mitosis, as revealed by expression of the CDK1 partner, cyclin B1, and in phospho-histone H3 at 8 hours in TOPK depleted cells.

### 4.2.3 TOPK depletion causes alteration of nuclear morphology and apoptosis after IR

Failure to activate the $G_2$/M DNA damage checkpoint can lead to premature entry into mitosis with unrepaired DNA [114]. Should the cell attempt to divide with unrepaired DNA, this can lead to changes in nuclear morphology, failure to complete cytokinesis, and cell death via apoptosis or mitotic catastrophe. The effects of TOPK depletion were therefore investigated in terms of nuclear morphology and apoptosis.

One of the mechanisms of cell death after IR is mitotic catastrophe which occurs during or as a result of an aberrant mitosis. This process may be caused by incorrect chromosome separation with a consequent formation of giant cells (where the nucleus occupies the majority of the cellular volume), micronucleation (where a cell contains a nucleus and a smaller portion of a second nucleus in the cytoplasm) or multinucleation (where a single cytoplasm contains two nuclei) and typically occurs after DNA damage and deficient checkpoint activation. Cell death due to mitotic catastrophe typically occurs few days post DNA damage and is considered a delayed type of cell death [10], [114].

Alterations in the nuclear morphology were studied with an immunofluorescence approach. HCT116 cells were transfected with

siRNA targeting *TOPK* (si*TOPK*) and compared to a control siRNA (siNT). 72 hours after transfection cells were irradiated at 4 Gy, returned to the incubator and then fixed 72 hours post IR. The immunostaining was performed using DAPI, a fluorescent DNA-binding agent used to stain the nucleus, and FITC, a protein binding agent used to stain the cytoplasm. Samples were mounted on a microscope slide and analysed under a confocal fluorescent light microscope. Cells were manually scored for micronucleation, binucleation and multinucleation, counting a minimum of 100 cells per condition. Figure 4.5A shows an example of altered morphology of HCT116 cells after TOPK depletion and 4 Gy IR, with micronuclei highlighted by the white arrows. The result of the cell morphology scoring is presented in Figure 4.5B.

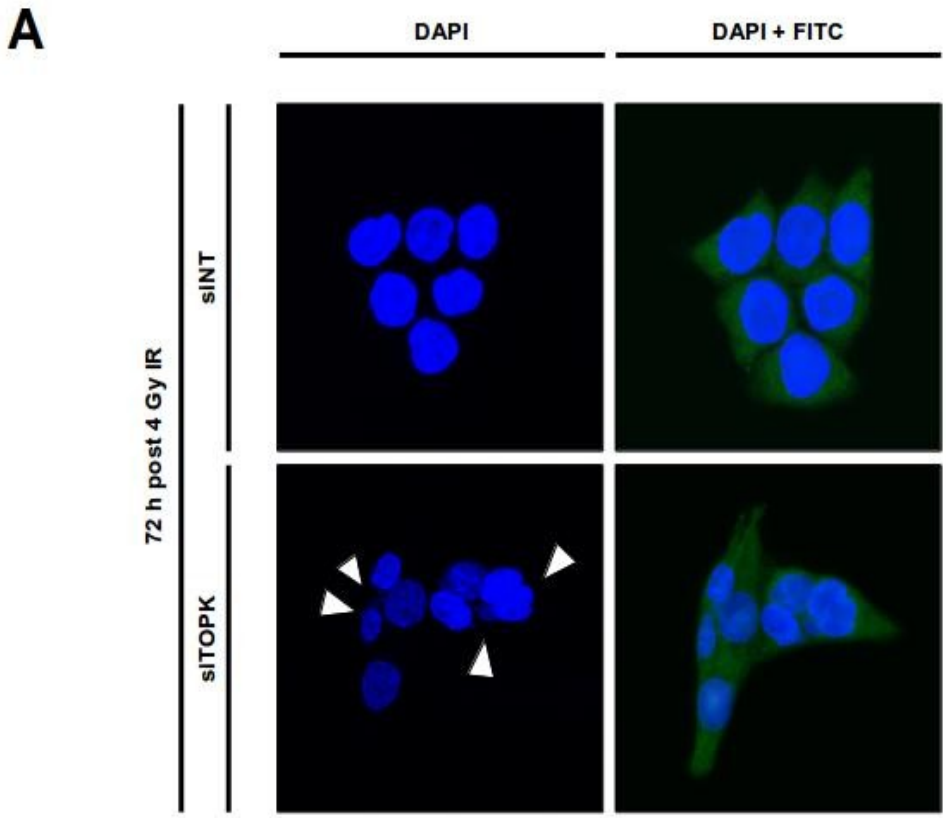

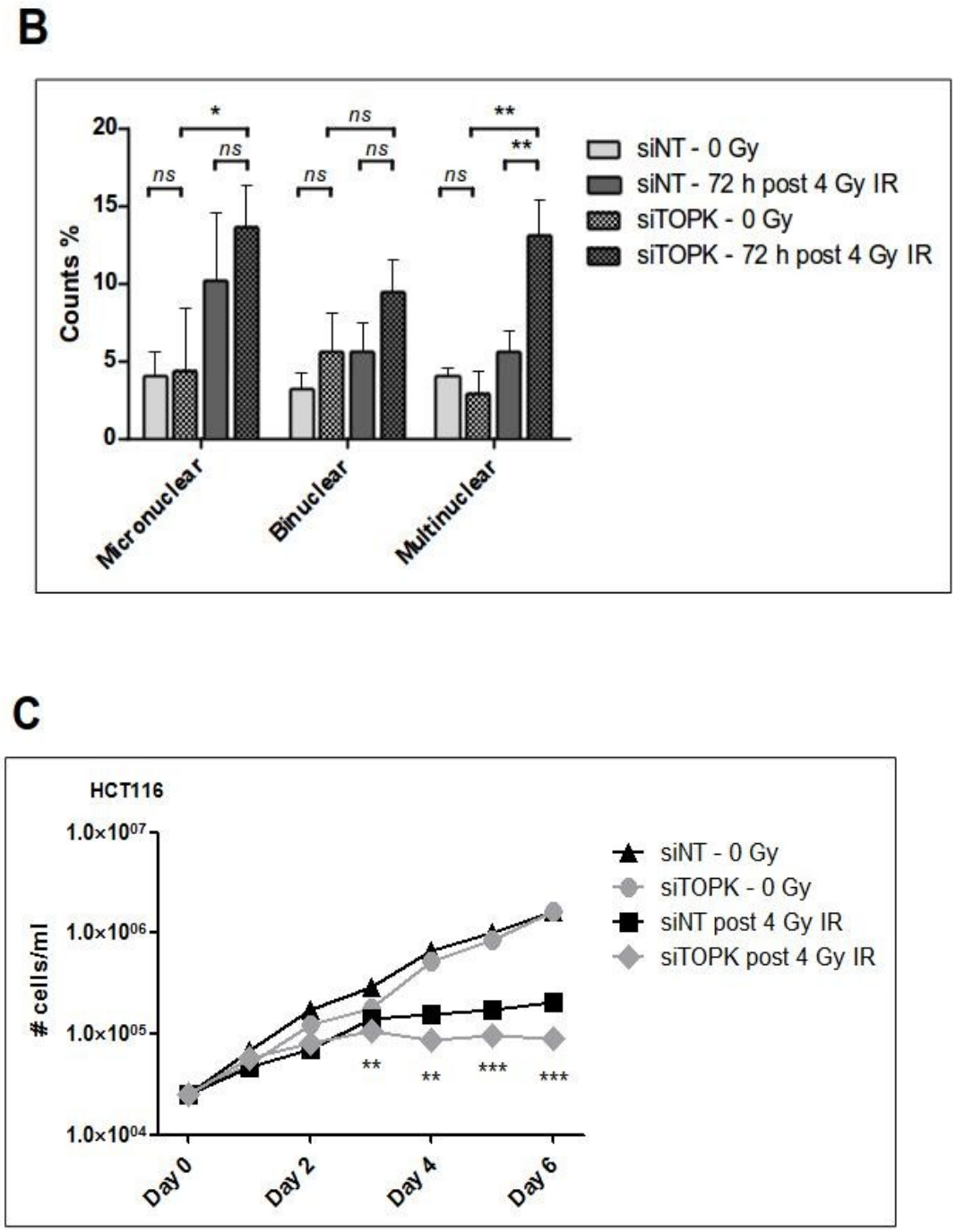


*Figure 4.5: Cellular morphology and cell survival alterations in HCT116 cells after TOPK siRNA silencing. (A) Representative field of view of the immunofluorescence analysis of HCT116 cells. 72 hours after 4 Gy irradiation. DAPI-stained nuclei (blue) showed a high number of multinuclei. FITC-stained cytoplasm is shown in green. The multinuclei in the siTOPK samples are labelled with white arrows as an*

*example. (B) Quantification of the percentage counts of micronuclear, binuclear and multinuclear cells showed a statistically significant difference between siNT and siTOPK after 4 Gy IR in the number of micronuclei and multinuclei. At least 100 cells were counted per condition. (C) Growth delay in vitro from 0 to 6 days after 4 Gy IR in HCT116. Cell growth was measured by resuspending cells in 800 µl fresh medium after 200 µl trypsin, and counting their concentration in triplicate.*

*Average of n = 3 independent experiments. Unpaired two-sided student's t-test comparing siNT 72 hours post 4 Gy IR to siTOPK 72 hours post 4 Gy IR, *p<0.05, **p<0.01, ***p<0.001.*

Figure 4.5A presents an example of a field of view of the stained cells. At 0 Gy, there was no significant difference in multinucleation between the control and TOPK depleted samples. In the irradiated samples, TOPK depleted cells showed a higher degree of multinucleation as shown by the white arrows in the DAPI view in Figure 4.5A, bottom left box. A significant increase in micronucleated and multinucleated cells was observed after 4 Gy IR in the TOPK depleted cells compared to the control cells (Figure 4.5B), with an unpaired two-sided student's t-test showing a p-value of less than 0.05 and less than 0.01 respectively. This finding suggested a role for TOPK in accurate cellular division, leading to the formation of two daughter cells from a single progenitor. IR has been shown to induce multinucleation via DSBs and premature transition into mitosis [120] and *TOPK* knockdown has been previously shown to induce an increase in multinucleated HeLa cells in the absence of radiation [74]. In this experiment an increase in multinuclear cells was not detectable in unirradiated HCT116 cells, although a significant increase was observed in irradiated cells at 72 hours post IR. This discrepancy could be due to differences between the two cell lines.

In order to study the growth rate and to understand how IR might induce cell death in TOPK-depleted cells, HCT116 cells were counted daily for six days following irradiation. Cells were first transfected with

either NT or *TOPK* siRNAs and then irradiated 72 hours post transfection. On the day of counting, one sample was lifted in 200 µl trypsin and 800 µl fresh medium. Samples were then counted in triplicate in order to obtain the number of cells/ml, which is plotted in Figure 4.5C. Irradiated control and TOPK-depleted samples showed a slower growth rate when compared to the unirradiated samples. Irradiated TOPK-depleted cells also showed a further decrease in growth rate when compared to irradiated control cells at 3, 4, 5 and 6 days after IR, with p-values less than 0.01, 0.01, 0.001 and 0.001, respectively. There was no significant difference in the growth of unirradiated cells transfected with NT or *TOPK* siRNAs during the course of the experiment suggesting that depletion of TOPK only has an effect on cell growth following IR in HCT116 cells, and that these differences are only observed 4 to 6 days after IR.

In order to determine whether TOPK-depleted cells also die by apoptosis in response to IR, levels of apoptosis were measured after *TOPK* siRNA depletion paired with radiation in HCT116 cells at 24, 48 and 72 hours post IR. The first approach was to test annexin V incorporation via flow cytometry (Figure 4.6A and B). Annexin V is known to migrate to the external cellular membrane during apoptosis, so a fluorescent marker targeting annexin V can be used to count apoptotic cells with a flow-cytometer [121]. Propidium iodide (PI) was also included for analysis of DNA-content. The second approach adopted was to identify apoptotic cells with bright condensed DNA by assessing Hoechst incorporation using the InCell Analyzer (Figure 4.6C).

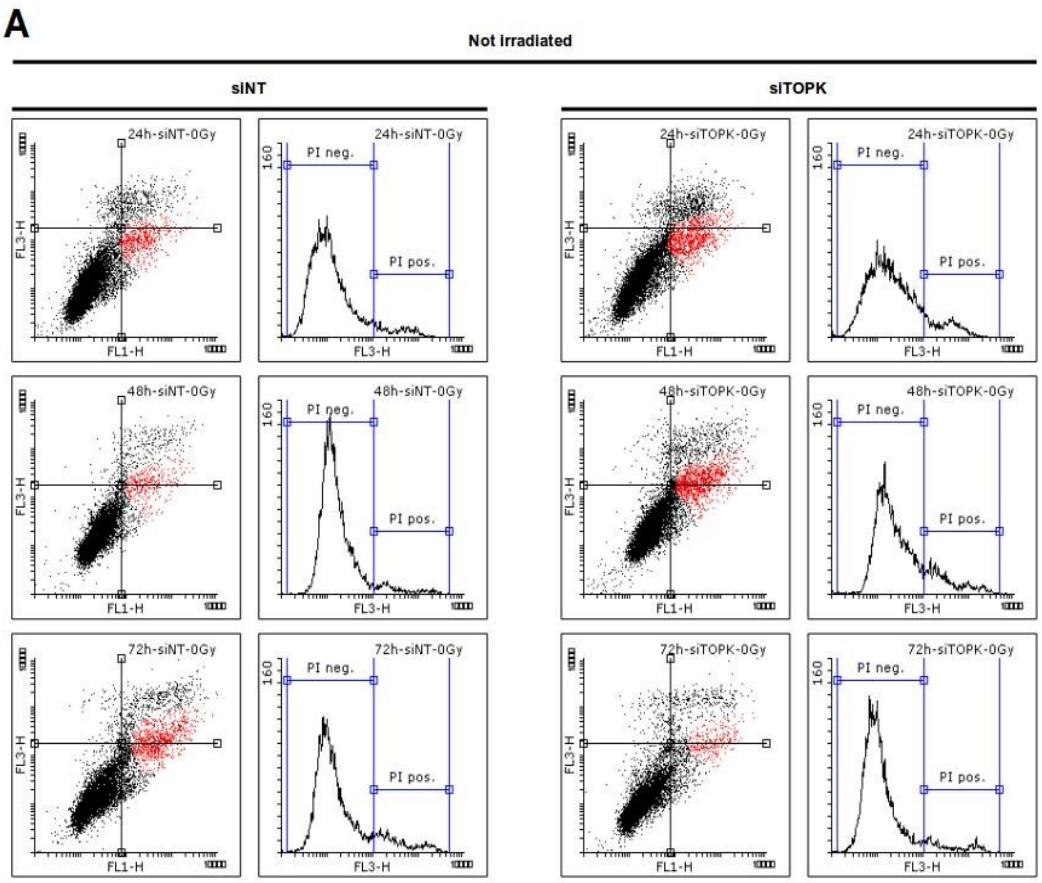
A
Not irradiated
siNT
siTOPK
24h-siNT-0Gy
24h-siTOPK-0Gy
48h-siNT-0Gy
48h-siTOPK-0Gy
72h-siNT-0Gy
72h-siTOPK-0Gy
PI neg.
PI pos.
FL1-H
FL3-H

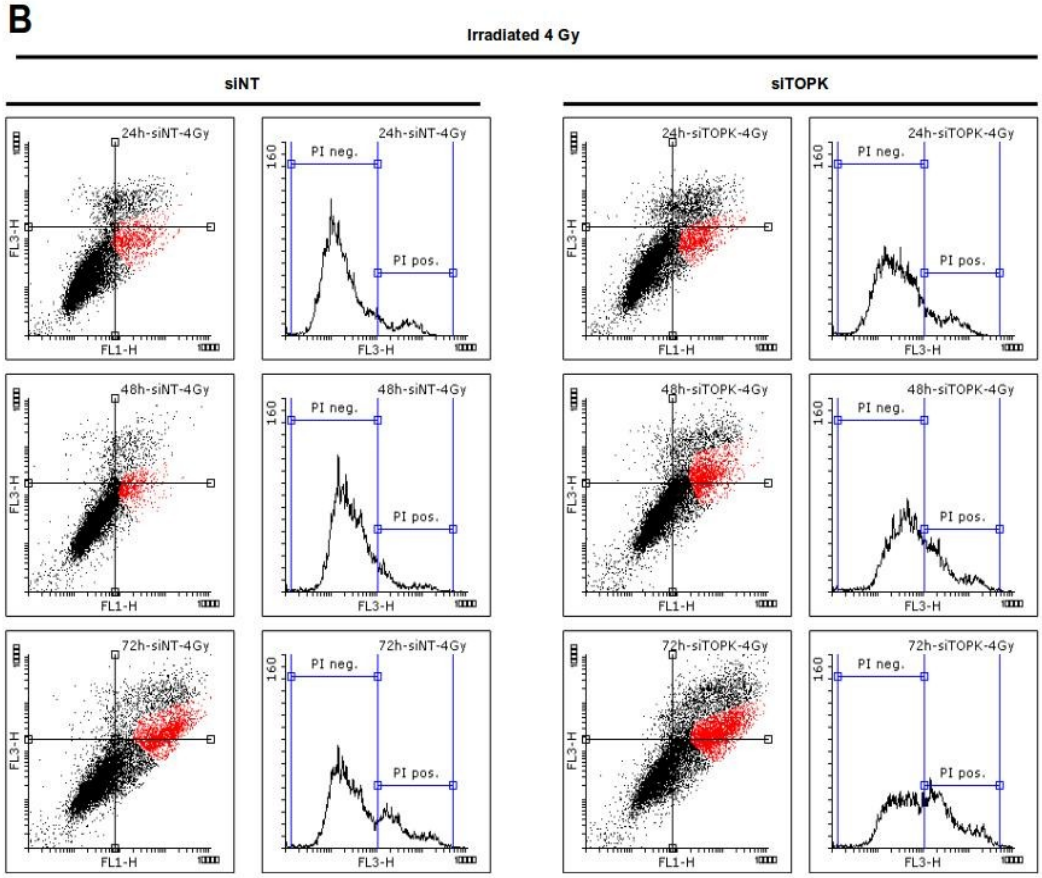
B
Irradiated 4 Gy
siNT
siTOPK
24h-siNT-4Gy
24h-siTOPK-4Gy
48h-siNT-4Gy
48h-siTOPK-4Gy
72h-siNT-4Gy
72h-siTOPK-4Gy
PI neg.
PI pos.
FL1-H
FL3-H

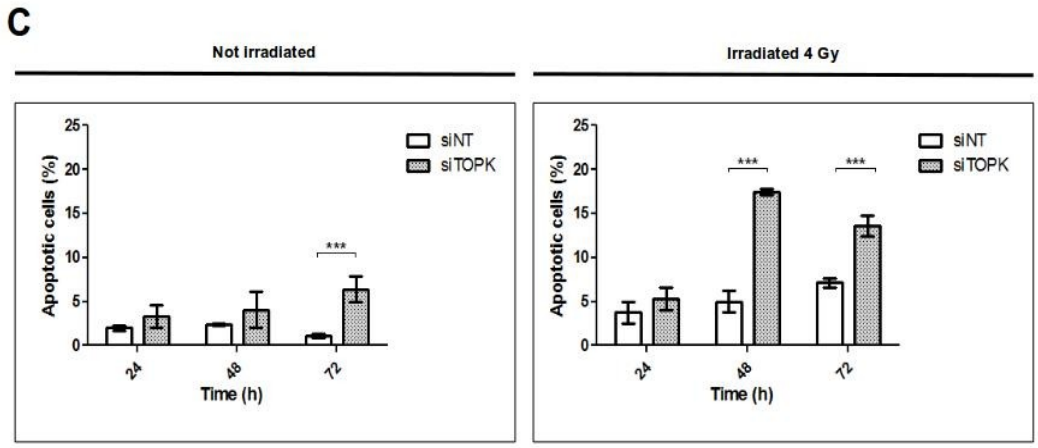


*Figure 4.6: Levels of apoptosis in HCT116 cells after TOPK depletion. (A) Flow cytometry dot plots of PI vs annexin V (left boxes) and PI histograms (right boxes) of unirradiated samples comparing siNT and siTOPK transfected HCT116 cells. (B) flow cytometry sorting dot plots of PI vs annexin V (left boxes) and PI histograms (right boxes) of 4 Gy irradiated samples comparing siNT and siTOPK transfected cells at 24, 48 and 72 hours post IR. (C) Bright, hoechst positive cells observed using the InCell Analyzer to investigate levels of apoptosis in siTOPK cells compared to siNT at 24, 48 and 72 hours post 4 Gy IR. The threshold was adjusted for each experiment to include apoptotic cells with bright, condensed DNA, but to exclude mitotic cells that also have less bright, condensed DNA. Unpaired two-sided student's t-test comparing siNT to siTOPK 72 hours post 4 Gy IR,* ***p<0.001*.*

*A quantitative description of the Annexin V results can be found in Table 4.4 below.*

The quantification of the above Annexin V experiment is presented in Table 4.4. The percentage of apoptotic cells, displayed as red dots in the dot plots in Figure 4.6A and Figure 4.6B, is shown with respect to the total number of cells analysed for each condition.

| | Apoptotic population (%) | | | |
|---|---|---|---|---|
| | Not irradiated | | Irradiated | |
| | **siNT** | **si*TOPK*** | **siNT** | **si*TOPK*** |
| **24 h** | 5.53 | 10.13 | 7.80 | 9.53 |
| **48 h** | 3.69 | 10.98 | 5.41 | 14.36 |
| **72 h** | 8.52 | 2.7 | 16.58 | 24.60 |

*Table 4.4: Quantification of the percentage level of apoptotic population for the Annexin V experiments described in Figure 4.6A and B.*

*Proportions calculated with Flowing Software. Apoptotic cells: red dots.*

In the absence of radiation, a higher number of apoptotic cells, identified as red dots in the PI vs Annexin V dot-plot, was observed following *TOPK* knockdown at 24 hours (10.13% apoptotic cells compared to 5.53% apoptotic cells in the control population, as shown in Table 4.4). The increase in apoptosis was also observable simply by analysing the number of PI positive cells, displayed as a histogram (right box). At 48 hours the percentage of apoptotic cells increased by 0.85% following *TOPK* knockdown, whilst the percentage decreased by -1.84% in the control. Conversely, in the 72 hours unirradiated samples, TOPK depletion caused 5.82% less apoptotic cells compared to the control. In the irradiated sample a significantly higher apoptotic population, labelled in red in the PI vs Annexin V dot-plot in Figure 4.6B, was consistently observed following *TOPK* knockdown at 24, 48 and 72 hours post 4 Gy IR when compared to the control cells, with increases of +1.73%, +8.95%, and +8.02% at 24, 48 and 72 hours, respectively. The same effect was also visible by PI staining alone (histograms displayed in the right boxes).

The number of apoptotic cells was also determined by quantifying the percentage of cells with bright, condensed DNA stained by Hoechst at 24, 48 and 72 hours. This showed a significant (p-value less than 0.001) increase in the percentage of apoptotic cells at 72 hours in the unirradiated TOPK depleted sample, with 1.12% apoptotic cells in the control compared to 6.41% apoptotic cells in the TOPK depleted samples, as shown in Figure 4.6C. Cells irradiated at 4 Gy showed a

statistically significant increase in apoptosis for the TOPK depleted samples at 48 and 72 hours post radiation, respectively. The percentage of apoptotic cells in the control was 4.99% at 48 hours and 7.14% at 72 hours, whereas the percentage of apoptotic cells in the TOPK depleted sample was 17.48% at 48 hours and 13.62% at 72 hours (p-values of less than 0.001).

Taken altogether these results suggested that *TOPK* knockdown causes apoptosis at 48 to 72 hours after 4 Gy IR in HCT116 cells.

### 4.2.4 *TOPK* overexpression and LC-Ms/Ms analysis

For the study of a role for TOPK in cancer cells, a series of different immunoprecipitation experiments was performed in HCT116 cells. Immunoprecipitation involves the extraction of the protein of interest, TOPK in this case, and its binding proteins from a cell lysate, which can subsequently be identified by mass spectrometry or western blotting. The identification of those proteins that may physically interact with TOPK may give an insight into the observed response to radiation following TOPK depletion, and may determine which future directions should be explored. At the time of writing, there were no publications on the role of TOPK in response to IR-induced DNA damage or the proteins with which TOPK interacts in response to ionising radiation.

Immunoprecipitation experiments were performed in HCT116 colorectal cells. The interactions were first investigated after overexpression of either *TOPK* WT (TOPK wild-type, pCMV6-TOPK-Myc-DDK) or *TOPK* KD (TOPK K64M kinase dead mutant, pCMV6-TOPK-K64M-Myc-DDK) using proprietary overexpression vectors (Figure 4.7A). HCT116 cells were transfected with the TOPK WT, TOPK KD and empty vectors, using four T175 flasks per condition. After 48 hours, adherent cells were irradiated with 4 Gy IR and immunoprecipitation was performed on ice 8 hours later. Samples were lysed with 250 µl of RIPA lysis buffer per flask containing protease and phosphatase

inhibitors. The samples were then incubated with benzonase in order to disrupt the DNA and therefore avoid the pull-down of DNA-binding proteins rather than target-specific binding proteins. A pre-clearing step was included by incubation with the beads in the absence of antibody to avoid non-specific binding to the beads. Prior to the pull-down incubation, 25 µl input samples were collected. The pull-down incubation with the anti-Flag M2 agarose beads was performed overnight to allow the Flag/DDK-tagged TOPK WT or TOPK KD proteins to bind to the beads. After three washes with RIPA buffer, samples were eluted from the beads using 2 x loading buffer containing SDS.

A 2 µl input sample was run on a SDS-Page gel for immunoblotting. The immunoblotting, shown in Figure 4.7B, confirmed that *TOPK* WT and *TOPK* KD were overexpressed in the samples. The overexpressed proteins were identified by both the anti-TOPK and anti-Flag antibodies, as expected. 2 µl of each elute was run on a separate SDS-Page gel which was then stained with SYPRO Ruby protein stain and visualised with UV light (Figure 4.7C). This showed a number of proteins of different molecular weights that were pulled-down together with TOPK. Some bands were more intense in the samples overexpressing *TOPK* WT or *TOPK* KD compared to the empty vector control sample, suggesting that they could be TOPK-specific protein interactors.

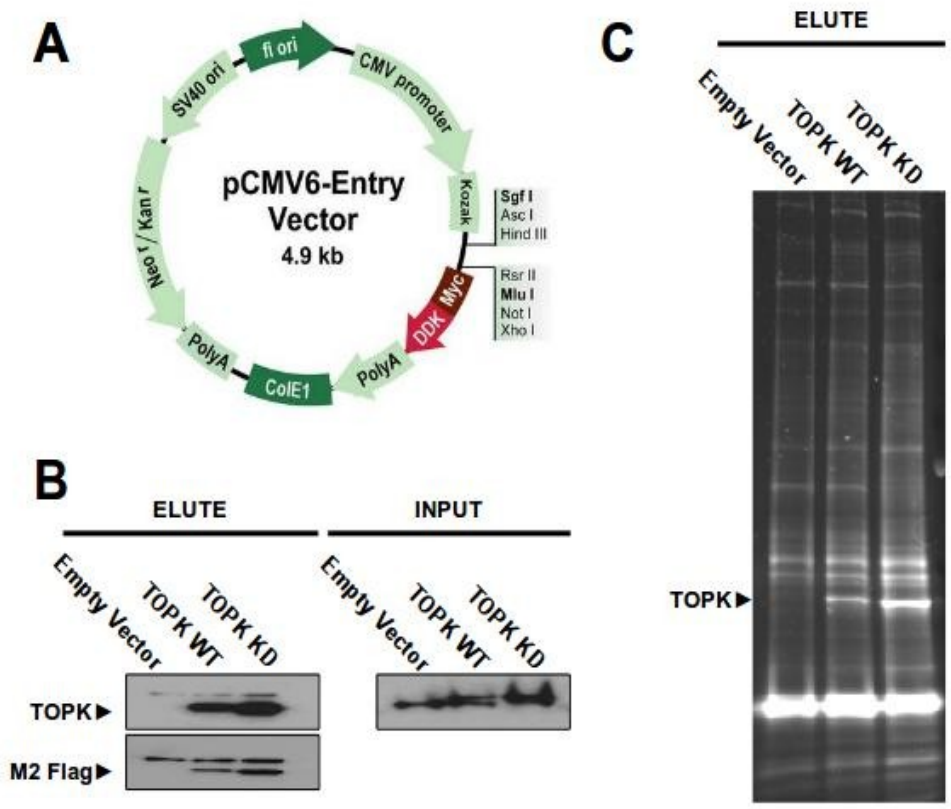


*Figure 4.7: Overexpression of TOPK in HCT116 cells. (A) TOPK was overexpressed in a C-terminal DDK (Flag) tagging pCMV6-Entry Vector (Origene). (B) TOPK and TOPK KD were overexpressed in HCT116 cells, which were then irradiated at 4 Gy. Immunoprecipitation was performed using anti-Flag M2 beads 8 hours after irradiation. In the elute sample the TOPK antibody recognises the overexpressed protein and the M2 Flag antibody confirms the overexpression. A non-specific band of a larger size is also visible this being the heavy chain of the antibody. (C) The elute SYPRO Ruby protein gel stain visualised under a UV lamp. A band at the right molecular weight for TOPK was identified with many other bands identifying proteins that were pulled-down with TOPK confirming the success of the immunoprecipitation technique.*

The remainder of the cell lysate was then processed for liquid chromatography mass spectrometry analysis (LC-Ms/Ms) by adding iodoacetamide alkylating agent (IAA) followed by Trichloroacetic acid

(TCA). After denaturation, samples were reconstituted with urea buffer and then digested in trypsin for 16 hours with shaking. After incubation, Trifluoroacetic acid (TFA) was added and samples were filtered through C18 Spin Tips for desalting and removing urea and other contaminants. LC-Ms/Ms analysis was completed by the laboratory of Professor Benedikt Kessler (Nuffield Department of Medicine, Medical Sciences Division, University of Oxford), in collaboration with Dr Iolanda Vendrell. The analysis was performed using the MASCOT Database (Search algorithm for Mass Spectral proteomics peak lists) [122] using the parameters shown in Table 4.5 (parameters from [123], [124]). The protein database used for matching the results of the *in silico* digestion was the UniProt_Swissprot 20150204 database sequence (http://www.uniprot.org). For proteins to be considered valid, an ion score cut-off of 20 was set, with a false discovery rate (FDR) of 1% with a p-value $< 0.05$. These parameters were set with the assumption that 1 in 100 peptides identified were false positive.

| MASCOT data search parameters | |
|---|---|
| **Database** | UniProt_SwissProt 20150204 |
| **Taxonomy** | Homo Sapiens (human) (20,274 sequences) |
| **Type of search** | Ms/Ms Ion Search |
| **Enzyme** | Trypsin |
| **Fixed modifications** | Carbamidomethyl (C) |
| **Variable modifications** | Oxidation (M), Phospho (ST, Y), Deamidation (N) |
| **Mass values** | Monoisotopic |
| **Protein mass** | Unrestricted |
| **Peptide charge** | +2, +3, +4 |
| **Decoy database** | ✓ |
| **Peptide mass tolerance** | 10 ppm |
| **Fragment mass tolerance** | 0.05 Da |
| **Max missed cleavages** | 1 |
| **Instrument type** | Q-Exactive |
| **#C13** | +1 |
| **Significance threshold p<** | 0.05 |
| **Max number of families** | AUTO |
| **Ions score cut-off** | 20 |
| **FDR** | 1% |
| **Threshold** | Homology threshold |

*Table 4.5: MASCOT database parameters used to identify valid hits from the LC-Ms/Ms analysis comparing the obtained protein score (sum of the scores of peptides matching a protein) to the UniProtSwissprot database. An ion score cut-off of 20 was set, with a false discovery rate (FDR) of 1% and a p-value < 0.05.*

The obtained results for the TOPK WT and TOPK KD elute are presented in Table 4.6 below.

| Proteins identified (FDR 1%; prot scores > 20, ions > 20, peptides ≥ 1) | | | | |
|---|---|---|---|---|
| **Acc N.** | **protein name** | **Protein score** | **Number of significant sequences** | ***TOPK* form overexpressed** |
| Q9NY65 | Tubulin alpha-8 chain OS=Homo sapiens GN=***TUBA8*** PE=1 SV=1 | 93 | 4 | WT and KD |
| P31947 | 14-3-3 protein sigma OS=Homo | 69 | 1 | KD |

| | | | | |
|---|---|---|---|---|
| | sapiens GN=***SFN*** PE=1 SV=1 | | | |
| Q14258 | E3 ubiquitin/ISG15 ligase TRIM25 OS=Homo sapiens GN=***TRIM25*** PE=1 SV=2 | 58 | 2 | WT |
| P36507 | Dual specificity mitogen-activated protein kinase kinase 2 OS=Homo sapiens GN=***MAP2K2*** PE=1 SV=1 | 53 | 1 | WT |
| P38936 | Cyclin-dependent kinase inhibitor 1 OS=Homo sapiens GN=***CDKN1A*** PE=1 SV=3 | 50 | 1 | WT |
| P78527 | DNA-dependent protein kinase catalytic subunit OS=Homo sapiens GN=***PRKDC*** PE=1 SV=3 | 48 | 2 | WT |
| P12956 | X-ray repair cross-complementing protein 6 OS=Homo sapiens GN=***XRCC6*** PE=1 SV=2 | 44 | 1 | KD |

*Table 4.6: List of some interacting proteins identified via LS-Ms/Ms in TOPK immunoprecipitation samples. The accession number in the first column is the unique protein identifier assigned to each peptide sequence upon inclusion in the UniProt database. The protein score is the MASCOT-calculated probabilistic score to allow comparison of the experimental data to the database sequences. The number of significant sequences is the number of significant peptides that match the identified protein. The TOPK form overexpressed column indicates if the interaction was identified in the TOPK WT (wild-type) or the TOPK KD (kinase dead) transfected sample.*

Table 4.6 shows the list of the most interesting candidates interacting proteins for TOPK. XRCC6, also known as Ku70 is a member of the DNA-PK complex which is a key non-homologous end joining (NHEJ) complex [10]. Interestingly, PRKDC, known as DNA-$PK_{cs}$ was identified and is also a component of the complex. SFN, also known as 14-3-3σ, has been shown to be upregulated by p53 and BRCA1 in response to

IR, and binds to CDK1 and sequesters it into the cytoplasm [125], [126]. MAP2K2, also known as MEK2, phosphorylates and activates ERK2, a known TOPK substrate in absence of radiation [85] CDKN1A, also called p21, is a p53 target and has known roles in cancer cells and cell cycle regulation, including CDK1 inhibition in response to ionising radiation [53]–[55]. TRIM25 ubiquitinates 14-3-3σ and binds to p53 after IR [127] TUBA8, also known as tubulin alpha 8, a member of the α-tubulin family, is a known TOPK-interacting protein [74], [110].

### 4.2.5 Validation of the TOPK interactions

The scale and complexity of the LS-Ms/Ms experiment presented in the “TOPK overexpression and LC-Ms/Ms analysis“ section made it feasible to analyse only irradiated samples, without an unirradiated control. With this method it was possible to identify those proteins that interact with TOPK WT and KD after irradiation but it was not possible to state whether the interaction was induced or enhanced by radiation.

In an attempt to repeat the experiment and confirm the results obtained and presented in Table 4.6 above, a different approach was used. Overexpression of TOPK kinase dead (KD), TOPK wild type (WT) or the empty vector control was performed, samples were either unirradiated, or were irradiated with 4 Gy IR, and the IPs were carried out with anti-M2 Flag beads as described above. The entire immunoprecipitated elutes were then run on a SDS-Page gel and stained with InstantBlue coomassie stain. The bands that appeared to vary in intensity between the three different lanes were excised using a clean scalpel and cut in cubes of ~ 0.5 mm size. The samples were washed, and then the gel pieces were dehydrated and digested in trypsin before being analysed by LC-Ms/Ms.

The bands that were excised are indicated in Figure 4.8A with numbered red arrows. The results obtained by LC-Ms/Ms were then

compared to the expected molecular weight of each protein to confirm that the peptides identified correspond to the expected molecular weight of the predicted protein in kDa and are listed in Table 4.7.

| Proteins identified (FDR 1%; prot scores > 20, ions > 20, peptides ≥ 1) | | | | |
|---|---|---|---|---|
| **Acc N.** | **protein name** | **Protein score** | **Number of significant sequences** | **Band reference number on gel (Figure 4.8A) and molecular weight (kDa)** |
| Q9Y4A5 | DNA-dependent protein kinase catalytic subunit OS=Homo sapiens GN=***PRKDC*** PE=1 SV=3 | 3340 | 146 | 1 (470) |
| Q9BQE3 | Tubulin alpha-1C chain OS=Homo sapiens GN=***TUBA1C*** PE=1 SV=1 | 3180 | 24 | 7 (50) |
| Q96KB5 | Lymphokine-activated killer T-cell-originated protein kinase OS=Homo sapiens GN=***PBK/TOPK*** PE=1 SV=3 | 2502 | 20 | 9 (36) |
| Q96KB5 | Lymphokine-activated killer T-cell-originated protein kinase OS=Homo sapiens GN=***PBK/TOPK*** PE=1 SV=3 | 2137 | 28 | 16 (36) |
| P19474 | E3 ubiquitin-protein ligase TRIM21 OS=Homo sapiens GN=***TRIM21*** PE=1 SV=1 | 548 | 21 | 8 (54) |
| P06493 | Cyclin-dependent kinase 1 OS=Homo sapiens GN=***CDK1*** PE=1 SV=3 | 140 | 4 | 10 (34) |
| P0C0S8 | Histone H2A type 1 OS=Homo sapiens GN=***HIST1H2AG*** PE=1 SV=2 | 107 | 2 | 12 (14) |
| P38936 | Cyclin-dependent kinase | 65 | 3 | 11 (21) |

| | | | | |
|---|---|---|---|---|
| | inhibitor 1 OS=Homo sapiens GN=***CDKN1A*** PE=1 SV=3 | | | |

*Table 4.7: List of some potential TOPK interacting proteins identified via LS-Ms/Ms extracted from an SDS-Page gel. The accession number in the first column is the unique protein identifier assigned to each peptide sequence upon inclusion in the UniProt database. The protein score is the MASCOT-calculated probabilistic score to allow comparison of the experimental data to the database sequences. The number of significant sequences is the number of significant peptides that match the identified protein. The band number reference on gel column indicates the corresponding band as labelled by red arrows in Figure 4.8 below.*

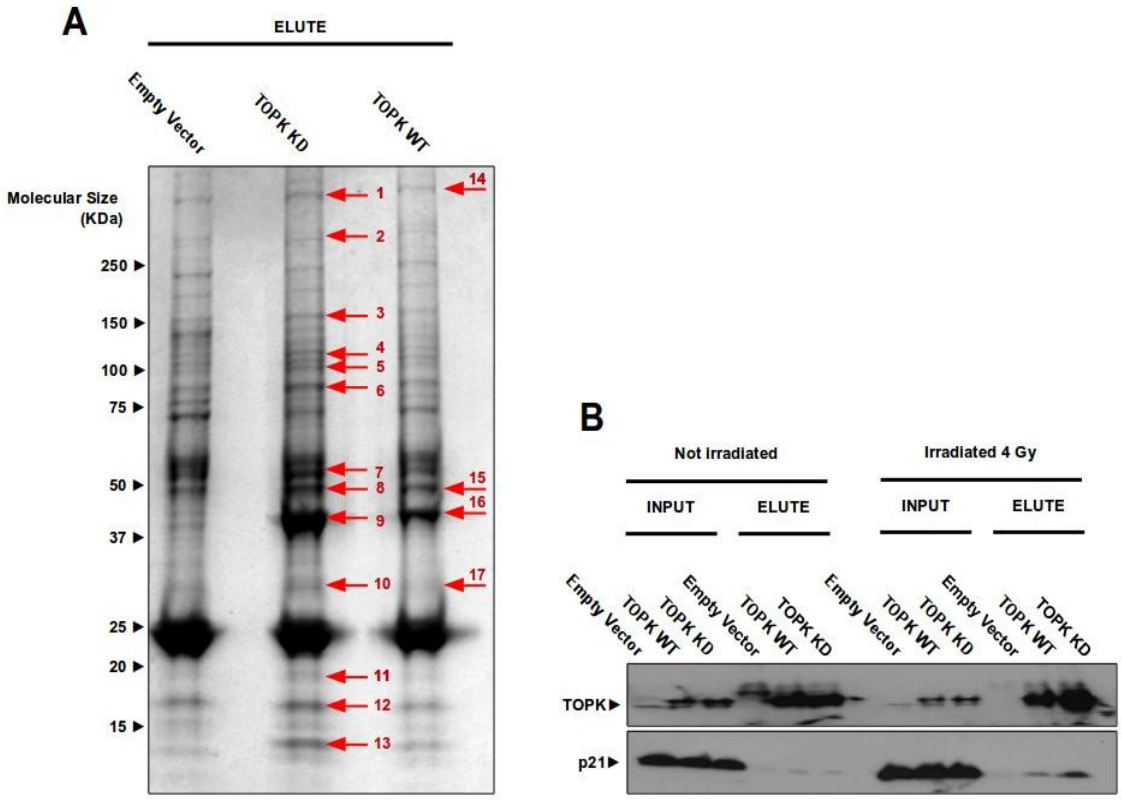


*Figure 4.8: Exogenously overexpressed TOPK interacts with p21. (A) SDS-Page gel stained with InstantBlue coomassie stain to identify proteins that were eluted from the M2 Flag beads following immunoprecipitation using TOPK WT or TOPK KD overexpressing cells, 8 hours after 4 Gy. The red arrows indicate the bands that vary in intensity between the three samples. A dashed red line indicates the band corresponding to the molecular weight of TOPK. (B) Immunoblotting of different immunoprecipitations comparing unirradiated to 4 Gy irradiated samples. The membrane was probed for TOPK (top) and p21 (bottom). The TOPK antibody identified TOPK expression in the input and TOPK overexpression in the TOPK WT and TOPK KD elute, whereas a band was not detectable in the empty vector control. The p21 antibody recognised a strong band in the input and a band in the 4 Gy irradiated elute for TOPK WT which increases in intensity in the TOPK KD sample.*

This method identified a list of interacting proteins as outlined in Table 4.7 and in Figure 4.8A. The highest protein score (3340) corresponded to PRKDC, or DNA-$PK_{cs}$, which was also identified from the first LC-

Ms/Ms (Table 4.6). TUBA1C (3180 protein score) is a different isoform of α-tubulin compared to TUBA8, which was identified by the previous experiment. Bands number 9 and 16 were identified as TOPK, confirming its overexpression. A different form of TRIM, TRIM 21, was identified compared to the previous run. This experiment also identified CDK1 as band number 10, at the correct molecular size (~ 34 kDa), confirming this previously-published interaction [74], [110]. another protein interaction that has been previously published and that was identified by this experiment was histone H2A [90]. This experiment also identified CDKN1A (p21) at 21 kDa, the predicted molecular weight for p21 [128].

The interaction between TOPK and p21 was selected for further study because it is novel, both TOPK and p21 have roles in cell cycle regulation, and because p21 was identified in both experiments. The immunoprecipitation experiment was repeated a third time with the inclusion of an unirradiated control for all conditions in order to check whether the interaction between TOPK and p21 was observable in the absence of IR. In this experiment, proteins were eluted using SDS loading buffer, and then run on a SDS-Page gel and transferred to a membrane for immunoblotting.

Figure 4.8B shows the membrane that was probed with anti-TOPK and anti-p21 antibodies. TOPK was present in the input samples as expected, and was overexpressed in the TOPK WT- and TOPK KD-transfected samples compared to the empty vector control. In the elute no band was detectable in the empty vector control at the correct molecular weight for TOPK. The p21 antibody recognised a strong band in the input and a band in the 4 Gy irradiated elute. A strong band was observable in the TOPK WT, but a stronger band was observable in the TOPK KD elute. Two bands are visible for TOPK in the input samples, with the lowest band thought to be the

endogenous protein, and the highest band, which is also stronger in intensity, thought to be the overexpressed form.

These results suggest that p21 and TOPK physically interact at a protein level when *TOPK* is overexpressed in HCT116 cells, 8 hours after the samples have been irradiated with 4 Gy IR. The band for p21 in Figure 4.8B seems to increase in intensity in the TOPK KD elute compared to the TOPK WT elute, but this might be due to higher expression of TOPK KD compared to TOPK WT, as also visible in Figure 4.7B and C, above.

### 4.2.6 Endogenous TOPK-p21 interaction

All of the previously presented IP experiments were performed in HCT116 cells after TOPK WT or TOPK KD were overexpressed. With the aim of investigating whether this specific radiation-dependent interaction was physiologically relevant, it was subsequently studied at an endogenous level.

Co-immunoprecipitation was performed in untransfected HCT116 cells using A/G agarose beads and antibodies against TOPK (Figure 4.9A) or p21 (Figure 4.9B). 4 Gy irradiated and unirradiated samples were compared to test whether the interaction was dependent upon IR. For this experiment, cells were plated in T75 flasks without being transfected and were irradiated when adherent. The immunoprecipitation was performed at 8 hours post IR. Cells were lysed with RIPA buffer and incubated on ice with benzonase to disrupt the DNA. Samples were then incubated with beads without antibody for pre-clearing. 25 µl of the samples were collected at this stage as inputs, and the remaining samples were incubated overnight with either TOPK or p21 antibodies depending on the desired pull-down. The following day, beads were added to the sample to bind to the antibody. Proteins were eluted from the beads using a 2 x loading buffer and then run on a SDS-Page gel. Samples were then transferred

to a membrane for immunoblotting using the reciprocal antibody and the obtained blots are shown in Figure 4.9.

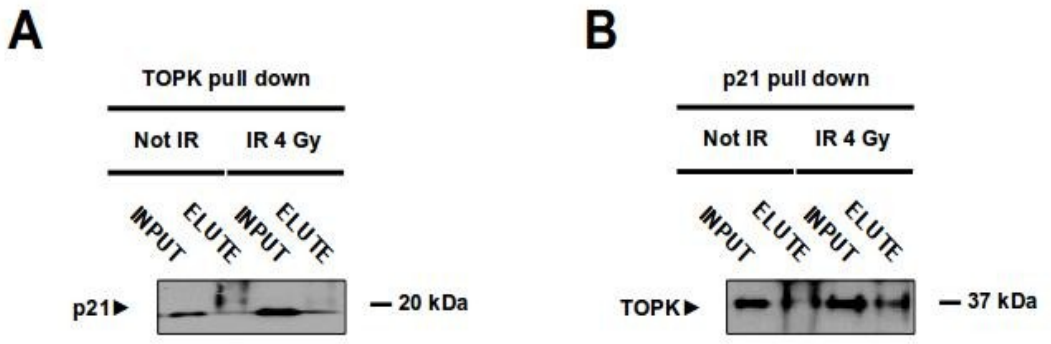


*Figure 4.9: Endogenous TOPK interacts with endogenous p21. (A) TOPK was immunoprecipitated from HCT116 cells, 8 hours after either 0 Gy or 4 Gy. The membrane was probed for p21 and showed a clear band in the input samples, which increased in intensity in the irradiated cells. A band which increases in intensity after radiation was also present in the elute lanes, suggesting the presence of p21 in the TOPK pull-down. (B) Co-immunoprecipitation was then performed pulling down p21 in HCT116 irradiated and unirradiated samples. The membrane was probed for TOPK. A clear band at 37 kDa was recognised by the anti-TOPK antibody in the input and in the elute lanes.*

TOPK was pulled-down in the irradiated and unirradiated samples, and p21 was identified by immunoblotting in both the input and elute for both samples (Figure 4.9A). Furthermore, when p21 was pulled-down (Figure 4.9B), the anti-TOPK antibody recognised a band at the appropriate size for TOPK in both the input and elute. In both cases a slight increase in band intensity in the irradiated elute was observed, suggesting that the interaction between TOPK and p21 is increased following IR. This result suggests that endogenous TOPK and endogenous p21 physically interact at 8 hours after 4 Gy IR in HCT116 cells.

## 4.3 Discussion

After TOPK was selected from a kinase screen as a target with clinical potential, this chapter investigated its role in modulating the observed radiosensitivity in HCT116 cells *in vitro*.

TOPK depleted cells showed a small but statistically significant reduction in γ-H2AX and 53BP1 foci at 30 minutes after radiation. However, this difference could not be explained in terms of residual DNA damage, as shown by the COMET experiment in Figure 4.1C, which showed no difference in DNA damage at 0.5, 2 or 8 hours. These time points were chosen to identify differences in the DNA damage repair following IR in *TOPK* depleted cells compared to the control cells, whereas the foci time range of 0.5-24 hours is the typical timing for formation and loss of DNA-repair related foci [25], [116]. It was speculated that in this context the difference in foci formation (γ-H2AX and 53BP1) at 30 minutes after IR might be due to differences in cell cycle progression after *TOPK* knockdown. TOPK depletion alters cell cycle progression in unirradiated cells [85], [86], [88], [111], [129]. This could lead to a reduction in the number of cells undergoing DNA replication, and therefore a smaller DNA content per cell. This discrepancy in DNA content might be the reason why a difference in foci formation is noted at 30 minutes after IR.

The cell cycle progression of irradiated, unsynchronised HCT116 cells was monitored after *TOPK* knockdown. BrdU vs PI plots presented in Figure 4.2 and Table 4.1 showed a detectable reduction of the $G_2$/M peak in TOPK depleted cells when compared to control cells. It is possible that this difference is due to an increase in $G_1$ arrested cells or an increase in cells progressing through mitosis without arresting at the $G_2$/M DNA damage checkpoint. In order to characterise the $G_1$/S transition, cells were synchronised in $G_1$ using a double-thymidine block, and then released. The TOPK depleted cells had a weaker synchronisation and a slower transition from $G_1$ into early S-phase as

shown in Figure 4.3, and quantified in Table 4.2 and Table 4.3. This phenotype was also observed after 4 Gy IR, and was supported by the finding of lower levels of cyclin E1 in TOPK depleted cells.

One of the events that allows the cell to survive the IR-induced DNA damage is the activation of DNA damage checkpoints, which promotes the correct repair of DNA damage before progression into the next cell cycle stage.

Immunoblotting analysis of $G_1$ synchronised, irradiated and released HCT116 cells was performed. In this experiment the mitotic markers, phospho-Histone H3 and cyclin B1 were observed in TOPK depleted cells at 8 hours, but were not observed in the control cells until 10 hours after IR, in agreement with what has been previously observed in unirradiated conditions in breast cancer [87]. Levels of total TOPK did not change significantly in time, in contrast with an increase in *TOPK* expression levels at 7-9 hours post $G_1$ synchronisation and release in HeLa cells which has been published previously [74]. In contrast to previous observations in doxorubicin-treated cells [88], levels of expression of p21 did not seem to be TOPK-dependent. Furthermore, *TOPK* knockdown inhibited the phosphorylated form of CDK1 without affecting the levels of expression of CDK1, suggesting an inability to activate the $G_2$/M checkpoint in the absence of TOPK.

These results suggest an impaired checkpoint activation with effects on the $G_1$/S transition and on the $G_2$/M arrest post IR and these cell cycle modifications could be a cause of the observed radiosensitisation.

In order to correlate these findings to the observed radiosensitivity, cell fate was investigated. Nuclear morphology was monitored (Figure 4.5A and B) as well as the *in vitro* growth rate (Figure 4.5C). A significant difference was observed in the growth rate in irradiated cells when TOPK had been depleted at 3-6 days after IR, together with

an increase in multinucleated cells at 72 hours post IR when comparing *TOPK* depleted cells to control cells. These results, presented in Figure 4.5, suggest a role for TOPK in modulating mitotic catastrophe after IR in HCT116 cells which would also agree with the known roles of TOPK in mitosis [72], [73], [86], [87], [108], [109]. TOPK has been shown to be a master mitotic regulator in HeLa cells by phosphorylating C2H2 zinc finger protein [108] and to be phosphorylated by CDK1 [72], [110]. It has also been shown to interact with PRC1 in $G_2$/M [110] and to be associated with microtubules [73], [74]. None of the previously published studies was performed in the context of ionising radiation.

Apoptosis was investigated with two different approaches as shown in Figure 4.6 and quantified in Table 4.4. TOPK depleted cells had increased levels of apoptosis at 48 and 72 hours after 4 Gy IR. These results are consistent with the hypothesis that in TOPK depleted samples, the $G_2$/M DNA damage checkpoint is impaired, promoting premature entry into mitosis. It is possible that the entry into mitosis with unrepaired damage leads to cytokinetic issues, with a subsequent increase in multinucleation and apoptosis observed at later time points. This result is in agreement with what has been already published in unirradiated samples after shRNA-mediated TOPK depletion [88].

In order to outline the role of TOPK in modulating radiosensitivity, the proteins with which TOPK physically interacts were investigated. To study TOPK interacting proteins after radiation a set of immunoprecipitations were performed with multiple approaches. First TOPK was overexpressed (Figure 4.7) and pulled-down 8 hours after 4 Gy IR, and samples were analysed with LC-Ms/Ms using the parameters described in Table 4.5. The results are presented in Table 4.6. LC-Ms/Ms analysis was also carried out on samples cut from an SDS-Page gel after TOPK was overexpressed and pulled-down (Figure

4.8A and Table 4.7). Finally the IP experiment was repeated including an unirradiated control and the elutes were transferred to a membrane which was immunoblotted with specific antibodies binding to the previously identified TOPK interacting proteins (Figure 4.8B). The identified interaction between TOPK and p21 was then studied at the endogenous level with co-IP (Figure 4.9).

LC-Ms/Ms experiments revealed that TOPK may interact with a series of different proteins which are listed in Table 4.6 and Table 4.7. These proteins are of interest because they are involved in DNA repair (DNA-$PK_{cs}$, XRCC6) or cell cycle regulation (14-3-3σ, TRIM25, CDK1, p21) after IR or because they were previously identified for interaction with TOPK (histone H2A, α-tubulin, MAPK2K, CDK1). From the presented list only p21 was confirmed by the three different approaches adopted.

CDKN1A, or p21, is a CDK inhibitor with many roles in cell cycle regulation after IR [24], [52], [54], [55], [130]. p21 has been shown to modulate transition through different stages of the cell cycle [52] under normal conditions or after UV- or IR-induced DNA damage [57], [131]. p21 can promote the kinase activity of CDK4 or CDK6 in complex with cyclin D and as a consequence promotes $G_1$ progression. It has been shown to inhibit CDK2/Cyclin E complex formation, thus inhibiting RB phosphorylation and progression into and through S-phase. It has also been shown to inhibit CDK2/Cyclin A and CDK1/Cyclin A complexes, therefore inhibiting S phase and $G_2$ progression. Additionally it has been shown to inhibit the activity of CDK1/Cyclin B1, which is necessary to progress into $G_2$/M phase after DNA damage [22], [24], [52], [55], [57], [132]. p21 expression is upregulated after DNA damage through a p53-dependent mechanism, but can also be expressed in a p53-independent manner [22], [24], [55].

The interaction between TOPK and p21 was detectable at the endogenous level in HCT116, as shown in Figure 4.9, and may be enhanced after IR.

It has to be noted that the list of proteins identified by LC-Ms/Ms (Table 4.6 and Table 4.7) does not include some known TOPK interacting proteins that have been previously published, such as p53 [88], [89]. This is probably due to the different conditions in the experimental set-up and to the different endpoints investigated. The presented immunoprecipitations were performed in HCT116 cells at 8 hours after 4 Gy irradiation and aimed at identifying interactions after IR. The interaction between TOPK and p21 seemed to be very weak in the unirradiated control and this might be the reason why this interaction has not been seen before in other studies without IR. The increase in this interaction after IR could be due to an increased expression of p21 after IR [24], [52], [54], [55], [57], [130] which makes it more likely to bind to TOPK.

Taken altogether these results showed a role for TOPK in the cellular response to radiation in terms of cell cycle modification, cell fate alterations, and protein interactions.

# CHAPTER 5

# CLINICAL SIGNIFICANCE OF TOPK

## 5.1 Introduction

The importance of looking for new modulators of radiosensitivity lies in the possibility of using them in the clinic. Radiotherapy can only be effective in tumour control if delivered within the therapeutic window which represents the balance between tumour control and normal tissue complications [10]. In order to widen this region of action, and in particular to shift the probability of achieving tumour control towards the left towards a lower radiation dose, a possible approach is the modulation of intrinsic radiosensitivity by the identification of novel tumour-specific modulators of radioresponse.

TOPK has been previously shown to be upregulated in most cancers and to be linked to poor clinical outcomes in different types of cancer. *TOPK* expression has been shown to correlate with adverse outcomes in terms of overall survival and recurrence free survival, identifying TOPK as a prognostic marker in breast cancer patients [77]. In non-small-cell lung cancer (NSCLC) *TOPK* expression has been associated with histological tumour type, lymph node metastasis and cancer stage (TNM, where T identifies the size of the primary tumour and whether it has invaded the surrounding tissue, N identifies involved nearby lymph nodes, and M identifies distant metastasis involved). The median survival for NSCLC patients with low TOPK levels was significantly longer (47 months) than patients with high levels of TOPK (18 months). Tumours positive for both TOPK and Ki67, or TOPK and mutant p53, had a significantly poorer prognosis in surgically removed tumour samples (279 samples) [78], [79]. Another study in NSCLC confirmed a correlation between high levels of TOPK and low overall survival, and between high levels of TOPK and poor disease-free survival, and showed that high levels of TOPK paired with low levels of PTEN give an even poorer survival (119 analysed samples) [80]. In 2009 a paper was published identifying the opposite

correlation: TOPK was shown to confer a better survival when overexpressed in cholangiocarcinoma, but the correlation was statistically weak and the cohort only contained 24 patients [133]. In colorectal cancer (CRC) patients TOPK was found to be overexpressed (study of n = 1044 patients) and to positively correlate with *KRAS* or *BRAF* mutations. Among patients with *KRAS* or *BRAF* mutations, those with diffuse TOPK staining had a significantly poorer prognosis [84]. In colorectal cancer, levels of TOPK have also been correlated with levels of interlukin-8 (IL-8 or CXCL8) and as a consequence with poorer prognosis in the examined cohort of 186 patients [83]. Levels of TOPK have been studied also in prostate cancer and high TOPK levels have a strong correlation with advanced grade of cancer in 71 human prostate cancer and 30 benign prostate hyperplasias [82] and to be correlated with invasiveness and distant metastasis formation (120 patient cohort) [81]. In contrast with the literature, a recent paper has shown the opposite effect in terms of a prognostic role for TOPK in oral cancer. The IHC data from a cohort of 287 patients identified TOPK as a favourable prognostic marker for overall survival in young patients, smokers, and patients with late stage disease [134].

In this thesis, TOPK is shown to be a tumour-specific modulator of radiosensitivity which is upregulated in most cancers and not expressed in normal tissues, to alter the DNA damage response in terms of foci formation at early time points, to alter the cell cycle profile, to interact with p21 and modulate expression and post-translational modifications of the mayor players in the cellular radiation response, and to increase levels of cell death via apoptosis and mitotic catastrophe *in vitro*.

Further studies are needed in order to understand the potential of TOPK as a clinical modulator of radiotherapy response in patients. It was therefore examined if expression levels of *TOPK* in tumour samples showed any correlation with the clinical outcome. The

publicly available early breast cancer patient cohort was used for the statistical analysis which was performed by Dr Francesca Buffa using the rmeta R package (http://cran.r-project.org/) as previously described [92], [93].

Prostate cancer is the commonest malignancy in men and the second leading cause of male cancer-related death worldwide [135]. External beam radiotherapy is a commonly used treatment modality for the radical treatment of localised and/or locally advanced prostate carcinoma within the United Kingdom before the introduction of hormone therapy combined with radiation [135], [136]. In order to determine whether there was a statistically significant correlation between levels of TOPK and clinical outcome post radiotherapy, diagnostic pre-radiotherapy prostate cancer samples with associated anonymous clinical follow up data from a cohort of 128 patients were investigated with immunohistochemistry (IHC), in collaboration with Dr Richard J Bryant.

As shown in “CHAPTER 3 “, TOPK siRNA depletion induces a significant reduction in colony formation after radiation. A limit of the use of siRNA constructs to decrease *TOPK* expression is the transient nature of this silencing method, which is problematic for *in vivo* experiments and for clinical applications.

In order to overcome this problem, two different methods of disrupting *TOPK* activity were investigated: shRNA silencing and kinase inhibition. Short hairpin RNA (shRNA) results in the constitutive expression of an interfering double-stranded RNA in the nucleus, and can induce a permanent stable knockdown of the targeted gene. Molecular inhibition of the TOPK kinase activity was achieved using a previously described TOPK inhibitor (TOPKi) to inhibit its kinase activity [111]. Both of these approaches have applications *in vivo,* allowing xenograft formation with shRNA TOPK-depleted cells or drug

administration to inhibit TOPK activity, allowing the study of TOPK in mouse models.

Finally, in order to test whether the observed effects were strictly dependent on the IR-induced type of damage and response, and to test whether TOPK could be exploited in clinical applications in combination with chemotherapeutic drugs, a set of four chemotherapeutic drugs including 5-FU, Cisplatin, Etoposide and Vinblastine were also tested *in vitro* on HCT116 cells where TOPK was depleted.

## 5.2 Results

### 5.2.1 Prognostic significance of TOPK expression in breast cancer patients

A correlation between high levels of *TOPK* expression and clinical data was explored in order to investigate a negative role on outcome and recurrence-free survival (RFS).

The prognostic meta-analysis was carried out by Dr Franceca Buffa using the rmeta R package. The patient numbers and treatment information for the data sets were as follows:

- GSE6532: Early stage breast cancer patients given adjuvant tamoxifen [94]. GSE6532OXF, GSE6532KI, GSE6532GUY datasets contain 98,136 and 87 patients, respectively.
- GSE2034: 286 patients with early breast cancer not receiving either adjuvant or neoadjuvant therapy. 219 patients received breast conserving surgery and 67 were given radical mastectomy. 248 patients received radiotherapy [95].
- GSE9195: 77 early stage breast cancer patients which were treated with adjuvant tamoxifen monotherapy [94].
- GSE1456: 159 early breast cancer patients. 104 receiving adjuvant tamoxifen or chemotherapy [96].

*TOPK* expression was investigated at an mRNA level in these cohorts for a total of 1050 early breast cancer patients, who received the treatments described above. The obtained result is shown in the Forest plot in Figure 5.1.

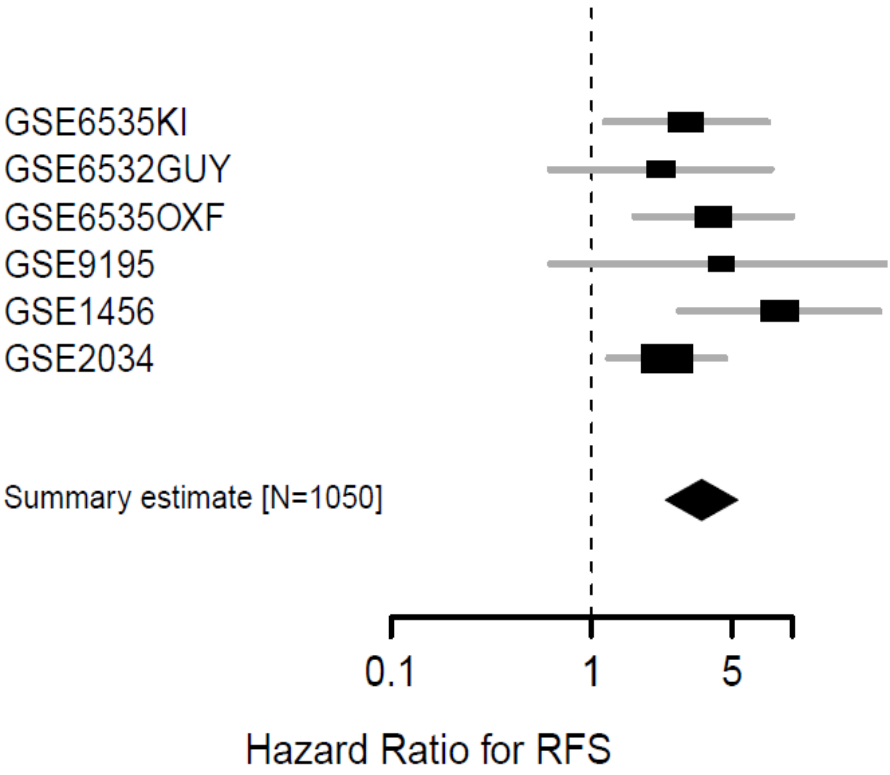


*Figure 5.1: TOPK expression strongly correlates with worse recurrence-free survival in breast cancer patients. Six different curated retrospective breast cancer datasets were analysed and the hazard-ratio for recurrence-free survival (RFS) is shown above at the 95% confidence interval (CI). The bottom diamond shows the summary effect for the whole cohort (1050 samples). Summary effect = 3.535, 95% CI (2.330; 5.364). Analysis performed by Dr Francesca Buffa.*

The different cohorts of patients showed different levels of correlation between *TOPK* expression and RFS. The strongest effect was identified in GSE1456 cohort, followed by GSE6535OXF. The summary effect was estimated to be 3.535 at 95% confidence interval (CI) 2.330-5.364 as shown in Figure 5.1 above, confirming a potent overall effect of *TOPK* mRNA expression levels on recurrence-free survival.

### 5.2.2 Immunohistochemistry analysis of prostate cancer cohort

A cohort of 128 patients with prostate cancer treated with primary radiotherapy was analysed with IHC in order to determine if levels of *TOPK* expression were associated with clinical outcome. All patients

were treated with primary radiotherapy with curative intent and had archived prostate biopsies available from their initial diagnosis. Importantly, this was a cohort where men had been treated with radiotherapy alone, rather than with the current strategy of treatment using radiotherapy with neoadjuvant and adjuvant androgen deprivation therapy. Levels of *TOPK* expression were investigated in relation to disease recurrence-free survival, metastatic recurrence-free survival (i.e. proven metastasis), local recurrence-free survival (i.e. PSA increase of >2 ng/ml above the PSA nadir post-treatment in the absence of proven metastases) and all-cause mortality. Demographics of the analysed prostate cancer cohort can be found in Table 5.1.

| | **Radical radiotherapy (n=128)**<br><br>**n (%)** |
|---|---|
| **Median age (range), years** | **69.4 (range 54.7 - 78.8)** |
| **Pre-treatment PSA** | |
| ≤10 | 46 (35.9) |
| 10.1-20 | 43 (33.6) |
| >20 | 32 (25) |
| Unknown | 7 |
| **cT-stage** | |
| ≤cT2 | 78 (60.9) |
| ≥cT3 | 42 (32.8) |
| Unknown | 8 (6.3) |
| **Gleason Grade** | |
| ≤6 | 30 (23.4) |
| 7 | 83 (64.9) |
| ≥8 | 15 (11.7) |

| | |
|---|---|
| **Median FU (range), years** | 7.9 (0.5 - 12.7) |
| **Any recurrence during follow-up** | 62 (48.4) |
| **Local recurrence during follow-up**<br>**Metastatic recurrence during follow-up**<br>**Death (all-cause) during follow-up** | 44 (34.4)<br>18 (14.1)<br>26 (20.3) |

*Table 5.1: Clinical characteristics of the radical radiotherapy prostate biopsy cohort. Abbreviations: PSA, prostate specific antigen; cT, clinical T-stage; FU, follow-up.*

The demographics of the analysed group of patients described in Table 5.1 show that in the 128 patients the median age was 69 years. The prostate specific antigen (PSA) baseline was found to be ≤ 10 ng/ml for 36% of the cohort, between 10.1 and 20 ng/ml for 34% of the cohort, and > 20 ng/ml for 25% of the cohort (unknown for 7 patients). Clinical T-stage (cT) was less than cT2 (i.e. organ-confined) for 78 patients and more than cT3 (i.e. locally advanced) for 42 patients (unknown for 8 patients). Gleason grade was ≤ 6 for 30 patients, equal to 7 for 83 patients, and ≥ 8 for 15 patients within the analysed cohort. Median follow-up after treatment was 7.9 years. 62 patients had a recurrence during follow-up, of whom 44 (34%) had local recurrence and 18 (14%) had metastatic recurrence. Deaths due to any cause during the follow-up period occurred for 26 patients (20%).

Nuclear, cytoplasmic and total *TOPK* expression scores were obtained by a pathologist (see section 2.16.2 of “MATERIALS AND METHODS” chapter), and the scores were dichotomised into high and low TOPK scores in order to perform Kaplan-Meier analyses to investigate potential associations with clinical outcomes following radiotherapy.

Examples of IHC stained slides can be found in Figure 5.2.

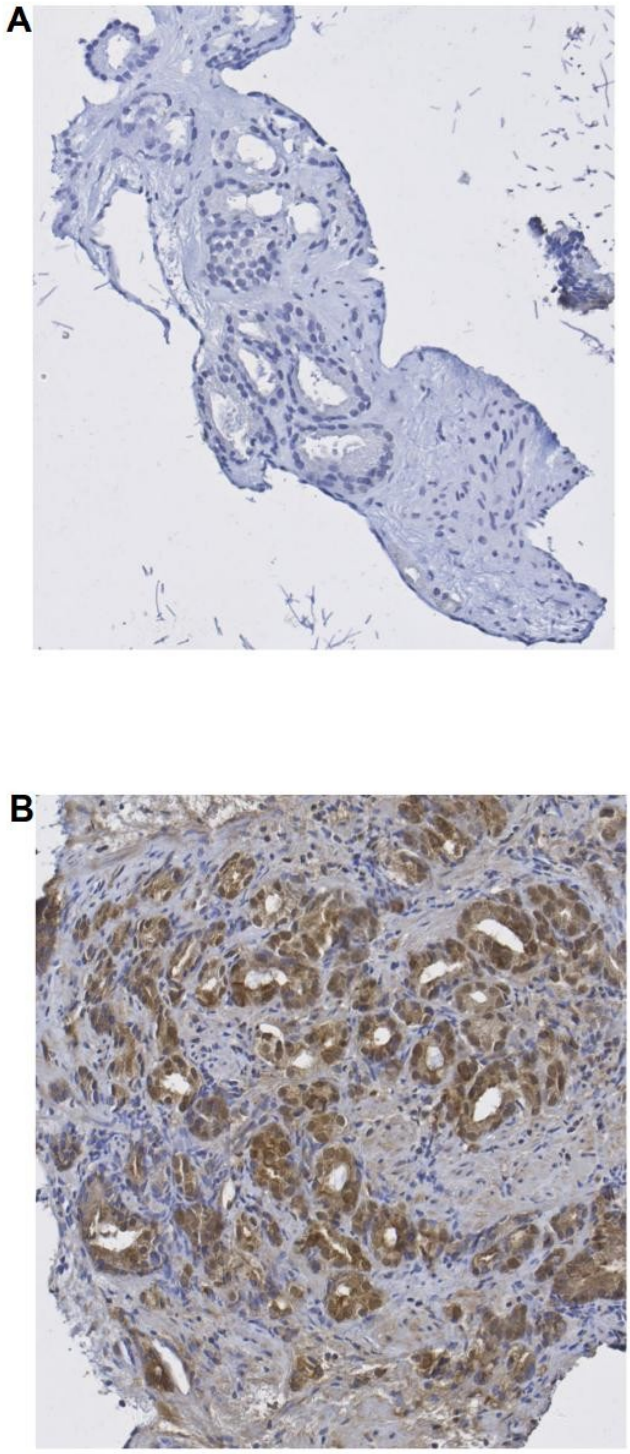


*Figure 5.2: Example of the field of view of prostate cancer IHC stained slides. 20X magnification. (A) Example of a section with absent/low levels of TOPK. (B) Example of a section with high levels of nuclear and cytoplasmic TOPK. TOPK*

*localisation is visible in brown, hematoxylin counterstain highlights the nuclei in blue.*

*Relative expression of TOPK in cancer specimens was determined using a four-point staining intensity scoring system. The maximum staining intensity score ranged from 0 (no expression) to 3 (maximal expression). Samples were scored for nuclear TOPK expression and for cytoplasmic TOPK expression. A relative percentage of cancer cells with the assigned protein intensity was also given. The intensity and percentage scores were multiplied to give a TOPK expression score (0-300) for nuclear or cytoplasmic expression. Total TOPK expression was obtained by addition of the nuclear and cytoplasmic score (0-600).*

*Various cut-off points were used to dichotomise TOPK expression as high versus low for Kaplan-Meier analysis. Staining performed by Lucia Cerundolo. Scoring performed by Dr Clare Verrill.*

Samples were scored by a pathologist and differentiated into low (Figure 5.2A) or high (Figure 5.2B) nuclear, cytoplasmic and total *TOPK* expression as well as depending on TOPK localisation (nuclear or cytoplasmic).

Figure 5.3 shows the results obtained for analysis of nuclear TOPK.

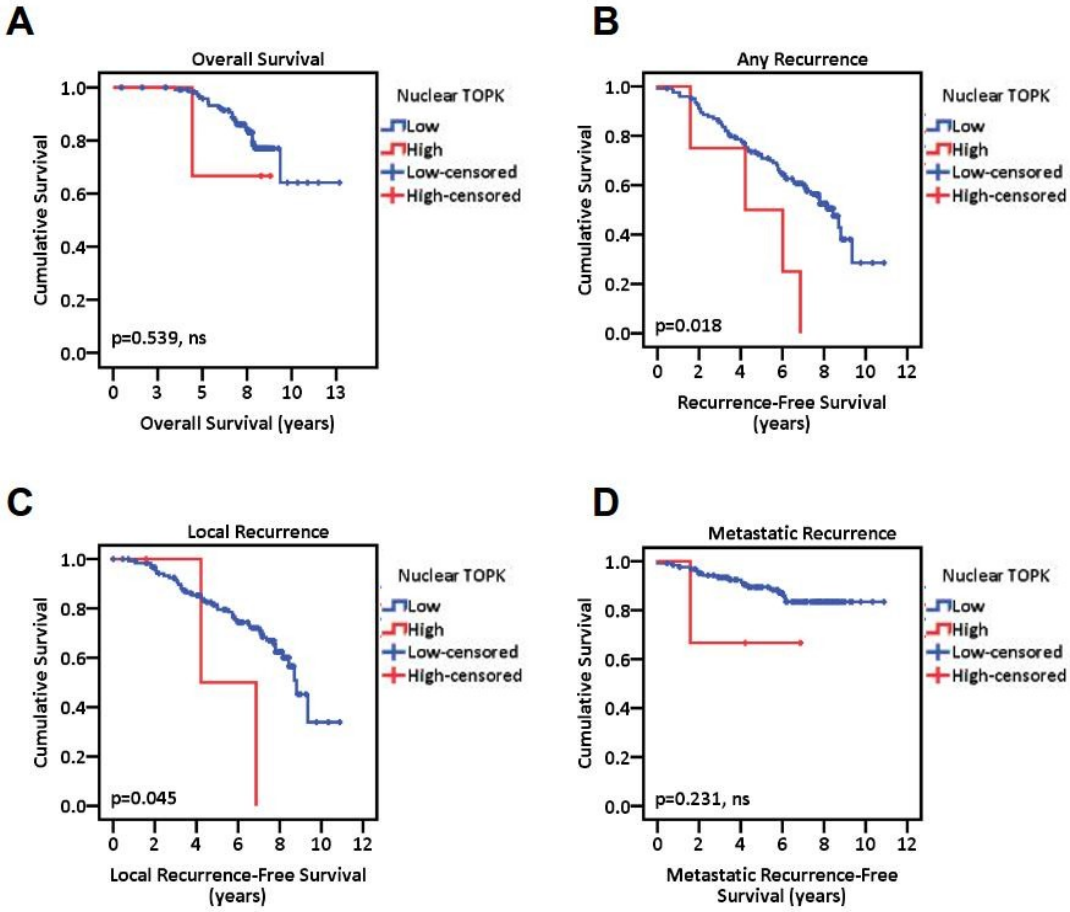


*Figure 5.3: Nuclear expression of TOPK and clinical outcome in the prostate cancer cohort. Kaplan-Meier analysis of nuclear TOPK levels and (A) overall survival, (B) recurrence-free survival, (C) local recurrence-free survival, and (D) metastatic recurrence-free survival.*

*High levels of nuclear TOPK were associated with significantly increased risk of local- and any-recurrence following radiotherapy.*

*Two-tailed p-value was considered significant at $p<0.05$.*

Figure 5.3A shows that there was no statistically significant difference between high and low levels of nuclear TOPK in terms of overall survival (p=0.539). Recurrence-free survival for any recurrence showed a significant effect (p=0.018) with high levels of TOPK correlating with a shorter recurrence-free time (Figure 5.3B), but only 4 patients were included in the high TOPK group with a cut-off point score of 200. Similarly, as shown in Figure 5.3C, a worse local recurrence-free survival seemed to correlate with high levels of nuclear TOPK, but this result was obtained with a cut-off point of 200 and included only 3 patients in the high TOPK group. Metastatic recurrence-free survival did not show any statistically significant correlation with the levels of nuclear TOPK (p>0.05) as shown in Figure 5.3D.

Sections were also scored based on the cytoplasmic TOPK expression. The obtained results are presented in Figure 5.4.

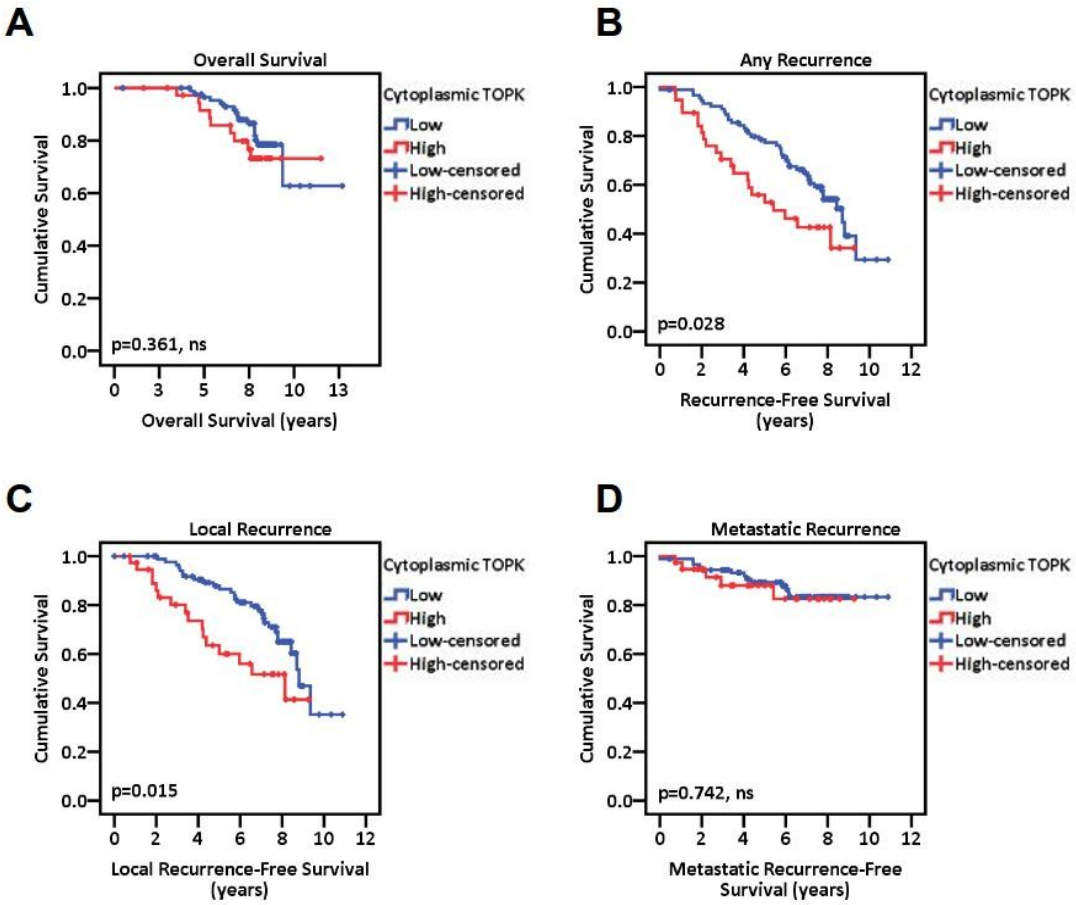


*Figure 5.4: Cytoplasmic expression of TOPK and clinical outcome in the prostate cancer cohort. Kaplan-Meier analysis of nuclear TOPK levels and (A) overall survival, (B) recurrence-free survival, (C) local recurrence-free survival, and (D) metastatic recurrence-free survival.*

*High levels of cytoplasmic TOPK were associated with significantly increased risk of local- and any-recurrence following radiotherapy.*

*Two-tailed p-value was considered significant at $p<0.05$.*

No association between levels of cytoplasmic TOPK and any-cause mortality was found (Figure 5.4A), with no statistically significant difference detectable between high and low levels of TOPK scoring in the cytoplasm in terms of overall survival (p=0.361). Figure 5.4B shows recurrence-free survival for any recurrence. High levels of TOPK in the cytoplasm were associated with poorer RFS with p=0.028 (protein expression cut-point 200). Similarly high levels of cytoplasmic

TOPK were associated with poorer (p=0.015) local recurrence-free survival as shown in Figure 5.4C. A similar effect was not observable in the context of metastatic recurrence-free survival (Figure 5.4D).

Samples were then analysed regarding total levels of TOPK calculated by adding cytoplasm total score and nuclear total score (range 0-600). Results are shown in Figure 5.5.

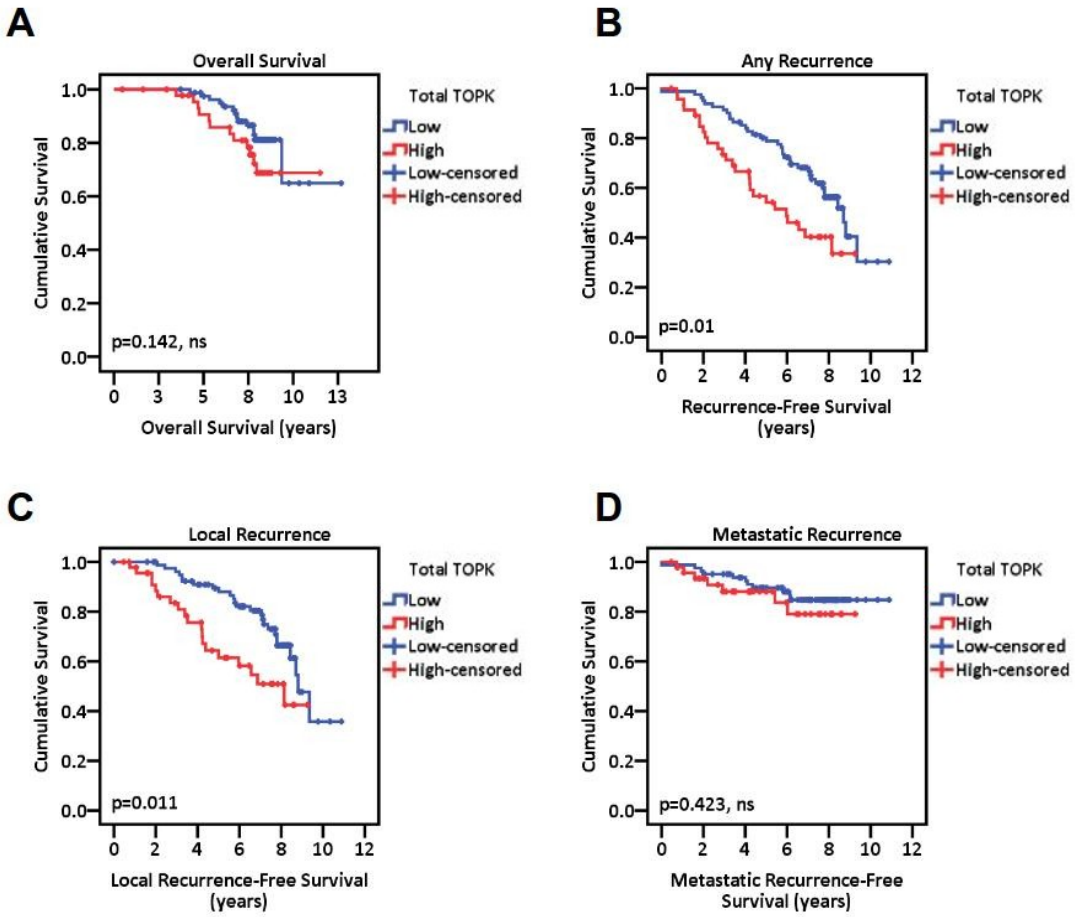


*Figure 5.5: Total expression of TOPK and clinical outcome in the prostate cancer cohort. Kaplan-Meier analysis of nuclear TOPK levels and (A) overall survival, (B) recurrence-free survival, (C) local recurrence-free survival, and (D) metastatic recurrence-free survival.*

*High levels of total TOPK were associated with significantly increased risk of local- and any-recurrence following radiotherapy.*

*Two-tailed p-value was considered significant at $p<0.05$.*

Analysis of the overall survival, presented in Figure 5.5A, did not reveal any association between total levels of TOPK and any-cause mortality. On the other hand, both recurrence-free survival and local recurrence-free survival were significantly shortened in cases with higher levels of TOPK (cut-off point of 200) with p-values of respectively 0.01 and 0.011 (Figure 5.5B and C). No statistically

significant effect was observed for metastatic recurrence-free survival based on levels of total TOPK, as shown in Figure 5.5D.

Taken together, these results suggest an effect on clinical outcome based on levels of expression of *TOPK*. In particular, high levels of TOPK correlate with a poorer therapy efficacy in terms of local recurrence and any recurrence-free survival. This effect was more evident in the analysis conducted on cytoplasmic and total TOPK staining compared with nuclear staining. Metastatic recurrence-free survival did not appear to be associated with levels of TOPK.

### 5.2.3 Generation of an shRNA stable knockdown cell line

Stable shRNA-induced *TOPK* knockdown was performed using the HCT116 cell line because of its potential utility for *in vivo* mice experiments and because it showed significant radiosensitisation after *TOPK* siRNA knockdown.

The first round of lentiviral transduction was performed at a MOI (multiplicity of infection, the ratio of agents to infection targets) of 20 in each well of a 96-well plate. As shown in Figure 5.6A, three different shRNA sequences were tested together with a non-specific control shRNA (shNS) and the levels of knockdown were shown by immunoblotting to detect TOPK.

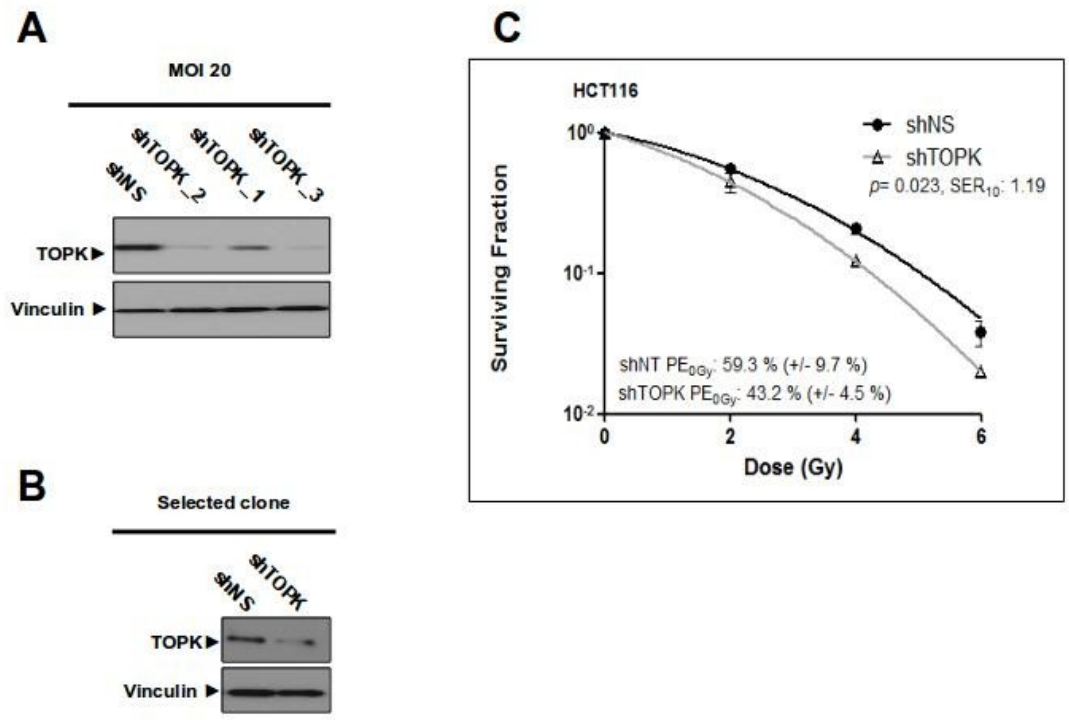


*Figure 5.6: (A) Immunoblotting of the first round of lentivirus transduction with 20 MOI shRNA targeting TOPK. Of the three shRNA constructs tested, shTOPK_1 and shTOPK_3 show the greatest reduction in band intensity when compared to the non-specific shRNA construct (shNS). (B) Immunoblotting of the selected clone from a single cell from the shTOPK_3 population showing a stable TOPK knockdown. Vinculin was used as a loading control. (C) CFA showing the radiosensitisation of HCT116 due to TOPK stable shRNA silencing with the selected clone.*

*Clonogenic data are representative of three independent experiments and presented as mean +/- SD from triplicate wells. Colonies were stained and counted about 2 weeks after IR depending on growth rate. p-values were generated by factorial 2-way ANOVA. PE = Plating Efficiency. $SER_{10}$ = Sensitisation Enhancement Ratio at 0.1 surviving fraction calculated from non-linear regression of linear quadratic model.*

The three shRNAs targeting *TOPK* caused a reduction in TOPK band intensity compared to shNS, which was more evident for constructs sh*TOPK*_1 and sh*TOPK*_3.

The population of mixed clones following sh*TOPK*_3 expression, was selected for clonal expansion and colony selection. The sh*TOPK*_3

clonal population was replated in a 96-well plate at a cell density of 0.6 cells/well in order to select colonies growing from a single knockdown cell. Cells were then monitored, grown in neomycin selection medium to select for cells expressing sh*TOPK*_3, and expanded. Different clones were tested by immunoblotting for levels of *TOPK* expression and one clone was selected with the best knockdown (Figure 5.6B). The obtained HCT116 shRNA stable *TOPK* knockdown cell line was tested in a colony formation assay, and significant radiosensitisation was observed with a p-value of 0.023 and a $SER_{10}$ of 1.19. The radiosensitisation observed was not as great at the radiosensitisation observed following transient *TOPK* knockdown, probably due to the remaining *TOPK* expression observed with this stable knockdown method (as shown in Figure 5.6B and C).

### 5.2.4 Inhibition of TOPK activity *in vitro*

Two different TOPK inhibitors have been described previously, HI-TOPK-032 [81], [129], [137] and OTS964 [111]. These inhibitors were tested in order to examine whether they induced radiosensitisation in cancer cell lines.

HI-TOPK-032 was selected by screening 36 drug candidates targeting TOPK in an *in vitro* kinase assay [129]. This inhibitor was shown to bind to the ATP-binding site of TOPK and to inhibit its kinase activity, to inhibit colon cancer cell growth, to induce apoptosis *in vitro* and to reduce colon cancer growth in a xenograft model *in vivo* [129]. HI-TOPK-032 has also been shown to reduce sphere formation capacity of glioma initiating cells (GICs) and to increase apoptosis at 5 µM *in vitro,* and to reduce tumour xenograft growth in mice at 5 mg/kg or 10 mg/kg [137].

OTS964 was developed through screening of a high-throughput compound library and extensive structure-activity relationship studies (SAR). It was shown to inhibit TOPK activity at a concentration of 1, 2, and 5 µM with effects on cell growth of HCT116 with a $IC_{50}$ value of 33

nM. It has been tested *in vivo* using liposomal intravenous administration at a concentration of 40 mg/kg or orally at 50 or 100 mg/kg, showing tumour xenograft shrinking and complete tumour regression [111].

As a first step both TOPK inhibitors were tested on HAP1 TOPK k.o. cells to test off-target toxicity. Cells were plated for a CFA, treated with the inhibitor for 24 hours, and then allowed to recover for 2 weeks in fresh medium. The tested concentrations were 2 and 3 µM, which are even lower concentrations than the published working concentration range of 5-10 µM for HCT116 *in vitro* experiments [81], [129], [137]. HI-TOPK-032 showed a high level of toxicity when added to adherent HAP1 TOPK k.o. cells at a concentration of 2 and 3 µM, suggesting an off-target effect at this concentration which impaired colony formation.

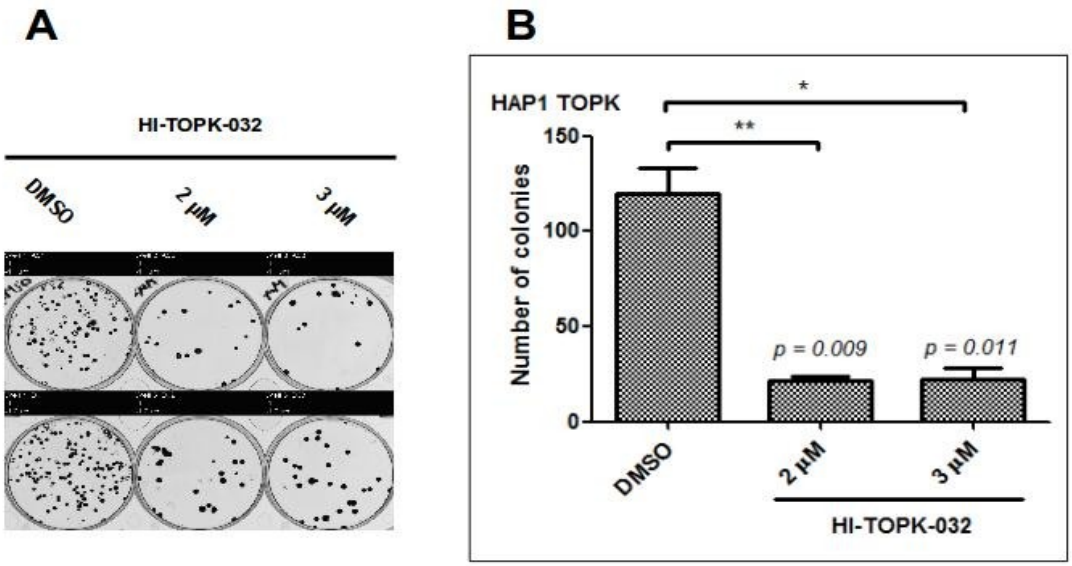


*Figure 5.7: HI-TOPK-032 showed a significant reduction in colony formation in unirradiated HAP1 TOPK k.o. cells at the published ([81], [129], [137]) working concentrations of 2 μM and 3 μM. After plating, cells were incubated for 24 hours with HI-TOPK-032 (A) Colonies formed after treatment with 2 or 3 μM of TOPKi HI-TOPK-032 (top and bottom wells represent two replicates of the same experiment). (B) Quantification of the number of colonies. Unpaired two-sided student's t-tests comparing DMSO to TOPKi *p<0.05, **p<0.01*

In contrast, OTS964 was tested on HAP1 WT and HAP1 TOPK k.o. cells in a CFA format and did not show toxicity on its own at 0 Gy as shown in Figure 5.8A below, with the following 0 Gy plating efficiencies for the HAP1 TOPK k.o. cell line: DMSO $PE_{0Gy}$ 56.7% (+/- 8.3%) and TOPKi $PE_{0Gy}$ 43.7% (+/- 6.1%). HAP1 cells were plated and then incubated with the optimised concentration of 70 nM OTS964 TOPK inhibitor for four hours before being irradiated at different doses. The survival curves are shown in Figure 5.8A and B. OTS964 induced significant radiosensitivity in the HAP1 WT cell line with an $SER_{10}$ of 1.36, which was comparable to the sensitisation due to *TOPK* deletion in HAP1 cells. Furthermore, OTS964 did not show a significant radiosensitising effect on the HAP1 TOPK k.o. cell line. Taken together, this suggests

that OTS964 is a specific TOPK inhibitor causing radiosensitisation at 70 nM in HAP1 cells.

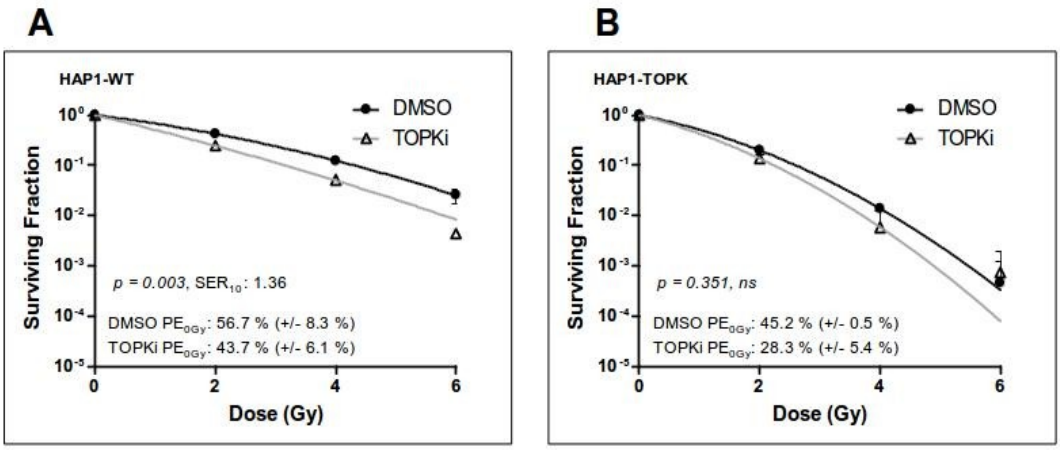


*Figure 5.8: Colony formation assay (CFA) of HAP1 cells and OTS964 TOPK inhibitor. The cell lines were incubated for 4 hours with the TOPK inhibitor at 70 nM concentration or a DMSO control before being irradiated at various doses. (A) HAP1 WT cells, expressing TOPK, showed a radiosensitising effect when TOPK activity was inhibited with 70 nM OTS964 with a $SER_{10}$ of 1.36, p-value = 0.003. OTS964 did not induce a significant drop in plating efficiency at 0 Gy: DMSO $PE_{0Gy}$ 56.7% (+/- 8.3%), TOPKi $PE_{0Gy}$ 43.7% (+/- 6.1%). (B) HAP1 TOPK k.o. cells did not show any significant radiosensitising effect of the OTS964 TOPK inhibitor at the stated concentration of 70 nM (p-value = 0.351, non significant).*

The OTS964 TOPKi was further tested on normal and cancer cell lines to verify its radiosensitising properties through inhibition of TOPK. Colony formation assays were performed in a 6-well plate format. Cells were incubated with 70 nM OTS964 for four hours prior to irradiation, and then the medium was replaced after a further 20 hours and the cells allowed to grow for 2 weeks. The results, shown in Figure 5.9, confirmed that OTS964 radiosensitised cancer cell lines HCT116 and SQ20B with $SER_{10}$ of respectively 1.40 and 1.54 but not normal tissue cell lines HFL-1 and MRC5.

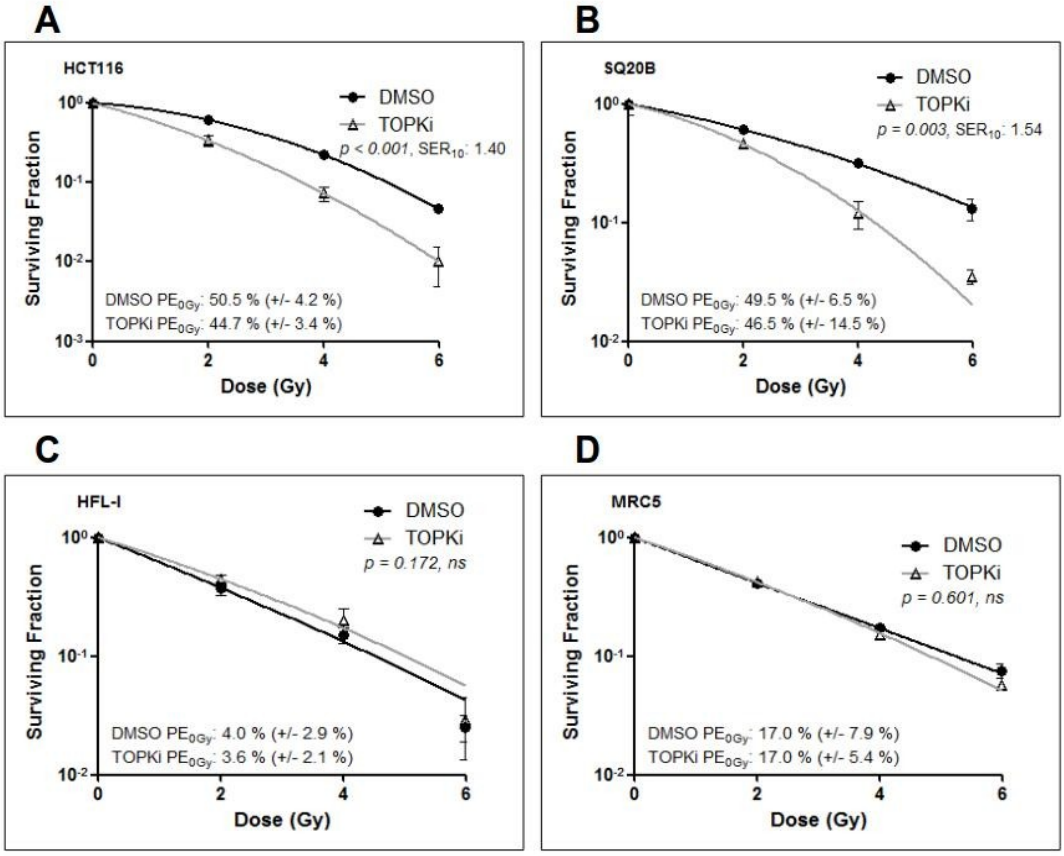


*Figure 5.9: CFA in two cancer cell lines (top) and two normal tissue cell lines (bottom). TOPK was inhibited with 70 nM OTS964. Cells were plated and incubated with the inhibitor for four hours before being irradiated at the indicated doses. (A) TOPK inhibition with the inhibitor showed a significant radiosensitisation in HCT116 cells. (B) Significant radiosensitisation was also observed in SQ20B cells. (C) HFL-1 normal fibroblasts, which do not express TOPK, were not affected by the TOPKi in terms of colony formation. (D) MRC5 do not express TOPK and did not show a significant radiosensitisation in a CFA format.*

*All data are representative of three independent experiments and presented as mean +/- SD from triplicate wells. Cells were treated with the indicated inhibitor at 70 nM concentration. Colonies were stained and counted about 2 weeks after IR depending on growth rate. p-values were generated by factorial 2-way ANOVA. PE = Plating Efficiency. $SER_{10}$ = Sensitisation Enhancement Ratio at 0.1 surviving fraction calculated from non-linear regression of linear quadratic model.*

### 5.2.5 Cellular response to chemotherapeutic drugs after TOPK depletion

TOPK has been previously studied in response to doxorubicin treatment [88], [89], and arsenite ($As^{3+}$) treatment [90]. Overexpression of *TOPK* in HT1080 cells attenuates the $G_2$/M checkpoint via p53 destabilisation after doxorubicin treatment [89]. *TOPK* knockdown in HCT116 cells increases p53-dependent overexpression of p21 and slows growth rate *in vitro* through accumulation in $G_2$/M together with an increase in the levels of apoptosis after doxorubicin treatment [88]. In RPMI7951 cells TOPK binds to H2AX and inhibits apoptosis after arsenite treatment [90].

In order to investigate if the observed role of TOPK in the cellular response to radiation was replicable with chemotherapeutic drugs, four different clinically used compounds were tested in a cell viability assay using alamarBlue® staining in HCT116 cells. Although not as sensitive as the CFA, the viability assay is a quicker way to investigate cell survival and allows the testing of multiple different drug doses in a 96-well plate format.

5-FU (fluoracil), Cisplatin, Etoposide and Vinblastine were tested on HCT116 cells in a range of concentrations to study dose-dependent effects (see Table 5.2 below). Cells were first transfected in a 6-well plate format with NT or *TOPK* siRNAs, and then transferred to a 96-well plate 48 hours post transfection. Cells were allowed to adhere for 4 hours, and then the chemotherapeutic drug was added to the medium for the following 24 hours. Finally cell viability was analysed with an alamarBlue assay using a plate reader.

| Drug | Mechanism of Action (brief description) | Tested concentration range |
|---|---|---|
| **5-FU** | Interferes with DNA synthesis by blocking the thymidylate synthetase conversion of deoxyuridylic acid to thymidylic acid. | 0 – 50 µg/ml |
| **Cisplatin** | Induction of DNA crosslinks. | 0 – 1.5 µg/ml |
| **Etoposide** | Topisomerase inhibitor, preventing ligation of the DNA strands, leading to strand breakage. | 0 – 5 µg/ml |
| **Vinblastine** | Suppressor of microtubule polymerisation. | 0 – 40.6 ng/ml |

*Table 5.2: List of the four chemotherapy compounds, a brief description of their mechanism of action, and the tested concentrations in HCT116 cells.*

The effect of these four chemotherapeutic drugs is shown in Figure 5.10.

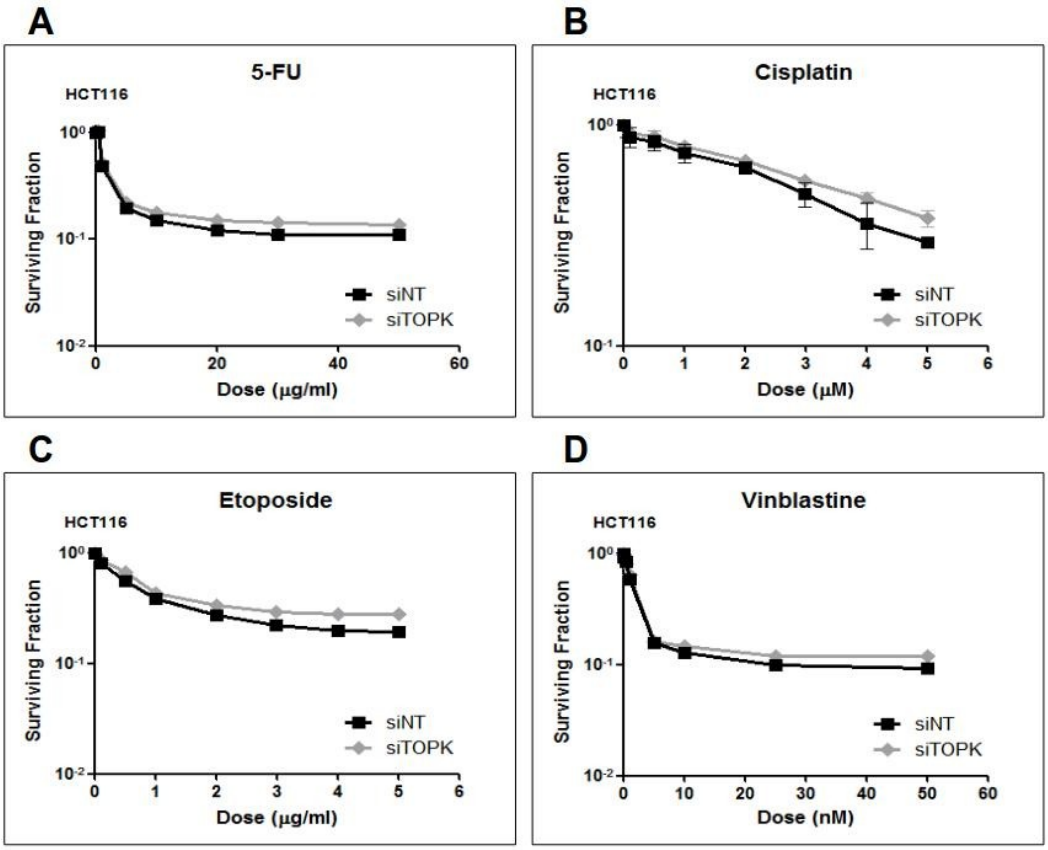


*Figure 5.10: HCT116 cells viability after siRNA TOPK depletion combined with different doses of four different chemotherapeutic drugs. (A) 5-FU was added to samples for a 24 hours incubation at a range of doses (B) The surviving fraction of siNT and siTOPK treated cells after Cisplatin administration. (C) Etoposide surviving fraction of siTOPK HCT116 cells when compared to siNT after 24 hours incubation with the drug. (D) TOPK siRNA depletion in the response to different doses of Vinblastine when compared to siNT in HCT116 cells.*

The tested concentrations for the four drugs presented in Figure 5.10 did not show any enhanced effect after TOPK depletion in HCT116 cells. This could be due to many different factors including the limited sensitivity of the alamarBlue assay and the tested concentrations for each drug, as well as differences in the mechanism of action of these drugs compared to ionising radiation. For these reasons it was decided to not proceed any further with these chemotherapeutic treatments.

## 5.3 Discussion

TOPK has been previously proposed as a clinical prognostic indicator of patient therapy outcome. In Figure 5.1 prognostic data from five different breast cancer patients cohorts was presented. The mRNA levels analysed showed a very solid correlation between *TOPK* expression and the hazard ratio for recurrence free survival (RFS). High levels of TOPK were shown to correlate with poor outcome in the clinic. The analysed database was chosen because of its free availability. The five cohorts included patients treated with different methods such as adjuvant tamoxifen (GSE6532, which included GSE6532Oxf, GSE6532KI, GSE6532GUY and 77 patients from the GSE9195 cohort) [94], radiotherapy (248 patients out of the GSE2034 cohort) [95], and adjuvant tamoxifen or chemotherapy (104 patients from GSE1456) [96]. The treatment heterogeneity of the analysed cohorts made it difficult to determine whether the effect was treatment-dependent and made it impossible to produce a radiation-only correlation between levels of TOPK and clinical outcome. A total of 1050 patients were analysed and the summary effect estimation was 3.535 at 95% confidence interval (CI) 2.330-5.364, suggesting a strong correlation between levels of TOPK and poor clinical outcome.

Immunohistochemistry analysis of TOPK expression has been previously published, showing correlations between levels of TOPK and clinical outcome. Most published papers have found that high levels of TOPK correlate with adverse outcome to therapy in many different cancer types, as previously discussed. At the time of writing, only two papers showed an opposite trend. In one of these papers, TOPK was shown to favour survival in cholangiocarcinoma by modifying the median survival form 8 months to 14 months in patients with high levels of TOPK [133], although this study was performed on a relatively small cohort of patients (n=24). A second published paper suggested a positive correlation between high levels of TOPK and prognosis in a multivariate analysis (n=287). High levels

of TOPK combined with young age (<57), smoking habit, and poorly or moderately differentiated tumour led to a significantly improved survival [134]. In contrast, TOPK has been demonstrated to correlate with poor prognosis in prostate cancer, especially in patients with Gleason score ≥ 8 (p=0.0016), PSA > 20 ng/ml (p=0.02), and stage > T2c (p=0.035) [82]. At the time of writing, to my knowledge, this thesis is the first work analysing a patient cohort receiving curative radiotherapy.

The results presented in Figure 5.3, Figure 5.4 and Figure 5.5 show that high levels of TOPK confer a poor clinical outcome in terms of recurrence-free survival and local recurrence-free survival following radiotherapy, which was more evident for total and cytoplasmic TOPK compared to nuclear TOPK. At ten years post treatment, the Kaplan-Meier graphs appeared to converge, suggesting that radiotherapy alone may be insufficient to cure many prostate cancers. Indeed, radiotherapy with concurrent androgen deprivation therapy is more effective that radiotherapy alone, and is now the “gold standard” in the clinics. Metastatic recurrence was not affected by levels of TOPK, suggesting that the observed effect on local recurrence might be radiation-specific and might not affect distant metastasis that could have formed before starting the treatment. Overall survival did not show any significant correlation with levels of TOPK. This might be due to the fact that follow-up data for the analysed prostate patients cohort did not distinguish between cancer deaths and any-cause deaths, and there were few deaths overall. Therefore it is not possible to state whether TOPK might have influenced the overall cancer-specific survival. These findings suggest that changes in *TOPK* expression may potentially be useful clinically as a biomarker predictive of local recurrence in prostate cancer patients treated with radiotherapy. These results may also suggest that modulation of TOPK might influence radiosensitivity in prostate cancer.

In order to be able to investigate modulation of radiosensitivity and a possible role for TOPK *in vivo* in future studies, an shRNA stable knockdown HCT116 cell line was developed (Figure 5.1) and two TOPK inhibitors were investigated. HI-TOPK-032 has been published to cause cell death at 5-10 μM in HCT116 cells *in vitro* [81], [129], [137]. Here it was shown to be highly toxic already at 2 and 3 μM in unirradiated cells not expressing TOPK. In the same cell line, 70 nM of the OTS964 inhibitor did not cause an anomalous decrease in plating efficiency, suggesting OTS964 to be the best TOPK inhibitor for radiation-response studies (Figure 5.1 and Figure 5.1). OTS964 was used in a CFA and showed radiosensitising effects in HCT116 and SQ20B cancer cell lines, but no effect was observed in HFL-1 and MRC5 normal cells (Figure 5.9) which is in agreement with the tumour-specific radiosensitisation observed after siRNA treatment.

The development of an HCT116 shRNA stable knockdown cell line would allow tumour growth and progression to be studied in mice. However, the level of *TOPK* knockdown is not as good as the knockdown observed with siRNA treatment. To solve this issue a possible approach could be to use the same stably knocked-down cell line for a further lentiviral transfection, which could reduce further the levels of expressed *TOPK* further. In addition, a colony-selection approach could be undertaken to select single cells with low levels of *TOPK* expression. Another problem with shRNA is the potential loss of knockdown or suppressor mutations in daughter generations of cells. *In vivo* pilot experiments could be performed in order to monitor xenograft growth differences and radiation response. An alternative solution to the incomplete knockdown achieved via shRNA would be the use of CRISPR/Cas9 to induce a stable knock-out.

The OTS964 TOPK inhibitor was shown to be a reasonably specific kinase inhibitor which causes tumour regression following treatment in mouse models. The inhibitor could be delivered to mice

intravenously (IV) or by gavage, and the working concentration should be optimised *in vivo* before investigating the radiation response after treatment.

As part of the mechanistic investigation of the role of TOPK and to evaluate its clinical potential, chemotherapeutic drugs were tested in HCT116 cells lacking TOPK expression. These experiments (Figure 5.10) did not show any significant TOPK-dependent changes in the cellular response in terms of surviving fractions. This confirmed that the observed sensitisation is ionising radiation dependent, suggesting a role for TOPK in the radiation response but not in the response to chemotherapeutic compounds. There could be multiple reasons behind this lack of sensitisation to chemotherapeutic drugs after TOPK depletion, including a difference in the mechanisms of action of the tested molecules compared to ionising radiation or the experimental set up. TOPK has been previously shown to alter the response to other DNA damaging agents including doxorubicin [88], [89], arsenite [90] and UV radiation [91] and therefore other agents might show a different effect.

# CHAPTER 6

# GENERAL DISCUSSION

## 6.1 Summary of findings

The goal of this thesis was to discover and validate novel molecular determinants of tumour radiosensitivity. This approach aimed to identify genes that could be targeted to modify the response to radiation in the clinic in order to widen the therapeutic window and allow tumour control.

Starting from a previously published high-throughput screen of 709 siRNAs targeting kinases [64], four possible candidate genes were selected for their ability to cause radiosensitivity after knockdown, *CSF1R*, *EPHB2*, *GAK* and *TOPK*. The criteria for candidate gene selection were novelty in the context of radiosensitivity, a differential expression in tumour cells compared to normal tissues, and the availability of reagents for expanded studies. After a preliminary validation of these four genes in cancer cell lines, siRNA-mediated knockdown of *TOPK* and *GAK* were shown to induce greater levels of radiosensitisation compared to *CSF1R* and *EPHB2* knockdown. Two normal tissue cell types were also tested in a CFA format to verify the effects of *GAK* and *TOPK* knockdown in normal tissues. In summary, only TOPK depletion was shown to radiosensitise a panel of different cancer cell lines including HeLa, SQ20B, T24, HCT116, H1299, DU145 and PC3 with no radiosensitising effect on normal tissue cell lines such as HFL-1 and MRC5. Based on the Oncomine 3.0 database [75] and the immunoblotting analysis of different cell lysates, *TOPK* was shown to only be expressed in cancer tissues and not in the normal tissues tested. From these experiments *TOPK* was chosen as the candidate for further investigation as a modulator of radiosensitivity with potential clinical applications.

A *TOPK* knock-out cell line (HAP1 TOPK k.o.) was purchased and shown to be radiosensitised when compared to the parental HAP1 WT cell line. This result, together with deconvolution CFAs performed in

HCT116 cells, using two different siRNA strands targeting different regions of the gene, suggested that the radiosensitivity was not induced by off-target effects.

In order to investigate the role of TOPK in the response to ionising radiation and to characterise the mechanism conferring impaired survival, the early DNA damage response was investigated by quantification of γ-H2AX and 53BP1 foci. These foci were monitored from 0.5 hours to 24 hours post 4 Gy IR, and a COMET assay was also performed in order to investigate changes in the levels of DNA damage repair. A statistically significant difference in the average number of foci per cell was only detected at 30 minutes but not at the later time points, and no detectable differences were noted in DNA damage with the COMET assay analysis.

Cell cycle modifications were next investigated. Cell cycle profiling outlined differences for TOPK-depleted cells, including a slower $G_1$/S transition and lack of a $G_2$/M arrest after IR. A role for TOPK in cell cycle progression has been described previously [79], [91], [138], and therefore a slower progression through the the cell cycle was expected in TOPK-depleted cells. Radiation caused a clear difference in checkpoint activation, with a fewer cells arresting in $G_2$/M following TOPK depletion, possibly as a result of the failure to activate the $G_2$/M checkpoint by phosphorylation of CDK1. This result suggests a malfunctioning of IR-induced checkpoint activation, which depends on TOPK levels. Levels of expression of phospho-TOPK, cyclin E1 and B1, phospho-histone H3, and phospho-CDK1 were also studied via immunoblotting and showed differences depending on the cell-cycle stage and the level of *TOPK* knockdown.

A role for *TOPK* in the ability to evade programmed cell death was studied by looking at levels of apoptosis and cell morphology alterations in HCT116 after *TOPK* siRNA depletion and IR. Levels of apoptosis increased after radiation in TOPK-depleted cells when

compared to the control, outlining the importance of *TOPK* as a potential target for clinical applications.

There was a significant increase in the number of multinucleated cells following TOPK depletion compared to the control, suggesting once again a crucial role for this protein in the radiation response. The presence of an increase in multinucleated cells at 72 hours after IR suggests possible mediation in mitotic catastrophe.

An IP experiment was then conducted to identify proteins that interact with TOPK after IR. The approach adopted was overexpression of a M2-flag tagging vector expressing *TOPK-Flag*, followed by IP at 8 hours post 4 Gy IR and analysis of the eluted lysates by mass spectrometry. CDKN1A (p21) was identified as an interacting partner of TOPK. The interaction was validated with different approaches and the inclusion of an unirradiated control showed that the interaction becomes stronger in the presence of radiation. To check whether this interaction was present between the endogenous proteins, further IP experiments were performed. TOPK and p21 were pulled down and immunoblotted for p21 and TOPK respectively. In both co-IPs there was a band in the elutes which increased in intensity after IR, suggesting that the interaction between TOPK and p21 is physiological, and is increased after IR.

In order to investigate the potential of using TOPK in the clinics, a prognostic meta-analysis was performed on five different early breast cancer cohorts for a total of 1050 patients. This analysis showed a strong correlation between high levels of *TOPK* mRNA expression and a higher hazard ratio for RFS, suggesting a potential for *TOPK* as a prognostic marker.

Furthermore, immunohistochemistry (IHC) was performed on prostate cancer samples from 128 patients treated with radiotherapy only to determine whether there was a statistically significant correlation

between levels of TOPK and clinical outcome. These results showed a statistically significant correlation between high levels of *TOPK* expression and a poorer clinical outcome in terms of local recurrence. This was mostly evident for total TOPK and cytoplasmic TOPK. Metastatic recurrence-free survival did not seem to be different for low or high levels of TOPK. From the analysed cohort it was not possible to determine a correlation between levels of TOPK and total overall survival.

Clinical data about TOPK have previously shown a correlation with adverse outcomes in terms of overall survival and recurrence free survival, identifying TOPK as a prognostic marker in breast cancer patients [77]. In non-small-cell lung cancer (NSCLC) TOPK expression has been associated with histological type, lymph node metastasis and cancer stage (TNM) and tumours positive for both TOPK and Ki67 or TOPK and mutant p53 had a significantly poorer prognosis [78], [79]. Another study in NSCLC confirmed a correlation between high levels of TOPK with low overall survival and disease-free survival and showed that high levels of TOPK paired with low levels of PTEN give an even poorer survival [80]. In colorectal cancer (CRC) patients TOPK was found to be overexpressed and to positively correlate with *KRAS* or *BRAF* mutations. Among patients with *KRAS* or *BRAF* mutations, those with diffuse TOPK staining had a significantly worse prognosis [84]. In colorectal cancer, levels of TOPK have also been correlated with levels of interlukin-8 (IL-8 or CXCL8) and as a consequence with poorer prognosis [83]. In prostate cancer a strong correlation with the advanced grade of cancer, metastasis and invasiveness and levels of TOPK were identified [81], [82].

In order to facilitate future *TOPK* studies in mice models, two different methods of disrupting *TOPK* activity were investigated: shRNA silencing and kinase inhibition. The obtained HCT116 shRNA stable *TOPK* knockdown cell line was tested in a colony formation assay, and

radiosensitisation was observed due to the low level of *TOPK* expression. Two different TOPK inhibitors have been described previously, HI-TOPK-032 [81], [129], [137] and OTS964 [111], and were tested in the context of IR. HI-TOPK-032 caused off-target effects which significantly reduced cell viability in the HAP1 TOPK k.o. cell line. In contrast, OTS964 had no radiosensitising effect in HAP1 TOPK k.o. cells, and showed significant radiosensitisation in a panel of cancer cell lines including HCT116 and SQ20B, but no effect on normal tissue cells such as HFL-1 and MRC5.

Finally, in order to test whether the observed effects were strictly dependent on IR-induced damage, and to test whether *TOPK* could be exploited in the clinic in combination with chemotherapeutic drugs, a set of four commonly used chemotherapeutic drugs including 5-FU, Cisplatin, Etoposide and Vinblastine were also tested *in vitro* in HCT116 cells in which TOPK was depleted. *TOPK* siRNA silencing in HCT116 did not show any chemosensitisation for the four tested compounds.

## 6.2 Significance of findings

Although *CSF1R* and *EPHB2* were not investigated in detail in this thesis due to insufficient radiosensitisation following knockdown in some of the cancer cell lines tested, their role as modulators of radiosensitivity could be studied in the context of different cancer types. It is possible that depletion of these genes could be an effective therapy in particular cancer types. GAK depletion showed a small radiosensitisation in the two normal cell lines tested which was not observed for *TOPK,* and data on the Oncomine 3.0 database showed *GAK* to be overexpressed in only two cancer types and underexpressed in at least four, whereas *TOPK* is overexpressed in most cancers suggesting a possible correlation between *TOPK* expression and cancer disease. Therefore *GAK* is unlikely to be a suitable candidate for future study. *CSF1R* is overexpressed in seven of the total number of considered cancers and is underexpressed in three of them including bladder cancer. This might explain why CFAs did not show radiosensitisation nor gene knockdown in the T24 bladder cancer cell line. *EPHB2* is overexpressed in the majority of the considered cancers and is underexpressed in two.

At the time of writing no studies have been published investigating the role of *TOPK* in the context of ionising radiation *in vitro* or *in vivo*.

CFAs were performed on a panel of different cancer cell lines and always revealed that TOPK depletion or inhibition influences survival after IR. CFA was also performed on DLD1 (colorectal cancer) and A549 (lung carcinoma) cell lines which did not show radiosensitisation despite a good level of *TOPK* knockdown (data not shown). Fewer normal tissue cell lines were tested because many do not form suitable colonies or are difficult to transfect, so are not useful for CFAs. The mechanistic investigation of the role of TOPK in modulating radiosensitivity was performed solely on the HCT116 colorectal cancer

cell line. This was chosen because of its high levels of *TOPK* expression and its ease of use *in vitro* and *in vivo*. Future studies should include the confirmation of the observed results in different cancer and normal tissue cell lines and using a TOPK inhibitor instead of siRNA knockdown.

The observed modulation of radiosensitivity was linked to cell cycle modifications. In order to better characterise the TOPK-dependent modifications of the $G_1$/S transition and checkpoint activation a deeper investigation would be needed, for example by looking at levels of phosphorylation of other CDKs including CDK2, CDK4/6. These experiments could also provide a better understanding on the modality of delaying $G_1$ exit in TOPK depleted cells. Given that TOPK-depletion inhibits CDK1 phosphorylation, it is possible that it also affects phosphorylation of other CDKs.

TOPK depleted cells showed increased levels of apoptosis and an increased number of multinucleated cells. These results suggest, once again, a role for TOPK in mitosis and suggest that cells lacking TOPK might undergo aberrant mitosis under unstable conditions, producing multinucleated daughter cells which will undergo apoptosis and mitotic catastrophe 3-6 days post IR. The roles of checkpoint activation and coordinated cell-cycle progression are known to be a crucial characteristic for cells to avoid the accumulation of potentially lethal mutations [46], [49]. Mitotic catastrophe typically occurs between 2-6 days after IR as the result of aberrant mitosis which produces atypical chromosome division and therefore modified nuclear morphology. This phenomenon has been suggested to occur after DNA damage with deficient cell cycle checkpoints or after hyperamplification of centrosomes [114].

A further experiment which would allow characterisation of the formation of multinucleated cells and the consequent increase in mitotic catastrophe would be to continuously monitor the cellular

behaviour via live cell imaging. This technique allows the division of cells to be studied over time. If H2B-GFP is expressed in the cells, chromatin condensation and nuclear division can be studied, allowing the different stages of mitosis to be defined. TOPK has been proposed to be involved in the mitotic checkpoint, in prophase, metaphase and also in cytokinesis [72], [86], [87], [108]–[110]. Live cell imaging could give a clearer idea of its role during mitosis. This technique could include overexpression of a fluorescently tagged TOPK plasmid to locate the protein inside the nucleus at each stage of the cell cycle. Furthermore, chromosomal morphology during mitosis could be investigated using metaphase spreads to get an insight of the role of TOPK in mitosis and to the cause of mitotic catastrophe in the absence of TOPK.

Most tumours have a mutated p53 status with consequent loss of their pro-apoptotic mechanisms [114]. Furthermore, uncontrolled proliferative capacity is considered to be one of the hallmarks of cancer [46], [49]. For these reasons, the observation of increased levels of apoptosis and impaired cell-cycle progression in TOPK-depleted cells suggest the potential of targeting TOPK for application in the clinic [114].

The interaction of TOPK with CDKN1A (p21) is a novel discovery and could be a possible explanation to the observed checkpoint inhibition and radioresponse. The physical interaction between TOPK and p21 after irradiation has never been described before and is a fundamental step in the understanding of the mechanisms of action of TOPK and a further step in the characterization of an important player for the tumour development such as p21. The observed increase in this interaction after IR could be due to the increased levels of p21 after IR [24], [53], [57]. The fact that TOPK interacts with p21 and the interaction is favoured by radiation could be linked to the observed radiosensitivity in TOPK-depleted cells. TOPK could be

altering p21 activity and, as a consequence, the cellular response to radiation leading to a difference in cell survival.

A further experiment to investigate whether the TOPK-p21 interaction is the main cause for the observed radiosensitivity would be to perform a CFA in HCT116 cells in which p21 is knocked-out (HCT116 $p21^{-/-}$). If in this cell line depletion of TOPK does not induce any further radiosensitisation compared to p21 depletion alone, that would suggest that TOPK modulates radiosensitivity solely through p21 interaction. Although, this approach might be misleading since HCT116 $p21^{-/-}$ cells might develop alternative pathways to deal with DNA damage in the lack of p21 and be viable.

Furthermore, the identified TOPK-p21 interaction did not investigate which domain of both proteins physically interact. In order to do that, an IP experiment with truncated proteins being overexpressed could be performed. Knowing the interacting regions could give a better insight about the function of the interaction between TOPK and p21.

A simplified graphical description of a possible role for TOPK in HCT116 cells in the response to IR leading to cell death is presented in Figure 6.1.

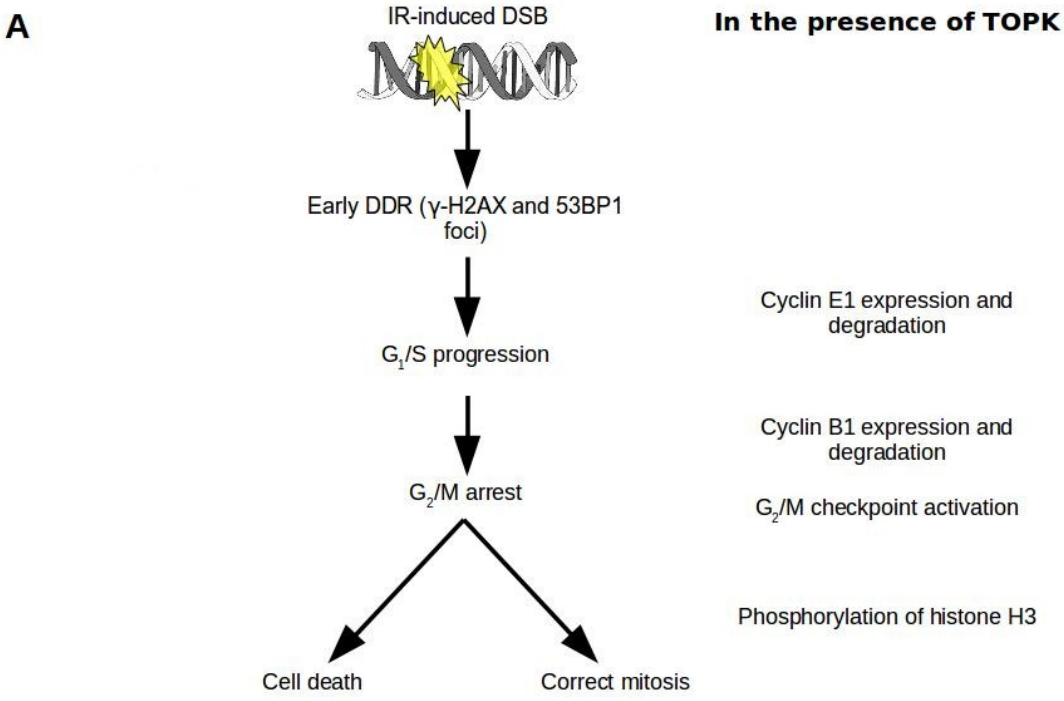
A
IR-induced DSB
In the presence of TOPK
Early DDR (γ-H2AX and 53BP1 foci)
G1/S progression
Cyclin E1 expression and degradation
Cyclin B1 expression and degradation
G2/M arrest
G2/M checkpoint activation
Phosphorylation of histone H3
Cell death
Correct mitosis

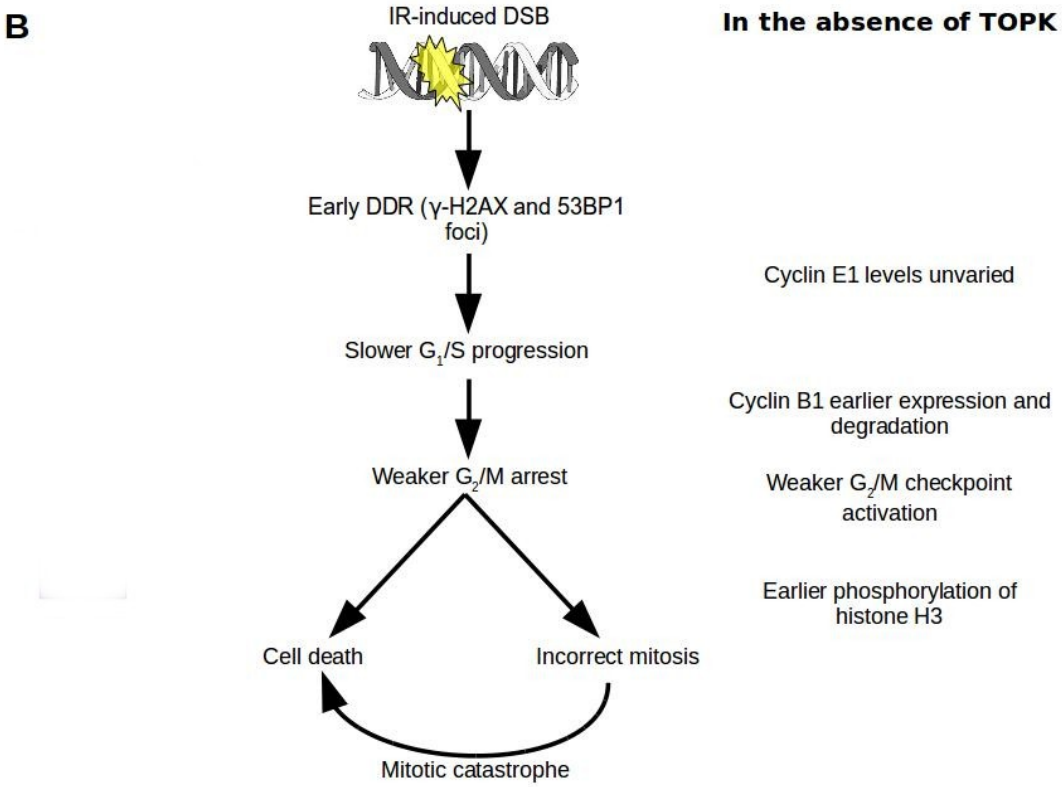


*Figure 6.1: Schematic representation of the role of TOPK in HCT116 cells. (A) The cellular response to radiation in HCT116 expressing cells. (B) The cellular response to IR-induced DNA damage in HCT116 cells where TOPK was depleted via siRNA.*

Figure 6.1A shows a simplified graphical description of the IR-induced DNA damage response in HCT116 normally expressing *TOPK*. The damage triggers the early set of events which characterise the DDR including γ-H2AX and 53BP1 foci formation and p53-dependent expression of p21 [10], [21]. Cyclin E1 is expressed and degraded in order to regulate transition from $G_1$ to the S phase of the cell cycle for cells that are ready to undergo DNA replication. At about 8 hours after 4 Gy IR, cells undergo $G_2$/M arrest to prevent mitosis and check that the DNA has been repaired and fully replicated. This process is regulated by cyclin B1. At this stage TOPK is bound to p21 and phosphorylated, favouring CDK1 phosphorylation. Phosphorylation of

histone H3 marks entry into mitosis of cells with correctly replicated DNA.

In the absence of TOPK (Figure 6.1B), despite an intact early DDR response, cyclin E1 expression remains constant, and the $G_1$/S progression is slower. Cyclin B1 is expressed earlier and the absence of TOPK inhibits phosphorylation of CDK1. The $G_2$/M checkpoint is inactive and cells undergo early mitosis as phosphorylation of histone H3 shows. Early mitosis of cells carrying unrepaired DNA damage leads to the formation of multinucleated cells which undergo mitotic catastrophe at 72 hours post IR. This difference in cell viability leads to the observed radiosensitisation in CFAs.

These results suggest a mechanistic role for TOPK in the radiation response in terms of cell cycle modifications, with altered entry into mitosis, and therefore decreased levels of cell death. In tumours, high levels of TOPK might prevent a positive response to radiation damage with a consequent tumour resistance and a poorer clinical outcome.

One of the reasons that *TOPK* is an attractive candidate as a clinical modulator of radioresponse is its differential expression between normal and cancerous tissues. It has been shown that *TOPK* is expressed only in testis and placenta [71]–[74] and is upregulated in most cancers [75], [76].

The presented prognostic data made it difficult to determine if the observed prognostic potential for *TOPK* was treatment-dependent and made it impossible to have a radiation-only correlation between levels of TOPK and clinical outcome because of the treatment heterogeneity of the analysed cohorts. A clearer analysis would involve a cohort including only radiation treated patients.

Immunohistochemistry analysis of a cohort of 128 patients showed a strong correlation between high levels of TOPK and a poorer recurrence-free survival and local recurrence-free survival. These data

suggest, once again, a role for TOPK in modulating the response to clinical radiation in patients with prostate cancer.

In order to further understand if *TOPK* can be successfully targeted in the clinic for cancer treatment, an *in vivo* characterisation is necessary. Xenograft mice models could be used to study the effects of TOPK depletion using either the stable knockdown cell line produced or the OTS964 inhibitor. The shRNA HCT116 cell line had a weak knockdown and this affected radiosensitivity *in vitro*. An inducible knockdown could be a better model to control off-target effects. The inhibitor (OTS964) has been used in the past for *in vivo* experiments [111] and is a promising tool. Although some optimisation will be needed to determine working concentrations and avoid excessive toxicity. These two tools for *in vivo* studies will be validated in mice models. Both of these approaches have wide applications *in vivo* allowing xenograft formation with shRNA TOPK-depleted cells or drug administration to inhibit TOPK activity in mice models. The key experiment *in vivo* will be to assess tumour growth delay in combination with radiation. Four groups will be used for this experiment; control, OTS964 alone, IR alone and the combination of OTS964 and IR. HCT116 xenografts should be the ideal model for this experiment.

Mechanistic *in vitro* studies were performed using siRNA depletion of TOPK and not the inhibitor or the shRNA. This decision was made because of the ease of transfecting HCT116 cells and the consistently high level of knockdown achieved with this technique. In order to use the inhibitor for mechanistic studies a further optimisation of its working conditions might be needed together with the identification of a suitable substrate effect which could be used to monitor the effectiveness of TOPK inhibition. These experiments will be essential if the OTS964 inhibitor is to be used *in vivo* or in the clinic.

## 6.3 Concluding remarks

This study focused on *TOPK* and its modulation of radiosensitivity. *CSF1R*, *EPHB2*, *GAK* and other genes were identified in the screen as well and will be considered for further investigation in the future.

This thesis added a further step to the research about *TOPK* by exploring the roles of this gene in the context of radiation.

*TOPK* is a novel regulator of radiosensitivity with enormous potential. Further *in vitro* investigation is needed to fully understand how it is involved in the cellular mechanisms that lead to the cancerous phenotype. Furthermore, *in vivo* experiments will confirm or dispute the importance of this gene in the response to radiation. Finally, a positive response to a TOPK inhibitor in clinical trials will be needed to confirm that a new target for radiotherapy has been discovered which will contribute to improve tumour control and to enhance patient treatment.

# REFERENCES


[1] ‘Worldwide cancer statistics | Cancer Research UK’. [Online]. Available: http://www.cancerresearchuk.org/health-professional/worldwide-cancer-statistics. [Accessed: 02-Mar-2016].

[2] J.-F. Bosset, L. Collette, G. Calais, L. Mineur, P. Maingon, L. Radosevic-Jelic, A. Daban, E. Bardet, A. Beny, J.-C. Ollier, and EORTC Radiotherapy Group Trial 22921, ‘Chemotherapy with preoperative radiotherapy in rectal cancer.’, *N. Engl. J. Med.*, vol. 355, no. 11, pp. 1114–23, 2006.

[3] G. Delaney, S. Jacob, C. Featherstone, and M. Barton, ‘The role of radiotherapy in cancer treatment: estimating optimal utilization from a review of evidence-based clinical guidelines.’, *Cancer*, vol. 104, no. 6, pp. 1129–37, Sep. 2005.

[4] ‘Cancer Statistics for the UK | Cancer Research UK’. [Online]. Available: http://www.cancerresearchuk.org/health-professional/cancer-statistics#heading-Zero. [Accessed: 02-Mar-2016].

[5] N. Choices, ‘Radiotherapy - NHS Choices’.

[6] C. R. UK, ‘Radiotherapy’. Cancer Research UK, 02-Oct-2016.

[7] B. Fisher, S. Anderson, J. Bryant, R. G. Margolese, M. Deutsch, E. R. Fisher, J.-H. Jeong, and N. Wolmark, ‘Twenty-year follow-up of a randomized trial comparing total mastectomy, lumpectomy, and lumpectomy plus irradiation for the treatment of invasive breast cancer.’, *N. Engl. J. Med.*, vol. 347, no. 16, pp. 1233–1241, 2002.

[8] J. S. Temel, J. A. Greer, A. Muzikansky, E. R. Gallagher, S. Admane, V. A. Jackson, C. M. Dahlin, C. D. Blinderman, J. Jacobsen, W. F. Pirl, J. A. Billings, and T. J. Lynch, ‘Early palliative care for patients with metastatic non-small-cell lung cancer.’, *N. Engl. J. Med.*, vol. 363, no. 8, pp. 733–42, 2010.

[9] B. Borgelt, R. Gelber, S. Kramer, L. W. Brady, C. H. Chang, L. W. Davis, C. A. Perez, and F. R. Hendrickson, ‘The palliation of brain metastases: Final results of the first two studies by the radiation therapy oncology group’, *Int. J. Radiat. Oncol.*, vol. 6, no. 1, pp. 1–9, 1980.

[10] M. Joiner and  a Van Der Kogel, *Basic Clinical Radiobiology Fourth Edition*. 2009.

[11] B. Halliwell and O. I. Aruoma, ‘DNA damage by oxygen-derived species’, *Febs*, vol. 281, no. April, pp. 9–19, 1991.

[12] M. Olcina and E. Hammond, ‘Hypoxia and the DNA Damage Response’, in *Hypoxia and Cancer SE - Cancer Drug Discovery and Development*, 2014, pp. 21–41.

[13] J. W. Harper and S. J. Elledge, ‘The DNA Damage Response: Ten Years After’, *Mol. Cell*, vol. 28, no. 5, pp. 739–745, 2007.

[14] E. M. Hammond and A. J. Giaccia, ‘The role of p53 in hypoxia-induced apoptosis’, *Biochemical and Biophysical Research Communications*, 2005. .

[15] C. J. Norbury and B. Zhivotovsky, ‘DNA damage-induced apoptosis.’, *Oncogene*, vol. 23, no. 16, pp. 2797–2808, 2004.

[16] J. Hall and Amato J. Giaccia, *Radiobiology for the Radiologist 7th edition*, 7th ed. Cambridge University Press, 2012.

[17] J. F. Ward, ‘DNA damage produced by ionizing radiation in mammalian cells: identities, mechanisms of formation, and reparability.’, *Progress in nucleic acid research and molecular biology*, vol. 35. pp. 95–125, 1988.

[18] B. Alberts, A. Johnson, J. Lewis, M. Raff, K. Roberts, and P. And Walter, *Molecular Biology of the Cell*, vol. 54. 2008.

[19] A. Ciccia and S. J. Elledge, ‘The DNA Damage Response: Making It Safe to Play with Knives’, *Molecular Cell*, vol. 40, no. 2. pp. 179–204, 2010.

[20] A. J. Morrison and X. Shen, ‘DNA repair in the context of chromatin’, *Cell Cycle*, vol. 4, no. 4. pp. 568–571, 2005.

[21] E. C. Friedberg, G. Walker, W. Siede, R. Wood, R. Shultz, and T. Ellenberger, *DNA repair and mutagenesis*, Second edi. ASM Press, 2006.

[22] T. a. Chan, P. M. Hwang, H. Hermeking, K. W. Kinzler, B. Vogelstein, H. Zhang, Y. Xiong, and D. Beach, ‘Cooperative effects of genes controlling the G2/M checkpoint’, *Genes Dev.*, vol. 4, no. 13, pp. 1584–1588, 1993.

[23] E. C. Friedberg, ‘DNA damage and repair.’, *Nature*, vol. 421, no. 6921, pp. 436–40, 2003.

[24] F. Bunz, a Dutriaux, C. Lengauer, T. Waldman, S. Zhou, J. P. Brown, J. M. Sedivy, K. W. Kinzler, and B. Vogelstein, ‘Requirement for p53 and p21 to sustain G2 arrest after DNA damage.’, *Science*, vol. 282, no. 5393, pp. 1497–1501, 1998.

[25] L. G. Mariotti, G. Pirovano, K. I. Savage, M. Ghita, A. Ottolenghi, K. M. Prise, and G. Schettino, ‘Use of the Gamma-H2AX assay to investigate DNA repair dynamics following multiple radiation exposures’, *PLoS One*, vol. 8, no. 11, pp. 1–12, 2013.

[26] M. Stucki and S. P. Jackson, ‘gamma-H2AX and MDC1: Anchoring the DNA-damage-response machinery to broken chromosomes’, *DNA Repair*, vol. 5, no. 5. pp. 534–543, 2006.

[27] M. Shrivastav, L. P. De Haro, and J. A. Nickoloff, ‘Regulation of DNA double-strand break repair pathway choice.’, *Cell Res.*, vol. 18, no. 1, pp. 134–147, 2008.

[28] E. Sonoda, H. Hochegger, A. Saberi, Y. Taniguchi, and S. Takeda, ‘Differential usage of non-homologous end-joining and homologous recombination in double strand break repair’, *DNA Repair (Amst).*, vol. 5, no. 9–10, pp. 1021–1029, 2006.

[29] A. Kakarougkas and P. A. Jeggo, ‘DNA DSB repair pathway choice: An orchestrated handover mechanism’, *British Journal of Radiology*, vol. 87, no. 1035. 2014.

[30] T. M. Gottlieb and S. P. Jackson, ‘The DNA-dependent protein kinase: Requirement for DNA ends and association with Ku antigen’, *Cell*, vol. 72, no. 1, pp. 131–142, 1993.

[31] K. I. Yano and D. J. Chen, ‘Live cell imaging of XLF and XRCC4 reveals a novel view of protein assembly in the non-homologous end-joining pathway’, *Cell Cycle*, vol. 7, no. 10. pp. 1321–1325, 2008.

[32] S. Costantini, L. Woodbine, L. Andreoli, P. A. Jeggo, and A. Vindigni, ‘Interaction of the Ku heterodimer with the DNA ligase IV/Xrcc4 complex and its regulation by DNA-PK’, *DNA Repair (Amst).*, vol. 6, no. 6, pp. 712–722, 2007.

[33] P. A. Jeggo and M. Löbrich, ‘Artemis links ATM to double strand break rejoining’, *Cell Cycle*, vol. 4, no. 3. pp. 359–362, 2005.

[34] U. Grawunder, M. Wilm, X. Wu, P. Kulesza, T. E. Wilson, M. Mann, and M. R. Lieber, ‘Activity of DNA ligase IV stimulated by complex formation with XRCC4 protein in mammalian cells.’, *Nature*, vol. 388, no. 6641, pp. 492–495, 1997.

[35] J. Gu, H. Lu, B. Tippin, N. Shimazaki, M. F. Goodman, and M. R. Lieber, ‘XRCC4:DNA ligase IV can ligate incompatible DNA ends and can ligate across gaps.’, *EMBO J.*, vol. 26, no. 4, pp. 1010–1023, 2007.

[36] P. Fortini and E. Dogliotti, ‘Base damage and single-strand break repair: Mechanisms and functional significance of short- and long-

patch repair subpathways', *DNA Repair (Amst).*, vol. 6, no. 4, pp. 398–409, 2007.

[37] M. Seki, C. Masutani, L. W. Yang, A. Schuffert, S. Iwai, I. Bahar, and R. D. Wood, 'High-efficiency bypass of DNA damage by human DNA polymerase Q.', *EMBO J.*, vol. 23, no. 22, pp. 4484–4494, 2004.

[38] M. J. Yousefzadeh, D. W. Wyatt, K. ichi Takata, Y. Mu, S. C. Hensley, J. Tomida, G. O. Bylund, S. Doubli??, E. Johansson, D. A. Ramsden, K. M. McBride, and R. D. Wood, 'Mechanism of Suppression of Chromosomal Instability by DNA Polymerase POLQ', *PLoS Genet.*, vol. 10, no. 10, 2014.

[39] M. J. Yousefzadeh and R. D. Wood, 'DNA polymerase POLQ and cellular defense against DNA damage', *DNA Repair*, vol. 12, no. 1. pp. 1–9, 2013.

[40] T. Kent, G. Chandramouly, S. M. McDevitt, A. Y. Ozdemir, and R. T. Pomerantz, 'Mechanism of microhomology-mediated end-joining promoted by human DNA polymerase theta', *Nat Struct Mol Biol*, vol. 22, no. 3, pp. 230–237, 2015.

[41] S. Ahrabi, S. Sarkar, S. X. Pfister, G. Pirovano, G. S. Higgins, A. C. G. Porter, and T. C. Humphrey, 'A role for human homologous recombination factors in suppressing microhomology-mediated end joining', *Nucleic Acids Res.*, p. gkw326, 2016.

[42] C. Richardson, M. E. Moynahan, and M. Jasin, 'Double-strand break repair by interchromosomal recombination: Suppression of chromosomal translocations', *Genes Dev.*, vol. 12, no. 24, pp. 3831–3842, 1998.

[43] P. Turner, A. McLennan, A. Bates, and M. White, *BIOS Instant Notes Molecular Biology*, Third edit. Taylor & Francis Group, 2005.

[44] H. F. Lodish, A. Berk, S. L. Zipursky, P. Matsudaira, D. Baltimore, and D. James, *Molecular Cell Biology*, vol. 5. 2008.

[45] M. B. Kastan and J. Bartek, 'Cell-cycle checkpoints and cancer.', *Nature*, vol. 432, no. 7015, pp. 316–323, 2004.

[46] D. Hanahan, 'The Hallmarks of Cancer', *Cell*, vol. 100, no. 1. pp. 57–70, 2000.

[47] E. J. Bernhard, a Maity, R. J. Muschel, and W. G. McKenna, 'Effects of ionizing radiation on cell cycle progression. A review', *Radiat Env. Biophys*, vol. 34, pp. 79–83, 1995.

[48] A. Maity, W. G. McKenna, and R. J. Muschel, ‘The molecular basis for cell cycle delays following ionizing radiation: a review’, *Radiother. Oncol.*, vol. 31, no. 1, pp. 1–13, 1994.

[49] D. Hanahan and R. A. Weinberg, ‘Hallmarks of cancer: the next generation.’, *Cell*, vol. 144, no. 5, pp. 646–74, 2011.

[50] D. P. Lane, ‘Cancer. p53, guardian of the genome.’, *Nature*, vol. 358, no. 6381. pp. 15–16, 1992.

[51] G. Iliakis, Y. Wang, J. Guan, and H. Wang, ‘DNA damage checkpoint control in cells exposed to ionizing radiation.’, *Oncogene*, vol. 22, no. 37, pp. 5834–5847, 2003.

[52] Y. Xiong, G. J. Hannon, H. Zhang, D. Casso, R. Kobayashi, and D. Beach, ‘p21 is a universal inhibitor of cyclin kinases.’, *Nature*, vol. 366, no. 6456, pp. 701–4, 1993.

[53] O. Cazzalini, A. I. Scovassi, M. Savio, L. A. Stivala, and E. Prosperi, ‘Multiple roles of the cell cycle inhibitor p21CDKN1A in the DNA damage response’, *Mutat. Res. Mutat. Res.*, vol. 704, no. 1–3, pp. 12–20, 2010.

[54] J. W. Harper, S. J. Elledge, K. Keyomarsi, B. Dynlacht, L. H. Tsai, P. Zhang, S. Dobrowolski, C. Bai, L. Connell-Crowley, and E. Swindell, ‘Inhibition of cyclin-dependent kinases by p21.’, *Mol. Biol. Cell*, vol. 6, no. 4, pp. 387–400, 1995.

[55] T. Abbas and A. Dutta, ‘p21 in cancer: intricate networks and multiple activities.’, *Nat. Rev. Cancer*, vol. 9, no. 6, pp. 400–14, 2009.

[56] M. Hollstein, D. Sidransky, B. Vogelstein, and C. C. Harris, ‘p53 mutations in human cancers.’, *Science*, vol. 253, no. 5015, pp. 49–53, 1991.

[57] W. R. Taylor and G. R. Stark, ‘Regulation of the G2/M transition by p53.’, *Oncogene*, vol. 20, no. 15, pp. 1803–1815, 2001.

[58] B. Emami, J. Lyman, A. Brown, L. Cola, M. Goitein, J. E. Munzenrider, B. Shank, L. J. Solin, and M. Wesson, ‘Tolerance of normal tissue to therapeutic irradiation’, *Int. J. Radiat. Oncol. Biol. Phys.*, vol. 21, no. 1, pp. 109–122, 1991.

[59] L. E. Gerweck, S. Vijayappa, A. Kurimasa, K. Ogawa, and D. J. Chen, ‘Tumor cell radiosensitivity is a major determinant of tumor response to radiation’, *Cancer Res.*, vol. 66, no. 17, pp. 8352–8355, 2006.

[60] W. Lutz, J. Lowry, S. M. Kopta, D. A. Einstein, and K. I. Howard, ‘Prediction of dose-response relations based on patient characteristics’, *J. Clin. Psychol.*, vol. 57, no. 7, pp. 889–900, 2001.

[61] C. M. West, S. E. Davidson, S. A. Roberts, and R. D. Hunter, ‘The independence of intrinsic radiosensitivity as a prognostic factor for patient response to radiotherapy of carcinoma of the cervix.’, *Br. J. Cancer*, vol. 76, no. 9, pp. 1184–90, 1997.

[62] N. a P. Franken, H. M. Rodermond, J. Stap, J. Haveman, and C. van Bree, ‘Clonogenic assay of cells in vitro.’, *Nat. Protoc.*, vol. 1, no. 5, pp. 2315–9, 2006.

[63] G. S. Higgins, R. Prevo, Y.-F. F. Lee, T. Helleday, R. J. Muschel, S. Taylor, M. Yoshimura, I. D. Hickson, E. J. Bernhard, and W. G. McKenna, ‘A small interfering RNA screen of genes involved in DNA repair identifies tumor-specific radiosensitization by POLQ knockdown.’, *Cancer Res.*, vol. 70, no. 7, pp. 2984–2993, 2010.

[64] G. S. Tiwana, R. Prevo, F. M. Buffa, S. Yu, D. V Ebner, A. Howarth, L. K. Folkes, B. Budwal, K.-Y. Chu, L. Durrant, R. J. Muschel, W. G. McKenna, and G. S. Higgins, ‘Identification of vitamin B1 metabolism as a tumor-specific radiosensitizing pathway using a high-throughput colony formation screen.’, *Oncotarget*, vol. 6, no. 8, pp. 5978–5989, 2015.

[65] D. Katz, E. Ito, and F. F. Liu, ‘On the Path to Seeking Novel Radiosensitizers’, *International Journal of Radiation Oncology Biology Physics*, vol. 73, no. 4. pp. 988–996, 2009.

[66] E. Iorns, C. J. Lord, N. Turner, and A. Ashworth, ‘Utilizing RNA interference to enhance cancer drug discovery.’, *Nat. Rev. Drug Discov.*, vol. 6, no. 7, pp. 556–68, 2007.

[67] X. Liu, F. Jiang, S. Kalidas, D. Smith, and Q. Liu, ‘Dicer-2 and R2D2 coordinately bind siRNA to promote assembly of the siRISC complexes.’, *RNA*, vol. 12, no. 8, pp. 1514–1520, 2006.

[68] J. a Bonner, P. M. Harari, J. Giralt, N. Azarnia, D. M. Shin, R. B. Cohen, C. U. Jones, R. Sur, D. Raben, J. Jassem, R. Ove, M. S. Kies, J. Baselga, H. Youssoufian, N. Amellal, E. K. Rowinsky, and K. K. Ang, ‘Radiotherapy plus cetuximab for squamous-cell carcinoma of the head and neck.’, *N. Engl. J. Med.*, vol. 354, no. 6, pp. 567–78, 2006.

[69] T. Akimoto, N. R. Hunter, L. Buchmiller, K. Mason, K. K. Ang, and L. Milas, ‘Inverse relationship between epidermal growth factor receptor expression and radiocurability of murine carcinomas.’, *Clin. Cancer Res.*, vol. 5, no. 10, pp. 2884–2890, 1999.

[70] L. Milas, K. Mason, N. Hunter, S. Petersen, M. Yamakawa, K. Ang, J. Mendelsohn, and Z. Fan, ‘In vivo enhancement of tumor radioresponse by C225 antiepidermal growth factor receptor antibody’, *Clin. Cancer Res.*, vol. 6, no. 2, pp. 701–708, 2000.

[71] Y. Abe, S. Matsumoto, K. Kito, and N. Ueda, ‘Cloning and expression of a novel MAPKK-like protein kinase, lymphokine-activated killer T-cell-originated protein kinase, specifically expressed in the testis and activated lymphoid cells.’, *J. Biol. Chem.*, vol. 275, no. 28, pp. 21525–31, 2000.

[72] S. Gaudet, D. Branton, and R. A. Lue, ‘Characterization of PDZ-binding kinase, a mitotic kinase.’, *Proc. Natl. Acad. Sci. U. S. A.*, vol. 97, no. 10, pp. 5167–72, 2000.

[73] T. Fujibuchi, Y. Abe, T. Takeuchi, N. Ueda, K. Shigemoto, H. Yamamoto, and K. Kito, ‘Expression and phosphorylation of TOPK during spermatogenesis.’, *Dev. Growth Differ.*, vol. 47, no. 9, pp. 637–44, Dec. 2005.

[74] S. Matsumoto, Y. Abe, T. Fujibuchi, T. Takeuchi, K. Kito, N. Ueda, K. Shigemoto, and K. Gyo, ‘Characterization of a MAPKK-like protein kinase TOPK’, *Biochem. Biophys. Res. Commun.*, vol. 325, no. 3, pp. 997–1004, Dec. 2004.

[75] D. R. Rhodes, S. Kalyana-Sundaram, V. Mahavisno, R. Varambally, J. Yu, B. B. Briggs, T. R. Barrette, M. J. Anstet, C. Kincead-Beal, P. Kulkarni, S. Varambally, D. Ghosh, and A. M. Chinnaiyan, ‘Oncomine 3.0: genes, pathways, and networks in a collection of 18,000 cancer gene expression profiles.’, *Neoplasia*, vol. 9, no. 2, pp. 166–180, 2007.

[76] ‘Oncomine Database’. [Online]. Available: https://www.oncomine.org/resource/login.html. [Accessed: 10-Mar-2016].

[77] P. C. O Leary, S. a Penny, R. T. Dolan, C. M. Kelly, S. F. Madden, E. Rexhepaj, D. J. Brennan, A. H. McCann, F. Pontén, M. Uhlén, R. Zagozdzon, M. J. Duffy, M. R. Kell, K. Jirström, and W. M. Gallagher, ‘Systematic antibody generation and validation via tissue microarray technology leading to identification of a novel protein prognostic panel in breast cancer.’, *BMC Cancer*, vol. 13, p. 175, 2013.

[78] B. Lei, S. Liu, W. Qi, Y. Zhao, Y. Li, N. Lin, X. Xu, C. Zhi, J. Mei, Z. Yan, L. Wan, and H. Shen, ‘PBK/TOPK expression in non-small-cell lung cancer: its correlation and prognostic significance with Ki67 and p53 expression.’, *Histopathology*, vol. 63, no. 5, pp. 696–703, 2013.

[79] B. Lei, W. Qi, Y. Zhao, Y. Li, S. Liu, X. Xu, C. Zhi, L. Wan, and H. Shen, ‘PBK/TOPK expression correlates with mutant p53 and affects patients’ prognosis and cell proliferation and viability in lung adenocarcinoma’, *Hum. Pathol.*, vol. 46, no. 2, pp. 217–224, 2015.

[80] M.-C. Shih, J.-Y. Chen, Y.-C. Wu, Y.-H. Jan, B.-M. Yang, P.-J. Lu, H.-C. Cheng, M.-S. Huang, C.-J. Yang, M. Hsiao, and J.-M. Lai, 'TOPK/PBK promotes cell migration via modulation of the PI3K/PTEN/AKT pathway and is associated with poor prognosis in lung cancer.', *Oncogene*, vol. 31, no. 19, pp. 2389–400, 2012.

[81] J. D. Brown-Clay, D. N. Shenoy, O. Timofeeva, B. V Kallakury, A. K. Nandi, and P. P. Banerjee, 'PBK/TOPK enhances aggressive phenotype in prostate cancer via β-catenin-TCF/LEF-mediated matrix metalloproteinases production and invasion', *Oncotarget*, vol. 6, no. 17, pp. 15594–609, Jun. 2015.

[82] H. Sun, L. Zhang, C. Shi, P. Hu, W. Yan, Z. Wang, Q. Duan, F. Lu, L. Qin, T. Lu, J. Xiao, Y. Wang, F. Zhu, and C. Shao, 'TOPK is highly expressed in circulating tumor cells, enabling metastasis of prostate cancer', *Oncotarget*, vol. 6, no. 14, pp. 12392–404, 2015.

[83] Y.-C. Xiao, Z.-B. Yang, X.-S. Cheng, X.-B. Fang, T. Shen, C.-F. Xia, P. Liu, H.-H. Qian, B. Sun, Z.-F. Yin, and Y.-F. Li, 'CXCL8, overexpressed in colorectal cancer, enhances the resistance of colorectal cancer cells to anoikis.', *Cancer Lett.*, vol. 361, no. 1, pp. 22–32, 2015.

[84] I. Zlobec, F. Molinari, M. Kovac, M. P. Bihl, H. J. Altermatt, J. Diebold, H. Frick, M. Germer, M. Horcic, M. Montani, G. Singer, H. Yurtsever, A. Zettl, L. Terracciano, L. Mazzucchelli, P. Saletti, M. Frattini, K. Heinimann, and A. Lugli, 'Prognostic and predictive value of TOPK stratified by KRAS and BRAF gene alterations in sporadic, hereditary and metastatic colorectal cancer patients', *Br. J. Cancer*, vol. 102, no. 1, pp. 151–61, 2010.

[85] F. Zhu, T. a Zykova, B. S. Kang, Z. Wang, M. C. Ebeling, Y. Abe, W.-Y. Ma, A. M. Bode, and Z. Dong, 'Bidirectional signals transduced by TOPK-ERK interaction increase tumorigenesis of HCT116 colorectal cancer cells.', *Gastroenterology*, vol. 133, no. 1, pp. 219–31, 2007.

[86] S. R. Shinde, N. R. Gangula, S. Kavela, V. Pandey, and S. Maddika, 'TOPK and PTEN participate in CHFR mediated mitotic checkpoint.', *Cell. Signal.*, vol. 25, no. 12, pp. 2511–7, 2013.

[87] J.-H. Park, M.-L. Lin, T. Nishidate, Y. Nakamura, and T. Katagiri, 'PDZ-Binding Kinase/T-Lak Cell-Originated Protein Kinase a putative cancer/testis antigen', *Cancer research*, 2006. .

[88] F. Hu, R. B. Gartenhaus, D. Eichberg, Z. Liu, H.-B. Fang, and a P. Rapoport, 'PBK/TOPK interacts with the DBD domain of tumor suppressor p53 and modulates expression of transcriptional targets including p21.', *Oncogene*, vol. 29, no. 40, pp. 5464–74, 2010.

[89] A. K. Nandi, T. Ford, D. Fleksher, B. Neuman, and A. P. Rapoport, ‘Attenuation of DNA damage checkpoint by PBK, a novel mitotic kinase, involves protein-protein interaction with tumor suppressor p53’, *Biochem Biophys Res Commun*, vol. 358, no. 1, pp. 181–188, 2007.

[90] T. A. Zykova, F. Zhu, C. Lu, L. Higgins, Y. Tatsumi, Y. Abe, A. M. Bode, and Z. Dong, ‘Lymphokine-activated killer T-cell-originated protein kinase phosphorylation of histone H2AX prevents arsenite-induced apoptosis in RPMI7951 melanoma cells.’, *Clin. Cancer Res.*, vol. 12, no. 23, pp. 6884–93, Dec. 2006.

[91] V. Ayllón and R. O’connor, ‘PBK/TOPK promotes tumour cell proliferation through p38 MAPK activity and regulation of the DNA damage response.’, *Oncogene*, vol. 26, no. 24, pp. 3451–3461, 2007.

[92] F. M. Buffa,  a L. Harris, C. M. West, and C. J. Miller, ‘Large meta-analysis of multiple cancers reveals a common, compact and highly prognostic hypoxia metagene.’, *Br. J. Cancer*, vol. 102, no. 2, pp. 428–435, 2010.

[93] F. M. Buffa, C. Camps, L. Winchester, C. E. Snell, H. E. Gee, H. Sheldon, M. Taylor, A. L. Harris, and J. Ragoussis, ‘microRNA-associated progression pathways and potential therapeutic targets identified by integrated mRNA and microRNA expression profiling in breast cancer’, *Cancer Res.*, vol. 71, no. 17, pp. 5635–5645, 2011.

[94] S. Loi, B. Haibe-Kains, C. Desmedt, P. Wirapati, F. Lallemand, A. M. Tutt, C. Gillet, P. Ellis, K. Ryder, J. F. Reid, M. G. Daidone, M. A. Pierotti, E. M. Berns, M. P. Jansen, J. A. Foekens, M. Delorenzi, G. Bontempi, M. J. Piccart, and C. Sotiriou, ‘Predicting prognosis using molecular profiling in estrogen receptor-positive breast cancer treated with tamoxifen.’, *BMC Genomics*, vol. 9, p. 239, 2008.

[95] Y. Wang, J. G. M. Klijn, Y. Zhang, A. M. Sieuwerts, M. P. Look, F. Yang, D. Talantov, M. Timmermans, M. E. Meijer-Van Gelder, J. Yu, T. Jatkoe, E. M. J. J. Berns, D. Atkins, and J. A. Foekens, ‘Gene-expression profiles to predict distant metastasis of lymph-node-negative primary breast cancer’, *Lancet*, vol. 365, no. 9460, pp. 671–679, 2005.

[96] Y. Pawitan, J. Bjöhle, L. Amler, A.-L. Borg, S. Egyhazi, P. Hall, X. Han, L. Holmberg, F. Huang, S. Klaar, E. T. Liu, L. Miller, H. Nordgren, A. Ploner, K. Sandelin, P. M. Shaw, J. Smeds, L. Skoog, S. Wedrén, and J. Bergh, ‘Gene expression profiling spares early breast cancer patients from adjuvant therapy: derived and validated in two population-based cohorts.’, *Breast Cancer Res.*, vol. 7, no. 6, pp. R953–R964, 2005.

[97] E. Sapi, ‘The role of CSF-1 in normal physiology of mammary gland and breast cancer: an update.’, *Exp. Biol. Med. (Maywood).*, vol. 229, no. 1, pp. 1–11, 2004.

[98] R. M. Tamimi, J. S. Brugge, M. L. Freedman, A. Miron, J. D. Iglehart, G. A. Colditz, and S. E. Hankinson, ‘Circulating colony stimulating factor-1 and breast cancer risk’, *Cancer Res.*, vol. 68, no. 1, pp. 18–21, 2008.

[99] S. D. Wang, P. Rath, B. Lal, J.-P. Richard, Y. L. Li, C. R. Goodwin, J. Laterra, and S. Xia, ‘EphB2 receptor controls proliferation/migration dichotomy of glioblastoma by interacting with focal adhesion kinase’, *Cancer Res.*, vol. 72, no. 8 Supplement, pp. 4311–4311, 2012.

[100] A. H. Sikkema, W. F. A. Den Dunnen, E. Hulleman, D. G. Van Vuurden, G. Garcia-Manero, H. Yang, F. J. G. Scherpen, K. R. Kampen, E. W. Hoving, W. A. Kamps, S. H. Diks, M. P. Peppelenbosch, and E. S. J. M. De Bont, ‘EphB2 activity plays a pivotal role in pediatric medulloblastoma cell adhesion and invasion’, *Neuro. Oncol.*, vol. 14, no. 9, pp. 1125–1135, 2012.

[101] M. R. Ray, L. A. Wafa, H. Cheng, R. Snoek, L. Fazli, M. Gleave, and P. S. Rennie, ‘Cyclin G-associated kinase: A novel androgen receptor-interacting transcriptional coactivator that is overexpressed in hormone refractory prostate cancer’, *Int. J. Cancer*, vol. 118, no. 5, pp. 1108–1119, 2006.

[102] D. C. Strachan, B. Ruffell, Y. Oei, M. J. Bissell, L. M. Coussens, N. Pryer, and D. Daniel, ‘CSF1R inhibition delays cervical and mammary tumor growth in murine models by attenuating the turnover of tumor-associated macrophages and enhancing infiltration by CD8(+) T cells.’, *Oncoimmunology*, vol. 2, no. 12, p. e26968, 2013.

[103] A. M. Jubb, F. Zhong, S. Bheddah, H. I. Grabsch, G. D. Frantz, W. Mueller, V. Kavi, P. Quirke, P. Polakis, and H. Koeppen, ‘EphB2 is a prognostic factor in colorectal cancer’, *Clin. Cancer Res.*, vol. 11, no. 14, pp. 5181–5187, 2005.

[104] W. Mao, E. Luis, S. Ross, J. Silva, C. Tan, C. Crowley, C. Chui, G. Franz, P. Senter, H. Koeppen, and P. Polakis, ‘EphB2 as a Therapeutic Antibody Drug Target for the Treatment of Colorectal Cancer’, *Cancer Research*, vol. 64, no. 3. pp. 781–788, 2004.

[105] P. Huusko, D. Ponciano-Jackson, M. Wolf, J. a Kiefer, D. O. Azorsa, S. Tuzmen, D. Weaver, C. Robbins, T. Moses, M. Allinen, S. Hautaniemi, Y. Chen, A. Elkahloun, M. Basik, G. S. Bova, L. Bubendorf, A. Lugli, G. Sauter, J. Schleutker, H. Ozcelik, S. Elowe, T. Pawson, J. M. Trent, J. D. Carpten, O.-P. Kallioniemi, and S. Mousses, ‘Nonsense-mediated decay

microarray analysis identifies mutations of EPHB2 in human prostate cancer.', *Nat. Genet.*, vol. 36, no. 9, pp. 979–83, 2004.

[106] M. E. Tanenbaum, T. Vallenius, E. F. Geers, L. Greene, T. P. M??kel??, and R. H. Medema, 'Cyclin G-associated kinase promotes microtubule outgrowth from chromosomes during spindle assembly', *Chromosoma*, vol. 119, no. 4, pp. 415–424, 2010.

[107] L. Zhang, O. Gjoerup, and T. M. Roberts, 'The serine/threonine kinase cyclin G-associated kinase regulates epidermal growth factor receptor signaling.', *Proc. Natl. Acad. Sci. U. S. A.*, vol. 101, no. 28, pp. 10296–301, 2004.

[108] R. Rizkallah, P. Batsomboon, G. B. Dudley, and M. M. Hurt, 'Identification of the oncogenic kinase TOPK / PBK as a master mitotic regulator of C2H2 zinc finger proteins', *Oncotarget*, vol. 6, no. 3, pp. 1446–61, 2015.

[109] J.-H. Park, T. Nishidate, Y. Nakamura, and T. Katagiri, 'Critical roles of T-LAK cell-originated protein kinase in cytokinesis.', *Cancer Sci.*, vol. 101, no. 2, pp. 403–11, 2010.

[110] Y. Abe, T. Takeuchi, L. Kagawa-Miki, N. Ueda, K. Shigemoto, M. Yasukawa, and K. Kito, 'A mitotic kinase TOPK enhances Cdk1/cyclin B1-dependent phosphorylation of PRC1 and promotes cytokinesis.', *J. Mol. Biol.*, vol. 370, no. 2, pp. 231–45, 2007.

[111] Y. Matsuo, J.-H. Park, T. Miyamoto, S. Yamamoto, S. Hisada, H. Alachkar, and Y. Nakamura, 'TOPK inhibitor induces complete tumor regression in xenograft models of human cancer through inhibition of cytokinesis.', *Sci. Transl. Med.*, vol. 6, no. 259, p. 259ra145, 2014.

[112] F. D. Sigoillot, S. Lyman, J. F. Huckins, B. Adamson, E. Chung, B. Quattrochi, and R. W. King, 'A bioinformatics method identifies prominent off-targeted transcripts in RNAi screens.', *Nat. Methods*, vol. 9, no. 4, pp. 363–6, 2012.

[113] J. H. Park, D. S. Yoon, H. J. Choi, D. H. Hahm, and S. M. Oh, 'Phosphorylation of IκBβ at serine 32 by T-lymphokine-activated killer cell-originated protein kinase is essential for chemoresistance against doxorubicin in cervical cancer cells', *J. Biol. Chem.*, vol. 288, no. 5, pp. 3585–3593, 2013.

[114] D. Eriksson and T. Stigbrand, 'Radiation-induced cell death mechanisms', *Tumor Biology*, vol. 31, no. 4. pp. 363–372, 2010.

[115] R. Hesketh, *Introduction to cancer biology*. Cambridge University Press, 2013.

[116] E. L. Leatherbarrow, J. V. Harper, F. A. Cucinotta, and P. O'Neill, 'Induction and quantification of gamma-H2AX foci following low and high LET-irradiation.', *Int. J. Radiat. Biol.*, vol. 82, no. 2, pp. 111–8, 2006.

[117] L. D. Attardi, A. de Vries, and T. Jacks, 'Activation of the p53-dependent G1 checkpoint response in mouse embryo fibroblasts depends on the specific DNA damage inducer.', *Oncogene*, vol. 23, pp. 973–980, 2004.

[118] H. T. Ma and R. Y. C. Poon, 'Synchronization of hela cells', *Methods Mol. Biol.*, vol. 761, pp. 151–161, 2011.

[119] F. Hans and S. Dimitrov, 'Histone H3 phosphorylation and cell division.', *Oncogene*, vol. 20, no. 24, pp. 3021–3027, 2001.

[120] H. Vakifahmetoglu, M. Olsson, and B. Zhivotovsky, 'Death through a tragedy: mitotic catastrophe.', *Cell Death Differ.*, vol. 15, no. 7, pp. 1153–1162, 2008.

[121] I. Vermes, C. Haanen, H. Steffens-Nakken, and C. Reutelingsperger, 'A novel assay for apoptosis. Flow cytometric detection of phosphatidylserine expression on early apoptotic cells using fluorescein labelled Annexin V', *J. Immunol. Methods*, vol. 184, no. 1, pp. 39–51, 1995.

[122] M. Brosch, L. Yu, T. Hubbard, and J. Choudhary, 'Accurate and sensitive peptide identification with mascot percolator', *J. Proteome Res.*, vol. 8, no. 6, pp. 3176–3181, 2009.

[123] S. Bursomanno, J. F. McGouran, B. M. Kessler, I. D. Hickson, and Y. Liu, 'Regulation of SUMO2 target proteins by the proteasome in human cells exposed to replication stress', *J. Proteome Res.*, vol. 14, no. 4, pp. 1687–1699, 2015.

[124] F. Lamoliatte, E. Bonneil, C. Durette, O. Caron-Lizotte, D. Wildemann, J. Zerweck, H. Wenshuk, and P. Thibault, 'Targeted identification of SUMOylation sites in human proteins using affinity enrichment and paralog-specific reporter ions.', *Mol. Cell. Proteomics*, vol. 12, no. 9, pp. 2536–50, 2013.

[125] D. K. Morrison, 'The 14-3-3 proteins: integrators of diverse signaling cues that impact cell fate and cancer development', *Trends in Cell Biology*, vol. 19, no. 1. pp. 16–23, 2009.

[126] H. Hermeking and A. Benzinger, '14-3-3 proteins in cell cycle regulation', *Seminars in Cancer Biology*, vol. 16, no. 3. pp. 183–192, 2006.

[127] K. Ozato, D.-M. Shin, T.-H. Chang, and H. C. Morse, ‘TRIM family proteins and their emerging roles in innate immunity.’, *Nat. Rev. Immunol.*, vol. 8, no. 11, pp. 849–860, 2008.

[128] ‘http://www.genecards.org/cgi-bin/carddisp.pl?gene=CDKN1A’. .

[129] D. J. Kim, Y. Li, K. Reddy, M. H. Lee, M. O. Kim, Y. Y. Cho, S. Y. Lee, J. E. Kim, A. M. Bode, and Z. Dong, ‘Novel TOPK inhibitor HI-TOPK-032 effectively suppresses colon cancer growth’, *Cancer Res.*, vol. 72, no. 12, pp. 3060–3068, 2012.

[130] G. Soria, J. Speroni, O. L. Podhajcer, C. Prives, and V. Gottifredi, ‘p21 differentially regulates DNA replication and DNA-repair-associated processes after UV irradiation.’, *J. Cell Sci.*, vol. 121, no. Pt 19, pp. 3271–3282, 2008.

[131] R. Fotedar, M. Bendjennat, and A. Fotedar, ‘Role of p21WAF1 in the cellular response to UV’, *Cell Cycle*, vol. 3, no. 2. pp. 134–137, 2004.

[132] J. Labaer, M. D. Garrett, L. F. Stevenson, J. M. Slingerland, C. Sandhu, H. S. Chou, A. Fattaey, and E. Harlow, ‘New functional activities for the p21 family of CDK inhibitors’, *Genes Dev.*, vol. 11, no. 7, pp. 847–862, 1997.

[133] F. He, Q. Yan, L. Fan, Y. Liu, J. Cui, J. Wang, L. Wang, Y. Wang, Z. Wang, Y. Guo, and G. Huang, ‘PBK/TOPK in the differential diagnosis of cholangiocarcinoma from hepatocellular carcinoma and its involvement in prognosis of human cholangiocarcinoma.’, *Hum. Pathol.*, vol. 41, no. 3, pp. 415–24, 2010.

[134] C.-F. Chang, S.-L. Chen, W.-W. Sung, M.-J. Hsieh, H.-T. Hsu, L.-H. Chen, M.-K. Chen, J.-L. Ko, C.-J. Chen, and M.-C. Chou, ‘PBK/TOPK Expression Predicts Prognosis in Oral Cancer’, *Int. J. Mol. Sci.*, vol. 17, no. 7, p. 1007, 2016.

[135] A. Dal and L. Souhami, ‘Prostate cancer radiation therapy : A physician ’ s perspective’, *Phys. Medica*, vol. 32, pp. 438–445, 2016.

[136] G. S. Higgins, D. B. McLaren, G. R. Kerr, T. Elliott, and G. C. W. Howard, ‘Outcome analysis of 300 prostate cancer patients treated with neoadjuvant androgen deprivation and hypofractionated radiotherapy’, *Int. J. Radiat. Oncol. Biol. Phys.*, vol. 65, no. 4, pp. 982–989, 2006.

[137] M. Joel, A. A. Mughal, Z. Grieg, W. Murrell, S. Palmero, B. Mikkelsen, H. B. Fjerdingstad, C. J. Sandberg, J. Behnan, J. C. Glover, I. A. Langmoen, and B. Stangeland, ‘Targeting PBK/TOPK decreases growth and survival of glioma initiating cells in vitro and attenuates tumor growth in vivo’, *Mol. Cancer*, vol. 14, p. 121, Jan. 2015.

[138] X. Dou, J. Wei, A. Sun, G. Shao, C. Childress, W. Yang, and Q. Lin, ‘PBK/TOPK mediates geranylgeranylation signaling for breast cancer cell proliferation.’, *Cancer Cell Int.*, vol. 15, p. 27, 2015.

# APPENDIX

Nucleic Acids Research Advance Access published April 29, 2016


doi: 10.1093/nar/gkw326

# A role for human homologous recombination factors in suppressing microhomology-mediated end joining

**Sara Ahrabi[1], Sovan Sarkar[1], Sophia X. Pfister[1], Giacomo Pirovano[1], Geoff S. Higgins[1], Andrew C.G. Porter[2] and Timothy C. Humphrey[1,*]**

[1]CRUK MRC Oxford Institute for Radiation Oncology, Department of Oncology, University of Oxford, Oxford, OX3 7DQ, UK and [2]Gene Targeting Group, Centre for Haematology, Imperial College Faculty of Medicine, London W12 0NN, UK

Received November 14, 2015; Revised April 13, 2016; Accepted April 14, 2016

## ABSTRACT

**DNA double-strand breaks (DSBs) are toxic lesions, which if improperly repaired can result in cell death or genomic instability. DSB repair is usually facilitated by the classical non-homologous end joining (C-NHEJ), or homologous recombination (HR) pathways. However, a mutagenic alternative NHEJ pathway, microhomology-mediated end joining (MMEJ), can also be deployed. While MMEJ is suppressed by C-NHEJ, the relationship between HR and MMEJ is less clear. Here, we describe a role for HR genes in suppressing MMEJ in human cells. By monitoring DSB mis-repair using a sensitive HPRT assay, we found that depletion of HR proteins, including BRCA2, BRCA1 or RPA, resulted in a distinct mutational signature associated with significant increases in break-induced mutation frequencies, deletion lengths and the annealing of short regions of microhomology (2–6 bp) across the break-site. This signature was dependent on CtIP, MRE11, POLQ and PARP, and thus indicative of MMEJ. In contrast to CtIP or MRE11, depletion of BRCA1 resulted in increased partial resection and MMEJ, thus revealing a functional distinction between these early acting HR factors. Together these findings indicate that HR factors suppress mutagenic MMEJ following DSB resection.**

## INTRODUCTION

DNA double strand breaks (DSBs) are deleterious lesions that if left unrepaired can lead to cell death, while if mis-repaired can give rise to genomic instability, thus leading to tumorigenesis (1). To survive such lesions and preserve genome integrity, cells possess two main evolutionarily conserved DSB repair mechanisms, namely homologous recombination (HR), and non-homologous end joining (NHEJ) (2). Other repair pathways generally referred to as alternative non-homologous end joining pathways (Alt-NHEJ) (3–5), have been of recent interest. A subset of these repair mechanisms relies on regions of microhomology on either side of the break, which anneal following limited resection in a process called microhomology-mediated end joining (MMEJ) (6–8).

HR is an error-free DSB repair pathway that proceeds through three phases. In mammalian cells the presynaptic phase is triggered by a two-step 5′ to 3′ end resection that produces 3′ single-stranded DNA (ssDNA) overhangs. Resection is initiated by the endonucleolytic activity of the MRE11-RAD50-NBS1 (MRN) complex and the C-terminal binding protein interacting protein (CtIP), which exposes short ssDNA tails (9,10). These become substrates for the extensive resection mediators, Exo1, DNA2 and BLM (11,12). BRCA1 also facilitates the initial resection step of HR (13,14) in conjunction with MRN (15) and CtIP (15,16), where it accelerates the DSB resection rate (17). The exposed ssDNA is initially protected by Replication Protein A (RPA) (18), which is then displaced by RAD51, following its recruitment by BRCA2, to form a nucleoprotein filament (19). The RAD51 nucleofilament promotes strand invasion of the undamaged sister chromatid, which is used as a repair template, resulting in a displacement loop (D-loop). During the synaptic phase of HR, the 3′ end is extended by DNA replication, which can subsequently proceed through a number of sub-pathways. During DSB repair, second end capture and annealing results in double Holliday junction (HJ) formation. In the post-synaptic phase of HR, HJ structures can be resolved with or without crossovers, or dissolved, thus preventing crossovers (20,21). Alternatively, during synthesis-dependent strand annealing (SDSA) (22), the invading and extended strand is expelled from the D-loop to anneal to the second end which, following gap filling and ligation, results in error-free repair (23).

Classical NHEJ (C-NHEJ) is triggered by recognition and protection of DNA ends by the Ku70/Ku80 heterodimer, which forms a ring that encircles duplex DNA.

*To whom correspondence should be addressed. Tel: +44 1865 617327; Fax: +44 1865 617318; Email: timothy.humphrey@oncology.ox.ac.uk

This protects ends from resection and creates a platform to recruit the DNA-PK catalytic subunit (DNA-PKcs) (24,25). Broken ends are then trimmed by Artemis and ligated by DNA Ligase 4 (Lig 4), X-ray repair cross-complementing protein 4 (XRCC4) complex, and XRCC4-like factor (XLF), depending on the nature of the damage (25–27). Although end-protection by Ku in this pathway minimizes resection, thus promoting error-free end joining, this pathway is widely referred to as error-prone as it ligates the ends in a homology-independent fashion potentially leading to small insertions, and/or deletions (indels) at the DSB sites. From a genome-wide perspective, however, C-NHEJ is not as threatening as alternative NHEJ (Alt-NHEJ) pathways for mammalian genome stability (24) and is even considered as a guardian of genome stability (28).

Alt-NHEJ refers to DSB end joining pathways that are independent of the C-NHEJ factors Ku70/Ku80, DNA-PKcs and DNA Lig4. Unlike C-NHEJ, these pathways are highly mutagenic, always associated with indels and commonly lead to chromosomal rearrangements. Importantly, a sub pathway of Alt-NHEJ events termed microhomology mediated end joining (MMEJ) rejoins the ends by base pairing between microhomologous sequences. MMEJ is mediated via CtIP, MRN complex, Poly [ADP-ribose] polymerases1 (PARP-1) and DNA ligase 3 (Lig 3) (29,30). In mammalian cells, PARP-1, a key component of the MMEJ pathway (31), initially competes with Ku heterodimer for binding to DNA ends resulting in PAR formation (32,33). This in turn promotes MRE11 recruitment and the initiation of resection by MRN complex and CtIP (34). Subsequently, DNA end ligation is mediated through DNA Lig 3 (7,35). Further, recent studies have identified a low fidelity DNA polymerase θ (Polθ also known as POLQ) (36) as an important MMEJ factor in mammalian cells. POLQ is recruited to DSB ends by PARP-1 where it facilitates end joining and microhomology annealing (37). While absent from yeast, the role for POLQ in MMEJ appears to be conserved in flies, worms, mice and humans (38). MMEJ generates deletions and translocations at the break points and thus is highly mutagenic (39). However, there are other types of Alt-NHEJ events that do not rely on such microhomologies. The ligation step in these pathways is facilitated through DNA ligase 1(Lig1) (6).

Impairment of a DSB repair pathway is a common feature in human cancers, rendering their survival highly dependent on secondary DSB repair pathways (40). Therefore, studies of the relationships between different DSB repair machineries are of interest as they can provide insight into how to target these defects for cancer therapy purposes. In this regard, HR has an inhibitory impact on C-NHEJ via initiation of resection (41). Conversely, C-NHEJ suppresses HR and Alt-NHEJ by Ku binding and preventing the resection initiation (42,43). However, the exact nature of the interplay between HR and Alt-NHEJ in human cells still remains elusive. A recent study in MEFs (Mouse Embryonic Fibroblast Cells) found elevated levels of PARP-1-dependent translocations following loss of the HR factor RAD54 (44). Moreover, a study in *Saccharomyces cerevisiae (S. cerevisiae)* showed that RPA impairs MMEJ by removing the secondary structures of ssDNA, which facilitates RAD51 filament assembly leading to HR and thereby suppression of annealing of the terminal microhomologies (45). On the other hand, two recent studies in mammalian cells suggested that POLQ-mediated Alt-NHEJ suppresses HR repair mechanisms (46,47). A role for BRCA1 in promoting NHEJ fidelity has been proposed (48). However, studies in MEFs have also shown that BRCA1 promotes Alt-NHEJ at uncapped telomeres (49).

Here, we have investigated the relationship between HR and MMEJ repair of DSBs. We have used a highly sensitive HPRT-based assay (50,51) together with other GFP-based reporter assays (52–54) to characterize DSB misrepair events observed following depletion or inhibition of HR and NHEJ factors. Following both physical and genetic analyses, we have established a role for HR factors in suppressing MMEJ at break point junctions. Further, our data suggest the existence of POLQ-dependent and POLQ-independent MMEJ pathways, both of which are suppressed by RPA. Last, we define a role for BRCA1 in functioning downstream of CtIP and MRE11 to promote resection, thereby preserving genome integrity by counteracting MMEJ.

## MATERIALS AND METHODS

### Cell culture

HT1080 (human fibrosarcoma, HPRT assay), U2OS (human osteosarcoma, GFP-based HR reporter (52)), and H1299 (human non-small cell lung carcinoma, GFP-based C-NHEJ reporter (54)) cells were cultured as described previously (51,55). C-NHEJ reporter cells were a kind gift from Atsushi Shibata and Takashi Kohno. MMEJ reporter cells (U2OS with integrated EJ2-GFP reporter) were a kind gift from Jeremy Stark (53) and were grown in high glucose DMEM supplemented with L-glutamine, 10% fetal bovine serum, and 1% Pen/Strep solution (10 000 U/ml penicillin, 10 000 mg/ml streptomycin), including 8 mg/ml plasmocin and 2 mg/ml puromycin.

### HAT to select for HPRT gain of function

HAT selection was carried out by adding 1× HAT supplement (Invitrogen) directly to the DMEM medium for 10 days before the I-SceI transfection.

### 6-TG to select for HPRT loss of function

6-TG selective medium was made by making up 1000 × 6-TG of 15 mg/ml by dissolving the 6-TG powder (sigma) in 1N NaOH and ddH2O. 1000 × 6-TG was added to DMEM and used at a final concentration of 15 mg/ml. 6-TG medium was added 5 days after the I-SceI transfections.

### HPRT-based I-SceI-cleavable reporter assay

The assay was based on human fibrosarcoma (HT1080) cells with a functional but I-SceI-cleavable *HPRT* gene (clone 5.2.1), as described previously (50). Use of this assay in conjunction with siRNA knockdowns has been previously described (51). Briefly, an I-SceI cut site was targeted into exon 6 of the endogenous human *HPRT* gene, without disrupting the functionality of the gene. These cells

were seeded in 6-well plates and were immediately transfected with siRNAs using RNAiMAX from Invitrogen according to the manufacturer's instructions. The following day, medium was replaced with fresh DMEM. 48 h after siRNA transfections, cells were lipofected with I-SceI plasmid, which was performed in a ratio of 6 μg DNA: 18 μl Fugene in a total of 300 μl transfection mix in DMEM with no Pen/Strep and fetal bovine serum to transfect each well of a 6-well plate using the Fugene 6 transfection reagent (Promega). 24 h later, medium was replaced with fresh DMEM. Five days after the I-SceI transfection, the cells were seeded in different densities within 100 mm plates (i.e., $10^5$, $5 \times 10^4$, $10^4$, and $10^3$ per plate). Cells used to determine the mutation frequencies were then exposed to 6-TG selection, while the cells used for determining plating efficiencies were kept in non-selective media. 6-TG medium was refreshed every 2–3 days. Cells were incubated for 10–12 days to form colonies, which were stained and counted for the purpose for calculating the mutation frequencies. Further, a total of 30 clones from each genetic background were isolated and grown in 48-well plates. These were subsequently expanded into 24-well plates. At full confluency cells for each clone were then trypsinised and collected for extraction of genomic DNA using a Qiagen Flexi gene DNA kit according to the manufacturer's instructions. Genomic DNA was then quantified and used for PCR amplification across the I-SceI break site and sequencing. Primers and PCR conditions to amplify across the I-SceI site have been previously described (51).

### Data analysis

Sequence alignment was conducted using DNA Data Bank of Japan (DDBJ) ClustalW program (version 2.1).

### Graphical display of results and statistical analysis

For all statistical analysis and graphical display, the program GraphPad Prism (www.graphpad.com) was used.

### siRNA transfections

HT1080 or U2OS or H1299 cells were transfected with siRNAs (10 nM final concentration) using RNAiMAX (Invitrogen) according to the manufacturer's instructions. Medium was replaced 24 h after transfection. The sequences of the siRNAs are listed below:

non-targeting (NT) proprietary sequence of supplier (Qiagen),

BRCA2 (Thermo Scientific): GGGAAACACUCAGAUUAAAUU, UUUAAUCUGAGUGUUUCCCUU;

BRCA1 (Dharmacon): AAUGCCAAAGUAGCUAAUGUAUUUU, AAUACAUUAGCUACUUUGGCAUUUU;

CtIP (Dharmacon): GAGGUUAUAUUAAGGAAGA, GGAGCUACCUCUAGUAUCA, GAACAGAAUAGGACUGAGU, GCACGUUGCCCAAAGAUUC;

MRE11 (Dharmacon): GGAGGUACGUCGUUUCAGA, GGAAAUGAUACGUUUGUAA, CGAAAUGUCACUACUAAGA, GAAAGGCUCUAUCGAAUGU;

RPA (Dharmacon): AACUGGUUGACGAAAGUGGUGUU, CACCACUUUCGUCAACCAGUUUU;

POLQ (Ambion, Lifetechnologies): CCGCUUUUGGAGUCAGUAATT, UUACUGACUCCAAAAGCGGTA.

### Western blotting

Whole cell extracts and the protein concentration measurements for western blotting were performed as described previously (51). Equal amounts of protein were separated on NuPAGE Tris-Acetate or Bis-Tris gel (Invitrogen) and transferred to a PVDF membrane (0.45 μm pore size) (Invitrogen). After blocking, the membranes were incubated with appropriate primary antibodies at 4°C overnight followed by secondary antibodies at room temperature for 1 h. Imaging of protein was performed by the BIO-RAD ChemiDoc Imaging sytem.

Primary antibodies used for western blotting are listed below:

BRCA2 (Santa Cruz, sc-28235); BRCA1 (Calbiochem, OP92); RAD51 (Santa Cruz, sc-8349); CtIP (GeneTex 19E8); MRE11 (Abcam, ab33125); RPA32 (Abcam, 2175); Tubulin (Sigma, T5168). All secondary antibodies were purchased from Invitrogen.

### Inhibitors

The PARP-1 inhibitor, Olaparib (AZD 2281) was dissolved in DMSO and used at 5 μM final concentration. The DNA-PKcs inhibitor, NU7441 (Axon) was dissolved in DMSO and used at 5, and 15 μM final concentrations.

### Quantitative RT-PCR

RNA was extracted using an RNeasy mini kit (Qiagen). A SuperScript® VILOTM (Invitrogen/Life Technologies) cDNA synthesis kit was used to reverse transcribe cDNA from total RNA according to manufacturer's instructions. Quantitative PCR was performed using 7500 Fast Real-Time PCR detection system (Applied Biosystems). Reactions (25 μl each) were prepared in triplicate in a 96-well reaction plate. Each reaction contained 20 ng cDNA, 200 nM of each primer, 10 μl water and 12.5 μl Absolute Blue QPCR SYBR low ROX Mix (Thermo Scientific). DNA levels were normalized to the GAPDH calculated using a 2-ΔΔCt method. QPCR settings were as follows: Initialization at 95°C for 15 min, denaturation at 95°C for 15 s, annealing at 60°C for 30 s, and extension at 72°C for 30 s and repeat for 40 cycles. Primers used for the qRT-PCR are listed below:

qRT-PCR F:5'-AGT CGC ACA CTG CTA CAG GAC GA-3'

qRT-PCR R: 5'-GGC ACA AAG GCA TGT CGC ATG C-3'

### GFP-based I-SceI-cleavable reporter assays (HR, C-NHEJ and MMEJ)

To examine the effects of gene loss of function on the HR, C-NHEJ, and MMEJ repair pathways a panel of GFP-based I-SceI-cleavable reporter cell lines was used. The cells were transfected with an I-SceI plasmid using

Lipofectamine 2000 (Invitrogen) according to the manufacturer's instructions in 6-well plates 48 h after the siRNA knockdowns. After 2 days, the cells from each well were trypsinised and dispersed in 200 μl medium. The 400 μl suspension was then immediately mixed with 200 μl of 10% formaldehyde, and vortexed for 2–3 s before FACS (FACSCalibur) to quantitate the number of GFP positive cells. For FACS analysis, non-overlapping gates were defined by three populations of cells from the same cell line: normal cells, cells transfected with EGFP or DsRed plasmids. 20 000 cells were analyzed for each sample.

## RESULTS

### BRCA2 depletion promotes DSB-induced deletions typical of MMEJ

We have previously shown that siRNA-mediated depletions of SETD2 or RAD51 had similar effects on I-SceI-induced DSBs in the *HPRT* gene, namely an increased overall frequency of *HPRT* mutagenesis associated with increases in both deletion lengths and use of microhomologies on either side of the deletions (51). These findings suggested a possible role for HR in suppressing MMEJ.

To test this further, we applied the same approach (Supplementary Figure S1) to assess a possible role for other HR factors in suppressing MMEJ. BRCA2, a key recombination mediator in mammalian cells, facilitates RAD51 loading onto ssDNA. We therefore anticipated that BRCA2 might also suppress MMEJ. We first depleted BRCA2 and measured the frequency of *HPRT* inactivation (mutation frequency) following I-SceI-induced DSBs. Knockdown of BRCA2 resulted in a significantly increased I-SceI-induced mutation frequency (2.8%; $P < 0.0001$), compared to cells treated with non-targeting control (NT) siRNA (1.1%) (Figure 1A). Sequence analysis of HPRT-negative clones derived from cells treated with NT siRNA (Figure 1B, and Supplementary Figure S2A–C) or BRCA2 siRNA (Figure 1B, and Supplementary Figure S3) indicated average deletion lengths of 5.6 and 49 bp, respectively. Thus BRCA2 depletion resulted in a 9-fold increase in deletion lengths ($P < 0.0001$) (Figure 1C). Insertions at the HPRT break site were also detected but their frequencies were not significantly altered by BRCA2-depletion (Supplementary Figure S14).

Further examination of the sequences at deletion junctions showed that the proportion of deletions appearing to have arisen by MMEJ rose significantly from 43%, for cells treated with NT control siRNA, to 72% for cells treated with BRCA2 siRNA ($P < 0.05$) (Figure 1D). BRCA2 depletion in HT1080 cells was confirmed by western blot (Figure 1E). To assess the effect of BRCA2 depletion on HR, we used a previously described (51) U2OS cell line carrying a well-characterized GFP-based reporter for HR (DR-GFP) (52). We found that the frequency of HR in BRCA2-depleted cells was significantly reduced by 41% compared to the NT controls ($P < 0.0001$), consistent with a role for BRCA2 in promoting HR (19) (Figure 1F). Thus BRCA2 depletion causes both a decrease in HR and an apparent increase in MMEJ suggesting roles for BRCA2 not only in promoting HR but also in suppressing MMEJ.

### BRCA1 depletion promotes DSB-induced deletions typical of MMEJ

BRCA1 is also an essential factor for HR but has a distinct function in HR compared to BRCA2, where BRCA1 facilitates 5′ to 3′ resection of DSBs to generate 3′ ssDNA tails (56). To investigate a possible role for BRCA1 in suppressing MMEJ, we examined the effect of BRCA1 depletion on DSB mutational signatures in the HPRT reporter system. Like BRCA2 depletion, BRCA1 depletion resulted in a significantly enhanced mutation frequency (3.5%; $P = 0.001$) following I-SceI-induced DSBs compared to that of NT controls (1.1%) (Figure 2A). Further, sequencing of individually isolated HPRT mutated clones from a BRCA1-depleted background (Figure 2B and Supplementary Figure S4) indicated an average deletion length of 17 bp, significantly (3-fold) greater than the deletion lengths in NT control siRNA-treated cells ($P = 0.04$) (Figure 2C). Interestingly, the deletion lengths in BRCA1-depleted cells were significantly (2.8-fold) smaller than to those in BRCA2-depleted cells ($P < 0.05$). This is consistent with the early role for BRCA1 in promoting resection during HR, prior to BRCA2-assisted RAD51 loading. Insertions at the HPRT break site were also detected but their frequency was not significantly altered by BRCA1-depletion (Supplementary Figure S14). Among the sequenced junctions in HPRT negative cells, 66% ($P < 0.05$) appeared to have been generated by MMEJ following BRCA1 depletion, a 1.5-fold increase over the 43% in cells with normal BRCA1 levels (Figure 2D). Therefore, BRCA1 depletion, like BRCA2-depetion, resulted in a significant increase in the proportion of mutagenic NHEJ events appearing to occur by MMEJ (Figure 2D). BRCA1 depletion in HT1080 cells was confirmed by western blot (Figure 2E). Consistent with the role of BRCA1 in HR (14), HR was significantly reduced by 52% ($P < 0.0001$) in the DR-GFP reporter (U2OS cells) (52) following BRCA1 knockdown (Figure 2F). Thus, BRCA1 depletion results in reduced HR repair and significantly increased mutation frequency associated with a larger proportion of MMEJ events. Together with the similar effects of BRCA2, RAD51 and SETD2 depletion, these results suggest a common role for HR factors in suppressing MMEJ.

### MMEJ-like DSB repair in HR deficient cells is independent of DNA-PKcs

Although the microhomologies we observed at repair junctions in HR-defective cells were highly suggestive that MMEJ is the key pathway involved, we wanted to test the possible involvement of C-NHEJ. Because C-NHEJ, but not MMEJ, is dependent on DNA-PKcs, we therefore, compared the HPRT mutational profile following treatment of cells with a DNA-PKcs inhibitor (NU7441), or siRNA against RAD51 in the presence and absence of NU7441. This inhibitor has previously been shown to disrupt the C-NHEJ repair pathway (57). We found that treating cells with NU7441 resulted in a significant increase in the deletion length (16 bp, $P = 0.015$) and a significantly increased presence of microhomologies at the break sites (60%, $P < 0.05$) compared to that of the NT background (Figure 3A–C and Supplementary Figure S5). This is consistent with a role for DNA-PKcs in conjunction with Ku in protecting DSB ends

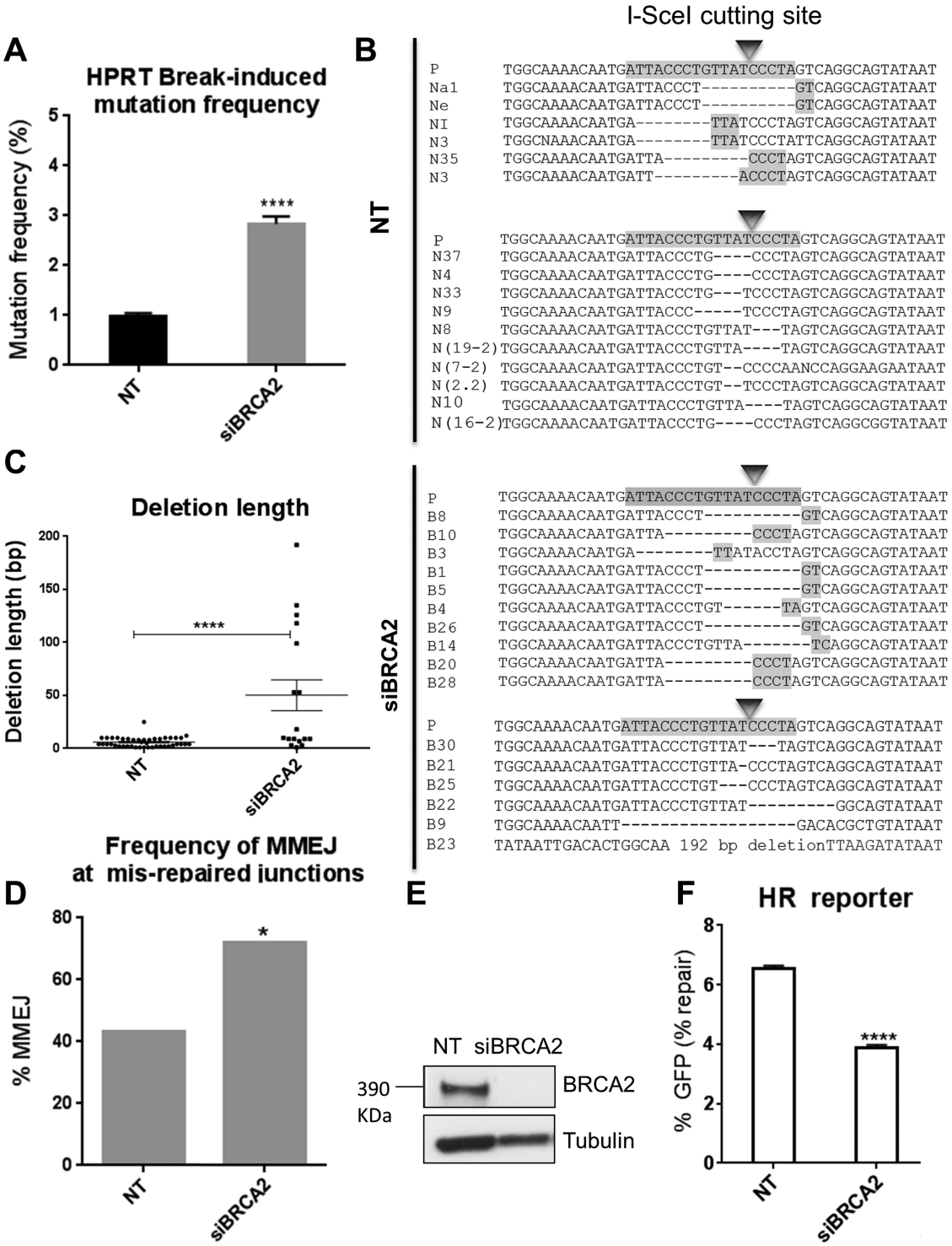


**Figure 1.** BRCA2 depletion promotes DSB-induced deletions typical of MMEJ. (**A**) Break-induced mutation frequency of HPRT reporter cells treated with NT control siRNA (NT), and BRCA2 siRNA (siBRCA2). Error bars represent SEM from three independent experiments. ****$P < 0.0001$. (**B**) Representative sequence alignments of the PCR products in NT control (NT), and BRCA2-depleted (siBRCA2) cells isolated from three independent experiments (see also Supplementary Figures S1A, S2A–C and S3). I-SceI recognition sequence and terminal microhomologies at the break sites are highlighted. (**C**) Average length of deletions (bp) in different genetic backgrounds. Each dot represents an independent clone. The lines represent mean and SEM, **** $P < 0.0001$. (**D**) Frequency of MMEJ at mis-repaired junctions in HPRT deletion mutants isolated from cells treated with NT control siRNA (NT) or BRCA2 siRNA (siBRCA2). $P$ values calculated by statistical analysis "difference between proportions", * $P < 0.05$. (E) Western blot showing BRCA2 knockdown in HT1080 cells 48 h following siRNA transfection. (F) HR repair efficacy of DR-GFP reporter cells treated with NT control siRNA (NT), and BRCA2 siRNA (siBRCA2), indicated by the percentage of GFP-positive cells. Error bars show SEM from three independent experiments, **** $P < 0.0001$.

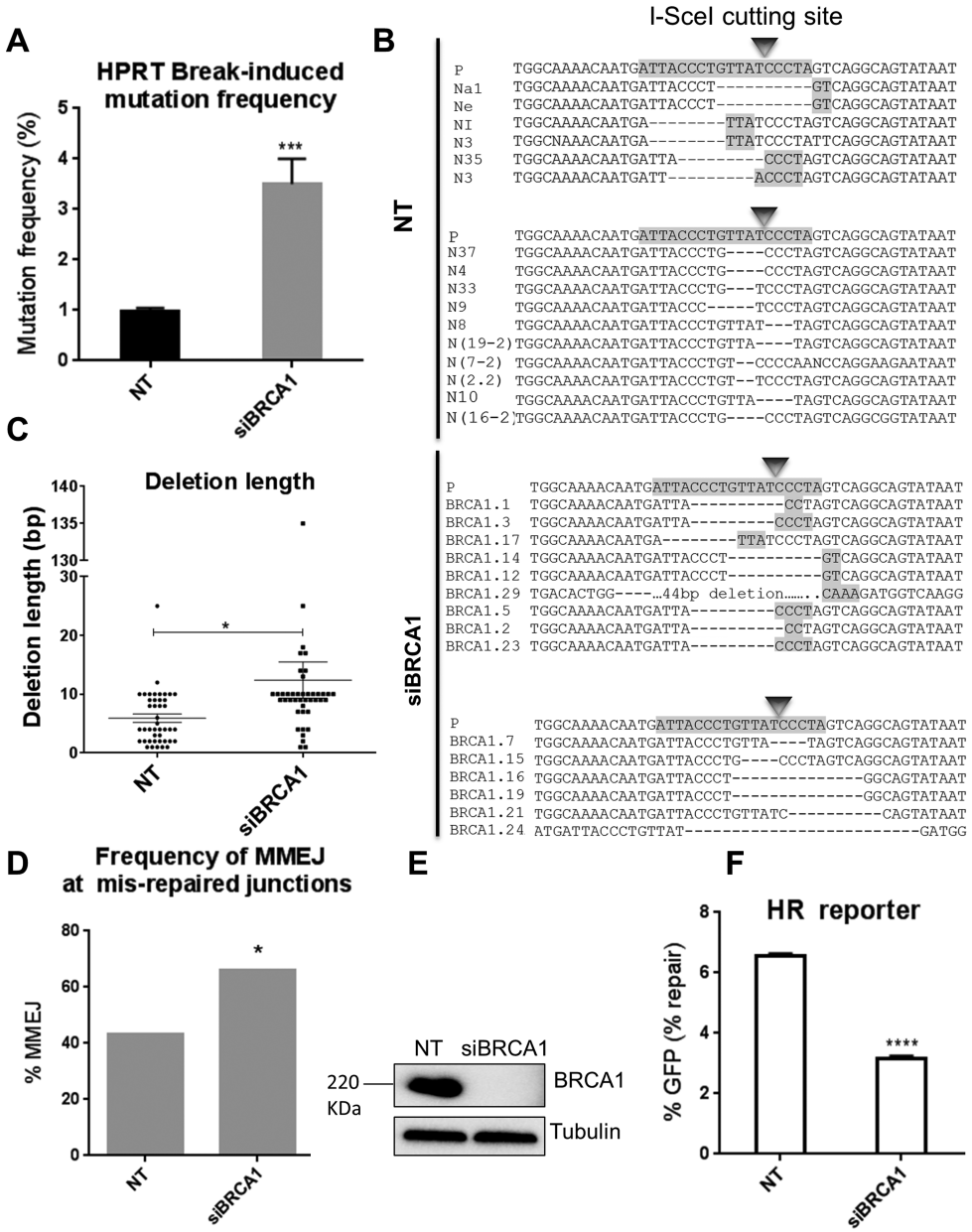


**Figure 2.** BRCA1 depletion promotes DSB-induced deletions typical of MMEJ. (**A**) Break-induced mutation frequency of HPRT reporter cells treated with NT control siRNA (NT), BRCA1 siRNA (siBRCA1). Error bars represent SEM from three independent experiments. *** $P < 0.001$. (**B**) Representative sequence alignments of the PCR products in NT control (NT), and BRCA1-depleted (siBRCA1) cells from three independent experiments (see also Supplementary Figures S1A, and S4). I-SceI recognition sequence and terminal microhomologies at the break sites are highlighted. (**C**) Average length of deletions (bp) in different genetic backgrounds. Each dot represents an independent clone. The lines represent mean and SEM, *$P < 0.05$, ***$P < 0.001$. (**D**) Frequency of MMEJ at mis-repaired junctions in HPRT deletion mutants isolated from cells treated with NT control siRNA (NT) or BRCA1 siRNA (siBRCA1). $P$ values calculated by statistical analysis "difference between proportions", *$P < 0.05$. (**E**) Western blot showing BRCA1 knockdown in HT1080 cells 48 h following siRNA transfection. (**F**) HR repair efficacy of DR-GFP reporter cells treated with NT control siRNA (NT), and BRCA1 siRNA (siBRCA1), indicated by the percentage of GFP-positive cells. Error bars show SEM from three independent experiments, **** $P < 0.0001$.

and thereby promoting C-NHEJ and counteracting MMEJ (25,58). Further, we found that the RAD51-depleted mutational pattern following DSB induction was largely unaffected by the presence of the DNA-PKcs inhibitor. In particular, similar deletion lengths and use of microhomologies at the HPRT break-sites were observed following RAD51 depletion in the absence or presence of NU7441 ($P > 0.05$) (Figure 3A–C, and Supplementary Figure S6). No statistical difference was found between the MMEJ levels in cells treated with NU7441, siRNA against RAD51 or siRNA against RAD51 in combination with NU7441 (Figure 3C). These observations suggested that the DSB mutational signature in the absence of HR is largely independent of DNA-PKcs, a core C-NHEJ factor. To confirm this in another system, we used a well-defined GFP-based MMEJ reporter integrated within a U2OS cell line (EJ2-

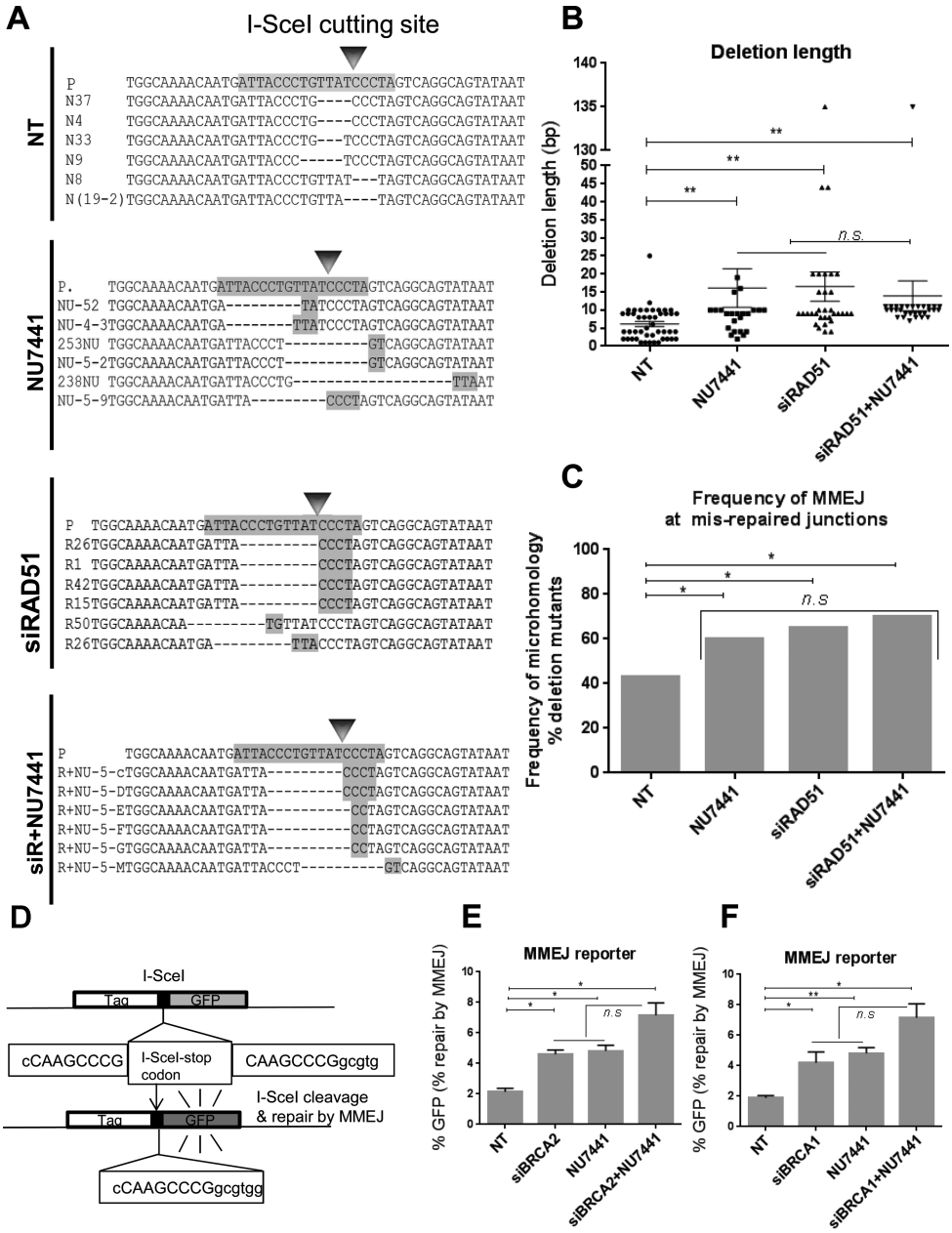


**Figure 3.** MMEJ-like DSB repair in HR-deficient cells is independent of DNA-PKcs. (**A**) Representative sequence alignments of PCR products obtained from HPRT negative cells treated with NT control siRNA (NT), a DNA-PKcs inhibitor (NU7441), siRNA against RAD51 (siRAD51) or siRNA against RAD51 plus NU7441 (siR+NU7441), from three independent experiments (see also Supplementary Figures S1A, S5-S6). I-SceI recognition sequence and terminal microhomologies at the break sites are highlighted. (**B**) Average length of deletions (bp) in different genetic backgrounds. Each dot represents an independent clone. The lines represent mean and SEM, n.s., not significant, ** $P < 0.01$. (**C**) Frequency of MMEJ at mis-repaired junctions in HPRT deletion mutants isolated from cells treated with NT control siRNA (NT), NU7441, RAD51 siRNA (siRAD51) or RAD51 and NU7441 (siRAD51+NU7441). $P$ values calculated by statistical analysis "difference between proportions", *$P < 0.05$. (**D**) Schematic map of the EJ2-GFP reporter (53) to assess MMEJ efficacy, where the I-SceI cut site is flanked by 8 nucleotide homologous sequences capable of bridging the I-SceI-induced DSB by MMEJ and thus restoring a functional GFP cassette. (**E**) MMEJ repair efficacy of EJ2-GFP reporter cells treated with NT control siRNA (NT), BRCA2 siRNA (siBRCA2), DNA-PKcs inhibitor (NU7441) or BRCA2 and DNA-PKcs co-depleted cells (siBRCA2+NU7441), indicated by the percentage of GFP-positive cells. Error bars show SEM from three independent experiments. *$P < 0.05$. (**F**) MMEJ repair efficacy of EJ2-GFP reporter cells treated with NT control siRNA (NT), BRCA1 siRNA (siBRCA1), DNA-PKcs inhibitor (NU7441) or BRCA1 siRNA and DNA-PKcs (siBRCA1+NU7441), indicated by the percentage of GFP-positive cells. Error bars show SEM from three independent experiments. *$P < 0.05$, ** $P < 0.01$.

GFP) (53) (Figure 3D). Knockdown of BRCA2 in this system significantly increased the GFP-positive cells, indicative of MMEJ repair, compared to the NT controls (1.95-fold, $P = 0.0105$) (Figure 3E), confirming that BRCA2 suppresses MMEJ. Also, DNA-PKcs inhibition by NU7441 in this reporter cell line significantly increased the MMEJ repair events by 2.24-fold ($P = 0.0129$) (Figure 3E), consistent with a well-established role for C-NHEJ factors in suppressing MMEJ (42). Further, inhibition of DNA-PKcs by NU7441 in BRCA2-depleted cells led to a slight increase of the GFP-positive cells compared to that of BRCA2-depleted cells (1.62-fold; $P = 0.0523$) or control cells treated with NU7441 (1.4-fold; $P > 0.05$) (Figure 3E). When we repeated these experiments using BRCA1 depletion in place of BRCA2 depletion, we obtained very similar results (Figure 3F). These data obtained from the GFP reporter are consistent with those from the HPRT assay; in neither system did treatment with DNA-PKcs inhibitor impair the increase in MMEJ resulting from depletion of an HR protein suggesting that DNA-PKcs is dispensable for the induction of MMEJ in the HR-deficient cells.

Finally, to confirm that NU7441 efficiently inhibits C-NHEJ, we treated the previously described GFP-based C-NHEJ reporter (IRES-TK-EGFP, H1299 cells) (54) (Supplementary Figure S7A) with NU7441 and observed a 93.6% ($P < 0.0001$) fall in C-NHEJ (Supplementary Figure S7B). RAD51 depletion was confirmed by western blot (Supplementary Figure S7C). Collectively these data suggest that MMEJ in HR-impaired cells is independent of DNA-PKcs, a key factor for the C-NHEJ pathway. Also, the GFP-based reporter data suggest that BRCA2 and BRCA1 suppress MMEJ.

### DSB-induced mutation signatures in HR-deficient cells require MMEJ factors

The above evidence shows clearly that DSB mis-repaired junctions with microhomologies typical of MMEJ are enhanced when HR is impaired, and that this effect is C-NHEJ-independent. We nevertheless sought direct evidence that MMEJ is indeed the pathway responsible for these mutational signatures. We therefore used the HPRT system to examine the DSB-induced mutational signatures following depletion of essential MMEJ factors. Given that HR and MMEJ share the initial resection step via CtIP and MRE11 (8,59,60), we investigated the impact of depleting these factors on the DSB-induced mutational signature. CtIP and MRE11 were depleted by siRNA-mediated knockdown in the HPRT reporter cells and the mutational frequencies following I-SceI-induced break were quantified. We found that, similar to the depletion of RAD51, SETD2, BRCA2 and BRCA1, depletion of either CtIP or MRE11 resulted in a significant increase in the I-SceI-induced mutation frequency (3.5%; $P = 0.0007$; and 3.6%; $P < 0.0001$, respectively) compared to 1.1% in NT controls (Figure 4A). The mutational frequencies in these backgrounds were slightly but significantly greater than those in BRCA2 depleted cells ($P<0.05$), consistent with roles for CtIP, and MRE11 upstream of BRCA2 during HR. Surprisingly, sequence analysis of HPRT-negative clones derived from CtIP- or MRE11-depleted cells identified a distinct mutational signature compared to that of SETD2-, RAD51-, BRCA2- or BRCA1-depleted cells (Figure 4B, and Supplementary Figures S8 and S9). This signature involved deletions with comparable lengths to those in NT controls (mean 5.6 bp), in contrast to the increased deletion lengths seen in BRCA2-depleted cells (mean 49 bp; $P < 0.0001$, and $P < 0.001$, respectively) (Figures 1C and 4C). Further analysis of the mis-repaired junctions of HPRT-negative clones from these backgrounds identified a significant decrease in the proportion of repair junctions associated with microhomologies in both CtIP- (13%; $P < 0.05$), and MRE11- (31%; $P < 0.05$) depleted cells, compared to NT controls (43% Figure 4D), or to BRCA2 72 (Figure 1D) and BRCA1-depleted cells (65%, Figure 2D). In summary, depletion of CtIP or MRE11, essential MMEJ factors that promote the initiation of resection, significantly reduced the proportion of DSB-induced deletions that were associated with microhomologies, relative to the NT controls. This contrasts sharply with depletion of the HR proteins SETD2, RAD51, BRCA2 or BRCA1, which significantly enhanced the same proportion (Figures 1D and 2D) (51).

To assess the effect of CtIP and MRE11 depletion on HR, we knocked down CtIP and MRE11 in the DR-GFP reporter (U2OS cells) (52) and found that the frequency of HR was significantly reduced by 92% ($P < 0.0001$), and 71% ($P < 0.0001$), respectively (Figure 4E). CtIP and MRE11 depletions were confirmed by western blot (Figure 4F). Together, these findings are in accordance with roles for CtIP and MRE11 in the initiation of resection during both HR and MMEJ.

PARP-1 is also known to play a key role in MMEJ by competing with Ku to bind DSBs, which in turn leads to the recruitment of MRE11 and CtIP to trigger resection (33,61). Consistent with this, Olaparib has recently been shown to decrease the Alt-NHEJ levels in the MMEJ-GFP reporter assay (62). Therefore, we treated the HR-proficient HT1080 cells (HPRT reporter) with a PARP-1 inhibitor, Olaparib (AZD2281) (63), and examined the DSB mutational pattern. The effects of Olaparib were similar to those of CtIP or MRE11 depletion. Thus Olaparib significantly increased the mutation frequency (2.6%; $P = 0.0073$; Figure 4A) compared to the 1.1% in NT controls, generating deletion lengths (mean 7 bp) comparable to the controls (mean 5.6 bp; $P > 0.05$; Figure 4B and C), and significantly shorter than deletion lengths in BRCA2-depleted HPRT mutants (mean 49 bp; $P = 0.0005$). Similarly, HPRT mutants arising following DSB induction in cells treated with Olaparib showed a significant reduction in the proportion of deletion junctions associated with microhomologies (25%; $P <0.05$) relative to NT controls (57%) (Figure 4B, D and Supplementary Figure S10), Collectively, these results suggest that microhomologies at DSB mis-repaired junctions in the HPRT reporter do indeed originate from the MMEJ repair machinery.

To confirm that the MMEJ-like signature in HR-compromised cells arises from MMEJ, we aimed to see whether knocking down a core MMEJ factor could abolish the MMEJ signature in these cells. We therefore, co-depleted BRCA1 and MRE11 in the HPRT system and monitored the DSB mutational signature. Simultaneous knockdown of BRCA1 and MRE11 resulted in a signifi-

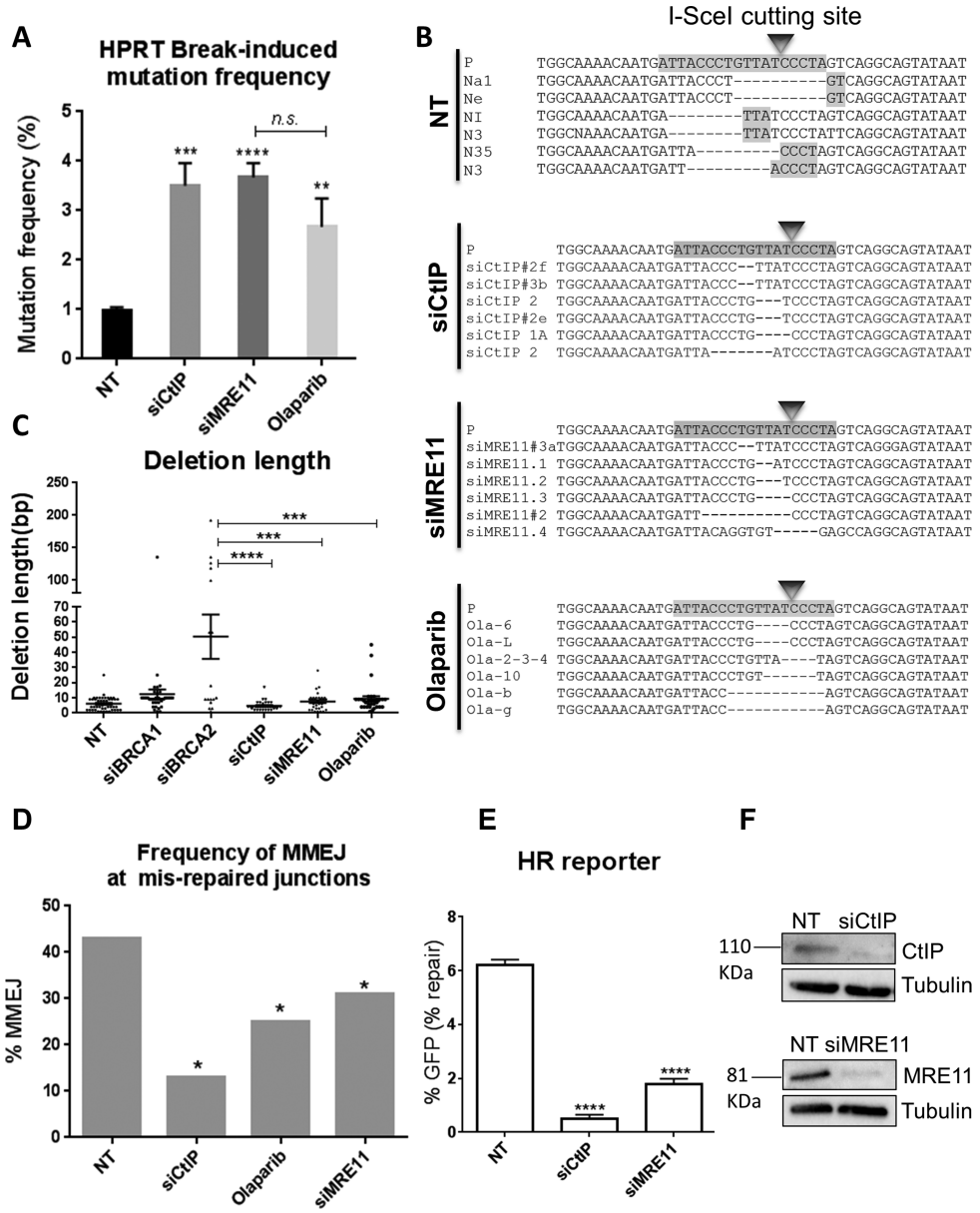


**Figure 4.** DSB-induced mutation signatures in HR-deficient cells require MMEJ factors. (**A**) Break-induced mutation frequency of HPRT reporter cells treated with NT control siRNA (NT), CtIP siRNA (siCtIP), MRE11 siRNA (siMRE11) or PARP-1 inhibitor (Olaparib). Error bars represent SEM from three independent experiments, n.s., not significant, $^{**}P < 0.01$, $^{***}P < 0.001$, $^{****}P < 0.0001$. (**B**) Representative sequence alignments of the HPRT negative PCR products in cells treated with NT control siRNA (NT), CtIP siRNA (siCtIP), MRE11 siRNA (siMRE11) or PARP-1 inhibitor (Olaparib), from three independent experiments (see also Supplementary Figures S1A, S8–10). I-SceI recognition sequence and terminal microhomologies at the break sites are highlighted. (**C**) Average deletion lengths (bp) in different genetic backgrounds. Each dot represents an independent clone. The lines represent mean and SEM, $^{***}P < 0.001$, $^{****}P < 0.0001$. (**D**) Frequency of MMEJ at mis-repaired junctions in HPRT deletion mutants isolated from cells treated with NT control siRNA (NT) or CtIP siRNA (siCtIP), MRE11 siRNA (siMRE11) or Olaparib. *P* values calculated by statistical analysis "difference between proportions", $^{*}P < 0.05$. (**E**) HR repair efficacy of DR-GFP reporter cells treated with NT control siRNA (NT), CtIP siRNA (siCtIP), or MRE11 siRNA (siMRE11), indicated by the percentage of GFP-positive cells. Error bars show SEM from three independent experiments. $^{****}P < 0.0001$. (**F**) Western blot showing CtIP and MRE11 knockdowns 48 h following siRNA transfection.

cantly increased mutation frequency of 3.4% compared to that of the NT background (1.1%, $P = 0.0013$) (Supplementary Figure S11A). This increased frequency of HPRT loss is consistent with the roles for BRCA1 and MRE11 in promoting DSB repair (14,15). Further, the MMEJ signature was absent in cells co-depleted for BRCA1 and MRE11. This was associated with deletion lengths comparable to that of NT cells (mean 5.6 bp), and a significantly reduced proportion of MMEJ (27%) compared to that of NT cells (43%, $P < 0.05$) (see Supplementary Figures S11 and S12). Together these data confirm that the MMEJ-like signature in the absence of HR factors is arising from the MMEJ pathway.

### RPA suppresses MMEJ

RPA is a heterotrimeric ssDNA binding protein with roles in DNA replication, recombination and DSB repair, including HR. RPA displacement by RAD51 is a critical step in HR (18). In this regard, it has been previously shown in *S. cerevisiae* that RPA antagonizes MMEJ (45). Therefore, to test a possible role for RPA in repressing MMEJ repair in human cells, we used the GFP-based reporter for MMEJ repair (53) (Figure 3D). RPA knockdown (Figure 5C) resulted in significantly enhanced MMEJ levels compared to the NT controls (2.9-fold; $P < 0.0001$) (Figure 5A), suggesting that human RPA also suppresses MMEJ. POLQ has recently been identified as an MMEJ-promoting factor in mammalian cells (46,47). Thus siRNA knockdown of POLQ was used as a control for the GFP-based MMEJ reporter, which led to 94% reduction in *POLQ* gene expression levels, as evaluated by qRT-PCR (Figure 5B). This was found to significantly reduce MMEJ repair by 58% ($P = 0.0112$), consistent with its role in the mammalian MMEJ pathway (Figure 5A). Further, co-depletion of RPA and POLQ in the GFP-based MMEJ reporter led to significantly reduced levels of MMEJ compared to that of RPA-depleted cells ($P = 0.0007$). Surprisingly, however, MMEJ levels in cells co-depleted for POLQ and RPA were still significantly greater than NT controls ($P = 0.0022$) (Figure 5A), suggestive of the possible existence of POLQ-dependent and POLQ-independent MMEJ pathways being suppressed by RPA. Finally, to confirm the role for POLQ in promoting MMEJ in the HPRT assay, we depleted POLQ in this system and monitored the DSB mutational pattern. Analysis of the mutational signature in cells treated with siRNA against POLQ showed a significantly decreased MMEJ levels compared to that of the NT background, (Figure 5D and E and Supplementary Figure S13). These results resemble our findings in the MMEJ-GFP assay, confirming that the HPRT and the GFP reporter assays measure the same process.

## DISCUSSION

Mutations arising from aberrant DSB repair are deleterious for cells and can give rise to genomic instability, a hallmark of cancer (64). Yet how DSB-induced chromosomal rearrangements are suppressed is poorly characterized. Further, there is little mechanistic insight into the relationship between disrupting repair pathways and the mechanisms of DSB mis-repair. Here, using an I-SceI-cleavable reporter assay based on the human endogenous *HPRT* gene (50,51), together with an array of I-SceI-cleavable GFP-based reporter assays (52–54), in different cancer cell lines we have established a role for HR factors in suppressing mutagenic MMEJ following DSB resection. In this context, we consider MMEJ to arise as the default pathway following HR inactivation rather than being actively suppressed by HR (see model in Figure 6). Following on from our initial observations in RAD51- and SETD2-depleted cells (51), this study confirms that depletion of other HR factors (BRCA2, BRCA1 and RPA) also results in significantly elevated levels of a common DSB mutational signature in which DSB-induced deletions are associated with microhomologies of 2–6 bp at the break junctions. Our observations are in alignment with the recent studies in human cells indicating that chromosomal rearrangement junctions formed by MMEJ contain 2–6 bp of microhomology regions (38). Further, our data also indicate that while failed HR leads to an increase in MMEJ-induced deletions, surprisingly no effect was observed on insertions, suggesting that these arise through other mutagenic NHEJ events in this context. In this respect, insertions were still observed, albeit at low levels, following inhibition of DNA-PKcs or following knockdown or inhibition of MMEJ factors, suggesting these insertions arise through other end-joining mechanisms. However, this needs to be investigated in more detail.

Because the junctional microhomologies can potentially represent DSB mutational signatures of either C-NHEJ or MMEJ pathways (65,66), it is important to know which of these pathways is involved. However the abrogation of these signatures following depletion or inhibition of CtIP, MRE11, PARP-1, all of which facilitate MMEJ, provides strong genetic evidence that the MMEJ pathway is responsible. The observation that MMEJ levels are decreased following PARP-1 inhibition with Olaparib in the HPRT system, is in agreement with a recent study in which a similar finding was found using a GFP-based reporter assay (62).

Additionally, the persistence of junctional microhomologies in HR-depleted cells treated with DNA-PKcs inhibitor excludes the possibility that C-NHEJ is required. These conclusions are further supported by the significantly greater levels of MMEJ events detected by a GFP-based reporter following depletion of HR factors, even when DNA-PKcs is inhibited (Figure 3E and F). Our findings therefore indicate that, following DSB induction, HR proteins preserve genomic integrity by suppressing mutations arising through the MMEJ pathway. MMEJ can be considered an important DSB repair pathway in its own right. However our data suggest that its levels can be increased as a result of disrupted HR. In this respect, we know MMEJ has been proposed to be higher during S/G2 (59), which may arise through incomplete HR. For example, one-ended breaks arising from replication collapse may give rise to both MMEJ and HR.

While the role of CtIP and the MRN complex in resection initiation is well established (67), the exact role of BRCA1 in resection remains uncertain (68–70). It has recently been reported that, although the BRCA1-CtIP interaction is not crucial for DNA end-resection, it enhances the speed of CtIP-mediated resection (17). It is also known that CtIP and MRE11 are required for both HR and MMEJ repair pathways by triggering resection (59). Differing results regarding the contribution of BRCA1 in MMEJ have been reported. Thus, while one recent study in MEFs found that BRCA1 facilitates MMEJ at uncapped telomeres (49), work in DT40 (chicken) B cells suggested that MMEJ is not influenced by BRCA1 (70). Various studies of plasmid-based (exogenous) DSB repair substrates in human cells, however, provide evidence that BRCA1 represses Alt-NHEJ events by promoting the fidelity of NHEJ. (48,71–73). Here, using an endogenous HPRT assay together with GFP reporter assays in different human cell lines, we identified a DSB-induced mutational signature for BRCA1-depleted cells, which is distinct from that of CtIP-depleted or MRE11-

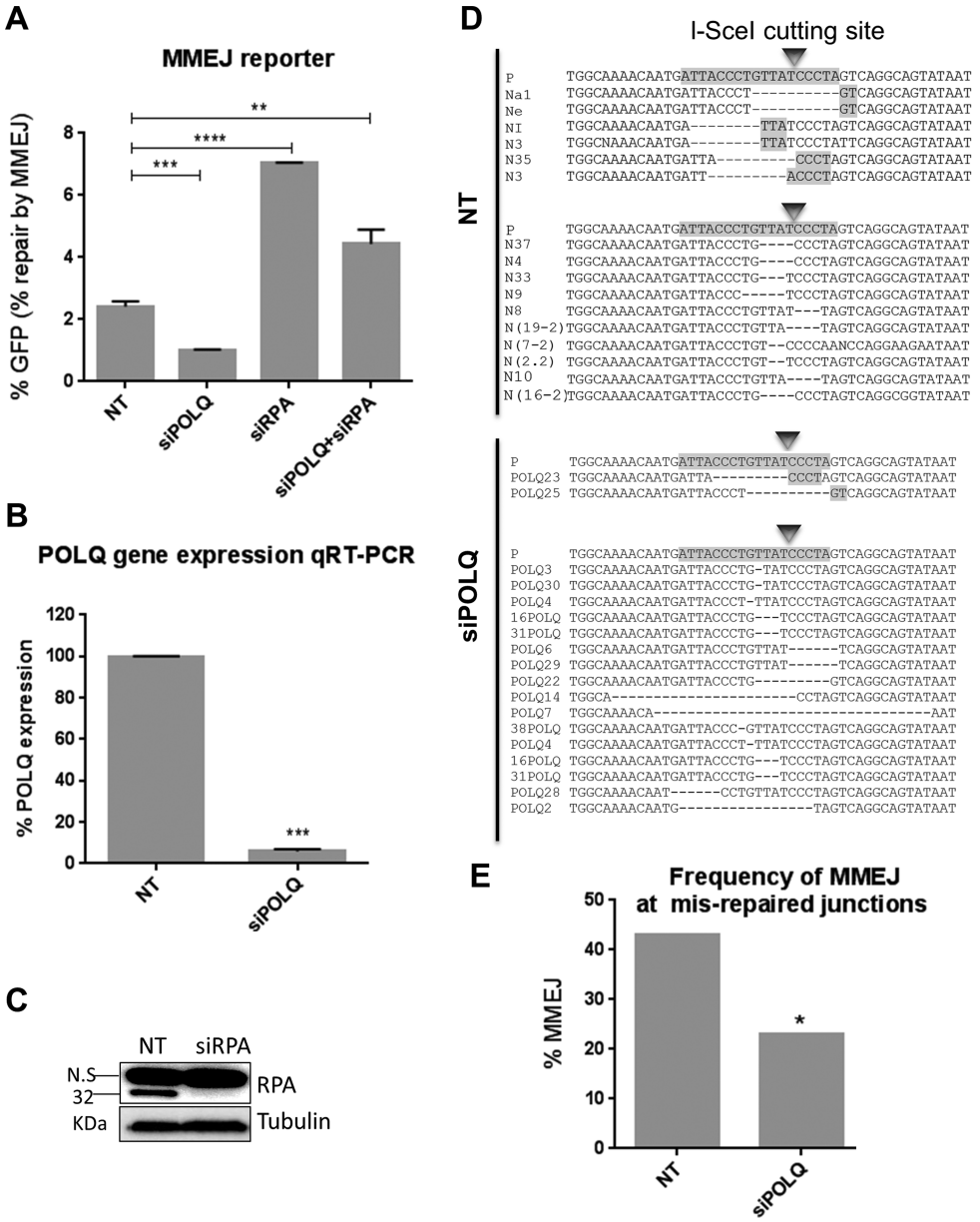


**Figure 5.** RPA suppresses MMEJ. (**A**) MMEJ repair efficacy of EJ2-GFP reporter cells treated with NT control siRNA (NT), POLQ siRNA (siPOLQ), RPA siRNA (siRPA) and POLQ plus RPA (siPOLQ+siRPA) indicated by the percentage of GFP-positive cells. Error bars show SEM from three independent experiments. $^{**}P < 0.01$, $^{***}P < 0.001$, $^{****}P < 0.0001$. (**B**) POLQ gene expression measured by RT-qPCR using the primers indicated in Materials and Methods. (**C**) Western blot showing RPA knockdown 48 h following siRNA transfection. (**D**) Representative sequence alignments of the PCR products (see Supplementary Figure S13) in NT control (NT), and POLQ-depleted (siPOLQ) cells. I-SceI recognition sequence and terminal microhomologies at the break sites are highlighted. (**E**) Frequency of MMEJ at mis-repaired junctions in HPRT deletion mutants isolated from cells treated with NT control siRNA (NT) or POLQ siRNA (siPOLQ). *P* values calculated by statistical analysis "difference between proportions", $^{*}P < 0.05$.

depleted cells. The significantly greater HPRT deletion lengths in BRCA1-depleted cells compared to those of CtIP or MRE11-depleted cells supports the notion that BRCA1 operates downstream of CtIP and MRE11. Further, the significantly smaller HPRT deletion lengths in BRCA1-depleted cells compared to those of BRCA2-depleted cells, suggests that BRCA1 functions downstream of CtIP and MRE11 but upstream of BRCA2 during HR to promote genome stability by facilitating resection and thereby suppressing the mutagenic MMEJ. Moreover, the significantly increased levels of MMEJ, detected by both the HPRT and GFP assays, following BRCA1 depletion suggest that BRCA1 suppresses MMEJ repair. This is in agreement with previous studies using plasmid-based reporter systems (48,71).

POLQ has recently been identified as a polymerase that contributes to mammalian MMEJ by promoting DNA end joining and microhomology annealing (37,38). Further, recent studies have suggested that cancer cells with defective HR are dependent on POLQ-mediated MMEJ repair (46,47). Moreover, POLQ is upregulated in a range of human cancers, and indicates a poor clinical prognosis, espe-

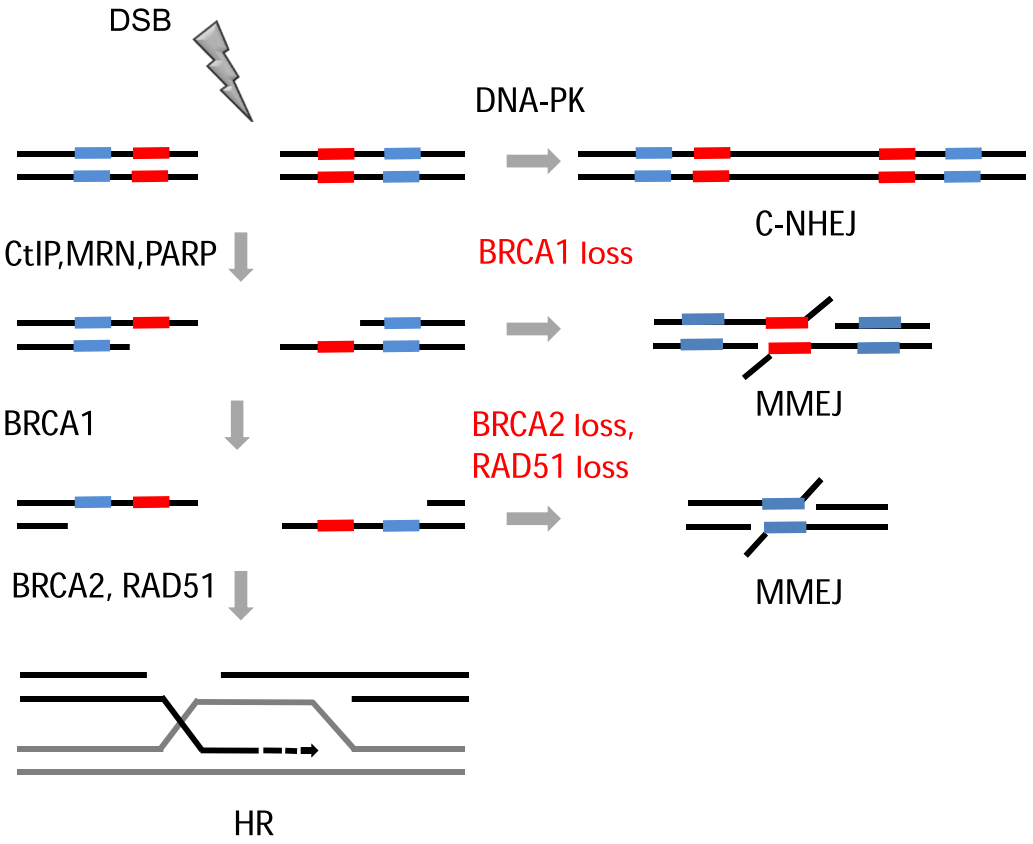


**Figure 6.** Model. DSBs are mainly repaired by C-NHEJ, however upon resection initiation by CtIP and MRN complex repair occurs via HR pathway. If HR is disrupted after initiation of resection, regions of microhomology on either side of the break will anneal, resulting in repair via the mutagenic MMEJ pathway.

cially in breast tumours (74–76). In agreement with these reports, our observations support a role for POLQ in facilitating MMEJ in human cancer cells. Also RPA has an established role in repressing MMEJ in *S. cerevisiae* by removing DNA secondary structures, which prevent RAD51 loading and therefore HR (45,77). Consistent with this, we demonstrate a striking role for RPA in suppressing mutagenic MMEJ in human cancer cells. This could reflect roles for RPA in early HR, thereby suppressing MMEJ and/or in binding ssDNA, thereby preventing spontaneous MMEJ, as previously proposed in *S. cerevisiae* (45). Our data, however, also identify dramatically increased MMEJ levels in cells following simultaneous depletion of POLQ and RPA. This is indicative of a role for RPA in suppressing MMEJ independently of POLQ, which could be explained by the suggested involvement of POLQ in a subset of Alt-NHEJ repair pathways specifically leading to insertions (78,79). Our results also suggest that there might be POLQ-dependent and POLQ-independent MMEJ pathways in human cancer cells, both of which are suppressed by RPA. Our data do not, however, exclude the possibility that the slight residual activity of POLQ following its siRNA-mediated knockdown, may contribute to the great MMEJ levels in cells co-depleted for RPA and POLQ. In this regard, a more in-depth analysis is required.

While our data show that MMEJ is enhanced when HR is impaired, the nature of the corresponding decrease in other forms of mutagenic NHEJ is less clear and could indicate inhibition of indel-forming C-NHEJ or other Alt-NHEJ events that are not dependent on junctional microhomologies (6). Further analyses are required to identify which DSB repair pathways are affected.

Our combined observations support a model (Figure 6) in which DSB repair in HR-proficient cells, results in a mutational signature with a particular balance between deletions with and without associated microhomologies. When HR is impaired, however, this balance is channeled toward deletions associated with microhomologies as a result of enhanced MMEJ. Mechanistically, we propose that, following DSB induction and initiation of resection, the repair pathway choice can switch from HR to MMEJ, depending on the availability of HR downstream proteins. In the absence of HR factors, HR is blocked, and the resected ends are poor substrates for C-NHEJ. As a result, microhomologous sequences present on ssDNA either side of the resected ends anneal via the mutagenic MMEJ repair mechanism leading to microhomology-mediated deletions. Also consistent with our findings, a recent study using MEFs found increased translocation levels following Rad54 deletion (44). RAD54 is a key HR factor promoting recombination through interactions with RAD51 (80). Although there is no sequence-based evidence for the use of microhomologies in generating translocation junctions, translocations were largely PARP-

1- and Lig 3-dependent suggesting that they had arisen via the MMEJ pathway (39,81).

Mutations in DNA DSB repair genes are common features in different human cancer types. Among the DSB repair pathways, MMEJ is necessarily mutagenic and is frequently associated with genomic rearrangements (39,82). Importantly, high-resolution sequencing studies have identified microhomologies as a prevalent mutational signature at rearrangement breakpoints in several cancer types including breast, colorectal and prostate adenocarcinomas (83,84). Our observations therefore suggest that the microhomology mutational signature in different types of malignancies may arise from failed HR at a stage after the initiation of resection. This mechanistic understanding of the interplay between HR and MMEJ repair pathways could be exploited to develop therapies for cancer patients deficient in these DSB repair pathways.

## SUPPLEMENTARY DATA

Supplementary Data are available at NAR Online.

## ACKNOWLEDGEMENTS

We would like to thank Jeremy Stark for the MMEJ reporter cell line, Atsushi Shibata and Hideaki Hogiwara for the NHEJ reporter cell line and Fereydoon Ahrabi for his advice on statistical analysis.

## FUNDING

Medical Research Council [MC_PC_12003 to S.S. and T.C.H.]; Cancer Research UK [C5255/A15935 to S.A., C38302/A12981 to G.P., C34326/A13092 to G.S.H.]; Clarendon Scholarship [to S.A., S.X.P., G.P]; BBSRC [BB/H003371/1 to A.C.G.P.]. Funding for open access charge: Medical Research Council [MC_PC_12003].
*Conflict of interest statement.* None declared.

## REFERENCES

1. Jeggo,P. and Lavin,M.F. (2009) Cellular radiosensitivity: how much better do we understand it? *Int. J. Radiat. Biol.*, **85**, 1061–1081.
2. Symington,L.S. and Gautier,J. (2011) Double-strand break end resection and repair pathway choice. *Annu. Rev. Genet.*, **45**, 247–271.
3. Kabotyanski,E.B., Gomelsky,L., Han,J.O., Stamato,T.D. and Roth,D.B. (1998) Double-strand break repair in Ku86- and XRCC4-deficient cells. *Nucleic Acids Res.*, **26**, 5333–5342.
4. Liang,F. and Jasin,M. (1996) Ku80-deficient cells exhibit excess degradation of extrachromosomal DNA. *J. Biol. Chem.*, **271**, 14405–14411.
5. Boulton,S.J. and Jackson,S.P. (1996) Saccharomyces cerevisiae Ku70 potentiates illegitimate DNA double-strand break repair and serves as a barrier to error-prone DNA repair pathways. *EMBO J.*, **15**, 5093–5103.
6. Decottignies,A. (2013) Alternative end-joining mechanisms: a historical perspective. *Front. Genet.*, **4**, 48.
7. Simsek,D., Brunet,E., Wong,S.Y., Katyal,S., Gao,Y., McKinnon,P.J., Lou,J., Zhang,L., Li,J., Rebar,E.J. *et al.* (2011) DNA ligase III promotes alternative nonhomologous end-joining during chromosomal translocation formation. *PLoS Genet.*, **7**, e1002080.
8. Bennardo,N., Cheng,A., Huang,N. and Stark,J.M. (2008) Alternative-NHEJ is a mechanistically distinct pathway of mammalian chromosome break repair. *PLoS Genet.*, **4**, e1000110.
9. Sartori,A.A., Lukas,C., Coates,J., Mistrik,M., Fu,S., Bartek,J., Baer,R., Lukas,J. and Jackson,S.P. (2007) Human CtIP promotes DNA end resection. *Nature*, **450**, 509–514.
10. Takeda,S., Nakamura,K., Taniguchi,Y. and Paull,T.T. (2007) Ctp1/CtIP and the MRN complex collaborate in the initial steps of homologous recombination. *Mol. Cell*, **28**, 351–352.
11. Gravel,S., Chapman,J.R., Magill,C. and Jackson,S.P. (2008) DNA helicases Sgs1 and BLM promote DNA double-strand break resection. *Genes Dev.*, **22**, 2767–2772.
12. Nimonkar,A.V., Ozsoy,A.Z., Genschel,J., Modrich,P. and Kowalczykowski,S.C. (2008) Human exonuclease 1 and BLM helicase interact to resect DNA and initiate DNA repair. *Proc. Natl. Acad. Sci. U.S.A.*, **105**, 16906–16911.
13. Stark,J.M., Pierce,A.J., Oh,J., Pastink,A. and Jasin,M. (2004) Genetic steps of mammalian homologous repair with distinct mutagenic consequences. *Mol. Cell. Biol.*, **24**, 9305–9316.
14. Moynahan,M.E., Chiu,J.W., Koller,B.H. and Jasin,M. (1999) Brca1 controls homology-directed DNA repair. *Mol. Cell*, **4**, 511–518.
15. Zhong,Q., Chen,C.F., Li,S., Chen,Y., Wang,C.C., Xiao,J., Chen,P.L., Sharp,Z.D. and Lee,W.H. (1999) Association of BRCA1 with the hRad50-hMre11-p95 complex and the DNA damage response. *Science*, **285**, 747–750.
16. Yu,X., Wu,L.C., Bowcock,A.M., Aronheim,A. and Baer,R. (1998) The C-terminal (BRCT) domains of BRCA1 interact in vivo with CtIP, a protein implicated in the CtBP pathway of transcriptional repression. *J. Biol. Chem.*, **273**, 25388–25392.
17. Cruz-Garcia,A., Lopez-Saavedra,A. and Huertas,P. (2014) BRCA1 accelerates CtIP-mediated DNA-end resection. *Cell Reports*, **9**, 451–459.
18. Wold,M.S. (1997) Replication protein A: a heterotrimeric, single-stranded DNA-binding protein required for eukaryotic DNA metabolism. *Annu. Rev. Biochem.*, **66**, 61–92.
19. Moynahan,M.E., Pierce,A.J. and Jasin,M. (2001) BRCA2 is required for homology-directed repair of chromosomal breaks. *Mol. Cell*, **7**, 263–272.
20. Wu,L. and Hickson,I.D. (2003) The Bloom's syndrome helicase suppresses crossing over during homologous recombination. *Nature*, **426**, 870–874.
21. West,S.C. (2003) Molecular views of recombination proteins and their control. *Nat. Rev. Mol. Cell Biol.*, **4**, 435–445.
22. Nassif,N., Penney,J., Pal,S., Engels,W.R. and Gloor,G.B. (1994) Efficient copying of nonhomologous sequences from ectopic sites via P-element-induced gap repair. *Mol. Cell. Biol.*, **14**, 1613–1625.
23. Ciccia,A. and Elledge,S.J. (2010) The DNA damage response: making it safe to play with knives. *Mol. Cell*, **40**, 179–204.
24. Deriano,L. and Roth,D.B. (2013) Modernizing the nonhomologus end-joining repertoire: alternative and classical NHEJ share the stage. *Annu. Rev. Genet.*, **47**, 433–455.
25. Mahaney,B.L., Meek,K. and Lees-Miller,S.P. (2009) Repair of ionizing radiation-induced DNA double-strand breaks by non-homologous end-joining. *Biochem. J.*, **417**, 639–650.
26. Lieber,M.R. (2010) The mechanism of double-strand DNA break repair by the nonhomologous DNA end-joining pathway. *Annu. Rev. Biochem.*, **79**, 181–211.
27. Meek,K., Dang,V. and Lees-Miller,S.P. (2008) DNA-PK: the means to justify the ends? *Adv. Immunol.*, **99**, 33–58.
28. Ferguson,D.O., Sekiguchi,J.M., Chang,S., Frank,K.M., Gao,Y., DePinho,R.A. and Alt,F.W. (2000) The nonhomologous end-joining pathway of DNA repair is required for genomic stability and the suppression of translocations. *Proc. Natl. Acad. Sci. U.S.A.*, **97**, 6630–6633.
29. Ghezraoui,H., Piganeau,M., Renouf,B., Renaud,J.B., Sallmyr,A., Ruis,B., Oh,S., Tomkinson,A.E., Hendrickson,E.A., Giovannangeli,C. *et al.* (2014) Chromosomal translocations in human cells are generated by canonical nonhomologous end-joining. *Mol. Cell*, **55**, 829–842.
30. Jones,R.E., Oh,S., Grimstead,J.W., Zimbric,J., Roger,L., Heppel,N.H., Ashelford,K.E., Liddiard,K., Hendrickson,E.A. and Baird,D.M. (2014) Escape from telomere-driven crisis is DNA ligase III dependent. *Cell Reports*, **8**, 1063–1076.
31. Audebert,M., Salles,B. and Calsou,P. (2004) Involvement of poly(ADP-ribose) polymerase-1 and XRCC1/DNA ligase III in an alternative route for DNA double-strand breaks rejoining. *J. Biol. Chem.*, **279**, 55117–55126.

32. Wang,M., Wu,W., Wu,W., Rosidi,B., Zhang,L., Wang,H. and Iliakis,G. (2006) PARP-1 and Ku compete for repair of DNA double strand breaks by distinct NHEJ pathways. *Nucleic Acids Res.*, **34**, 6170–6182.
33. Hochegger,H., Dejsuphong,D., Fukushima,T., Morrison,C., Sonoda,E., Schreiber,V., Zhao,G.Y., Saberi,A., Masutani,M., Adachi,N. *et al.* (2006) Parp-1 protects homologous recombination from interference by Ku and Ligase IV in vertebrate cells. *EMBO J.*, **25**, 1305–1314.
34. Haince,J.F., McDonald,D., Rodrigue,A., Dery,U., Masson,J.Y., Hendzel,M.J. and Poirier,G.G. (2008) PARP1-dependent kinetics of recruitment of MRE11 and NBS1 proteins to multiple DNA damage sites. *J. Biol. Chem.*, **283**, 1197–1208.
35. Wang,H., Rosidi,B., Perrault,R., Wang,M., Zhang,L., Windhofer,F. and Iliakis,G. (2005) DNA ligase III as a candidate component of backup pathways of nonhomologous end joining. *Cancer Res.*, **65**, 4020–4030.
36. Seki,M., Masutani,C., Yang,L.W., Schuffert,A., Iwai,S., Bahar,I. and Wood,R.D. (2004) High-efficiency bypass of DNA damage by human DNA polymerase Q. *EMBO J.*, **23**, 4484–4494.
37. Yousefzadeh,M.J., Wyatt,D.W., Takata,K., Mu,Y., Hensley,S.C., Tomida,J., Bylund,G.O., Doublie,S., Johansson,E., Ramsden,D.A. *et al.* (2014) Mechanism of suppression of chromosomal instability by DNA polymerase POLQ. *PLoS Genet.*, **10**, e1004654.
38. Kent,T., Chandramouly,G., McDevitt,S.M., Ozdemir,A.Y. and Pomerantz,R.T. (2015) Mechanism of microhomology-mediated end-joining promoted by human DNA polymerase theta. *Nat. Struct. Mol. Biol.*, **22**, 230–237.
39. McVey,M. and Lee,S.E. (2008) MMEJ repair of double-strand breaks (director's cut): deleted sequences and alternative endings. *Trends Genet.*, **24**, 529–538.
40. Kennedy,R.D. and D'Andrea,A.D. (2006) DNA repair pathways in clinical practice: lessons from pediatric cancer susceptibility syndromes. *J. Clin. Oncol.*, **24**, 3799–3808.
41. Huertas,P. (2010) DNA resection in eukaryotes: deciding how to fix the break. *Nat. Struct. Mol. Biol.*, **17**, 11–16.
42. Iliakis,G. (2009) Backup pathways of NHEJ in cells of higher eukaryotes: cell cycle dependence. *Radiother. Oncol.*, **92**, 310–315.
43. Cheng,Q., Barboule,N., Frit,P., Gomez,D., Bombarde,O., Couderc,B., Ren,G.S., Salles,B. and Calsou,P. (2011) Ku counteracts mobilization of PARP1 and MRN in chromatin damaged with DNA double-strand breaks. *Nucleic Acids Res.*, **39**, 9605–9619.
44. Soni,A., Siemann,M., Grabos,M., Murmann,T., Pantelias,G.E. and Iliakis,G. (2014) Requirement for Parp-1 and DNA ligases 1 or 3 but not of Xrcc1 in chromosomal translocation formation by backup end joining. *Nucleic Acids Res.*, **42**, 6380–6392.
45. Deng,S.K., Gibb,B., de Almeida,M.J., Greene,E.C. and Symington,L.S. (2014) RPA antagonizes microhomology-mediated repair of DNA double-strand breaks. *Nat. Struct. Mol. Biol.*, **21**, 405–412.
46. Mateos-Gomez,P.A., Gong,F., Nair,N., Miller,K.M., Lazzerini-Denchi,E. and Sfeir,A. (2015) Mammalian polymerase theta promotes alternative NHEJ and suppresses recombination. *Nature*, **518**, 254–257.
47. Ceccaldi,R., Liu,J.C., Amunugama,R., Hajdu,I., Primack,B., Petalcorin,M.I., O'Connor,K.W., Konstantinopoulos,P.A., Elledge,S.J., Boulton,S.J. *et al.* (2015) Homologous-recombination-deficient tumours are dependent on Poltheta-mediated repair. *Nature*, **518**, 258–262.
48. Jiang,G., Plo,I., Wang,T., Rahman,M., Cho,J.H., Yang,E., Lopez,B.S. and Xia,F. (2013) BRCA1-Ku80 protein interaction enhances end-joining fidelity of chromosomal double-strand breaks in the G1 phase of the cell cycle. *J. Biol. Chem.*, **288**, 8966–8976.
49. Badie,S., Carlos,A.R., Folio,C., Okamoto,K., Bouwman,P., Jonkers,J. and Tarsounas,M. (2015) BRCA1 and CtIP promote alternative non-homologous end-joining at uncapped telomeres. *EMBO J.*, **34**, 410–424.
50. Gravells,P., Ahrabi,S., Vangala,R.K., Tomita,K., Brash,J.T., Brustle,L.A., Chung,C., Hong,J.M., Kaloudi,A., Humphrey,T.C. *et al.* (2015) Use of the HPRT gene to study nuclease-induced DNA double-strand break repair. *Hum. Mol. Genet.*, **24**, 7097–7110.
51. Pfister,S.X., Ahrabi,S., Zalmas,L.P., Sarkar,S., Aymard,F., Bachrati,C.Z., Helleday,T., Legube,G., La Thangue,N.B., Porter,A.C. *et al.* (2014) SETD2-dependent histone H3K36 trimethylation is required for homologous recombination repair and genome stability. *Cell Reports*, **7**, 2006–2018.
52. Pierce,A.J., Johnson,R.D., Thompson,L.H. and Jasin,M. (1999) XRCC3 promotes homology-directed repair of DNA damage in mammalian cells. *Genes Dev.*, **13**, 2633–2638.
53. Gunn,A. and Stark,J.M. (2012) I-SceI-based assays to examine distinct repair outcomes of mammalian chromosomal double strand breaks. *Methods Mol. Biol.*, **920**, 379–391.
54. Ogiwara,H., Ui,A., Otsuka,A., Satoh,H., Yokomi,I., Nakajima,S., Yasui,A., Yokota,J. and Kohno,T. (2011) Histone acetylation by CBP and p300 at double-strand break sites facilitates SWI/SNF chromatin remodeling and the recruitment of non-homologous end joining factors. *Oncogene*, **30**, 2135–2146.
55. Porter,A.C. and Itzhaki,J.E. (1993) Gene targeting in human somatic cells. Complete inactivation of an interferon-inducible gene. *Eur. J. Biochem.*, **218**, 273–281.
56. Prakash,R., Zhang,Y., Feng,W. and Jasin,M. (2015) Homologous recombination and human health: the roles of BRCA1, BRCA2, and associated proteins. *Cold Spring Harb. Perspect. Biol.*, **7**, a016600.
57. Zhao,Y., Thomas,H.D., Batey,M.A., Cowell,I.G., Richardson,C.J., Griffin,R.J., Calvert,A.H., Newell,D.R., Smith,G.C. and Curtin,N.J. (2006) Preclinical evaluation of a potent novel DNA-dependent protein kinase inhibitor NU7441. *Cancer Res.*, **66**, 5354–5362.
58. Iliakis,G. (2009) Backup pathways of NHEJ in cells of higher eukaryotes: cell cycle dependence. *Radiother. Oncol.*, **92**, 310–315.
59. Truong,L.N., Li,Y., Shi,L.Z., Hwang,P.Y., He,J., Wang,H., Razavian,N., Berns,M.W. and Wu,X. (2013) Microhomology-mediated End Joining and Homologous Recombination share the initial end resection step to repair DNA double-strand breaks in mammalian cells. *Proc. Natl. Acad. Sci. U.S.A.*, **110**, 7720–7725.
60. Jasin,M. and Rothstein,R. (2013) Repair of strand breaks by homologous recombination. *Cold Spring Harb. Perspect. Biol.*, **5**, a012740.
61. Beck,C., Robert,I., Reina-San-Martin,B., Schreiber,V. and Dantzer,F. (2014) Poly(ADP-ribose) polymerases in double-strand break repair: Focus on PARP1, PARP2 and PARP3. *Exp. Cell Res.*, **329**, 18–25.
62. Howard,S.M., Yanez,D.A. and Stark,J.M. (2015) DNA damage response factors from diverse pathways, including DNA crosslink repair, mediate alternative end joining. *Plos Genet.*, **11**, e1004943.
63. Zimmermann,M., Lottersberger,F., Buonomo,S.B., Sfeir,A. and de Lange,T. (2013) 53BP1 regulates DSB repair using Rif1 to control 5' end resection. *Science*, **339**, 700–704.
64. Hanahan,D. and Weinberg,R.A. (2011) Hallmarks of cancer: the next generation. *Cell*, **144**, 646–674.
65. Gauss,G.H. and Lieber,M.R. (1996) Mechanistic constraints on diversity in human V(D)J recombination. *Mol. Cell. Biol.*, **16**, 258–269.
66. Pannunzio,N.R., Li,S., Watanabe,G. and Lieber,M.R. (2014) Non-homologous end joining often uses microhomology: implications for alternative end joining. *DNA repair*, **17**, 74–80.
67. Symington,L.S. (2014) End resection at double-strand breaks: mechanism and regulation. *Cold Spring Harb. Perspect. Biol.*, **6**, a016436.
68. Nakamura,K., Kogame,T., Oshiumi,H., Shinohara,A., Sumitomo,Y., Agama,K., Pommier,Y., Tsutsui,K.M., Tsutsui,K., Hartsuiker,E. *et al.* (2010) Collaborative action of Brca1 and CtIP in elimination of covalent modifications from double-strand breaks to facilitate subsequent break repair. *PLoS Genet.*, **6**, e1000828.
69. Reczek,C.R., Szabolcs,M., Stark,J.M., Ludwig,T. and Baer,R. (2013) The interaction between CtIP and BRCA1 is not essential for resection-mediated DNA repair or tumor suppression. *J. Cell Biol.*, **201**, 693–707.
70. Yun,M.H. and Hiom,K. (2009) CtIP-BRCA1 modulates the choice of DNA double-strand-break repair pathway throughout the cell cycle. *Nature*, **459**, 460–463.
71. Thompson,E.G., Fares,H. and Dixon,K. (2012) BRCA1 requirement for the fidelity of plasmid DNA double-strand break repair in cultured breast epithelial cells. *Environ. Mol. Mutagen.*, **53**, 32–43.
72. Baldeyron,C., Jacquemin,E., Smith,J., Jacquemont,C., De Oliveira,I., Gad,S., Feunteun,J., Stoppa-Lyonnet,D. and Papadopoulo,D. (2002) A single mutated BRCA1 allele leads to impaired fidelity of double strand break end-joining. *Oncogene*, **21**, 1401–1410.

73. Wang,H.C., Chou,W.C., Shieh,S.Y. and Shen,C.Y. (2006) Ataxia telangiectasia mutated and checkpoint kinase 2 regulate BRCA1 to promote the fidelity of DNA end-joining. *Cancer Res.*, **66**, 1391–1400.
74. Higgins,G.S., Harris,A.L., Prevo,R., Helleday,T., McKenna,W.G. and Buffa,F.M. (2010) Overexpression of POLQ confers a poor prognosis in early breast cancer patients. *Oncotarget*, **1**, 175–184.
75. Kawamura,K., Bahar,R., Seimiya,M., Chiyo,M., Wada,A., Okada,S., Hatano,M., Tokuhisa,T., Kimura,H., Watanabe,S. *et al.* (2004) DNA polymerase theta is preferentially expressed in lymphoid tissues and upregulated in human cancers. *Int. J. Cancer*, **109**, 9–16.
76. Lemee,F., Bergoglio,V., Fernandez-Vidal,A., Machado-Silva,A., Pillaire,M.J., Bieth,A., Gentil,C., Baker,L., Martin,A.L., Leduc,C. *et al.* (2010) DNA polymerase theta up-regulation is associated with poor survival in breast cancer, perturbs DNA replication, and promotes genetic instability. *Proc. Natl. Acad. Sci. U.S.A.*, **107**, 13390–13395.
77. McVey,M. (2014) RPA puts the brakes on MMEJ. *Nat. Struct. Mol. Biol.*, **21**, 348–349.
78. Koole,W., van Schendel,R., Karambelas,A.E., van Heteren,J.T., Okihara,K.L. and Tijsterman,M. (2014) A Polymerase Theta-dependent repair pathway suppresses extensive genomic instability at endogenous G4 DNA sites. *Nat. Commun.*, **5**, 3216.
79. Yu,A.M. and McVey,M. (2010) Synthesis-dependent microhomology-mediated end joining accounts for multiple types of repair junctions. *Nucleic Acids Res.*, **38**, 5706–5717.
80. Golub,E.I., Kovalenko,O.V., Gupta,R.C., Ward,D.C. and Radding,C.M. (1997) Interaction of human recombination proteins Rad51 and Rad54. *Nucleic Acids Res.*, **25**, 4106–4110.
81. Liang,L., Deng,L., Nguyen,S.C., Zhao,X., Maulion,C.D., Shao,C. and Tischfield,J.A. (2008) Human DNA ligases I and III, but not ligase IV, are required for microhomology-mediated end joining of DNA double-strand breaks. *Nucleic Acids Res.*, **36**, 3297–3310.
82. Ottaviani,D., LeCain,M. and Sheer,D. (2014) The role of microhomology in genomic structural variation. *Trends Genet.*, **30**, 85–94.
83. Conrad,D.F., Bird,C., Blackburne,B., Lindsay,S., Mamanova,L., Lee,C., Turner,D.J. and Hurles,M.E. (2010) Mutation spectrum revealed by breakpoint sequencing of human germline CNVs. *Nat. Genet.*, **42**, 385–391.
84. Bass,A.J., Lawrence,M.S., Brace,L.E., Ramos,A.H., Drier,Y., Cibulskis,K., Sougnez,C., Voet,D., Saksena,G., Sivachenko,A. *et al.* (2011) Genomic sequencing of colorectal adenocarcinomas identifies a recurrent VTI1A-TCF7L2 fusion. *Nat. Genet.*, **43**, 964–968.

nature COMMUNICATIONS

ARTICLE

Received 4 Dec 2015 | Accepted 17 Jun 2016 | Published 25 Jul 2016

DOI: 10.1038/ncomms12308 OPEN

# The anti-malarial atovaquone increases radiosensitivity by alleviating tumour hypoxia

Thomas M. Ashton[1], Emmanouil Fokas[1], Leoni A. Kunz-Schughart[1,2], Lisa K. Folkes[1], Selvakumar Anbalagan[1], Melanie Huether[2], Catherine J. Kelly[1], Giacomo Pirovano[1], Francesca M. Buffa[1], Ester M. Hammond[1], Michael Stratford[1], Ruth J. Muschel[1], Geoff S. Higgins[1,*] & William Gillies McKenna[1,*]

Tumour hypoxia renders cancer cells resistant to cancer therapy, resulting in markedly worse clinical outcomes. To find clinical candidate compounds that reduce hypoxia in tumours, we conduct a high-throughput screen for oxygen consumption rate (OCR) reduction and identify a number of drugs with this property. For this study we focus on the anti-malarial, atovaquone. Atovaquone rapidly decreases the OCR by more than 80% in a wide range of cancer cell lines at pharmacological concentrations. In addition, atovaquone eradicates hypoxia in FaDu, HCT116 and H1299 spheroids. Similarly, it reduces hypoxia in FaDu and HCT116 xenografts in nude mice, and causes a significant tumour growth delay when combined with radiation. Atovaquone is a ubiquinone analogue, and decreases the OCR by inhibiting mitochondrial complex III. We are now undertaking clinical studies to assess whether atovaquone reduces tumour hypoxia in patients, thereby increasing the efficacy of radiotherapy.

[1] CRUK/MRC Oxford Institute for Radiation Oncology, Old Road Campus Research Building, Roosevelt Drive, Oxford OX3 7DQ, UK. [2] OncoRay – National Center for Radiation Research in Oncology, Faculty of Medicine and University Hospital Carl Gustav Carus, TU Dresden, and Helmholtz-Zentrum Dresden-Rossendorf, Institute of Radiooncology, Dresden, P.O. Box 41, 01307, Germany. * These authors contributed equally to this work. Correspondence and requests for materials should be addressed to G.S.H. (email: geoffrey.higgins@oncology.ox.ac.uk) or to W.G.M. (email: gillies.mckenna@gmail.com).

Solid malignancies frequently have regions of hypoxia[1]. Many studies have focused on the abnormal tumour vasculature as a determinant of tumour hypoxia. However, tumour oxygenation reflects the balance between delivery and consumption, and because tumour cells have a high level of oxygen consumption, and reduced delivery of oxygen to the tumour due to abnormal vasculature, both components play a role[2]. Hypoxia is associated with poor clinical outcomes due to both local recurrence and an increased probability of metastasis[3]. Gray and his colleagues in the 1950s were the first to suggest that hypoxia would affect the outcome of radiotherapy because hypoxic tumour cells are up to three times more radioresistant than normoxic tumour cells[1,3,4]. This radioresistance is due to the absence of the oxygen enhancement effect, which is a result of the direct physicochemical reaction of oxygen with the broken ends of the DNA strands that result from radiation, creating stable organic peroxides that are more difficult for the cell to repair.

Vascular remodelling has been used previously as a strategy to relieve tumour hypoxia and improve radiation response, and it has been demonstrated that a number of signal transduction inhibitors have such an effect[5]. A possible alternative strategy to reduce tumour hypoxia, and therefore to increase radiosensitivity, is to reduce the cellular oxygen consumption rate (OCR). Reduction of the OCR in three-dimensional (3D) multicellular tumour spheroids causes a decrease in the volume of the central region of hypoxia by increasing the availability of oxygen throughout the spheroid[6–8]. These studies in spheroids demonstrate that reducing the OCR can alleviate hypoxia in an avascular system. Mathematical modelling suggests that a 30% decrease in the OCR would even abolish severe tumour hypoxia, and that this could be a more effective approach to reduce hypoxia than attempts at elevating blood flow or increasing the oxygen levels in blood[8]. An additional advantage of assessing the OCR is that it is amenable to high-throughput screening, which vascular remodelling is not. Drugs that reduce the OCR have been identified previously by screens designed to identify inhibitors of the HIF-1 pathway[9,10], but to our knowledge, no high-throughput screens designed to identify novel inhibitors of the OCR in cancer cells have been published.

The anti-diabetic, metformin, is the only FDA-approved drug that has been shown to reduce both the OCR and tumour hypoxia, and its mechanism of action is inhibition of mitochondrial complex I (refs 11,12). However, at pharmacological concentrations of metformin there is a reduction in the OCR of only 10–20%, suggesting that compounds with a more significant effect on the OCR may have a more profound effect on tumour hypoxia[12]. Thus there is a need to identify more drugs that alleviate tumour hypoxia by reducing the OCR.

To identify drugs that decrease the OCR of cancer cells and could be used as modifiers of tumour hypoxia in a clinical setting, we screen a library of 1,697 FDA-approved compounds. This screen identifies atovaquone, a drug primarily used to treat malaria and pneumocystis pneumonia. Atovaquone reduces the OCR by inhibition of mitochondrial complex III (the cytochrome $bc_1$ complex) at pharmacologically achievable concentrations, alleviates hypoxia both in spheroids and in xenografted tumours, and causes a significant tumour growth delay in combination with radiation.

## Results

**High-throughput screening to assess oxygen consumption**. To identify compounds that reduce the OCR, FaDu hypopharyngeal carcinoma cells were incubated with 1,697 FDA-approved compounds at 2 or 10 μM for 24 h (Fig. 1a). The growth medium was replaced with an assay medium containing 5 mM galactose, 5 mM pyruvate and 4 mM glutamine. Growth in galactose promotes oxidative phosphorylation[13]. The mitochondrial-specific OCR was determined by measuring basal OCR and subtracting the OCR measured following injection of 2 μM antimycin A to inhibit mitochondrial respiration. The OCR measurements were corrected for cell number using the relative Hoechst fluorescence of the cells fixed immediately after the assay. Compounds that caused a reduction in cell number of more than 66% compared with the DMSO control wells for each plate were excluded. The compounds with the top 130 rank products were chosen for the secondary screen (Supplementary Data 1). The secondary screen was conducted using the same protocol as the primary screen, except FaDu cells were incubated with the compounds at 80 nM, 400 nM, 2 μM or 10 μM, and the assay medium contained 5 mM glucose instead of 5 mM galactose to more closely mimic the physiological setting (Fig. 1b and Supplementary Data 1). The highest ranked compounds that caused a decrease in the OCR in FaDu cells at 10 μM and are approved for systemic use in humans are shown in Table 1.

Compounds were subsequently excluded from further study based on a range of criteria (Supplementary Table 1): Known *in vivo* hypoxia modifiers or radiosensitisers such as acriflavinium[14], compounds with an unsuitable safety profile such as emetine[15], anti-helminths with poor bioavailability such as pyrvinium[16], and compounds for which the maximum achievable plasma concentration in patients is lower than the concentration required to cause a significant reduction in the OCR, such as dactinomycin[17]. The anti-malarial, atovaquone was selected for further evaluation, because it is not known to reduce hypoxia *in vivo*, it has an excellent safety profile, it has ideal pharmacokinetic properties for a hypoxia modifier, and has low cost[18].

To evaluate the effect of atovaquone on other cell lines, the OCR was measured for 4.5 h after its addition. A significant decrease in the OCR of 78.7% to 90.0% compared with the DMSO control was observed after 2 h at 10 μM in FaDu, HCT116 colorectal carcinoma, DLD-1 colorectal adenocarcinoma, H1299 lung carcinoma, A549 lung carcinoma, H460 large cell lung carcinoma, MCF7 breast ductal carcinoma and T24 bladder carcinoma cells, with a lesser but still significant decrease of 57.6% in PSN-1 pancreatic adenocarcinoma cells (Fig. 1c–e and Supplementary Fig. 1a). This was a dose-dependent effect, with a smaller, but still significant, decrease observed at 2 μM, and no significant decrease observed at 1 μM. There was no significant effect on the cell number relative to the DMSO control in FaDu, HCT116 and H1299 cells at concentrations between 10 and 100 μM, or in the other cell lines at 10 μM during the course of the experiment (Supplementary Fig. 1b,c). Statistically significant decreases in cell survival of 25.9–56.2% were observed in FaDu, HCT116 and H1299 cells after a longer incubation of 24 h with 20 or 30 μM atovaquone, but cell survival was partially rescued following 4 days recovery in drug-free medium (Supplementary Fig. 1d). The widely used anti-cancer therapeutics, 5-fluorouracil, docetaxel and cytarabine caused a significant decrease in FaDu cell survival of 18.7–37.8% after 24 h incubation at either 2 μM or 10, but this did not correspond with a significant decrease in the OCR (Supplementary Fig. 2a,b). This demonstrates that a decrease in cell survival observed following protracted incubation with an anti-proliferative drug does not necessarily correlate with a decrease in the OCR. Thus atovaquone reduces the OCR in cancer cells from a wide range of tumour types.

**ATO affects spheroid hypoxia and radiation response**. Reduction of the OCR in 3D multicellular tumour spheroids can lead to a decrease in hypoxia[6–8]. FaDu, HCT116 and H1299 spheroids of 550–650 μm in diameter were treated with 10, 20 or 30 μM atovaquone for 24 h, and the hypoxic fraction was evaluated by

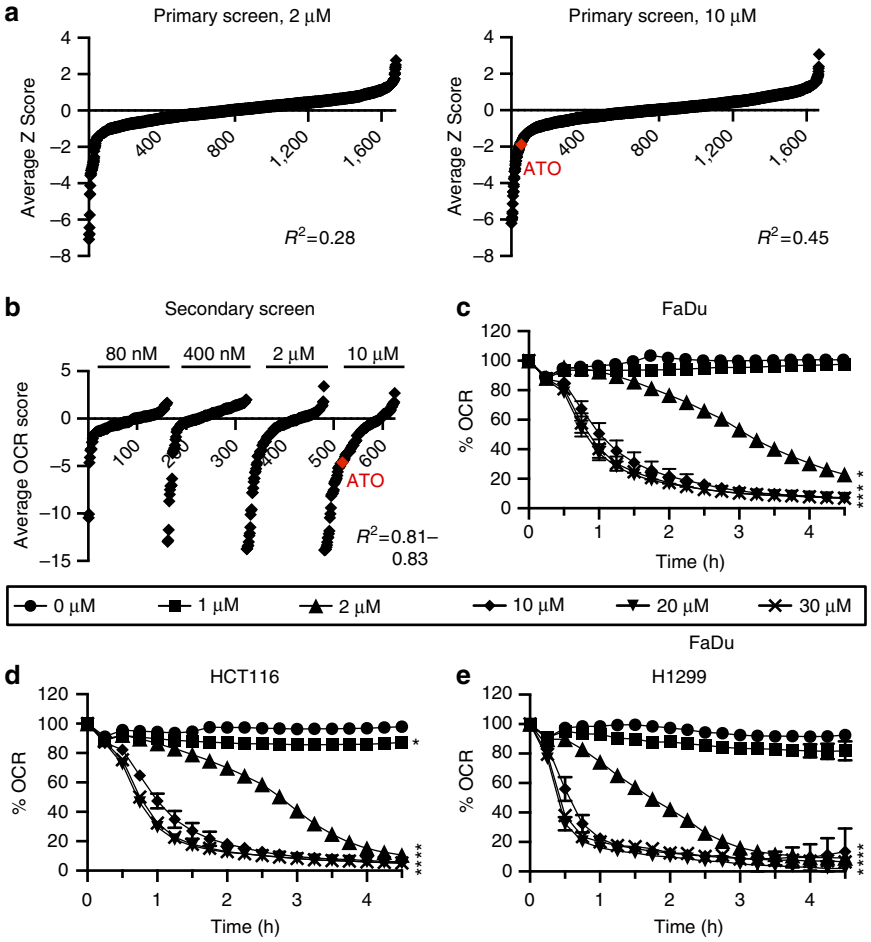


**Figure 1 | A screen to discover compounds that decrease the OCR of FaDu cells.** (**a**) For the primary screen, FaDu cells were grown in galactose-containing medium and incubated with a library of 1697 FDA-approved compounds for 24 h. The mitochondrial specific OCR was measured, and subsequent hoechst staining was used to correct for cell number. (**b**) For the secondary screen, FaDu cells were grown in glucose-containing medium, incubated with the compounds for 24 h, and then the mitochondrial-specific OCR was measured and normalized to cell number. (**c**–**e**) The OCR of FaDu, HCT116 and H1299 cells were measured for 4.5 h after injection of atovaquone. The % OCR post injection is shown relative to the DMSO control and normalized to the relative cell number obtained by hoechst staining at the end of the experiment. The data are representative of three independent experiments (mean ± s.d.). One-way ANOVA were performed to assess statistical significance at 4.5 h after injection of atovaquone with Bonferroni post correction (*$P<0.0001$). ATO, atovaquone.

**Table 1 | The highest ranked compounds that reduce the OCR of FaDu cells at 10 μM.**

| Rank | Compound |
|---|---|
| 1 | Pyrvinium |
| 2 | Berberine |
| 3 | Niclosamide |
| 4 | Acriflavinium |
| 5 | Sorafenib |
| 6 | Emetine |
| 7 | Plicamycin |
| 8 | Suloctidil |
| 9 | Pentamidine |
| 10 | Amsacrine |
| 11 | Phenformin |
| 12 | Irinotecan |
| 13 | Itraconazole |
| 14 | Mitomycin |
| 15 | Atovaquone |
| 16 | Hydroxyprogesterone |
| 17 | Cyclosporine |
| 18 | Fenofibrate |

EF5 staining. There was complete loss of hypoxia in FaDu spheroids at 30 μM, and in HCT116 and H1299 spheroids at 20 μM atovaquone (Fig. 2a,b). It is possible that a decrease in EF5 staining could be caused by an increase in cell death[7]. To exclude this possibility, the spheroids were washed and allowed to recover in drug-free medium for 24 h, resulting in the return of hypoxia (Fig. 2a,b). None of the treatments caused a significant decrease in the diameter of FaDu, HCT116 or H1299 spheroids (Fig. 2c). Taken together, these results indicate that the observed decrease in the OCR induced by atovaquone corresponds to a decrease in hypoxia in an avascular 3D tumour environment.

To determine whether the alleviation of spheroid hypoxia translated to an improvement in radiation response, FaDu spheroids were treated for 24 h with 30 μM atovaquone, irradiated at 10 Gy, and then allowed to recover in fresh medium. For unirradiated spheroids, atovaquone treatment did not cause a significant difference in spheroid growth after 20 days (Fig. 2d). Irradiation at 10 Gy caused dissociation of both the DMSO and atovaquone-treated spheroids, but 90.91% of the DMSO-treated spheroids reformed by 60 days after irradiation, compared with only 37.93% of atovaquone treated spheroids

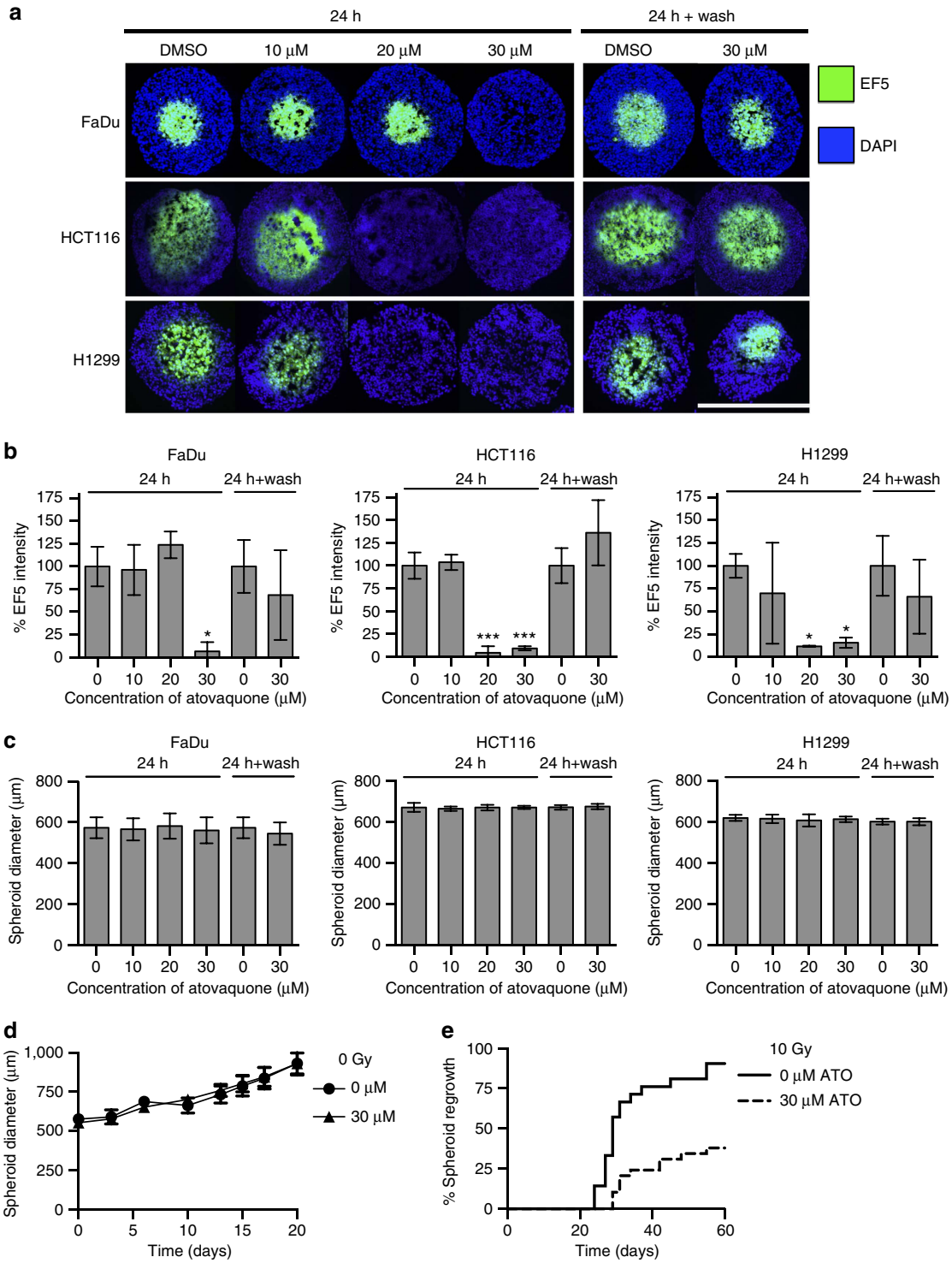


**Figure 2 | Atovaquone alleviates spheroid hypoxia and improves radiation response.** (**a**,**b**) FaDu, HCT116 and H1299 spheroids were treated with DMSO or atovaquone either for 24 h, or for 24 h followed by recovery for 24 h in drug-free medium, as indicated. Hypoxia was assessed by staining central spheroid sections for EF5 (green), with DAPI as a nuclear counterstain (blue). Scale bar, 600 μm. % Mean EF5 fluorescence intensity is presented relative to the DMSO controls. (**c**) Average spheroid diameter. Hypoxia was assessed in at least five spheroids per treatment for each experiment ($n=3$). One-way ANOVA was performed to assess statistical significance with Bonferroni post correction ($^{*}P>0.05$, $^{***}P<0.001$). (**d**,**e**) FaDu spheroids were treated with DMSO or 30 μM atovaquone for 24 h, and then received either 0 Gy (**d**) or 10 Gy (**e**). After treatment, the spheroids were allowed to recover in drug-free medium. Time post treatment is shown (days). One replicate of the experiment was conducted with at least 22 spheroids in each treatment group. All values are presented as mean ± s.d.

(Fig. 2e). This decrease in irradiated spheroid regrowth following atovaquone treatment is likely due to the observed reduction in spheroid hypoxia.

**ATO inhibits mitochondrial complex III.** As a ubiquinone analogue, the primary clinical mechanism of action of atovaquone is inhibition of *Plasmodium* and *Pneumocystis* complex III

(refs 19–21). To investigate whether atovaquone also inhibits complex III in human cancer cells, the activity of the ETC complexes I–IV was assessed in FaDu cells permeabilized with digitonin. Digitonin (0.005%) was sufficient to permeabilize the cells, allowing respiration of succinate, a substrate that does not cross intact cell membranes (Supplementary Fig. 2c). Complex I-dependent respiration was significantly inhibited by 30 μM atovaquone, the complex III inhibitor, myxothiazol and the complex I inhibitor, rotenone (Fig. 3a). Complex II-dependent respiration was significantly inhibited by 30 μM atovaquone, myxothiazol and the complex II inhibitor, malonate. Complex III-dependent respiration was significantly inhibited by 30 μM atovaquone, myxothiazol and the complex III inhibitor, antimycin A. Complex IV-dependent respiration was significantly inhibited by the complex IV inhibitor, sodium azide, but not by 30 μM atovaquone, and was less significantly inhibited by myxothiazol. Taken together, these results suggest that the primary mechanism of action of atovaquone in FaDu cells is inhibition of complex III, which then causes a decrease in the activity of the upstream ETC complexes.

To study complex III in isolation from the other ETC complexes, the reduction of excess cytochrome *c* was measured in mitochondria isolated from FaDu cells, a reaction catalysed by complex III. There was a significant decrease in complex II/III activity by the complex II inhibitor, malonate, and by the complex III inhibitors, antimycin, myxothiazol and 30 μM atovaquone (Fig. 3b). Due to the dependence of this assay on complex II activity, a complex II-specific assay was performed in parallel using mitochondria isolated from FaDu cells. There was a significant decrease in complex II activity by the complex II inhibitor, malonate (Fig. 3c). However, there was no inhibition of complex II activity by the complex III inhibitors, antimycin,

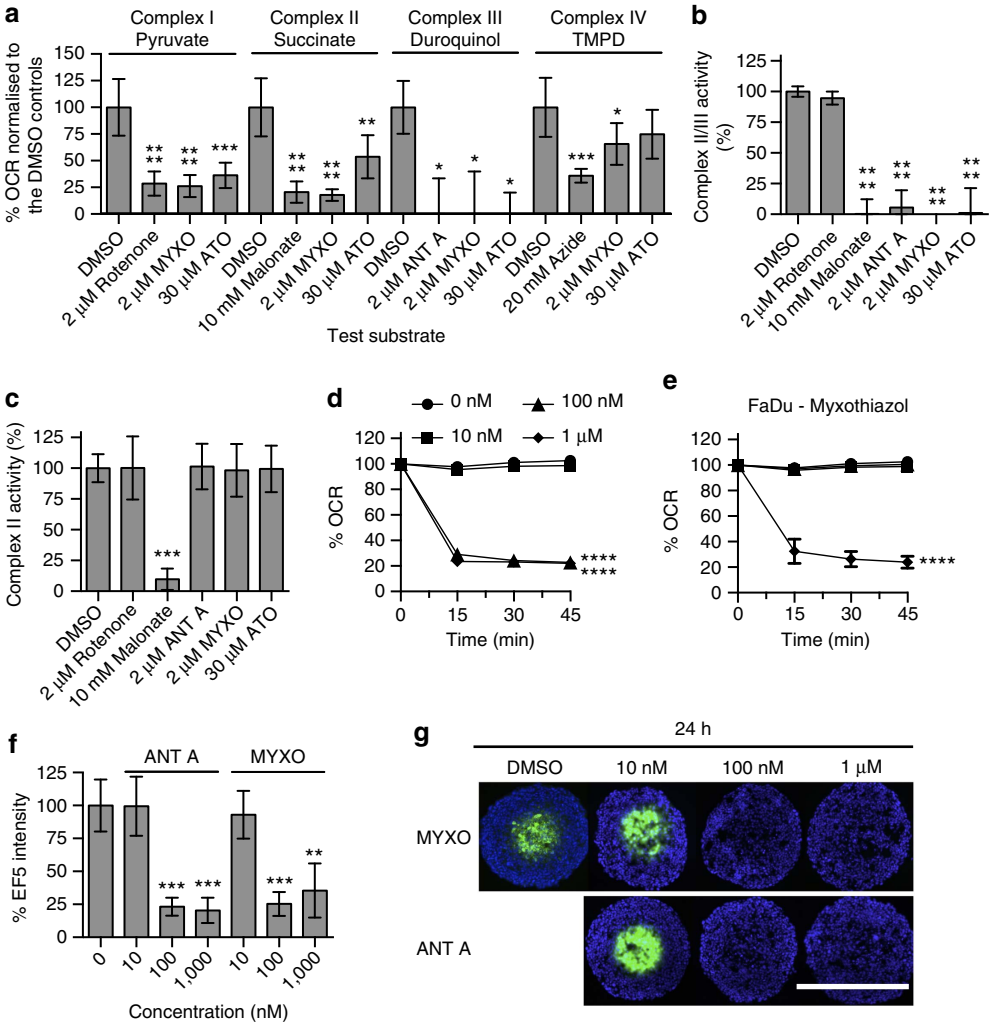


**Figure 3 | Atovaquone inhibits complex III activity.** (**a**) The effect of atovaquone on complex I-, II-, III- or IV-dependent respiration in FaDu cells permeabilized with 0.005% digitonin. The % OCR was measured immediately after permeabilization. (**b**) Complex II/III activity was measured in mitochondria isolated from FaDu cells 15 min after compound addition. (**c**) Complex II activity was measured in mitochondria isolated from FaDu cells 15 min after compound addition. (**d**,**e**) The OCR of FaDu cells was measured for 45 min after injection of antimycin A (**d**) or myxothiazol (**e**). The % OCR post injection is shown relative to the DMSO control and normalized to the relative cell number obtained by hoechst staining at the end of the experiment. The data is representative of three independent experiments. (**f**,**g**) FaDu spheroids were treated with DMSO, antimycin A or myxothiazol for 24 h. Hypoxia was assessed by staining central spheroid sections for EF5 (green), with DAPI as a nuclear counterstain (blue). Scale bar, 600 μm. % Mean EF5 fluorescence intensity is presented relative to the DMSO controls. Hypoxia was assessed in at least five spheroids per treatment for each experiment ($n=3$). One-way ANOVA with Bonferroni was performed for all of the experiments ($n=3$, mean ± s.d., $^{****}P<0.0001$, $^{***}P<0.001$, $^{**}P<0.01$, $^{*}P<0.05$). ANT A, antimycin A; ATO, atovaquone; MYXO, myxothiazol.

myxothiazol or 30 μM atovaquone. These findings were also observed in mitochondria isolated from bovine heart (Supplementary Fig. 2d,e). To demonstrate that complex III inhibition is sufficient to reduce the OCR, FaDu cells were incubated with antimycin A or myxothiazol and the OCR was measured for 45 min. A rapid and significant decrease in the OCR was observed in a dose-dependent manner for both inhibitors, with no decrease at 10 nM, but a significant decrease at 1 μM (Fig. 3d,e). Furthermore, incubation of FaDu spheroids for 24 h with 1 μM antimycin or myxothiazol eliminated spheroid hypoxia without affecting spheroid size, whereas no reduction in hypoxia was observed at 10 nM (Fig. 3f,g and Supplementary Fig. 2f). These findings indicate that atovaquone specifically inhibits complex III in FaDu cells, and that complex III inhibition is sufficient to reduce both the OCR and spheroid hypoxia.

**ATO inhibits pyrimidine synthesis**. Dihydroorotate dehydrogenase (DHODH) is an enzyme of the *de novo* pyrimidine synthesis pathway situated on the inner mitochondrial membrane (Fig. 4a). In biochemical assays, atovaquone inhibits not only complex III, but also DHODH[22]. To investigate whether a known DHODH inhibitor could reduce the OCR, FaDu cells were incubated for 2 h with leflunomide[23,24], which caused a dose-dependent decrease in the OCR (Fig. 4b). However, inhibition of the pyrimidine synthesis pathway downstream of DHODH by the orotidylic acid decarboxylase inhibitor, 6-azauridine (6-Aza), or by the ribonucleotide reductase inhibitor, hydroxyurea[25,26] did not cause a decrease in the OCR of FaDu cells after 24 h incubation (Fig. 4c). The levels of nucleoside triphosphates were measured by high-performance liquid chromatography (HPLC) in FaDu cells treated for 24 h with atovaquone or 6-Aza. In the cells treated with atovaquone, there was a significant decrease in UTP levels, a non-significant decrease in CTP levels, and no significant changes in GTP or ATP levels (Fig. 4d and Supplementary Fig. 2g). Therefore atovaquone appears to specifically affect pyrimidine synthesis. In the cells treated with 6-Aza, there were significant decreases in UTP and CTP levels, a non-significant decrease in GTP levels, and a non-significant increase in ATP levels, indicating that 6-Aza primarily affects pyrimidine synthesis under these conditions. Furthermore, the observed decrease in the OCR induced by incubation with atovaquone for 2 h was not rescued by addition of the pyrimidine precursor, uridine, in FaDu cells (Fig. 4e). These results suggest that inhibition of DHODH by atovaquone causes a decrease in both the OCR and pyrimidine synthesis, but that the decrease in pyrimidine synthesis is unlikely to cause the decrease in the OCR.

**ATO doesn't affect HIF-1α or intrinsic radiosensitivity**. HIF-1 is a heterodimeric transcription factor that promotes angiogenesis and increased proliferation[1]. The HIF-1α subunit is rapidly degraded under normoxia, but is stabilized under hypoxia. To assess the effect of atovaquone on HIF-1α expression *in vitro*, FaDu, HCT116 and H1299 cells were incubated with atovaquone for 2 or 24 h in either normoxic (20% $O_2$) or hypoxic (0.5% $O_2$) conditions. HIF-1α was not stabilized by atovaquone under normoxic conditions and no significant differences in HIF-1α

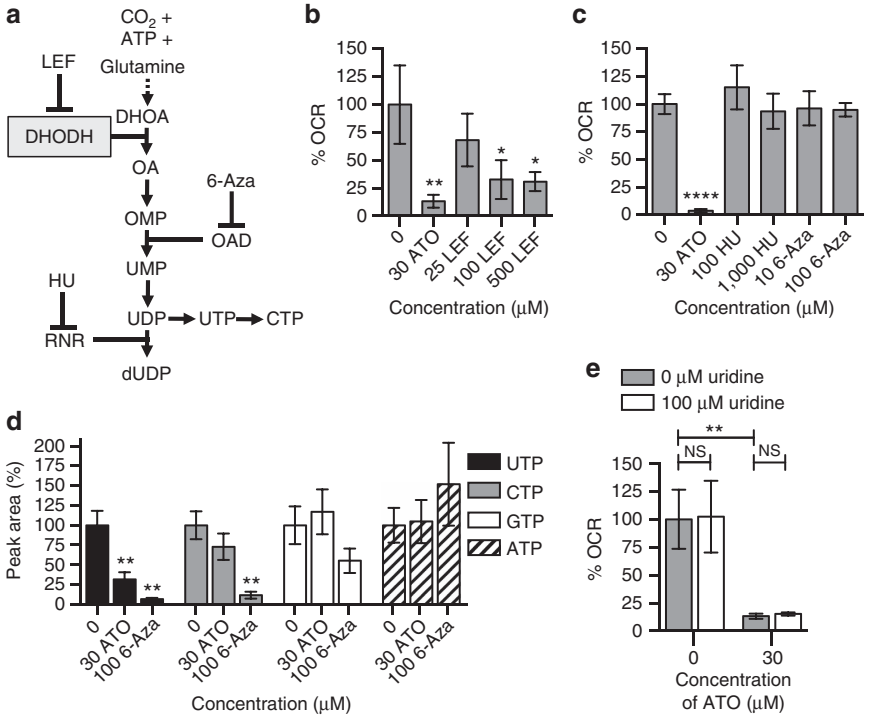


**Figure 4 | Atovaquone inhibits pyrimidine synthesis.** (**a**) The pyrimidine synthesis pathway. 6-Aza, 6-azauridine; DHODH, dihydroorotate dehydrogenase; HU, hydroxyurea; LEF, leflunomide; OAD, orotidylic acid decarboxylase; RNR, ribonucleotide reductase. (**b**) The % OCR following 2 h incubation of FaDu cells with LEF or 30 μM ATO. (**c**) The % OCR following 24 h incubation of FaDu cells with HU, 6-Aza or 30 μM ATO. (**d**) NTP peak area levels relative to the DMSO control and normalized to cell number after 24 h incubation with 30 μM ATO or 100 μM 6-Aza. (**e**) The % OCR following 2 h incubation of FaDu cells with either 100 μM uridine, 30 μM ATO or both 100 μM uridine and 30 μM ATO. % OCR is presented relative to the DMSO control and corrected for cell number ($n \geq 3$). One-way ANOVA with Bonferroni was performed for all of the experiments apart from **e**, for which an unpaired two-tailed *T*-test was performed (****$P<0.0001$, ***$P<0.001$, **$P<0.01$, *$P<0.05$). All values are presented as mean ± s.d. except for the HPLC data, which are presented as mean ± s.e.m. ATO, atovaquone.

protein levels were observed under hypoxic conditions (Supplementary Fig. 3a,b).

Radiation sensitivity can be affected not only by tumour hypoxia, but also by alteration of the intrinsic radiosensitivity of the cancer cells[1,3,4]. Therefore colony formation assays were conducted to investigate whether atovaquone alters intrinsic radiation sensitivity in monolayer FaDu, HCT116 or H1299 cells. Assessment of colony formation revealed that atovaquone did not alter radiosensitivity under either normoxia (20% $O_2$) or severe hypoxia ($<0.1\%$ $O_2$) (Supplementary Fig. 3c and Supplementary Table 2). This indicates that, as expected, atovaquone is not an intrinsic radiation sensitizer.

**ATO affects tumour hypoxia and radiation response**. Given that atovaquone completely alleviated spheroid hypoxia at pharmacologically relevant doses, mice bearing FaDu and HCT116 xenografts were treated with atovaquone for 7 days to investigate the effect on tumour hypoxia. The tumours were harvested on day 7, and EF5 staining confirmed that tumour hypoxia was virtually abolished in both the FaDu and HCT116 xenografts (Fig. 5a,b). As expected, the tumour volume was not significantly altered during the course of the experiment (Fig. 5c). The mean concentration of atovaquone in the blood plasma after 5 days treatment was 68.6 μM, and mean concentration in the HCT116 tumours was 36.0 μM (Fig. 5d).

Given the dramatic decrease in tumour hypoxia observed following atovaquone treatment, radiation response was assessed in mice bearing FaDu xenografts. The mice were treated with atovaquone for 7 days prior to irradiation with a single dose of 6 Gy, and then atovaquone treatment was continued for a further 3 days. In the unirradiated mice, the average time taken for the tumours to reach 500 $mm^3$ was 14.2 days for mice treated with DMSO, and 12.3 days for mice treated with atovaquone, a non-significant difference, indicating that atovaquone alone does not alter tumour volume (Fig. 5e,f). In the irradiated mice, the average time taken for the tumours to reach 500 $mm^3$ was 15.3 days for mice treated with DMSO, but 28.5 days for mice treated with atovaquone, a significant synergistic growth delay of 13.2 days between the two irradiated groups ($P<0.0001$). One tumour, excluded from analysis, treated with both atovaquone and radiation had an excellent response, reaching 500 $mm^3$ 42 days after the initiation of drug treatment. The observed tumour growth delay is likely due to the reduction in tumour hypoxia observed with atovaquone treatment.

**Biguanides affect spheroid hypoxia and radiation response**. Previous publications have demonstrated that the anti-diabetic biguanide, metformin, reduces the OCR and tumour hypoxia[11,12]. To evaluate the relative efficacy of atovaquone, metformin and its precursor, phenformin, the OCR was measured in FaDu, HCT116 and H1299 cells following 24 h treatment. A significant decrease in the OCR of over 90.0% was observed in all three cells lines treated with 30 μM atovaquone (Fig. 6a). A significant decrease of 70.7% in FaDu cells and 59.0% in HCT116 cells was observed at 2 mM metformin. However, metformin was less potent in H1299 cells, causing a decrease of 33.1% at 2 mM, which was not statistically significant. A significant decrease in the OCR of 52.2% in FaDu cells and 43.3% in HCT116 cells was observed at 10 μM phenformin. Phenformin was also less potent in H1299 cells, causing a non-significant decrease of 23.4%. There were no significant changes in the OCR at 200 or 20 μM metformin, or at 2 or 0.4 μM phenformin in any of the cell lines. Metformin and phenformin did not affect cell survival at any concentration tested (Supplementary Fig. 4a). To investigate the kinetics of this effect in FaDu cells, the OCR was measured for 15 h after injection of atovaquone, metformin or phenformin. The OCR was reduced by 87.3% by atovaquone within 2 h (Supplementary Fig. 4b). However, a slower decrease in the OCR was observed following treatment with 2 mM metformin or 10 μM phenformin, with a reduction of $<10\%$ within 2 h and a reduction of 55.9% and 36.0%, respectively, after 10 h.

To assess whether the observed decrease in the OCR translated to a decrease in spheroid hypoxia, FaDu, HCT116 and H1299 spheroids were treated with atovaquone, metformin or phenformin for 24 h, and the hypoxic fraction was evaluated by EF5 staining. There was near-complete loss of hypoxia in FaDu and HCT116 spheroids at 30 μM atovaquone, 2 mM metformin and 10 μM phenformin (Fig. 6b,c, Supplementary Fig. 4c). In contrast, there were non-significant decreases of 41.8% and 9.8% in H1299 spheroids following treatment with 2 mM metformin and 10 μM phenformin, respectively. No significant decreases in hypoxia were observed at 20 μM or 200 μM metformin, or at 0.4 μM or 2 μM phenformin in FaDu spheroids. No treatments caused a significant change in spheroid diameter (Supplementary Fig. 4d). These results are in accordance with the OCR results shown in Fig. 6a, suggesting that a significant reduction in the OCR by metformin and phenformin is required to reduce spheroid hypoxia.

Nimorazole is a 2-nitroimidazole that acts as an oxygen mimetic, which has previously been shown to improve loco-regional control when combined with radiotherapy in head and neck cancer[27,28]. To compare the ability of nimorazole, atovaquone, metformin, phenformin and antimycin A to improve radiation response, FaDu spheroids were treated for 24 h with these drugs, irradiated at 10 Gy, and then allowed to recover in fresh medium. Fifty days after irradiation, 90.5% of the DMSO-treated spheroids were reformed (Fig. 6d). In comparison, the percentage reformation of spheroids for the highest concentration of each treatment was 53.7% for 10 mM nimorazole, 48.6% for atovaquone, 58.3% for 2 mM metformin, 53.2% for 10 μM phenformin, and 50.5% for 1 μM antimycin A (Fig. 6d,e). A less-dramatic decrease in spheroid regrowth was observed at the lower concentrations of the drugs, with a percentage spheroid reformation of 72.1% for 1 mM nimorazole, 75.6% for 20 μM metformin, 75.0% for 0.4 μM phenformin and 60.4% for 0.1 μM antimycin A. For unirradiated spheroids, no drug treatment caused a significant decrease in spheroid growth compared with the DMSO control after 35 days (Supplementary Fig. 5a,b). These results demonstrate that the greatest improvement in radiation response is observed at concentrations of the drugs that eliminate spheroid hypoxia, and that this is sufficient to improve radiation response in a manner comparable to 10 mM nimorazole.

Having demonstrated that metformin and phenformin reduce hypoxia in spheroids, their effect on hypoxia was next examined *in vivo*. Mice bearing FaDu xenografts were treated with DMSO for 7 days, 50 mg $kg^{-1}$ atovaquone for 7 days, a single dose of 250 mg $kg^{-1}$ metformin, 250 mg $kg^{-1}$ per day metformin for 7 days or 100 mg $kg^{-1}$ per day phenformin for 7 days. The tumours were harvested 2.5 h after the final dose of drug, and EF5 staining was performed. Atovaquone caused a significant 73.7% reduction in hypoxia, and 7 days metformin treatment caused a 43.1% decrease in hypoxia, although this was not statistically significant. There were no significant changes in hypoxia following a single dose of metformin or 7 days phenformin (Fig. 6f and Supplementary Fig. 5c). After a single dose of metformin the mean plasma concentration was 109 μM, and mean tumour concentration was 151 μM (Supplementary Fig. 5d).

## Discussion

Our screen, designed to find compounds that decrease tumour hypoxia by inhibiting oxygen consumption, identified

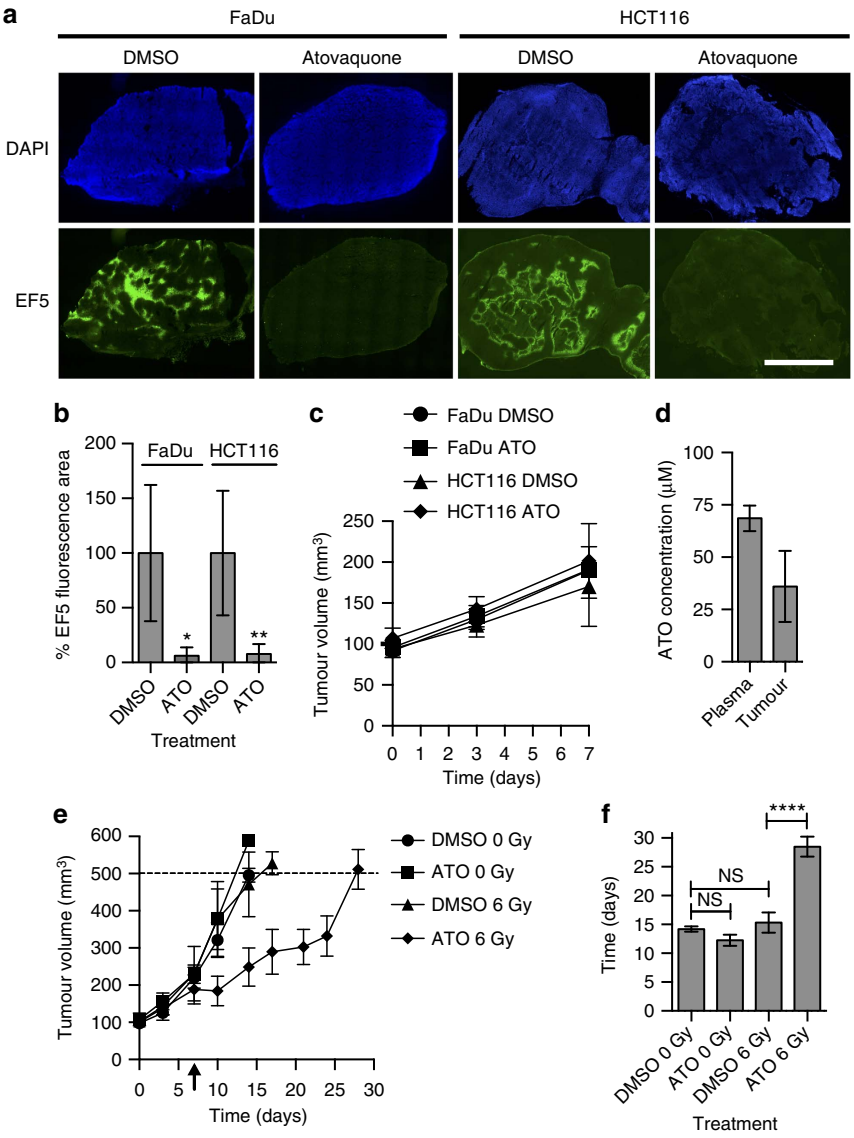


**Figure 5 | ATO reduces tumour hypoxia and improves tumour radiation response.** Mice bearing FaDu and HCT116 xenograft tumours were treated with atovaquone for 7 days, and were injected with EF5 on day 7. (**a**) Immunostaining for EF5 with DAPI as a nuclear counterstain. Scale bar, 2 mm. (**b**) % EF5 fluorescent area relative to the DMSO-treated tumours. (**c**) Average tumour size on days 0, 3 and 7. (**d**) Mean concentration of atovaquone in the blood plasma after 5 days treatment, and mean concentration in the excised HCT116 tumours. (**e**) Mice bearing FaDu xenograft tumours were treated with atovaquone for 10 days, with 6 Gy radiation on day 7 (indicated by arrow). Average tumour volume is shown ($mm^3$). One tumour from a mouse treated with atovaquone and radiation took 42 days to reach 500 $mm^3$ and was excluded from analysis. (**f**) Average time taken for tumours to reach the maximum volume of 500 $mm^3$ (days). At least five mice were used for each treatment group. One-way ANOVA were performed to assess statistical significance with Bonferroni post correction (****$P<0.0001$, **$P<0.01$, *$P<0.05$). All values are presented as mean ± s.d. except for the HPLC data, which are presented as mean ± s.e.m. ATO, atovaquone.

atovaquone. Atovaquone caused a rapid decrease in oxygen consumption in a wide range of cancer cell lines. It virtually abolished both spheroid hypoxia and tumour hypoxia, and augmented the effects of radiotherapy. Its mechanism of action is likely the inhibition of the mitochondrial cytochrome $bc_1$ complex (complex III).

The efficacy of radiotherapy can be improved by the reoxygenation of radioresistant hypoxic tumour cells[1,3,4]. This study reveals that atovaquone inhibits oxygen consumption, spheroid hypoxia and tumour hypoxia, but has no effect on intrinsic radiosensitivity *in vitro* under normoxic or hypoxic conditions. However, atovaquone improved radiation sensitivity in both spheroids and xenograft tumours. Therefore we propose that the radiation sensitization following atovaquone treatment could be due to a decrease in hypoxia rather than an increase in intrinsic radiosensitivity. It is not expected that atovaquone would exacerbate radiation-induced side effects in a clinical setting because irradiated normal tissues are not generally hypoxic. The improvement in radiation response in spheroids was comparable to 10 mM nimorazole, although the percentage reformation of spheroids was 72.1% for 1 mM nimorazole, compared with 48.6% for atovaquone, and the concentration of nimorazole in the blood plasma of patients is in the sub-millimolar range[29–31]. This indicates that the improvement of radiation response in spheroids is superior for atovaquone compared with nimorazole at pharmacological concentrations.

Atovaquone is FDA approved as a single agent to treat pneumocystis pneumonia, which is caused by *Pneumocystis*

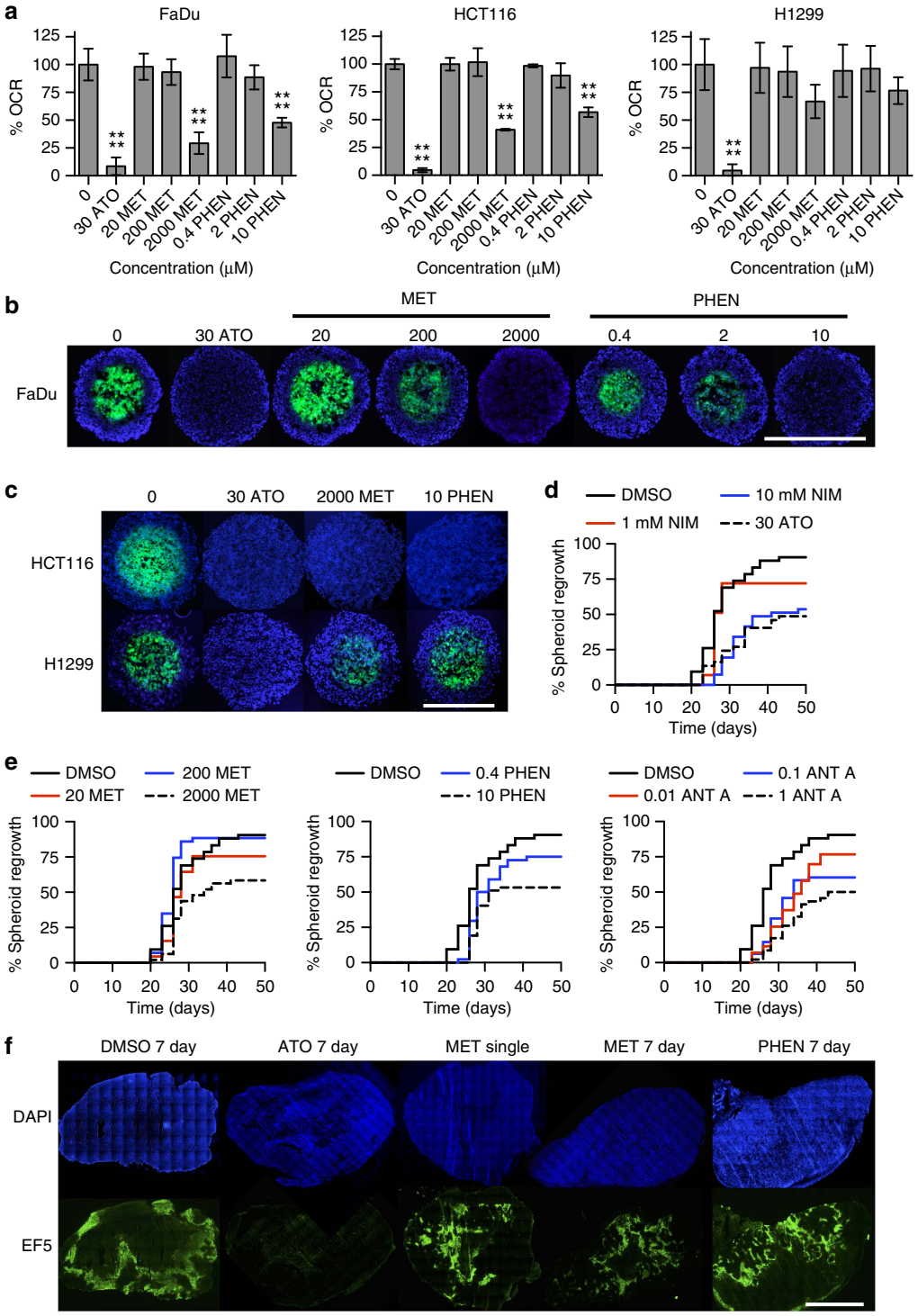


**Figure 6 | Biguanides alleviate spheroid hypoxia and improve radiation response.** (**a**) The OCR of FaDu, HCT116 and H1299 cells were measured after 24 h incubation with atovaquone, metformin or phenformin at the indicated concentrations. The % OCR is shown relative to the DMSO control and normalized to the relative cell number obtained by hoechst staining at the end of the experiment. The data are an average of three independent experiments. One-way ANOVA were performed to assess statistical significance with Bonferroni post correction (mean ± s.d., $^{****}P<0.0001$). (**b**,**c**) FaDu (**b**), HCT116 and H1299 (**c**) spheroids were treated with DMSO, atovaquone, metformin or phenformin for 24 h at the indicated concentrations (μM). Hypoxia was assessed by staining central spheroid sections for EF5 (green), with DAPI as a nuclear counterstain (blue). Scale bar, 600 μm. Hypoxia was assessed in at least five spheroids per treatment for each experiment ($n=3$), and the data are representative of three independent experiments. (**d**,**e**) FaDu spheroids were treated with DMSO, atovaquone, nimorazole, antimycin A, metformin or phenformin for 24 h at the indicated concentrations (μM). After 24 h the spheroids received 10 Gy, and were then allowed to recover in drug-free medium. Time post treatment is shown (days). One replicate of the experiment was conducted with at least 37 spheroids in each treatment group. (**f**) Mice bearing FaDu xenograft tumours were treated with 50 mg kg$^{-1}$ per day atovaquone for 7 days, 250 mg kg$^{-1}$ metformin single dose, 250 mg kg$^{-1}$ per day metformin for 7 days or 100 mg kg$^{-1}$ per day phenformin for 7 days. EF5 was injected 30 min after the final dose, and then the mice were killed after a further 2 h. Immunostaining for EF5 with DAPI as a nuclear counterstain is shown. Scale bar, 2 mm. Five mice were used for each treatment group. ANT A, antimycin A; ATO, atovaquone; MET, metformin; NIM, nimorazole; PHEN, phenformin.

*jirovecii*[18]. It is also used, primarily in combination with proguanil, as chemoprophylaxis against malaria, or to treat malaria, which is caused by *Plasmodium falciparum*. Atovaquone has a good safety profile with only mild side effects, is well absorbed, can accumulate in tissues, is eliminated by the liver after 50–84 h, and is not metabolized *in vivo* to a significant extent[18,32–34]. It is an analogue of the electron carrier, ubiquinone, which is reduced to ubiquinol by DHODH, complex I and complex II, and is then oxidized back to ubiquinone by complex III (ref. 18). In parasites, the primary mechanism of action of atovaquone is inhibition of complex III (refs 20,21). In biochemical assays, atovaquone inhibits *P. falciparum* complex III with an $IC_{50}$ of 3 nM, but is far less potent against human complex III, which it inhibits with an $IC_{50}$ of 70–460 nM (refs 20,21). It was previously assumed that this comparably low efficacy against purified human complex III would not translate to the inhibition of this enzyme *in vitro*. However, several experiments conducted in this study indicate that atovaquone inhibits complex III in cancer cells. First, the OCR is inhibited by atovaquone under conditions promoting complex III-dependent respiration in digitonin-permeabilized cells. Second, the reduction of cytochrome *c* is inhibited by atovaquone under conditions promoting complex III-dependent respiration in isolated mitochondria, but the reduction of dichlorophenolindophenol by complex II is not inhibited by atovaquone. Furthermore, complex III inhibition by atovaquone, antimycin A or myxothiazol is sufficient to markedly reduce the OCR and consequently to eradicate spheroid hypoxia and improve radiation response.

Complex III and DHODH, an enzyme of the *de novo* pyrimidine synthesis pathway, are situated in the inner mitochondrial membrane in higher eukaryotes, and their activities are closely linked. Cellular DHODH activity is inhibited by ETC agonists such as antimycin A and nitric oxide, and by DHODH agonists such as leflunomide and brequinar, but only DHODH agonists inhibit the activity of purified DHODH[24,35,36]. Atovaquone is a much more potent inhibitor of purified human complex III ($IC_{50}$ = 70–460 nM) than human DHODH ($IC_{50}$ = 14.5 μM), suggesting that it primarily acts as a complex III inhibitor in cancer cells[20–22]. For these reasons, it is our conjecture that atovaquone primarily inhibits complex III, which causes depletion of the DHODH cofactor, ubiquinone, and subsequent inhibition of DHODH activity and downstream pyrimidine synthesis.

The anti-diabetic drug metformin, reduces the OCR by inhibition of complex I, and decreases tumour hypoxia[11,12]. This study demonstrated that metformin and phenformin reduce the OCR in FaDu and HCT116 cells, eliminate hypoxia in FaDu and HCT116 spheroids, and elicit an improved radiation response. In contrast, metformin and phenformin were ineffective in reducing the OCR in H1299 cells, or in alleviating H1299 spheroid hypoxia. In comparison, the efficacy of atovaquone is very similar in a wide range of tumour cell lines, and it eliminates hypoxia in FaDu, HCT116 and H1299 spheroids.

In accordance with a previous publication[12], this study demonstrated a decrease in tumour hypoxia following 7 days metformin treatment, albeit non-significant. The reason that metformin eliminated spheroid hypoxia but caused a less significant reduction in tumour hypoxia could be due to a discrepancy between the dose required to elicit this effect in spheroids and the concentration achieved in tumours. There is an ongoing debate concerning the doses of metformin used in murine cancer models, and whether they are clinically relevant[37,38]. Diabetics treated with the standard clinical doses of 1,500–2,500 mg per day metformin have maximum plasma levels in the range of 10–25 μM, and non-diabetic cancer patients receiving 1,500–2,000 mg per day have maximum plasma levels of 2.8–7 μM (refs 38,39). In comparison, the maximum plasma levels achieved in murine models following oral administration of 125–350 mg $kg^{-1}$ per day metformin for 2 weeks are 5–47 μM, with a level of metformin in the tumours of 32–200 μM (refs 37,38). At first glance, this may make the observed effects of metformin on the OCR and spheroid hypoxia at 2 mM appear irrelevant both *in vivo* and in the clinic. However, several explanations have been proposed to explain this discrepancy[12,37,38]. These include the predicted accumulation of metformin in the mitochondria over time to achieve doses required for complex I inhibition, the effects of the tumour microenvironment, and a lower concentration of glucose, serine and glutamine in the tumour, metabolites that have been shown to cause resistance to metformin *in vitro*. It is possible that the dose of metformin could be raised to achieve higher plasma concentrations in cancer patients, but this may increase potentially serious adverse effects such as lactic acidosis. Indeed, phenformin was withdrawn from clinical use in the 1970s due to a high risk of lactic acidosis. This may preclude its use as an anti-cancer therapeutic, although it is possible that a good therapeutic ratio exists for phenformin at lower doses.

In contrast to metformin, the concentration of atovaquone required to reduce the OCR *in vitro* and to alleviate tumour hypoxia *in vivo* is achievable in patients. It reaches a steady-state concentration in the blood plasma of 65 μM or more after 1–2 weeks administration in pneumocystis pneumonia patients at doses that are used routinely in the clinic, but reduces the OCR by up to 90% within 2 h (refs 32,33). The mean concentration of atovaquone in the mouse blood plasma after 5 days treatment was 68.6 μM, suggesting that doses required to reduce tumour hypoxia could be achieved without toxicity in patients.

Although atovaquone did not have a significant effect on the cell number after 4.5 h, there was a significant decrease in the cell number after 24 h in monolayer cells. We do not believe that this finding effects the interpretation of any of our data or the potential clinical applicability of atovaquone because it reduces the OCR within 2 h without a significant effect on cell number, it does not effect the growth of spheroids or xenograft tumours in the absence of radiation, and it has an excellent clinical safety profile.

Some studies have described cycling hypoxia in tumours, characterized by periods of hypoxia followed by periods of reoxygenation, which can lead to excessive ROS production and may cause increased resistance to therapy[40,41]. This phenomenon is thought to occur as a result of changes in vessel perfusion and fluctuations in the flux of red blood cells within perfused vessels[40]. However, the contribution of tumour cells that undergo cycling hypoxia to poor patient outcome is currently unclear. Reoxygenation has also been shown to increase the potential risk of metastasis[42,43]. These studies highlight potential issues with reoxygenating tumours. However, the literature overwhelmingly suggests that the benefits of eradicating hypoxia outweigh any theoretical risks, with a recent meta-analysis supporting hypoxia modification as a strategy to improve response to therapy in head and neck squamous cell carcinoma[1,3,4].

This study suggests that attenuation of tumour hypoxia by atovaquone may be a highly appealing clinical strategy to increase the sensitivity of tumour cells to radiation in multiple different tumour types. Accordingly, we are now initiating a proof of principle, 'window of opportunity' clinical trial to investigate whether atovaquone reduces tumour hypoxia in lung cancer patients prior to surgical resection, on the basis of imaging, serological markers and immunohistochemical markers.

## Methods

**Cell lines and compounds.** All cell lines were purchased from the American Type Culture Collection (ATCC). STR profiling (DNA Diagnostics Centre, UK) and

mycoplasma testing (Lonza) are conducted routinely for these cell lines. Cells were cultured at 37 °C with 5% $CO_2$ in Dulbecco's modified Eagle's medium (DMEM, Sigma) supplemented with 10% fetal bovine serum (FBS, Lonza). All compounds were obtained from Sigma except duroquinol (Tokyo Chemical Industry), and EF5, a gift from Cameron Koch's Laboratory, University of Pennsylvania). All compounds were prepared from powder. For the experiments under hypoxic conditions, cells were grown at 0.5% $O_2$ in an *in vivo* 2400 Ruskinn chamber (Biotrace Fred Baker), and at $<0.1\%$ $O_2$ in a Bactron II chamber (Shell Labs).

**OCR primary screen.** FaDu cells were incubated with either the Pharmakon 1,600 (Microsource) or the 97-compound TDI Oncology Drug Set (Target Discovery Institute, Oxford University) compound libraries at 2 and 10 μM for 24 h in DMEM containing 5 mM glucose and 4 mM L-glutamine. The mitochondrial-specific OCR was determined by taking a basal OCR measurement in XF assay medium (Seahorse Biosciences) containing 5 mM galactose, 5 mM sodium pyruvate and 4 mM L-glutamine using an XF96 Analyzer (Seahorse Biosciences) and subtracting the OCR measured following injection of 2 μM antimycin A. The cells were then fixed in ice-cold methanol for 5 min, and incubated in 1 × PBS, 4 μg ml$^{-1}$ Hoechst 33258 (Sigma) for 30 min before measuring fluorescence using a POLARstar Omega plate reader (BMG Labtech) to obtain the relative cell number per well. The mitochondrial-specific OCR was corrected using the relative cell numbers, and compounds that caused a reduction in cell number of more than 66% compared with the DMSO control wells for each plate were excluded. Two repetitions of the screen were conducted. The *Z* scores were generated and used to rank the compounds for each repeat, and the rank product was used to sort the compounds. The compounds with the top 130 rank products were chosen for the secondary screen.

**OCR secondary screen.** The secondary screen was conducted using the same protocol as the primary screen, except FaDu cells were incubated with 80 nM, 400 nM, 2 μM and 10 μM of the compounds, the assay medium contained 5 mM glucose, 5 mM sodium pyruvate and 4 mM L-glutamine, and three replicates were conducted. The analysis was conducted as described for the primary screen, using the OCR score to rank the compounds for each repeat. The OCR score is defined as the 'OCR normalized to cell number' − 'Average of OCR normalized to cell number for the DMSO wells for each plate'/'s.d. of OCR normalized to cell number for the DMSO wells for each plate'. The list was filtered to include only compounds approved for systemic use in humans, excluding those approved for topical or veterinary use. The rank product was used to sort the compounds. Compounds were excluded based on prospectively defined criteria: OCR, cell viability, pharmacokinetics, FDA-approved use and known hypoxia modification.

**OCR.** The cells were grown for 24 h in DMEM containing 5 mM glucose and 4 mM L-glutamine, and then measurements of the OCR were taken in XF assay medium (Seahorse Biosciences) containing 5 mM glucose, 5 mM sodium pyruvate and 4 mM L-glutamine using an XF96 Analyzer (Seahorse Biosciences). For the kinetics experiments, measurements were collected every 15 min following injection of atovaquone. For the experiments with uridine and pyrimidine synthesis inhibitors, the cells were incubated with the compounds for 2 or 24 h as indicated, the medium was replaced with the assay medium also containing the compounds, and then measurements were made. The OCR measurements were corrected for cell number using Hoechst staining, as described above. For the experiments using permeabilized FaDu cells, 0.005% digitonin was the permeabilization agent, and the % OCR was measured within 15 min of its addition. Permeabilization of the plasma membrane allows the substrates respired by the mitochondria to be dictated by the added medium, and allows non-membrane permeable substrates to access the mitochondria[44]. The activities of complexes I and II were assayed using substrates specific to each complex in conjunction with an inhibitor of the other complex: 5 mM pyruvate with 1 mM malic acid to promote complex I-dependent respiration, and 10 mM succinate with 1 μM rotenone to promote complex II-dependent respiration. Complex III-dependent respiration was assayed using 500 μM duroquinol as a substrate. Complex IV-dependent respiration was assayed using 500 μM *N*,*N*,*N*′,*N*′-tetramethyl-*p*-phenylenediamine (TMPD) as a substrate, in conjunction with 2 mM ascorbate to maintain TMPD in reduced form. The inhibitors used for the assay were 2 μM rotenone for complex I, 10 mM malonate or 1 mM malic acid for complex II, 2 μM myxothiazol or 2 μM antimycin A for complex III, and 20 mM sodium azide for complex IV.

**Spheroids.** FaDu spheroids were grown using the liquid overlay technique, and HCT116 and H1299 spheroids were grown in lipidure-coated U-bottom plates (UMS Bio). Half of the medium was replaced twice per week. Spheroid hypoxia was quantified by EF5 staining, using an anti-EF5 antibody (both reagents obtained from University of Pennsylvania)[7]. Two hundred micromolar EF5 was added to the spheroids for 6 h before fixation in 4% paraformaldehyde for 24 h, incubation in 30% sucrose for 2.5 h, and then addition of OCT (VWR, TissueTek) for cryosectioning. Spheroid sections were incubated for 40 min in TNB blocking reagent (Perkin Elmer), washed for 5 min in 1 × PBS, 0.3% Tween 20, and then incubated overnight with 70 μl of undiluted 75 μg ml$^{-1}$ anti-EF5 antibody. Three washes of 45 min were then performed using 1 × PBS, 0.3% Tween 20 before addition of DAPI vectorshield mounting medium (Vector Laboratories) and fluorescence microscopy (Nikon 90i, Nikon). Spheroid diameter was derived from the spheroid cross-sectional area measured by the Gelcount colony counter (Oxford Optronix) or Axiovert200M (Carl Zeiss MicroImaging GmbH).

**Complex II/III and complex II assays.** The complex II/III and complex II assays were performed according to the manufacturer's instructions (Cayman Chemicals), using either mitochondria isolated from FaDu cells or bovine heart mitochondria (Cayman Chemicals). The complex III assay uses the complex II substrate, succinate, to allow generation of the complex III substrate, ubiquinol, by complex II. One micromolar rotenone and 1 mM cyanide were added to inhibit the activities of complexes I and IV, respectively, so the activities of complexes II and III were assayed. The complex II assay uses succinate as a substrate for complex II, and measures reduction of the redox dye, dichlorophenolindophenol, by the ubiquinol generated by complex II. One micromolar rotenone, 10 μM antimycin A and 1 mM cyanide were added to inhibit the activities of complexes I, III and IV, respectively, so the activity of complex II was assayed in isolation. For isolation of mitochondria, FaDu cells were resuspended in 1 ml homogenization buffer at 4 °C: 10 mM Tris, 0.1 mM EDTA, 11.5% sucrose, 1% complete mini protease inhibitor cocktail (Roche), pH 7.4 (ref. 47). The cells were snap frozen on dry ice and then thawed at 37 °C ten times, centrifuged at 750*g*, resuspended in 500 μl homogenization buffer, and centrifuged again, collecting the supernatants at each stage. Finally the pellet was resuspended in 100 μl homogenization buffer omitting EDTA, and stored at − 80 °C.

**High-performance liquid chromatography.** To quantify NTPs, the cells were lifted and lysed in 100 μl of 6% TCA (ref. 48). Nucleotides were neutralized by extracting the samples with 100 μl of freon (1,1,2 trichlorotrifluorethane): trioctylamine (4:1). The aqueous upper layer was removed and then 40 μl was injected. Chromatography was performed on a Waters 2695 system with diode array detection (Waters 2996), monitoring at 254 nm, with an Ace column (3 μm, 3 × 125 mm) maintained at 30 °C. The samples were maintained at 10 °C. Separation was attained with eluent A (10 mM potassium dihydrogen phosphate, 10 mM tetrabutylammonium hydroxide, 10% methanol, pH 6.9) and eluent B (50 mM potassium dihydrogen phosphate, 6 mM tetrabutylammonium hydroxide, 30% methanol, pH 7), using a flow rate of 0.6 ml min$^{-1}$ and a gradient of 25–80% B over 20 min, and a run time of 25 min. Nucleotides were quantitated against commercially available dNTPs. Peak areas are presented relative to the DMSO control and normalized to the cell number obtained by a Sceptre cell counter (Millipore). Plasma and tumour atovaquone concentrations were determined using lapachol as an internal standard[45] by negative electrospray ionization on a Waters EMD1000. HPLC was performed on a Cortecs C18 column, 100 × 3 mm (Waters), with eluents of 5 mm ammonium formate in 50% acetonitrile (A) and acetonitrile (B) using a gradient of 10–100% B in 5 min. The flow rate was 0.5 ml min$^{-1}$. Plasma and tumour metformin concentrations were determined using HPLC with absorbance detection at 330 nm using phenformin as an internal standard[46]. Tumours were weighed and homogenized in four volumes of water. To 20 μl plasma or tumour homogenate was added 20 μl phenformin (25 μM), 10 μl 50 mM HCl and 0.5 ml acetonitrile. Samples were centrifuged and the supernatant dried down in a heated centrifugal evaporator. Samples were reconstituted in 100 μl Synergy water. HPLC was performed on a Gemini C18 column, 150 × 3 mm, 3 μm (Phenomenex) at 35 °C, with eluents of 10 mM ammonium bicarbonate pH 10.4 (A) and acetonitrile (B) using isocratic elution of 60% B and a flow rate of 0.4 ml min$^{-1}$.

**Animal models.** The project licence covering the animal work (PPL30/2922) was approved by the Oxford University Animal Welfare and Ethical Review Body (AWERB) and granted by the UK Home Office Animals in Science Regulation Unit (ASRU) under the Animals (Scientific Procedures) Act 1986 (ASPA)). FaDu ($1 \times 10^6$) or HCT116 ($5 \times 10^6$) cells were inoculated subcutaneously with matrigel (BD Biosciences) in athymic BALB/c nude female mice at age 55–70 days. Once the tumours had reached 100 mm$^3$, atovaquone was administered in the drinking water at 50 mg kg$^{-1}$ per day with 2% DMSO and 0.1% carboxymethylcellulose to reflect the clinical administration of atovaquone as an oral suspension[18,32,33], assuming that a 20 g mouse would consume 5 ml water per day. Mice were given this dose for 7 days because atovaquone takes 1–2 weeks to reach a steady-state plasma concentration in patients[32,33]. Tumours were harvested after i.p. administration of 0.01 ml g$^{-1}$ body weight of 10 mM EF5 after 7 days treatment. Tumours were measured with calipers. For the radiation treatments, a single dose of 6 Gy was given on day 7 with a 250-kV orthovoltage irradiator (Philips RT 250) at a dose rate of 2.63 Gy min$^{-1}$, using copper shielding. Necrosis was quantified by inspection of Hematoxylin and Eosin (H&E) stained sections. Animals were randomly assigned to each treatment group on the day on which their tumours reached 100 mm$^3$ using a random number generator (Excel), but the experiment was not blinded. A sample size of five mice per group was used and has 90% power (s.d. = 30%, alpha = 0.05) to detect a 70% decrease, based on our previous experience and published data[5,7]. A one-tailed test was performed for this determination. Use of five animals per treatment group allowed us to overcome the problem of differences in variance between groups being statistically compared. One tumour treated with both atovaquone and radiation had an excellent response, reaching 500 mm$^3$ 42 days after the initiation of drug treatment, and was excluded from our analyses.

**Immunoblotting.** Protein lysates were made using RIPA lysis buffer (Thermo Scientific). SDS–PAGE electrophoresis was conducted followed by immunoblotting. The primary antibodies used were anti-HIF-1α (1:500, clone 54, BD Biosciences) and anti-GAPDH (1:1,000 6C5, Novus Biologicals). The Alexa Fluor 680 secondary antibody (1:10,000, LICOR) was detected using the Odyssey imaging system (LICOR).

**Colony formation assay.** Cells were plated, incubated at 20% $O_2$ for 4 h, and then incubated at either 20% $O_2$ or $<0.1\%$ $O_2$ for 6 h with atovaquone prior to irradiation by a ceasium-137 irradiator (Gamma Service: GSR D1; dose rate 1.94 Gy min$^{-1}$). Half an hour after irradiation, all cells were placed at 20% $O_2$ for a further 18 h before medium replacement. Colonies were stained with crystal violet and counted using the Gelcount colony counter (Oxford Optronix).

**Statistics.** Statistical analysis was performed with Prism 5 software (GraphPad Software Inc.). All values are presented as mean ± s.d. except for the colony formation assays and HPLC data, which are presented as mean ± s.e.m. Unpaired two-tailed *T*-tests were performed for the uridine and colony formation assays, and for the cell survival assays in Supplementary Fig. 1c. For all other experiments, one-way ANOVAs were performed to assess statistical significance with Bonferroni post correction. *P* values $<0.05$ were considered significant. All *in vitro* experiments were repeated at least three times.

**Data availability.** The data supporting the findings of this study are contained within the Article and Supplementary Information files or available from the corresponding authors upon request.

## References


1. Dhani, N., Fyles, A., Hedley, D. & Milosevic, M. The clinical significance of hypoxia in human cancers. *Semin. Nucl. Med.* **45,** 110–121 (2015).
2. Okunieff, P. *et al.* Angiogenesis determines blood flow, metabolism, growth rate, and ATPase kinetics of tumors growing in an irradiated bed: 31P and 2H nuclear magnetic resonance studies. *Cancer Res.* **51,** 3289–3295 (1991).
3. Wilson, W. R. & Hay, M. P. Targeting hypoxia in cancer therapy. *Nat. Rev. Cancer* **11,** 393–410 (2011).
4. Overgaard, J. Hypoxic modification of radiotherapy in squamous cell carcinoma of the head and neck--a systematic review and meta-analysis. *Radiother. Oncol.* **100,** 22–32 (2011).
5. Fokas, E. *et al.* Dual inhibition of the PI3K/mTOR pathway increases tumor radiosensitivity by normalizing tumor vasculature. *Cancer Res.* **72,** 239–248 (2012).
6. Grimes, D. R., Kelly, C., Bloch, K. & Partridge, M. A method for estimating the oxygen consumption rate in multicellular tumour spheroids. *J. R. Soc. Interface* **11,** 20131124 (2014).
7. Kelly, C. J. *et al.* Regulation of O consumption by the PI3K and mTOR pathways contributes to tumor hypoxia. *Radiother. Oncol.* **111,** 72–80 (2014).
8. Secomb, T. W., Hsu, R., Ong, E. T., Gross, J. F. & Dewhirst, M. W. Analysis of the effects of oxygen supply and demand on hypoxic fraction in tumors. *Acta Oncol. (Madr).* **34,** 313–316 (1995).
9. Ellinghaus, P. *et al.* BAY 87-2243, a highly potent and selective inhibitor of hypoxia-induced gene activation has antitumor activities by inhibition of mitochondrial complex I. *Cancer Med.* **2,** 611–624 (2013).
10. Lin, X. *et al.* A chemical genomics screen highlights the essential role of mitochondria in HIF-1 regulation. *Proc. Natl Acad. Sci. USA* **105,** 174–179 (2008).
11. Wheaton, W. W. *et al.* Metformin inhibits mitochondrial complex I of cancer cells to reduce tumorigenesis. *eLife* **3,** e02242 (2014).
12. Zannella, V. E. *et al.* Reprogramming metabolism with metformin improves tumor oxygenation and radiotherapy response. *Clin. Cancer Res.* **19,** 6741–6750 (2013).
13. Reitzer, L. J., Wice, B. M. & Kennell, D. Evidence that glutamine, not sugar, is the major energy source for cultured HeLa cells. *J. Biol. Chem.* **254,** 2669–2676 (1979).
14. Lee, K. *et al.* Acriflavine inhibits HIF-1 dimerization, tumor growth, and vascularization. *Proc. Natl Acad. Sci. USA* **106,** 17910–17915 (2009).
15. Khaw, M. & Panosian, C. B. Human antiprotozoal therapy: past, present, and future. *Clin. Microbiol. Rev.* **8,** 427–439 (1995).
16. Harada, Y., Ishii, I., Hatake, K. & Kasahara, T. Pyrvinium pamoate inhibits proliferation of myeloma/erythroleukemia cells by suppressing mitochondrial respiratory complex I and STAT3. *Cancer Lett.* **319,** 83–88 (2012).
17. Veal, G. J. *et al.* Pharmacokinetics of dactinomycin in a pediatric patient population: a United Kingdom Children's Cancer Study Group Study. *Clin. Cancer Res.* **11,** 5893–5899 (2005).
18. Nixon, G. L. *et al.* Antimalarial pharmacology and therapeutics of atovaquone. *J. Antimicrob. Chemother.* **68,** 977–985 (2013).
19. Birth, D., Kao, W. C. & Hunte, C. Structural analysis of atovaquone-inhibited cytochrome bc1 complex reveals the molecular basis of antimalarial drug action. *Nat. Commun.* **5,** 4029 (2014).
20. Biagini, G. A. *et al.* Acridinediones: selective and potent inhibitors of the malaria parasite mitochondrial bc1 complex. *Mol. Pharmacol.* **73,** 1347–1355 (2008).
21. Nilsen, A. *et al.* Quinolone-3-diarylethers: a new class of antimalarial drug. *Sci. Transl. Med.* **5,** 177ra137 (2013).
22. Knecht, W., Henseling, J. & Loffler, M. Kinetics of inhibition of human and rat dihydroorotate dehydrogenase by atovaquone, lawsone derivatives, brequinar sodium and polyporic acid. *Chem. Biol. Interact.* **124,** 61–76 (2000).
23. Hail, Jr N., Chen, P. & Bushman, L. R. Teriflunomide (leflunomide) promotes cytostatic, antioxidant, and apoptotic effects in transformed prostate epithelial cells: evidence supporting a role for teriflunomide in prostate cancer chemoprevention. *Neoplasia* **12,** 464–475 (2010).
24. Loffler, M., Jockel, J., Schuster, G. & Becker, C. Dihydroorotat-ubiquinone oxidoreductase links mitochondria in the biosynthesis of pyrimidine nucleotides. *Mol. Cell. Biochem.* **174,** 125–129 (1997).
25. Elford, H. L. Effect of hydroxyurea on ribonucleotide reductase. *Biochem. Biophys. Res. Commun.* **33,** 129–135 (1968).
26. Pasternak, C. A. & Handschumacher, R. E. The biochemical activity of 6-azauridine: interference with pyrimidine metabolism in transplantable mouse tumors. *J. Biol. Chem.* **234,** 2992–2997 (1959).
27. Overgaard, J. *et al.* A randomized double-blind phase III study of nimorazole as a hypoxic radiosensitizer of primary radiotherapy in supraglottic larynx and pharynx carcinoma. Results of the Danish Head and Neck Cancer Study (DAHANCA) Protocol 5-85. *Radiother. Oncol.* **46,** 135–146 (1998).
28. Overgaard, J. *et al.* Five compared with six fractions per week of conventional radiotherapy of squamous-cell carcinoma of head and neck: DAHANCA 6 and 7 randomised controlled trial. *Lancet* **362,** 933–940 (2003).
29. Sugie, C. *et al.* Reevaluation of the radiosensitizing effects of sanazole and nimorazole *in vitro* and *in vivo*. *J. Radiat. Res.* **46,** 453–459 (2005).
30. Hassan Metwally, M. A., Jansen, J. A. & Overgaard, J. Study of the population pharmacokinetic characteristics of nimorazole in head and neck cancer patients treated in the DAHANCA-5 trial. *Clin. Oncol. (R. Coll. Radiol).* **27,** 168–175 (2015).
31. Overgaard, J., Overgaard, M. & Timothy, A. R. Studies of the pharmacokinetic properties of nimorazole. *Br. J. Cancer* **48,** 27–34 (1983).
32. Dixon, R., Pozniak, A. L., Watt, H. M., Rolan, P. & Posner, J. Single-dose and steady-state pharmacokinetics of a novel microfluidized suspension of atovaquone in human immunodeficiency virus-seropositive patients. *Antimicrob. Agents Chemother.* **40,** 556–560 (1996).
33. Falloon, J. *et al.* Atovaquone suspension in HIV-infected volunteers: pharmacokinetics, pharmacodynamics, and TMP-SMX interaction study. *Pharmacotherapy* **19,** 1050–1056 (1999).
34. Rolan, P. E., Mercer, A. J., Tate, E., Benjamin, I. & Posner, J. Disposition of atovaquone in humans. *Antimicrob. Agents Chemother.* **41,** 1319–1321 (1997).
35. Beuneu, C. *et al.* Indirect inhibition of mitochondrial dihydroorotate dehydrogenase activity by nitric oxide. *Free Radic. Biol. Med.* **28,** 1206–1213 (2000).
36. Khutornenko, A. A. *et al.* Pyrimidine biosynthesis links mitochondrial respiration to the p53 pathway. *Proc. Natl Acad. Sci. USA* **107,** 12828–12833 (2010).
37. Chandel, N. S. *et al.* Are metformin doses used in murine cancer models clinically relevant? *Cell Metab.* **23,** 569–570 (2016).
38. Dowling, R. J. *et al.* Metformin pharmacokinetics in mouse tumors: implications for human therapy. *Cell Metab.* **23,** 567–568 (2016).
39. Graham, G. G. *et al.* Clinical pharmacokinetics of metformin. *Clin. Pharmacokinet.* **50,** 81–98 (2011).
40. Kimura, H. *et al.* Fluctuations in red cell flux in tumor microvessels can lead to transient hypoxia and reoxygenation in tumor parenchyma. *Cancer Res.* **56,** 5522–5528 (1996).
41. Koritzinsky, M. & Wouters, B. G. The roles of reactive oxygen species and autophagy in mediating the tolerance of tumor cells to cycling hypoxia. *Semin. Radiat. Oncol.* **23,** 252–261 (2013).
42. Miao, Z. F. *et al.* Influence of different hypoxia models on metastatic potential of SGC-7901 gastric cancer cells. *Tumour Biol.* **35,** 6801–6808 (2014).
43. Okajima, M. *et al.* Anoxia/reoxygenation induces epithelial-mesenchymal transition in human colon cancer cell lines. *Oncol. Rep.* **29,** 2311–2317 (2013).
44. Salabei, J. K., Gibb, A. A. & Hill, B. G. Comprehensive measurement of respiratory activity in permeabilized cells using extracellular flux analysis. *Nat. Protoc.* **9,** 421–438 (2014).
45. Gurule, S., Goswami, D., Khuroo, A. H. & Monif, T. LC-APCI mass spectrometric method development and validation for the determination of atovaquone in human plasma. *Biomed. Chromatogr.* **24,** 497–505 (2010).
46. Porta, V. *et al.* HPLC-UV determination of metformin in human plasma for application in pharmacokinetics and bioequivalence studies. *J. Pharm. Biomed. Anal.* **46,** 143–147 (2008).
47. Chaiyarit, S. & Thongboonkerd, V. Comparative analyses of cell disruption methods for mitochondrial isolation in high-throughput proteomics study. *Anal. Biochem.* **394,** 249–258 (2009).

48. Moss, J. *et al.* Break-induced ATR and Ddb1-Cul4(Cdt)(2) ubiquitin ligase-dependent nucleotide synthesis promotes homologous recombination repair in fission yeast. *Genes Dev.* **24,** 2705–2716 (2010).

## Acknowledgements

We thank Graham Brown, Lucy Sansom, Daniel V. Ebner and Alison Howarth for technical assistance. EF5 (2-(2-Nitro-1H-imidazol-1-yl)-*N*-(2,2,3,3,3-pentafluoropropyl) acetamide) was a gift from the laboratory of Cameron Koch. The funding sources were Cancer Research UK, Medical Research Council and National Institute for Health Research Biomedical Research Centre, Oxford. G.S.H. is supported by a Cancer Research UK Clinician Scientist Award (Grant number C34326/A13092).

## Author contributions

T.M.A. designed, executed and analysed all experiments with the following exceptions: E.F. and T.M.A. conducted the *in vivo* experiments. S.A. contributed to the experiments in hypoxic conditions. L.K.F. and M.S. performed the HPLC. M.S. formulated the atovaquone for the *in vivo* studies. M.H. performed the spheroid regrowth experiments and T.M.A. analysed the data. G.P. contributed to the analysis of the spheroid data. C.J.K. and F.M.B. advised on the screen design and analysis, respectively. G.S.H., W.G.McK. and R.J.M. supervised the project. T.M.A. wrote the article with advice from G.S.H., W.G.McK., R.J.M., L.A.K.-S. and E.M.H.

## Additional information

**Supplementary Information** accompanies this paper at http://www.nature.com/naturecommunications

**Competing financial interests:** The authors declare no competing financial interests.

**Reprints and permission** information is available online at http://npg.nature.com/reprintsandpermissions/

**How to cite this article:** Ashton, T. M. *et al.* The anti-malarial atovaquone increases radiosensitivity by alleviating tumour hypoxia. *Nat. Commun.* 7:12308 doi: 10.1038/ncomms12308 (2016).